FERMILAB-THESIS-2025-22

STUDY OF NEUTRINO OSCILLATIONS AND FLUX SYSTEMATICS IN THE NOνA EXPERIMENT AT FERMILAB

A THESIS

Submitted to the

PANJAB UNIVERSITY, CHANDIGARH

For the Award of

DOCTOR OF PHILOSOPHY

2025

in

FACULTY OF SCIENCE

BY

PRACHI SHARMA

GUIDE

Prof. VIPIN BHATNAGAR

DEPARTMENT OF PHYSICS
PANJAB UNIVERSITY
CHANDIGARH, INDIA

DEPARTMENT OF PHYSICS
PANJAB UNIVERSITY, CHANDIGARH-160 014 (INDIA)

Phone: 91-172-2541741
EPABX: 91-172-2534466, 2534446
Email: casphy@pu.ac.in
physics@pu.ac.in

No.PHS/ 3015/PHS

Date 01/12/25

CORRECTION CERTIFICATE

It is certified that there were no specific corrections recommended by the examiner of **Ms. Prachi Sharma** in her Ph.D. thesis entitled **"STUDY OF NEUTRINO OSCILLATIONS AND FLUX SYSTEMATICS IN THE NOvA EXPERIMENT AT FERMILAB"**. The thesis submitted by **Ms. Prachi Sharma** in the present form, is acceptable.

Vipin Bhatnagar

(Prof. Vipin Bhatnagar)
Deptt.of Physics
Panjab University
Chandigarh
(Supervisor)

S.K. Tripathi

(Prof.Surya Kant Tripathi)
Deptt. of Physics
Panjab University
Chandigarh
(Chairperson)
Chairperson
Department of Physics
Panjab University
Chandigarh-160014

MARCH 2025

DECLARATION

I declare that the thesis entitled **"STUDY OF NEUTRINO OSCILLATIONS AND FLUX SYSTEMATICS IN THE NOνA EXPERIMENT AT FERMILAB"** has been prepared by me under the guidance of Prof. Vipin Bhatnagar, Professor, Department of Physics, Panjab University, Chandigarh. No part of this thesis has formed the basis for the award of any degree or fellowship previously.

Prachi Sharma

Department of Physics,
Panjab University,
Chandigarh, 160014

DATE:

This Thesis is

Dedicated to

My Family

for their

endless

sacrifices &

unwavering support.

Acknowledgements

I extend my deepest gratitude to Prof. Vipin Bhatnagar for his invaluable guidance, unwavering support, and encouragement. His technological expertise has inspired me to explore new techniques and stay updated with advancements, while his trust allowed me the freedom to pursue my research.

I am thankful to Prof. Suryakant Tripathi, Head of the Department of Physics, Panjab University, Chandigarh, for ensuring that I had access to all the necessary facilities for my research. I also extend my gratitude to the technical, computing, and purchase section staff of the Department of Physics at Panjab University, as well as the HEP office at Panjab University, for their assistance and support throughout my academic journey.

My heartfelt thanks go to my mentors at Fermilab, Dr. Leo Bellantoni, Dr. Jonathan Paley, and Dr. Pavel Snopok, for their invaluable mentorship, weekly meetings, and for making my stay at Fermilab a smooth and enriching experience. I am also grateful to the spokespersons of the NOνA Experiment, Dr. Alex Himmel and Dr. Patricia Vahle, and the spokespersons of EMPHATIC, Dr. Jonathan Paley and Dr. Laura Fields, for hosting me at Fermilab. Furthermore, I extend my gratitude to the NOνA and EMPHATIC collaborations for their support and for providing an intellectually stimulating environment.

I am deeply grateful to my labmates at Panjab University, including Riya Gaba, Dr. Jyoti Babbar, Dr. Jyoti Tripathi, Dr. Harjot Kaur, Dr. Amandeep Kaur Virdhi, Dr. Amandeep Kaur, Dr. Sunil Kumar, Dr. Kanishka, Dr. Maitreyee Mukherjee, Aayushi Singla, Tanvi Sheokand, Bhumika Mehta, Anureet Kaur, Latika, Dr. Sandeep Kumar, and Dr. Rajat. Additionally, I extend my gratitude to the wonderful individuals I met at Fermilab, including Dr. Abhishek Tripathi and his wife Nupur, Shivam Choudhary, Lipsarani Panda, Daniel Correla, Barnali Bhrama, Ishwar Singh, and Robert Chirco.

Above all, I owe my deepest gratitude to my family. My parents, Dr. P.P. Sharma and Mrs. Kiran Sharma, have been my role models, providing unwavering support and encouragement. My brother, Mr. Parth Sharma, has been my best friend throughout this journey, and I feel incredibly fortunate to have a family that serves as a close-knit support group where I can share anything and everything. My husband, Mr. Ankit Nautiyal, has been a pillar of strength, standing by my side through every challenge, offering patience, encouragement, and unconditional support. I am truly blessed to call him my better half. I am also grateful to my in-laws for their kindness, support, and encouragement throughout this journey. I also wish to acknowledge my best friend, Sheenu Sharma, who, after 12 years of friendship, is more like a sister to me. The blessings of my grandparents, whose unwavering support, kindness, and humility have guided me, have been instrumental in shaping my path.

I am sincerely grateful to the funding agencies, including CSIR (Council of Scientific & Industrial Research) and DST (Government of India) and Fermilab Neutrino Division, U.S. Department of Energy, for financially supporting my research throughout this journey.

Lastly, I offer my heartfelt thanks to Lord Mahasu for granting me this extraordinary opportunity, guiding me through challenges, and blessing me with the strength and perseverance to complete this journey.

Date: ***[Prachi Sharma]***

Abstract

The Standard Model of particle physics explains many experimental results using three generations of quarks, leptons, and their interactions, but fails to account for phenomena such as neutrino masses, matter-antimatter asymmetry, gravity, and the hierarchy problem. The study of neutrinos, especially neutrino oscillations, is crucial for advancing Beyond Standard Model physics and the future of particle physics.

Experiments employ powerful accelerator-based neutrino beams to investigate the properties and interactions of the elusive fundamental particles. The NOνA experiment uses two identical detectors: one near detector at Fermilab and one far detector 810 km away in northern Minnesota. NOνA utilizes the NuMI beam facility at Fermilab to generate a 99% pure beam of muon neutrinos. The near detector records a high rate of neutrino interactions, providing an excellent opportunity to study neutrino flux and interactions. For precise oscillation analysis and accurate cross-section measurements, a precise prediction of the neutrino flux is necessary. This thesis discusses the simulations of the NuMI beam and reports comparisons of neutrino flux and its parental flux predictions between the old and new Geant 4 based simulations i.e. g4numi (G4.9.2) and new g4numi (G4.10.04) respectively. Additionally, studies at various virtual detector planes downstream of Horn 1 in the NuMI Beamline are presented.

The EMPHATIC, a Fermilab table-top experiment using a Halbach array magnet to measure secondary particle momentum is also explored. The Phase 1 magnet uses Neodymium permanent magnets and is modeled with COMSOL Multiphysics® Software to create a magnetic field map. The fitting approach presented fits the model to Hall probe data measurements and determines a 1 mm-spacing map of the entire magnet volume, as well as extending beyond the measured volume, using COMSOL.

Furthermore, experimental properties of an assembled straw tube and simulation studies with Garfield++ are presented. This straw tube tracking detector is used in the Near Detector for the DUNE long-baseline neutrino experiment at Fermilab. Our group at Panjab University assembled a single straw tube and designed a prototype for the SAND STT modules. Simulation studies with GARFIELD++ for different gas mixtures are reported.

Contents

List of Figures

List of Tables

Chapter 1

Introduction

Neutrinos are one of the most abundant and elusive particles in the Universe. The neutrino, a fermion with no electric charge and nearly negligible mass, primarily interacts through the weak force and to a lesser extent through gravitational interactions, albeit stronger than that of most elementary particles. In the last fifteen years, neutrinos have been at the forefront of fundamental discoveries in particle physics, with the discovery of the Higgs boson being a notable exception. Neutrinos are the neutral counterparts to the charged leptons (e^-, μ^-, τ^-) and like other leptons in the Standard Model (SM), they exist in three flavors: electron (ν_e), muon (ν_μ), and tau (ν_τ) neutrinos.

The discovery of radioactivity and the perplexing continuous electron energy spectrum in beta decay [1] led prominent physicists like Niels Bohr in the 1920s to doubt the validity of energy conservation in this process. In 1930, Wolfgang Pauli reinstated confidence in energy conservation by postulating the existence of a neutral, light, spin 1/2 particle [2]. Four years later, Enrico Fermi named this particle the neutrino in his theory of β-decay.

The first experimental confirmation of neutrinos, observed as anti-neutrinos, was a Nobel Prize-winning achievement by Clyde Cowan and Frederic Reines [3]. Their experiment used a large interaction volume filled with water and cadmium as a liquid scintillator near a nuclear reactor. The recorded signal had two parts: a

rapidly annihilating positron signal and a neutron capture in the cadmium, which caused a photon signature from nuclear de-excitation. This initial discovery was of an electron antineutrino, one of the three types of neutrinos, detected through an inverse beta decay reaction.

$$p + \overline{\nu_e} \longrightarrow n + e^- \tag{1.1}$$

The muon neutrino was discovered in 1962 during the Brookhaven Experiment [4], which led to the Nobel Prize in Physics being awarded in 1988 for its discovery and the innovative neutrino beam technique employed [5]. In 1998, the DONUT experiment at Fermilab inferred the tau neutrino (ν_τ)[6]. Brookhaven utilized a 10-ton aluminum spark chamber to study pion decays that generated neutrinos and muons, while DONUT used emulsion cloud chambers to detect tau neutrinos from the leptonic decays of mesons. Figure 1.1 illustrates a chronological timeline of key milestones and discoveries in neutrino research over the years.

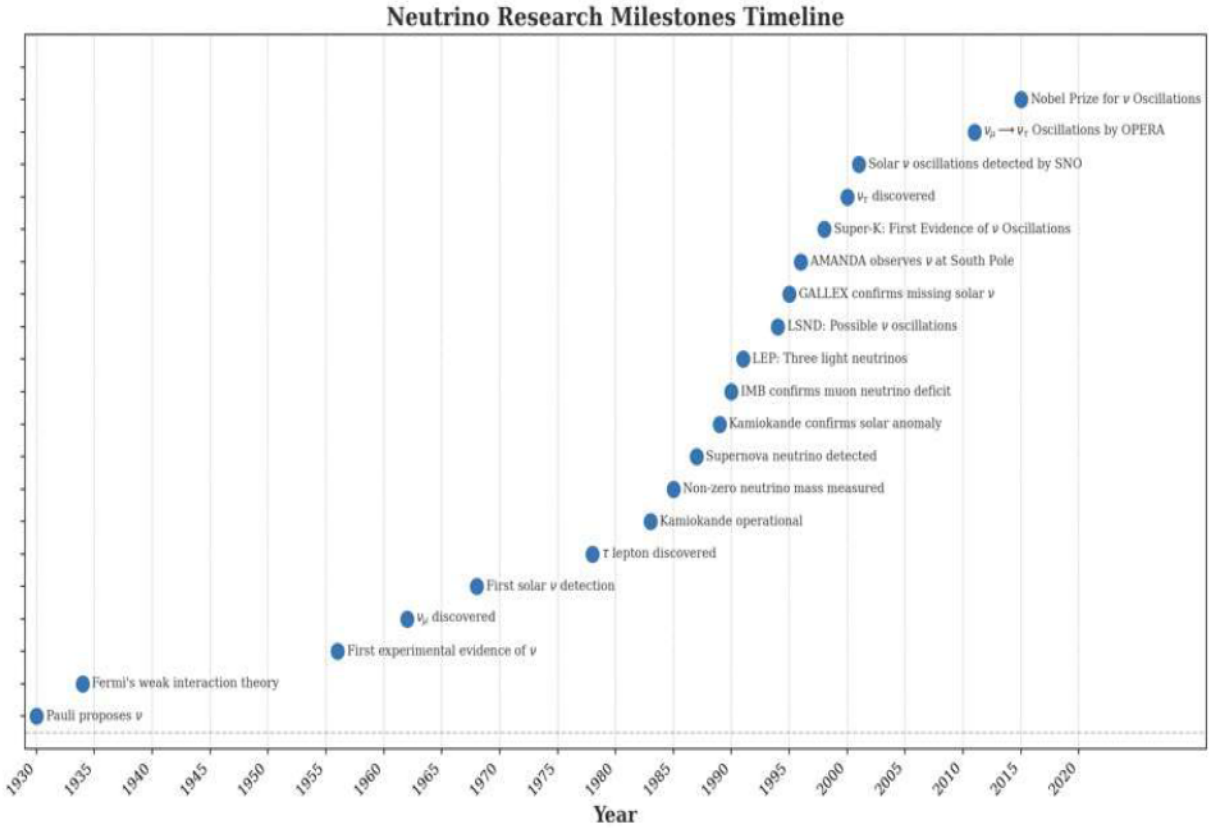

Figure 1.1: Neutrino Research: Major Milestones and Discoveries Timeline

As neutrinos have an extremely low interaction cross-section, the neutrino experiments require either a powerful neutrino source or large detectors to gather sufficient interactions for measurements. Particle accelerators provide a controlled means of generating neutrino beams with specific intensity, energy distribution, and composition. This capability makes them well-suited for experiments requiring high-statistics data and a well-defined neutrino energy spectrum for precise measurements. The reliability of these measurements depends on accurately characterizing the neutrino flux produced by the accelerator. Determining the neutrino flux and minimizing associated uncertainties are fundamental aspects of any neutrino experiment, often requiring extensive collaborative efforts.

Several high-intensity neutrino beam facilities are currently in operation, including the Neutrinos from the Main Injector (NuMI) [7] in the United States and the Tokai to Kamioka (T2K) [8] in Japan. Furthermore, the Long Baseline Neutrino Facility (LBNF) [9] is being developed in the United States to support future experiments. Accurately determining the neutrino flux and minimizing uncertainties are essential components for achieving the physics objectives of accelerator-based neutrino experiments. Neutrino beams in laboratories are typically generated by directing a high-intensity proton beam onto a dense target made of light material, producing hadrons that yield neutrinos. The process of measuring the production of these hadrons is referred to as hadron production measurements. Notable examples of such experiments include HARP, MIPP, NA61/SHINE, and EMPHATIC. The data from these experiments are crucial for accurately predicting the neutrino flux in neutrino oscillation experiments, which are essential for understanding the complex properties of neutrinos.

1.1 The Standard Model and Neutrinos

The Standard Model of particle physics provides a concise framework for understanding the composition of matter in the universe, detailing its fundamental components and how they interact. Matter is primarily composed of fermions categorized into

leptons and quarks, distinguished by intrinsic properties and interactions mediated through exchange of gauge bosons. The fundamental bosons responsible for mediating interactions include the photon (γ) for electromagnetism, the gluon (g) for the strong force, and the Z^0 and $W^{\pm}$ bosons for weak interactions. Each of these particles has a corresponding antiparticle with opposite quantum numbers. Furthermore, the Higgs boson (H) plays a vital role in explaining the mechanism by which particles acquire mass.

Quarks, which experience strong, weak, and electromagnetic interactions, exist in six flavors: up (u), down (d), charm (c), strange (s), top (t), and bottom (b). These quarks are arranged in three generations of doublets, where the upper quarks possess an electric charge of $+\frac{2}{3}$, while the lower quarks carry a charge of $-\frac{1}{3}$.

Similarly, leptons are categorized into six types: three charged ones—electron (e), muon (μ), and tau (τ)—and their three associated neutrinos—electron neutrino (ν_e), muon neutrino (ν_μ), and tau neutrino (ν_τ). While charged leptons engage in both electromagnetic and weak interactions, neutrinos interact solely via the weak force.

Figure 1.2 shows the particles of the Standard Model (SM) include spin-1/2 fermions, consisting of quarks and leptons. The three columns represent the three generations of these fermions. The spin-1 vector bosons and the Higgs scalar boson are also represented. Additionally, the graviton, which lies outside the Standard Model, is shown separately.

The initial description in the SM did not specify the mass of neutrinos, leading to the conventional assumption that they were massless and had a single chirality: left-handed for neutrinos and right-handed for anti-neutrinos. However, the discovery of neutrino oscillations has demonstrated that neutrinos do have mass. Neutrino oscillations are a quantum mechanical interference phenomenon where the detected flavour of a neutrino can differ from its originally measured flavour due to the mixing of mass states (ν_1, ν_2, ν_3) and flavour states (ν_e, ν_μ, ν_τ). This will be explained in more detail in section 1.3.

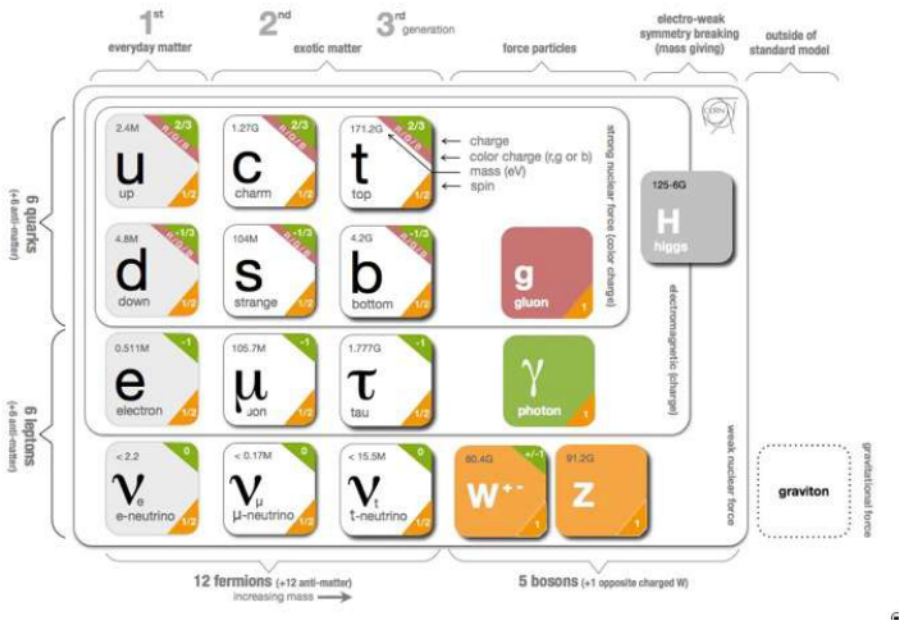

Figure 1.2: Standard Model of Particle Physics Infographic [10]

1.2 Neutrino Interactions

Neutrinos are never observed directly; instead, their presence is inferred through indirect detection in particle interactions. These interactions are comprehensively explained within the Standard Model (SM). Neutrinos interact solely through the weak force, mediated by three bosons: the positively charged W^+, negatively charged W^-, and neutral Z^0 bosons.

There are two distinct pathways determined by which boson mediates the interaction when a neutrino interacts with matter. When the exchanged boson is a W, it constitutes the charged-current (CC) channel. In this process, a neutrino transforms into its corresponding lepton flavor, with the W boson chosen such that electric charge is conserved during the interaction. Conversely, when the exchanged boson is a Z, it constitutes the neutral-current (NC) channel, where no conversion occurs.

Figure 1.3 illustrates two Feynman diagrams: the left diagram represents the CC channel, and the right diagram represents the NC channel.

Figure 1.3: Feynman diagram for charged current (left) and neutral current (right) electron neutrino interaction.

NC interactions follow a standard pattern:

$$\nu_\alpha + N \longrightarrow \nu_\alpha + X \tag{1.2}$$

$$\overline{\nu_\mu} + N \longrightarrow \overline{\nu_\mu} + X \tag{1.3}$$

In this context, N signifies a nucleon, which may be either a proton or a neutron. The symbol α corresponds to any lepton flavor, including e, μ, or τ, while X represents a specific set of hadrons resulting from the interaction. The first equation describes neutrino interactions, whereas the second one corresponds to antineutrino interactions. Since neutrinos themselves are not directly detectable, information about the interaction is inferred solely from what is observed in the target nucleus. Therefore, distinguishing between different neutrino flavors in NC interactions is not feasible [11].

Charged current (CC) interactions occur via the exchange of the charged $W^\pm$ boson. In these processes, the lepton flavor remains unchanged, as evidenced by the production of a corresponding charged lepton in the final state:

$$\nu_\alpha + N \longrightarrow l_\alpha^- + X \tag{1.4}$$

$$\overline{\nu_\alpha} + N \longrightarrow l_\alpha^+ + X \tag{1.5}$$

Here, l_α represents a charged lepton, and the other symbols retain their previous meanings.

There are three main types of CC neutrino interactions that describe how a neutrino interacts with a nucleus. These are quasi-elastic scattering (QE), where the neutrino scatters off a nucleon and potentially knocks it out of the nucleus, resonant pion production (RES), where the neutrino excites a nucleon to a resonance state like Δ^{++}, and deep inelastic scattering (DIS), where the neutrino transfers sufficient momentum to resolve individual quark constituents within the nucleus, causing it to fragment into a shower of hadrons. Less frequent neutrino interaction mechanisms include coherent scattering (COH), where the neutrino interacts collectively with the entire nucleus, and meson exchange currents (MEC), which involve interactions between nucleon pairs. The overall neutrino interaction cross section is obtained by summing the contributions from each of these interaction modes.

Neutrino interactions with nuclei exhibit considerable variation depending on energy levels. For low energies ($E_\nu < 1$ GeV), quasielastic (QE) interactions are the most prominent. Resonance (RES) interactions peak in the energy range of 1 GeV to 3 GeV. At energies exceeding 10 GeV ($E_\nu > 10$ GeV), deep inelastic scattering (DIS) interactions dominate.

These interactions, characterized by their dependence on energy and respective cross-sections, are illustrated in Figure 1.4. This figure demonstrates the predominant type of interaction at various energy ranges and provides details regarding the total cross-section for neutrino and antineutrino interactions [11].

The cross sections for various interaction modes in the few GeV energy range are relatively small, approximately $\sigma \approx 10^{-38}$ cm^2, as illustrated in Figure 1.4. However, these measurements are not well-constrained, with uncertainties generally around 20%. Such large uncertainties pose a major challenge for both ongoing and upcoming neutrino experiments, often contributing significantly to the overall systematic uncertainty in precise neutrino measurements.

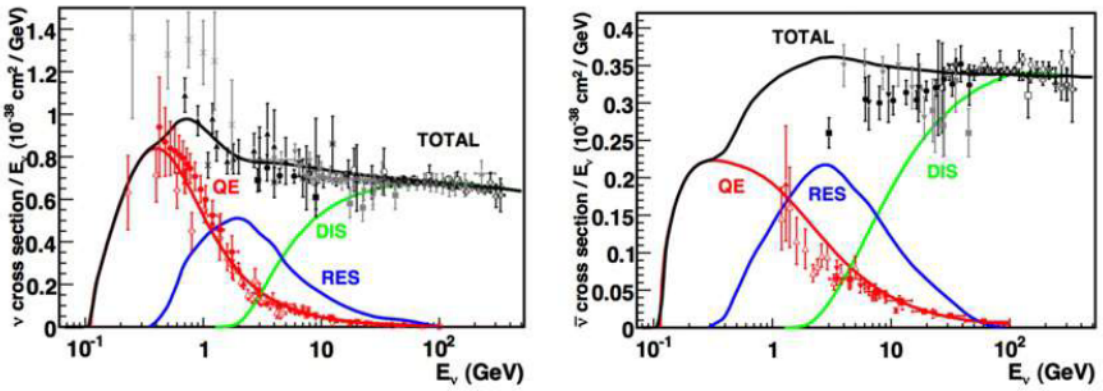

Figure 1.4: Graphs depicting the cross-section variations for different interaction modes as a function of neutrino energy, with neutrino interactions on the left and antineutrino interactions on the right.

1.3 Neutrino Oscillations

According to the Standard Model, neutrinos were believed to be without mass. This meant that experiments involving muon neutrinos would only result in muons through CC interactions, while electron neutrinos would exclusively produce electrons—indicating no mixing among the three active neutrino flavors. However, experimental evidence has shown that muon neutrinos can sometimes transform into electrons, and vice versa. The theory of neutrino oscillations was first proposed by Pontecorvo in the 1950s [12], but his early work did not fully describe the oscillation theory as it is now understood, due to the initial belief in only one flavor of neutrino. The first signs of neutrino oscillations emerged in 1968 [13], when Ray Davis conducted an experiment in the Homestake mine to measure electron neutrinos from the Sun, confirming theoretical models of solar nuclear processes. Shielded deep underground to minimize interference from cosmic rays, the experiment counted ^{37}Ar atoms produced through the process $\nu_e + ^{37}Cl \longrightarrow e^- + ^{37}Ar$, finding an interaction rate about one-third of theoretical predictions. In 1998, the Super Kamiokande experiment provided definitive evidence that neutrinos change flavor as they travel [11]. The Nobel Prize in Physics in 2015 recognized Takaaki Kajita and Arthur B. McDonald for their contributions to understanding neutrino flavor transformation and confirming neutrino mass. Neutrino oscillations provide compelling evidence

that neutrinos have mass, a property not accounted for in the Standard Model. Consequently, they represent the only confirmed experimental indication of physics extending beyond the Standard Model.

1.3.1 Neutrino Mixing

The fundamental concept of neutrino oscillations involves the mixing of neutrino flavor states $(\nu_e, \nu_\mu, \nu_\tau)$ and mass states (ν_1, ν_2, ν_3). This implies that the neutrino flavor states, represented as $|\nu_\alpha\rangle$, are linear combinations of the mass eigenstates, $|\nu_i\rangle$. Mathematically, this relationship is expressed as[14]:

$$|\nu_\alpha\rangle = \sum_k U^*_{\alpha k} |\nu_k\rangle \tag{1.6}$$

wherein parameter α represents the three neutrino flavor states $(\alpha = (e, \mu, \tau))$, while k denotes the mass states $(k = (1, 2, 3))$. The unitary matrix U facilitates the transformation between the mass eigenstate basis and the flavor eigenstate basis, governing the relationship between neutrino flavors and their corresponding masses.

In matrix notation, these oscillations are described by the Pontecorvo-Maki-Nakagawa-Sakata (PMNS) matrix [14]::

$$\begin{pmatrix} \nu_e \\ \nu_\mu \\ \nu_\tau \end{pmatrix} = \begin{pmatrix} U_{e1} & U_{e2} & U_{e3} \\ U_{\mu 1} & U_{\mu 2} & U_{\mu 3} \\ U_{\tau 1} & U_{\tau 2} & U_{\tau 3} \end{pmatrix} \begin{pmatrix} \nu_1 \\ \nu_2 \\ \nu_3 \end{pmatrix} \tag{1.7}$$

Thus, an electron neutrino, generated through a charged current weak interaction alongside a positron, travels as a linear combination of the mass eigenstates:

$$|\psi\rangle = U_{e1}|\nu_1\rangle + U_{e2}|\nu_2\rangle + U_{e3}|\nu_3\rangle \tag{1.8}$$

During a charged current interaction, the wavefunction collapses to a specific weak eigenstate, resulting in the production of a charged lepton of a specific flavor. Variations in the masses of the three neutrino mass eigenstates cause phase discrepancies

among their contributions to the neutrino wavefunction. Consequently, there exists a probability that the observed lepton flavor upon interaction differs from the lepton flavor associated with the initial production of the neutrino. This phenomenon is known as neutrino oscillations. This section will delve into two-flavor and three-flavor neutrino oscillations, as well as neutrino oscillations in the presence of matter.

1.3.2 Neutrino Oscillations of Two Flavours

In numerous experimental scenarios, it is often sufficient to approximate neutrino oscillations by considering only two neutrino flavors, rather than the full three-flavor mixing. The primary characteristics of neutrino oscillations can be effectively described using just two neutrino flavors, ν_α and ν_β. In this two-flavor model, the weak eigenstates and mass eigenstates are connected by a 2×2 unitary matrix characterized by a mixing angle θ,

$$\begin{pmatrix} \nu_\alpha \\ \nu_\beta \end{pmatrix} = \begin{pmatrix} Cos\theta & Sin\theta \\ -Sin\theta & Cos\theta \end{pmatrix} \begin{pmatrix} \nu_1 \\ \nu_2 \end{pmatrix} \tag{1.9}$$

Therefore, the wavefunction ν_α, formed as a combination of ν_1 and ν_2, evolves over time t in position-space $\vec{x}$ as described by:

$$|\psi(\vec{x}, t)\rangle = \cos\theta|\nu_1\rangle e^{-i\phi_1} + \sin\theta|\nu_2\rangle e^{-i\phi_2} \tag{1.10}$$

Here, $\phi_i = E_i t - \vec{p_i} \cdot \vec{x}$ represents a phase factor involving the energy E_i and three-momentum $\vec{p_i}$ of the ν_i mass state. Equation 1.10 can be expressed as a linear combination of weak eigenstates by inverting Equation 1.9. The probability that a neutrino initially in the ν_α state oscillates to the ν_β state upon interaction, after propagating a certain distance, is given by:

$$P(\nu_\alpha \to \nu_\beta) = |\langle\nu_\beta|\psi(\vec{x}, t)\rangle|^2 = \sin^2 2\theta \, \sin^2\left(\frac{\phi_2 - \phi_1}{2}\right) \tag{1.11}$$

Assuming that the neutrino mass eigenstates have identical energy E and travel

relativistically over a distance $L = |\vec{x}|$, the difference in phase factors can be approximated as:

$$\phi_2 - \phi_1 \approx (m_2^2 - m_1^2)\frac{L}{2E} \tag{1.12}$$

Here, m_2^2 and m_1^2 denote the squared masses of the ν_2 and ν_1 mass eigenstates respectively. Substituting this approximate phase difference into Equation 1.11 provides the two-flavor oscillation probability, tailored to the typical length and energy scales observed in neutrino oscillation experiments. In terms of GeV for energy, eV^2 for mass-squared differences, and kilometers for distance, the two-flavour oscillation probability finally becomes:

$$P(\nu_\alpha \to \nu_\beta) = \sin^2(2\theta)\sin^2\left(1.27 \cdot \frac{\Delta m_{21}^2[eV^2] \cdot L[km]}{E[GeV]}\right) \tag{1.13}$$

where $\Delta m_{21}^2 = m_2^2 - m_1^2$. The probability of a neutrino maintaining its initial flavor upon interaction, known as the survival probability, is simply given by $P(\nu_\alpha \to \nu_\alpha) = 1 - P(\nu_\alpha \to \nu_\beta)$.

In experimental planning, it is crucial to optimize variables such as the baseline length L and the neutrino beam energy E to maximize the probability of observing neutrino oscillations. This optimization can be guided by exploring scenarios where:

$$1.27 \cdot \frac{\Delta m_{21}^2 \cdot L}{E} = \frac{\pi}{2}$$

allowing for calculations to achieve optimal conditions for observing oscillatory behavior.

1.3.3 Neutrino Oscillations of Three Flavours

Oscillation probabilities for multiple neutrino flavors can be determined using the same method as for two-flavor oscillations. Since there are three neutrino flavors, the oscillation framework needs to be extended from two to three flavors. The weak eigenstates are linked to the mass eigenstates through the 3×3 unitary PMNS matrix shown in Equation 1.7. In the case of three flavors, a neutrino initially in the weak

eigenstate ν_j will propagate as a linear combination of the three mass eigenstates, ν_k, and at a later time t, the wavefunction will be

$$|\psi(\vec{x},t)\rangle = \sum_k U_{\mu k} e^{-i\phi k} |\nu_k\rangle \tag{1.14}$$

After expressing the above equation in terms of the weak eigenstates, the probability of detecting a neutrino of flavor ν_e after it has traveled a distance L is

$$P(\nu_\mu \to \nu_e) = |\langle \nu_e | \psi(\vec{x},t)\rangle|^2 = \sum_{k,j} U_{\mu k} U^*_{ek} U^*_{\mu j} U_{ej} e^{-i(\phi_k - \phi_j)} \tag{1.15}$$

Applying the same approximations for the phase differences as outlined in Section 1.3.2, the oscillation probability can be represented as

$$\begin{aligned} P(\nu_\mu \to \nu_e) =& \delta_{\mu e} - 4 \sum_{k>j} \mathrm{Re}(U_{\mu k} U^*_{ek} U^*_{\mu j} U_{ej}) Sin^2 \left(\frac{\Delta m^2_{kj} L}{4E} \right) \\ &+ (-)2 \sum_{k>j} \mathrm{Im}(U_{\mu k} U^*_{ek} U^*_{\mu j} U_{ej}) Sin \left(\frac{\Delta m^2_{kj} L}{4E} \right) \end{aligned} \tag{1.16}$$

where $\delta_{\mu e}$ is the Kronecker delta function. As in Equation 1.13, Δm^2_{kj} represents the squared mass difference between the mass eigenstates ν_k and ν_j, with the valid combinations being Δm^2_{21} and Δm^2_{32}.

The imaginary component of Equation 1.16 changes sign (becomes negative) in the case of $\overline{\nu_\mu} \to \overline{\nu_e}$ antineutrino oscillations, which is the CP conjugate process to $\nu_\mu \to \nu_e$ oscillations. Consequently, if the PMNS matrix elements are complex, $P(\nu_\mu \to \nu_e) \neq P(\overline{\nu_\mu} \to \overline{\nu_e})$. This suggests a potential violation of CP symmetry in three-flavor neutrino oscillations.

In three-flavor oscillations, the PMNS matrix is typically represented in an extended form, incorporating three mixing angles θ_{12}, θ_{23}, and θ_{13}, a CP-violating phase δ_{CP}, and two Majorana phases $\alpha_{1,2}$:

$$U \equiv \begin{pmatrix} 1 & 0 & 0 \\ 0 & c_{23} & s_{23} \\ 0 & -s_{23} & c_{23} \end{pmatrix} \begin{pmatrix} c_{13} & 0 & s_{13}e^{-i\delta_{CP}} \\ 0 & 1 & 0 \\ -s_{13}e^{i\delta_{CP}} & 0 & c_{13} \end{pmatrix} \times \begin{pmatrix} c_{12} & s_{12} & 0 \\ -s_{12} & c_{12} & 0 \\ 0 & 0 & 1 \end{pmatrix} \begin{pmatrix} e^{-i\alpha_1/2} & 0 & 0 \\ 0 & e^{i\alpha_1/2} & 0 \\ 0 & 0 & 1 \end{pmatrix} \tag{1.17}$$

where $s_{ij} = Sin\theta_{ij}$ and $c_{ij} = Cos\theta_{ij}$.

In the decomposition of the mixing matrix U, the first matrix represents the 2-3 sector, also known as the atmospheric component, which predominantly governs the mixing observed in atmospheric neutrinos. It depends on the mixing angle θ_{23}, approximately corresponding to the atmospheric mixing angle θ_{atm}. This sector is studied using atmospheric and accelerator neutrinos with short baselines ($L \leq 104$ km) and high energies ($E \sim 1$ GeV), resulting in a relatively small L/E ratio. The atmospheric sector is associated with a significant mass splitting $\Delta m^2_{32} \approx \Delta m^2_{31} \approx 3 \times 10^{-3}\,\text{eV}^2$.

The second matrix, also called as Cross-Mixing matrix, corresponds to the 13 sector, involving the small mixing angle θ_{13}, which characterizes the ν_e component of ν_3 and may contribute to CP violation. The CP-violating phase δ appears in the mixing matrix only in relation to $\sin\theta_{13}$.

The third matrix is known as the 12 sector or the solar mixing matrix, which dominates the mixing observed in solar neutrinos. The mixing angle θ_{12} approximates the solar mixing angle θ_{sol}, determined from solar neutrino experiments assuming a two-neutrino scenario. This angle is primarily determined through observations of solar neutrinos (with typical distances $L \sim 108$ km) and reactor neutrinos (typically with energies $E \sim 1$ MeV), where the ratio L/E is substantial. The corresponding mass difference is relatively small, approximately $\Delta m^2_{21} \approx 8 \times 10^{-5}\,\text{eV}^2$.

In the fourth matrix of the equation, the Majorana phases are significant only if neutrinos exhibit Majorana behavior. Nevertheless, their specific values do not

affect the computation of oscillation probabilities and can be omitted in Equation 1.17. Therefore, discerning whether neutrinos are of Dirac or Majorana nature via neutrino oscillation studies is not possible. The dynamics of all neutrino oscillations are determined by the three mixing angles, the three mass differences, and δ_{CP}, contingent upon the energy and propagation distance of the neutrinos.

In experimental measurements, another critical consideration is the interaction of neutrinos with the material they traverse before being detected. This matter interaction will be elaborated upon in the following section.

1.3.4 Neutrino Oscillations in Matter

When neutrinos traverse through matter, their oscillations are influenced by the surrounding material, a phenomenon originally explained by L. Wolfenstein and referred to as the matter effect or Mikheyev-Smirnov-Wolfenstein (MSW) effect [15]. This effect stems from the surplus of electrons in matter compared to muons or taus, resulting in coherent forward scattering of electron neutrinos.

In experiments with accelerator-based neutrinos, these particles travel extensive distances through the Earth to reach distant detectors, where the matter effect significantly modifies their oscillation probabilities. While NC interactions affect all neutrino flavors equally and do not substantially impact oscillation measurements, all types of neutrinos can participate in NC interactions involving electrons and nucleons via Z exchange. However, electron neutrinos (ν_e) undergo additional CC interactions that alter their scattering potential. Specifically, ν_e interacts via CC with electrons in matter through W exchange. These interactions introduce additional interaction potentials:

$$V_W = +\sqrt{2} G_F N_e \tag{1.18}$$

$$V_Z = -G_F N_n / \sqrt{2} \tag{1.19}$$

where G_F is the Fermi coupling constant, and N_e and N_n denote the densities

of electrons and neutrons per unit volume, respectively. Assuming matter neutrality, the contribution to coherent forward scattering via Z exchange cancels out contributions from protons and electrons, leaving it determined solely by N_n. The sign of the interaction potential energy V_W changes when neutrinos are substituted with antineutrinos in the beam. This adjustment directly influences the oscillation parameters θ and Δm^2.

The oscillation probability in matter differs from that in vacuum primarily due to the replacement of θ and Δm^2 by their in-matter counterparts:

$$P_M(\nu_e \to \nu_\mu) = \sin^2 2\theta_M \sin^2\left(\Delta m^2_M \frac{L}{4E}\right) \tag{1.20}$$

where $x = \frac{V_W/2}{\Delta m^2/4E}$ measures the importance of the matter effect relative to the neutrino squared mass splitting. The in-matter oscillation parameters Δm^2_M and $\sin^2 2\theta_M$ are defined as:

$$\Delta m^2_M = \Delta m^2 \sqrt{\sin^2 2\theta + (\cos 2\theta - x)^2} \tag{1.21}$$

$$\sin^2 2\theta_M = \frac{\sin^2 2\theta}{\sin^2 2\theta + (\cos 2\theta - x)^2} \tag{1.22}$$

The impact of the matter effect increases with neutrino energy E, as indicated by the parameter x. Moreover, x depends on V_W, the interaction potential energy, which is positive for ν_e and negative for $\overline{\nu}_e$, leading to enhanced oscillation probabilities for neutrinos and reduced probabilities for antineutrinos. This distinction in oscillation probabilities is crucial in long baseline experiments (LBL) that seek to determine the neutrino mass hierarchy and CP phase through measurements of $\nu_\mu \to \nu_e$ transitions.

1.4 Neutrino Oscillation Experiments

Neutrino oscillation experiments study flavor transitions, focusing on mixing angles and mass-squared differences. These are two main types: disappearance experiments, which measure a reduction in the initial neutrino flavor, and appearance experiments, which detect neutrinos of a different flavor after the beam has traveled a certain distance.

For natural sources like the Sun, neutrino energy and distance are constant. Man-made sources allow detectors to be placed at chosen distances, with selectable or fixed neutrino energy. Early experiments studied natural sources, while current ones often use artificial sources like neutrino beams and nuclear reactors.

Neutrino experiments are categorized based on their source, energy, and baseline length. The ratio L/E, expressed in km/GeV, determines sensitivity to specific oscillation parameters. The three components of the PMNS matrix correspond to different mixing angles, each associated with distinct experiment types: atmospheric/accelerator, reactor, and solar neutrino studies, as discussed in Section 1.3.3.

Atmospheric experiments investigate neutrinos produced from cosmic ray interactions, specifically pion decays. These neutrinos originate either above the detector ($L \sim 10$ km) or traverse through the Earth ($L \sim 10^4$ km). The Super-Kamiokande (SuperK) experiment [16] in Japan observed a deficit in upward-going neutrinos, interpreted as ν_μ oscillating into ν_τ, with minimal impact on ν_e flux. These studies primarily probe θ_{23} and Δm_{32}.

Accelerator experiments explore atmospheric oscillation parameters by generating controlled neutrino beams in particle accelerators. This setup allows precise adjustments of the neutrino baseline, energy, and composition. Energy ranges typically span from 10^{-1} GeV to 10^{1} GeV, with baselines varying from $L \approx 1$ km in short-baseline experiments to 10^2–10^3 km in long-baseline experiments. Short-baseline experiments target high-frequency oscillations with large Δm^2, including LSND [17] and the SBN program [18]. Long-baseline experiments focus on atmospheric oscillation parameters and enable measurements of δ_{CP}, mass ordering, and

the θ_{23} octant via appearance channels. NOνA exemplifies a long-baseline experiment, alongside T2K [8], MINOS [19], and future projects like Hyper-K [20] and DUNE [21]. Further details on accelerator neutrino beams are provided in Section 1.5.

Reactor experiments study the disappearance of $\overline{\nu_e}$ emitted from β-decay in nuclear reactors. These experiments primarily determine θ_{13}, the last of the three mixing angles to be measured. Non-zero values for all three mixing angles are necessary for CP violation. Typical reactor experiments operate with baselines of approximately 1 km and energy ranges between 10^{-3} GeV and 10^{-2} GeV. Notable examples include Double Chooz [22], Daya Bay [23], and RENO [24].

Solar neutrino experiments analyze ν_e produced through fusion reactions in the Sun. Due to matter effects within the Sun's core, the ν_e state is nearly identical to the ν_2 mass state. Observations indicate that the detected ν_e flux is significantly lower than predictions. The Sudbury Neutrino Observatory (SNO) [13] resolved this discrepancy by detecting neutral current interactions involving all neutrino flavors, which matched expectations, unlike charged current interactions limited to ν_e. Other significant solar neutrino experiments include Kamiokande [25], SAGE [26], and GALLEX [27].

1.5 Accelerator Neutrino Beams

Generating a man-made neutrino beam involves several stages. Initially, a hadron beam, often composed of protons, is accelerated within an accelerator complex and directed to collide with a target. There are two primary types of targets used. In the first method, a dense material block serves as a beam dump, absorbing most protons and their long-lived secondary particles. However, short-lived particles like charmed mesons decay into neutrinos before interacting further, thereby producing a neutrino beam. This is known as the beam dump method.

The second method involves directing the accelerated proton beam onto a light nuclear target, such as carbon or beryllium, which produces various particles. Mag-

netic horns, made of aluminum and generating a toroidal magnetic field when an electric current passes through, are then used to select particles based on their charge. By controlling the current direction, the horns [28] can focus either positively or negatively charged particles. These particles travel through a decay volume long enough for them to decay into neutrinos, primarily producing muon neutrinos from pion and kaon decays. Positively charged hadrons result in neutrino beams, while negatively charged ones create anti-neutrino beams. The decay volume is either filled with helium or maintained under vacuum to minimize interactions.

Following the decay volume, a beam dump captures the majority of the leftover charged particles in the beam. However, high-energy muons can escape and are detected by muon monitors placed beyond the dump. These monitors help measure the beam's intensity and direction. Other particles are absorbed by the surrounding soil, allowing only neutrinos to continue in the intended direction, resulting in a focused, narrow-band neutrino beam. The initial part of Figure 1.5 illustrates a general setup of a Laboratory Beamline. The prominent beamlines discussed in this thesis are NuMI [29] and the test beam at the Fermilab Test Beam Facility (FTFP) [30].

1.6 Motivation

1.6.1 Importance of Neutrino Flux Determination

Precision in determining neutrino oscillation phenomena presents significant challenges. Achieving this requires precise knowledge of the un-oscillated neutrino flux. In long-baseline neutrino experiments, a conventional neutrino beam (discussed in Section 1.5) is utilized alongside two detectors: one placed near the neutrino production source, known as the near detector (ND), and another located further away, referred to as the far detector (FD). The positioning of the far detector, along with the energy spectrum of the beam, is optimized to capture oscillation maxima. Since both detectors observe the same neutrino beam, systematic uncertainties associated

with neutrino flux variations, cross-section modeling, and detector performance differences are significantly reduced. The dual-detector setup is depicted in Figure 1.5.

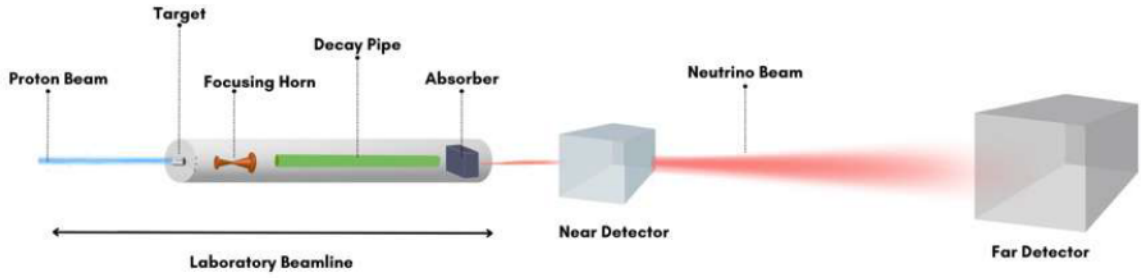

Figure 1.5: Setup of a General Long Baseline Experiment (Note: Not to Scale)

Understanding neutrino oscillation probabilities relies heavily on accurately determining the cross-section. This can be expressed as:

$$P(E_i) = \left(\frac{N_2}{N_1}\right)_i \left(\frac{A_1}{A_2}\right)_i \left(\frac{\phi_1}{\phi_2}\right)_i \tag{1.23}$$

Here, A_1 and A_2 denote the acceptance and efficiency of the respective detectors, while ϕ_1 and ϕ_2 correspond to the neutrino fluxes at each detector. The quantities N_1 and N_2 represent the number of detected events within a specific energy bin. Near Detector has $N_1 = (\phi_1 \sigma A_1)$ and the Far Detector has $N_2 = P(\phi_2 \sigma A_2)$ where σ is the neutrino-nucleon cross section, A is the acceptance and P is the oscillation probability.

Achieving precise accuracy in these measurements is challenging. Flux uncertainties are only partially mitigated because the near detector detects neutrinos from a spread-out source, while the far detector observes them as originating from a point source (e.g., like the NOνA far detector situated 810 km away). Additionally, cross-sections may not cancel out completely if detectors differ in their material composition, response characteristics, or acceptance rates.

Thus, flux uncertainties are crucial in accelerator neutrino experiments, impacting cross-section calculations and influencing predictions of baselines, single-detector

measurements, and neutrino backgrounds in searches beyond the Standard Model (BSM). These uncertainties stem from interactions within materials like the target and horn, as well as from insufficiently characterized energy or phase spaces. Enhancing the precision of flux predictions requires acquiring more detailed data on hadron production. A more detailed discussion on flux uncertainties is presented in Chapter 3.

1.6.2 Need for direct hadron production measurements

As discussed previously, generating a neutrino beam is a complex process. Approximately 90% of the neutrinos produced originate from hadron decays within the target. Others come from decays of particles resulting from interactions of secondary hadrons, such as those occurring in magnetic horns outside the target. Understanding the neutrino source is crucial for making accurate oscillation measurements. However, installing a detector in the intense beam of secondary hadrons following the target can disrupt the beam's evolution. Another method involves utilizing extensive Monte Carlo simulations of the entire process of generating the neutrino beam. Yet, these simulations can exhibit notable discrepancies in predicting hadron production, thereby influencing the composition and energy spectrum of the neutrino beam across specific momentum and angular ranges [31].

Due to the limitations of both direct measurements and simulations, uncertainties in neutrino flux at accelerator-based experiments are predominantly influenced by interactions in the hadronic beamline. To mitigate these uncertainties, data from external experiments on hadron production are used to constrain Monte Carlo models. These reference data provide information on interaction cross-sections and particle yields, often described in terms of momentum-angle phase space. It is important to note that Monte Carlo models continue to evolve with advancements in hadron production data.

The T2K experiment and the upcoming Hyper-K study neutrino oscillations using a neutrino beam produced by 30 GeV protons striking a graphite target at J-

PARC. At Fermilab, the NuMI beam is generated by 120 GeV protons on a graphite target, while the BNB beam originates from 8 GeV protons on beryllium. The DUNE experiment will utilize a newly designed beam, created using protons in the 60–120 GeV range impacting a graphite target. In each case, secondary interactions occur as hadrons interact with the target, focusing horns, and the walls of the decay region.

In accelerator-based neutrino experiments, the dominant systematic uncertainty in flux predictions originates from uncertainties in hadron production cross sections. Figure 1.6 illustrates the fractional flux uncertainty for the NuMI beam at the NOνA near detector, while Figure 1.7 presents the corresponding uncertainty for the LBNF on-axis beam at the DUNE far detector. Both NuMI and LBNF flux estimations consider a 40% uncertainty for secondary and tertiary interactions. Thus, the flux uncertainties for accelerator neutrino measurements remain large (~10%), primarily due to insufficient knowledge of interactions in target and focusing horn materials, especially at low energies. More low-energy proton and pion scattering data are needed to improve hadron production and flux predictions—one of the key goals of the EMPHATIC experiment, as discussed in Chapter 4.

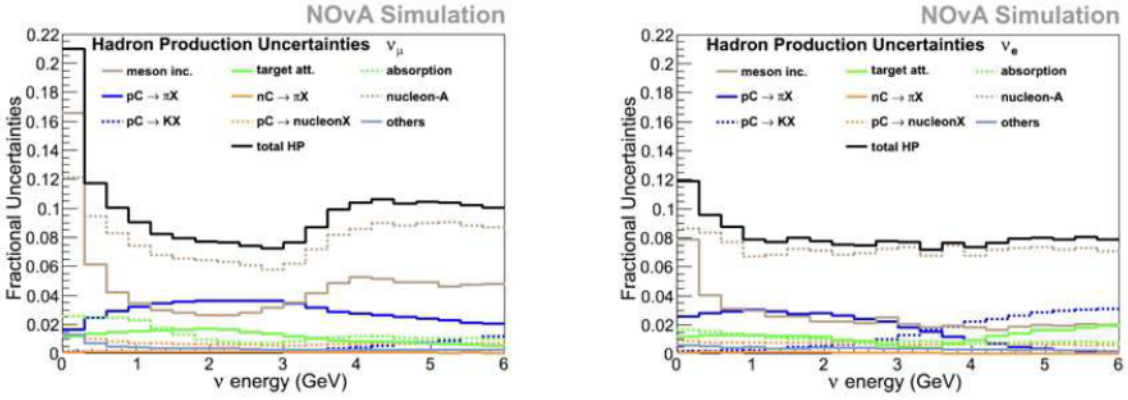

Figure 1.6: The fractional uncertainties in the ν_μ (left) and ν_e (right) fluxes, resulting from hadron production uncertainties, are presented as a function of neutrino energy in the 14.6 mrad off-axis NOνA near detector.

One of the motivations contributing to the main goals of the EMPHATIC experiment is the production of a high-resolution magnetic field map for the EMPHATIC

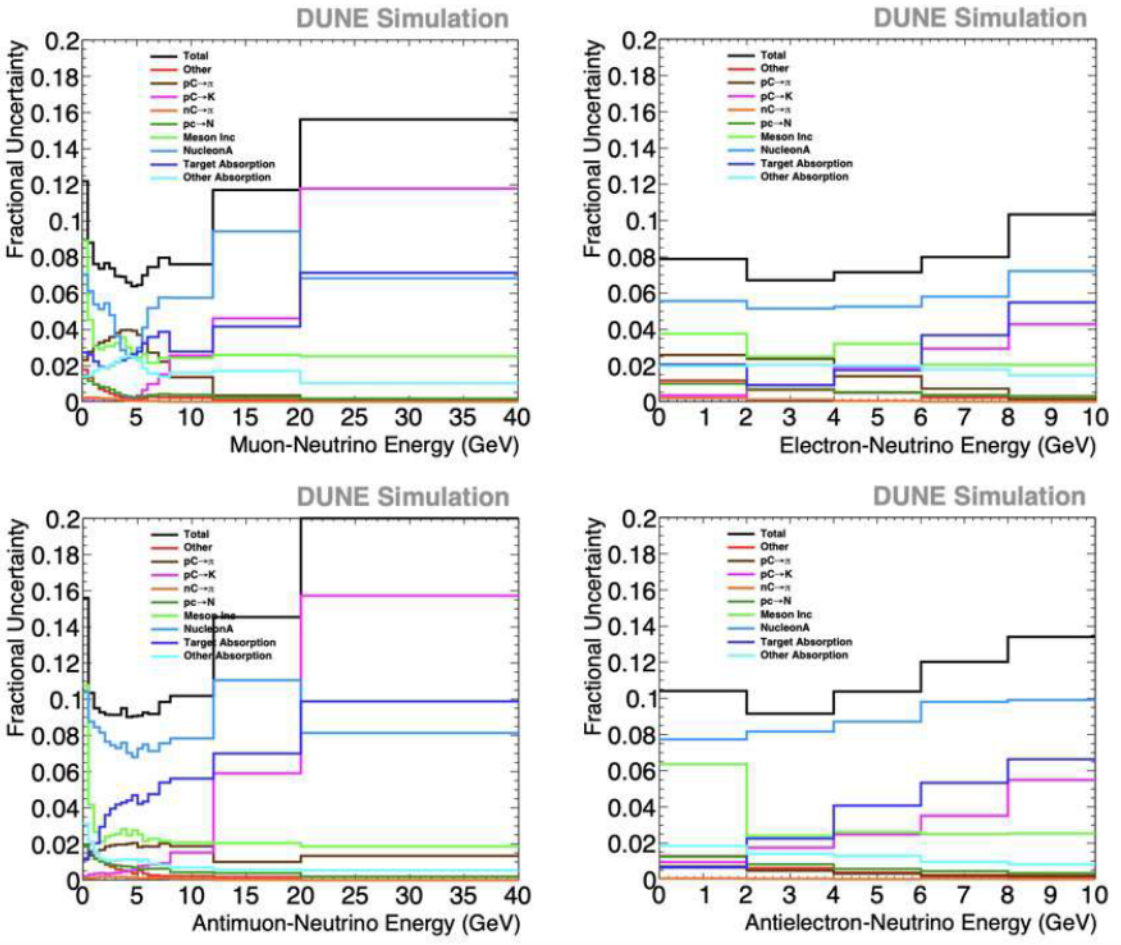

Figure 1.7: The fractional uncertainties in the flux, attributed to hadron production uncertainties, are presented as a function of neutrino energy for ν_μ (top left), ν_e (top right), $\bar{\nu}_\mu$ (bottom left), and $\bar{\nu}_e$ (bottom right) in the on-axis LBNF neutrino beam (forward-horn-current mode).

magnet, as discussed in Chapter 5. This study addresses the need for a more precise mapping than that previously achieved by AP-STD using hall probe measurements. Although the initial mapping provided valuable insights, increased precision is essential for several reasons.

Accurate reconstruction of particle bending angles as they traverse the magnetic field improves momentum and angular resolution, thereby enhancing momentum measurements at specific points in phase space. Furthermore, since particles with identical momenta can occupy different phase-space regions upon entering the spectrometer, a more detailed field map enables better differentiation of particles with

similar momenta or scattering angles, ultimately increasing the spectrometer's overall precision.

Enhanced detector acceptance is also achieved by extending the range of particle types and momenta that can be accurately tracked. This broader capability allows the detector to capture and analyze a wider spectrum of particle interactions, thereby expanding the experiment's overall performance.

In addition to higher spatial resolution, the improved magnetic field map offers comprehensive coverage of the entire magnet, including regions beyond the volume accessible by hall probe measurements—particularly at the edges and in hard-to-reach areas. Moreover, the same modeling and optimization procedures can be applied to the Phase 2 magnet, given its similar design, ensuring that high-precision mapping is available for the next phase of the experiment.

It is important to note that these advancements in field precision and coverage are critical for enhancing tracking accuracy and detector acceptance, thereby contributing to the overall success of the EMPHATIC experiment.

1.7 Hadron Production Measurements

Hadron production data can be integrated into hadronic interaction generators or used to adjust Monte Carlo output for accurate neutrino flux predictions in specific beamlines. These hadron production experiments, conducted over a broad range of incident beam momenta (10 to 450 GeV/c), involve proton and pion beams targeting various materials such as beryllium, carbon, and aluminum [32].

Hadron production experiments utilize two types of targets: thin targets and replica(thick) targets. Thin targets typically range a few centimeters in length, equivalent to a small percentage of the nuclear interaction length (λ_i), whereas replica targets extend to tens of centimeters, spanning multiple λ_i. In thin target measurements, hadron beams (protons, pions, or kaons) are directed at targets with only a few percent of the nuclear interaction length (λ_{int}). These experiments

aim to measure the inelastic cross-section, the differential cross-section of produced hadrons, and the yield of produced hadrons. The data from thin target measurements help reduce systematic uncertainties in the production of secondary hadrons from primary interactions.

Despite the availability of various thin target measurements for constraining primary interactions, a portion of the neutrino flux arises from decays of hadrons produced by secondary particle re-interactions. Thin target measurements alone do not fully cover the phase space of these production processes, limiting the precision of neutrino flux predictions. The replica target measurements aim to address these limitations by reducing systematic uncertainties not covered by thin target measurements. Proton beams with the same momentum used in neutrino oscillation experiments are directed at the replica target to measure the yields of produced hadrons exiting the target.

Thin and replica target measurements complement each other and have been conducted by multiple hadron production experiments. This discussion will focus on selected measurements, particularly from the ongoing NA61/SHINE and EMPHATIC experiments.

The NA20 and NA56/SPY experiments at CERN investigated hadron production from proton interactions with beryllium targets using beams at 400 and 450 GeV/c, respectively. They measured the yields of different particles and converted these measurements into inclusive cross sections for particle production [33]. The proposed empirical formula described their data with 10% accuracy.

The HARP experiment [34] at CERN's Proton Synchrotron measured pion production for proton beams of 1.5 to 15 GeV/c on various targets, presenting results as double-differential cross sections. These measurements helped constrain pion production for neutrino flux calculations in the K2K [35], MiniBooNE [36], and SciBooNe [37] experiments.

The MIPP experiment [38] collected data for Fermilab's NuMI Beamline, measuring charged particle production cross sections with beams of $\pi^{\pm}$, $K^{\pm}$, p, and $\overline{p}$

(5-120 GeV/c) on various targets. A dedicated 120 GeV/c proton run on the NuMI target provided "thick target" flux prediction to refine Monte Carlo predictions for the MINERνA experiment [39] and atmospheric neutrino studies.

NA61/SHINE at CERN [40], successor to the NA49 experiment [41], provides data for T2K and Fermilab neutrino experiments, including MINERνA, NOνA, and DUNE. Using beams of protons, pions, and kaons (30-120 GeV/c) on carbon, beryllium, and aluminum targets, NA61/SHINE's measurements have reduced the T2K flux uncertainty to about 5%. The NA61/SHINE collaboration plans additional hadron production measurements in the coming years, focusing on high-energy charged kaon production and interactions [42]. Future plans also include measurements with Hyper-K and LBNF replica targets.

The most recent addition to the list of hadron production experiments is the EMPHATIC experiment at the Fermilab Test Beam Facility [43], which will be thoroughly discussed in Chapter 4. It aims to perform high-precision measurements using proton and kaon beams with momenta ranging from 2 to 120 GeV/c on various thin nuclear targets. These measurements are expected to enhance flux predictions for both accelerator and atmospheric neutrino experiments. In 2018, EMPHATIC completed a test run to verify the detector's ability to perform forward scattering measurements. Over the next few years, three phases of data collection are planned, including runs in the underexplored low-momentum region below 10 GeV/c.

In addition to dedicated hadron production measurements, there are data originally collected to study nuclear interactions in high-energy hadron-nucleus collisions that are also used to constrain neutrino beam simulations [44] [45] [46]. These datasets provide cross-section estimates for various target materials (Li, Be, C, Al, Pb, etc.) and different beam types ($p, \pi^{\pm}, K^{\pm}, \overline{p}$) across a wide range of energies. These measurements are increasingly being replaced by more recent data from hadron production studies.

1.8 Outline of the Thesis

This thesis is structured to explore three main areas of research, each contributing to the understanding and advancement of neutrino physics and experimental techniques.

The current **Chapter 1** introduces fundamental concepts in neutrino physics, covering the Standard Model's relevance to neutrinos, their interactions, and oscillations, including mixing, two- and three-flavor oscillations, and matter effects.The chapter also discusses experiments in neutrino oscillations, laboratory neutrino beams, and the significance of precise neutrino flux determination, emphasizing, as part of the motivation, the necessity of direct hadron production measurements.

Chapter 2 focuses on the NOνA experiment, detailing the NuMI beamline, the experimental detectors utilized, and sophisticated detection techniques crucial for precise neutrino detection and oscillation measurements. Hardware contributions to the refurbishment of the Near Detector for the NOνA experiment are also outlined. Additionally, this chapter discusses the establishment of Asia's first Remote Operations Center in India for the NOνA experiment.

Chapter 3 delves into NuMI Beam Simulations, particularly emphasizing the prediction and comparison of neutrino flux using Geant 4-based simulations. Additionally, this chapter presents studies conducted at various virtual detector planes downstream of Horn 1 in the NuMI Beamline, providing insights into the spatial distribution and energy spectra of neutrinos essential for experimental analysis.

Chapter 4 introduces the EMPHATIC experiment, highlighting its role in enhancing neutrino flux predictions through precise measurements of hadron scattering and production cross-sections. This section outlines the experimental setup, measurement techniques employed, and significant findings contributing to improved accuracy in neutrino flux predictions.

Chapter 5 expands on the EMPHATIC experiment's methodology for precise magnetic field mapping using Halbach Array magnets, detailing measurement techniques, simulation methodologies, and fitting procedures crucial for understanding

particle trajectories and optimizing experimental conditions.

Chapter 6 focuses on the hardware aspects of the thesis, specifically detailing the assembly process of single straw tubes designed for DUNE's Near Detector SAND STT modules. This section also covers studies using GARFIELD++, a C++ based simulation tool, to analyze the dimensions and properties of assembled straw tubes with varying gas mixtures.

Chapter 7 provides a comprehensive summary of the thesis, consolidating key findings and insights gained from both experimental and simulation studies. It discusses the implications of the hardware work and physics analyses conducted throughout the thesis, outlining future directions and potential advancements in the field of neutrino physics and experimental techniques.

Finally, details on some of the topics covered in this manuscript are provided in the appendices.

Chapter 2

The NOνA Experiment

2.1 Introduction

The NOvA (NuMI Off-axis ν_e Appearance) experiment is a long-baseline, dual-detector experiment focused on studying the oscillation of muon neutrinos into electron neutrinos ($\nu_\mu \rightarrow \nu_e$) within a predominantly ν_μ beam, which contains small fractions of $\bar{\nu}_\mu$, ν_e, and $\bar{\nu}_e$ due to secondary particle decays. This experiment features two finely granulated tracking calorimeter detectors that are functionally identical, which significantly minimizes detector-related systematic uncertainties. The ND, weighing 300 tons, is located 1 km from the NuMI target, while the FD, with a mass of 14 kt, is situated 810 km away, as shown in Figure 2.1. Both detectors are positioned off-axis from the beam to produce a narrow energy peak at 1.8 GeV, the point at which oscillations are at their peak.

NOνA primarily focuses on four neutrino and antineutrino oscillation channels: $\overset{(-)}{\nu}_\mu \rightarrow \overset{(-)}{\nu}_\mu$, referred to as muon neutrino (or antineutrino) disappearance, and $\overset{(-)}{\nu}_\mu \rightarrow \overset{(-)}{\nu}_e$, known as electron neutrino (or antineutrino) appearance. The experiment is driven by three key physics objectives:

- Conducting precise measurements of the atmospheric mixing angle, θ_{23}.
- Determining the neutrino mass hierarchy, which involves measuring the sign of Δm^2_{32} to identify which of the three neutrino mass states is the heaviest.

- Investigating CP violation.

Figure 2.1: Placement of the NOνA detectors: The near detector (ND) is situated at Fermilab, close to Batavia, Illinois, while the far detector (FD) is located in Ash River, Minnesota, near the Canadian border. The NuMI beamline is aimed at the MINOS far detector, with the NOνA FD positioned 14.6 milliradians to the west of the beamline's center.[47]

This chapter describes the experimental setup of the NuMI Beamline and the NOvA detectors.

2.2 NuMI Beamline

The properties of the neutrino beam are critical in determining the experiment's physics reach. The Neutrinos at the Main Injector (NuMI) design was inspired by neutrino oscillation studies ([7]). Initially created for the MINOS experiment [19], which began collecting data in 2005, the NuMI beamline is now utilized by various other neutrino experiments, including NOνA, MINERνA, ArgoNeuT [48], and MINOS+ [49]. With its power reaching up to ~1 MW, it is currently the most intense neutrino source in the world. This ν_μ beam has a variable energy range from 0 to 20 GeV.

Figure 2.2 illustrates the Fermilab accelerator complex, which includes four accelerators—Linac, Booster, Recycler, and Main Injector(MI) —along with associated storage rings. Protons produced by the Booster enter the Recycler, where they are slip-stacked, a process that combines multiple proton batches to create a higher-intensity beam. The Main Injector then accelerates the proton beam from 8 GeV to 120 GeV.

Figure 2.2: A schematic diagram of Fermilab Accelerator Complex.

The NuMI beamline draws proton batches of 120 GeV from the Main Injector, with each batch lasting 10 μs and containing between 1.5×10^{11} and 4.5×10^{13} protons per pulse. These pulses are grouped into six batches per spill, with 1.33-second gaps between each. This segmentation of the beam is designed to help localize the neutrino signal in time, which aids in reducing cosmogenic background noise.

The NuMI beam is a tertiary beam that results from the decay of various short-lived particles, such as pions and kaons, produced within the NuMI target. Neutrinos are primarily produced by accelerating protons and colliding them with a fixed graphite target. However, the creation of these accelerator-based beams, with energies in the few GeV range, involves several stages. The details of the NuMI neutrino beam production process and its components are outlined in the following subsections.

2.2.1 Primary Proton Beam

In neutrino physics experiments that use accelerators, the phrase "proton beam" generally denotes the high-energy proton stream directed at a target to generate mesons. At Fermilab, the proton accelerator begins with H^- ions, which are accel-

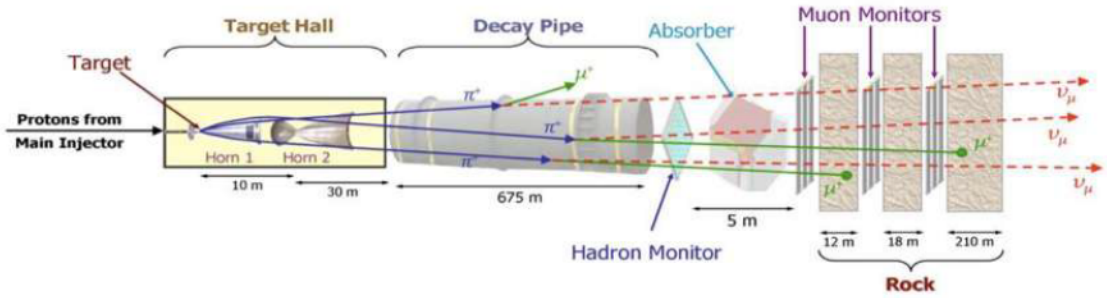

Figure 2.3: Schematic of the NuMI Beam. This diagram shows the various components of the NuMI beamline (not to scale) along with relevant dimensions, including the target, horns, decay pipe, hadron absorber, and the muon shield made of dolomite rock preceding the MINOS Near Detector. (Taken from [7])

erated to a kinetic energy of 400 MeV in the LINAC (LINear Accelerator). These ions are then converted into H^+ (protons) when they pass through a carbon foil, after which they are injected into the Booster synchrotron, where they are further accelerated to kinetic energy of 8 GeV. A fraction of these protons is utilized in short-baseline neutrino experiments before being transferred to the Main Injector (MI). The MI, a synchrotron accelerator with a 3.3 km circumference, increases their energy to 120 GeV.

These high-energy protons serve multiple purposes. Historically, the MI supplied protons and antiprotons for the Tevatron, and it remains instrumental in delivering beamlines for fixed-target studies, test beams, and neutrino generation. The proton beam is directed toward the Target Hall, located 41 meters underground, where the target and magnetic horns are situated.

2.2.2 Target

In accelerator-based neutrino experiments, the target is a crucial component. The target material is graphite, with a density of $1.78\,\mathrm{g/cm^3}$. It consists of 50 fins, each with a transverse area of $24 \times 7.4\,\mathrm{mm^2}$ as shown in Figure 2.4. The first two fins, known as Budal Monitors (BM), are used to measure the proton beam's horizontal and vertical positions on the target. The target's total length is 1200 mm, corresponding to 2.5 interaction lengths. Cooling is facilitated by directing water

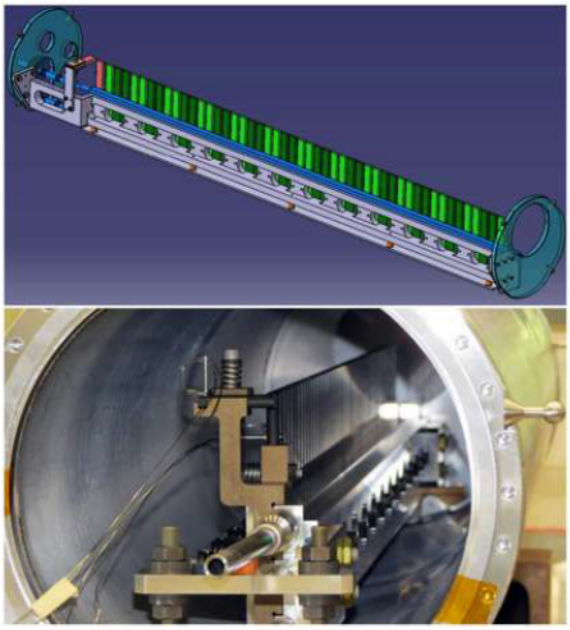

Figure 2.4: Illustration of the Medium Energy target core layout. The primary proton beam passes through the target from left to right (Above Figure). The core consists of 48 segments, along with two additional Budal monitors (highlighted in red) positioned at the upstream end.

through pipes that run along the upper and lower edges of each fin.

The entire target assembly is enclosed in a helium-filled container. To protect the target, the neck of the horn, and other support structures from potential beam misalignment that could result in damage, a 1.5 m-long baffle is employed. The baffle also assists in beam monitoring. It comprises a graphite core with a diameter of 57 mm and an 11 mm diameter hole, encased in an aluminum tube with two 0.5 mm-thick beryllium windows.

The target, Budal Monitors, and baffle are mounted together in a single carrier, allowing their positions to be adjusted simultaneously. This setup also helps control their distance relative to the horn when the beam configuration changes. When protons interact with the nucleons in the graphite target, they produce mesons such

as pions and kaons:

$$\pi^+ \rightarrow \mu^+ + \nu_\mu \tag{2.1}$$

$$\pi^- \rightarrow \mu^- + \overline{\nu}_\mu \tag{2.2}$$

$$K^+ \rightarrow \mu^+ + \nu_\mu \tag{2.3}$$

$$K^- \rightarrow \mu^- + \overline{\nu}_\mu \tag{2.4}$$

To optimize the neutrino beam, the secondary particles are focused using a specialized focusing system, as described in the following subsection.

2.2.3 Focusing Horns

The concept of focusing horns was first introduced by Simon Van de Meer [50]. For NOνA, two 3-meter parabolic magnetic horns, Horn 1 and Horn 2, enhance hadron acceptance into the decay region. Their focal length, proportional to meson momentum, collimates secondary charged particles produced in the graphite target and directs them into a beam. The toroidal magnetic field reduces their transverse momentum relative to the horn axis.

Each horn comprises two concentric current-carrying sheets: an inner aluminum conductor with a cone-shaped design and a cylindrical outer conductor. A strong current of approximately 200 kA flows outward along the inner conductor and returns along the outer conductor, creating a magnetic field confined between them. This focusing mechanism is illustrated in Figure 2.5, which depicts the trajectories of hadrons produced at different angles. Hadrons traveling along the beam axis pass through unaffected, while the first horn focuses those at various angles. In cases where the first horn under- or overfocuses, the second horn corrects the trajectory.

Depending on neutrino beam's polarity, two beam configurations are used: forward horn current (FHC, +200 kA) and reverse horn current (RHC, -200 kA). In the FHC configuration, NuMI produces a predominantly ν_μ beam, with a composition of 94.1% and 93.8% ν_μ at the NOνA Far Detector (FD) and Near Detector (ND),

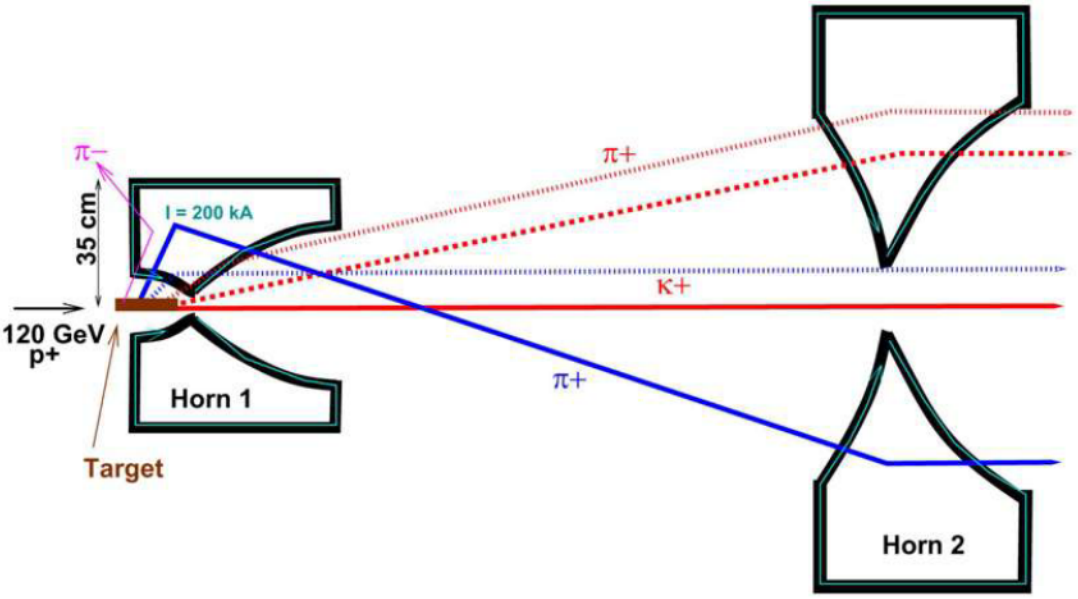

Figure 2.5: Focusing effect of the NuMI horns on hadrons arriving at various angles. The solid red line represents a particle traveling straight through. The red dashed line illustrates particles focused by Horn 2, while the red dotted line shows particles underfocused by Horn 1 and subsequently corrected by Horn 2. The solid blue line corresponds to particles overfocused by Horn 1 and adjusted by Horn 2, and the blue dotted line depicts particles focused by Horn 1. Adapted from [7].

respectively. Contamination from $\bar{\nu}_\mu$ is 4.9% (5.3%), and from $(\nu_e + \bar{\nu}_e)$ it is 1.0% (0.9%) for the FD (ND). In the RHC configuration, which enhances the production of anti-neutrinos, the wrong-sign contamination from ν_μ is 11.3% (11.7%) for the FD (ND).

2.2.4 Decay Pipe and Hadron Absorbers

The focused pions and kaons now travel through a 675 m long steel decay pipe. The decay pipe is located 46 m downstream of the target and is 2 m in diameter. To minimize interactions, the pipe is filled with helium, which offers a low-density environment as a cost-effective alternative to creating a perfect vacuum. The decay pipe is surrounded by concrete shielding, which stops particles traveling outward. A water-cooling system regulates the temperature of the shield, preventing overheating caused by energy deposition from off-angle particles.

The length of the decay pipe is determined by the decay length of the pions. NOvA primarily observes neutrinos from 5 GeV pions, which have a decay length of 336 m. However, the NuMI beamline also serves experiments like MINOS and MINERvA, whose neutrinos are produced from pions with energies up to 10 GeV, corresponding to a decay length of approximately 560 m. Most pions with energies below 10 GeV decay within the decay pipe, producing muons and neutrinos.

Residual protons and undecayed mesons are stopped in the hadron absorber located at the end of the decay pipe. The absorber has dimensions of 5.5 m in width, 5.6 m in height, and 8.5 m in length. It consists of a 4.75 m long aluminum core with water-cooling, encased in layers of steel and concrete for shielding. Muons with momentum below 3–4 GeV are also absorbed. Remaining high-energy muons are attenuated in the muon shield, a 240 m thick dolomite rock layer between the absorber and the Near Detector (ND) halls for MINOS and NOvA, ensuring the detector electronics are not overloaded. Approximately 85% of the 1 MW beam power is utilized for generating secondary particles, while the remaining 15% is effectively absorbed by the hadron absorber.

2.2.5 Beam Monitoring System

The beam monitoring system consists of four monitors: one hadron monitor and three muon monitors. The hadron monitor is positioned upstream of the hadron absorber and comprises a 7×7 grid of radiation-hardened ceramic pixels. This monitor measures the profile of the proton beam as well as any secondary hadrons that have not decayed. By analyzing the beam profile, it provides valuable insights into potential issues such as target malfunctions or beam scraping against components in the beamline.

2.2.6 Off-Axis Concept

The NOνA experiment uses an off-axis configuration to produce a narrow neutrino energy peak centered at $\sim$2 GeV, where there is maximal oscillation probability.

This off-axis strategy is based on analyzing the decay kinematics of pions and kaons. In their rest frames, these particles decay isotropically, generating neutrinos with a broad energy distribution. When these hadrons decay isotropically in their rest frames, they produce mono-energetic neutrinos. The energy of these neutrinos in the laboratory frame can be determined using relativistic kinematics, as expressed in the equation below:

$$E_\nu = \frac{(1 - \frac{m_\mu^2}{m_\pi^2})E_\pi}{1 + \gamma^2 \tan^2 \theta}, \tag{2.5}$$

where θ is the angle between the meson and the neutrino, E_π represents the pion energy, and $\gamma = \frac{1}{\sqrt{1-\beta^2}}$ is the Lorentz factor.

Applying the small-angle approximation and the rest masses of the muon and pion, the equation simplifies to:

$$E_\nu = \frac{0.43 E_\pi}{1 + \gamma^2 \theta^2}, \tag{2.6}$$

For neutrinos originating from charged kaon decays, the same equations apply, except the coefficient 0.43 is replaced by 0.96, leading to a higher-energy and broader spectrum compared to pions with equivalent energy.

From Equation 2.6, it is evident that when the detector is positioned on-axis ($\theta = 0$), E_ν increases proportionally with E_π. At $\theta = 14$ mrad, most neutrinos produced by pion decay have energies around 2 GeV, and at this angle, the dependence of neutrino energy on the parent pion's energy is minimal. This is illustrated in Figure 2.6.

Also, placing the detector off-axis minimizes two major backgrounds. First, neutral current (NC) events (where outgoing lepton is not observed), where undetected π^0 decays ($\pi^0 \to \gamma\gamma$) can mimic ν_e charged-current (CC) interactions, are reduced as the narrow-band beam shifts high-energy NC events below the signal region (1-3 GeV). Second, the intrinsic ν_e background from muon and pion decays, which follows broader three-body kinematics, is also minimized. The off-axis position enhances

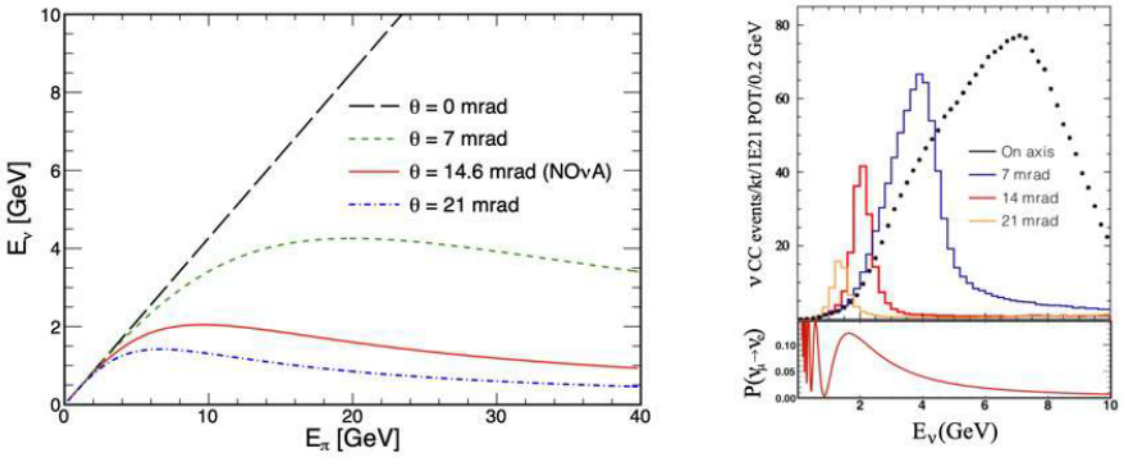

Figure 2.6: Off-Axis Neutrino Energy Spectrum. Left: The energy distribution of neutrinos emitted at an angle θ with respect to the pion's trajectory. Right: The anticipated ν_μ energy spectrum is shown at a distance of 810 km from the source for different off-axis angles. The NOνA detectors are placed 14.6 mrad off-axis to align the energy spectrum with the peak oscillation probability for $\nu_\mu \rightarrow \nu_e$.

the narrow ν_e appearance signal while reducing beam contamination.

2.3 NOνA Detectors

The NOνA experiment consists of two functionally identical detectors: the ND and the FD. The ND detects neutrinos before oscillations occur and helps constrain systematic uncertainties, while the FD detects neutrinos after oscillations. The Near Detector (ND) and the Far Detector (FD) share the same functional design, allowing for the cancellation of systematic uncertainties related to neutrino flux, interaction cross-sections, and detector response.

2.3.1 The NOνA cell and Liquid Scintillator

The NOvA Far and Near Detectors are built using rectangular PVC plastic cells that house liquid scintillator and a wavelength-shifting fiber loop, as shown in Figure 2.7.

The primary particle detection mechanism involves scintillation light, which is produced when charged particles interact with the liquid scintillator. The emitted light reflects within the cell until it is either absorbed by the plastic or scintillator,

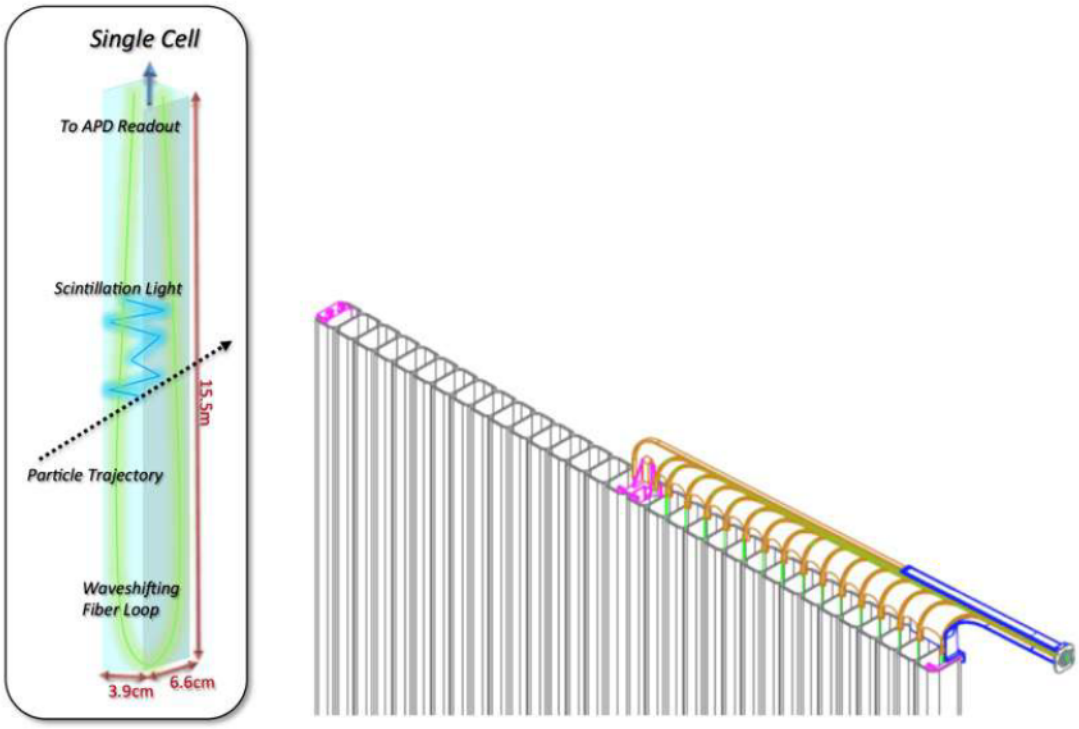

Figure 2.7: A single PVC cell, the basic building block of the NOvA detector. Right: Fiber routing to the optical connector for the first 16 cells. Each cell has two fiber ends routed to the optical connector.

or captured by the fiber.

Sixteen cells are joined to form an extrusion, and two extrusions are connected to create a module. These modules are arranged in alternating vertical and horizontal orientations to provide two orthogonal views of particle interactions. This configuration allows for the reconstruction of complete 3D particle tracks [51]. By mass, the detector is composed of 65% active scintillator and 35% PVC.

Component	**Mass Fraction**
Mineral oil (Solvent)	94.6%
Pseudocumene (Scintillant)	5.2%
PPO (Wavelength shifter)	0.1%
bis-MSB (Wavelength shifter)	0.002%
Stadis-425 (Anti-static)	0.001%
Vitamin-E (Antioxidant)	0.001%

Table 2.1: Composition of the liquid scintillator used in the detectors.

2.3.2 Wavelength Shifting Fiber

Each PVC cell in NOνA contains approximately 33.5 meters of 0.77 mm diameter double-clad Kuraray wavelength-shifting fiber, which is looped through the cell in a U-shape, as shown in green on the left side of Figure 2.7. The fiber has a polystyrene core infused with R27 dye to achieve wavelength-shifting properties. The fiber captures scintillation light in the violet-blue range (400–450 nm) and shifts it to a wavelength range of 490–550 nm. During attenuation, the red light within the 520–550 nm range persists and is detected by the Avalanche Photo Diodes (APDs) [52]. Both ends of the fiber loop are directed to a single pixel of the 32-pixel APD to improve light collection efficiency.

2.3.3 Avalanche Photodiodes(APDs)

Each cell's wavelength-shifting fiber has both ends read by photodetectors on a 32-pixel Hamamatsu avalanche photodiode (APD). At the top of the cell, the fiber is linked to an APD, temperature monitoring system and a thermoelectric cooler, maintaining the APD temperature at approximately -15°C to minimize thermal noise. APD is also connected to a dry nitrogen gas system to eliminate moisture and prevent ice formation. Each APD has a quantum efficiency of 85% for green light in the 520-550 nm range that it is collecting.

Within the APD, the collected light generates electron-hole pairs that are accelerated across a p-n junction under a reverse bias voltage of approximately 425 V. This voltage is individually calibrated for each channel to achieve a gain of 150 for the Far Detector and 100 for the Near Detector. The electron multiplication process occurs via an avalanche effect, and noise thresholds are set around 10 photoelectrons. The temperature of each APD is carefully controlled and monitored to ensure uniform amplification throughout the detector [52].

A diagram of an APD is shown in Figure 2.8. The signal from the APD is further amplified using specially designed low-noise electronics for NOνA.

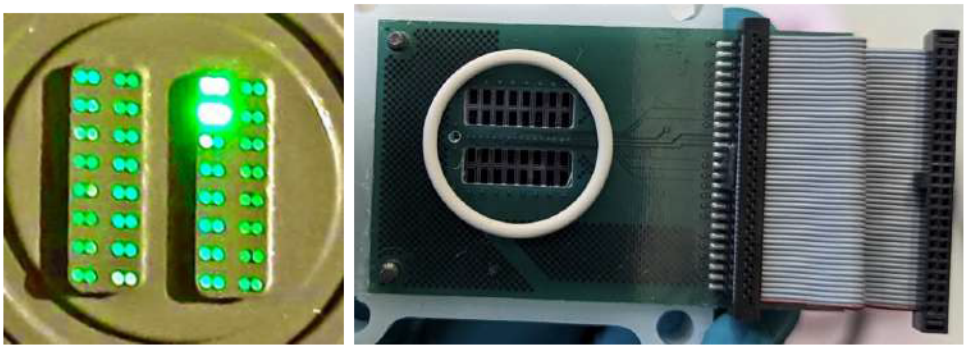

Figure 2.8: NOνA APD: the endpoint of the scintillator cells where the fibers connect to the APD (left) and the APD's front view (right).

2.3.4 The Data Aquisition System

The primary function of the data acquisition system (DAQ) is to collect data from the numerous APDs and consolidate it into a single stream for offline analysis and storage. Each APD is connected to a front-end board (FEB), which digitizes the signal from light into an electronic form, applies time tagging, and separates the signals. Each APD has a dedicated FEB.

The data from the FEBs is sent to data concentrator modules (DCMs), where one DCM processes signals from 64 FEBs, corresponding to 32 cells. The DCM organizes the data into 50 μs time blocks, called micro-slices, and further combines them into 5 ms intervals, referred to as milli-slices.

These milli-slices are transmitted to buffer nodes, with all DCMs synchronously routing data to provide each buffer node with a comprehensive view of the detector for each milli-slice. In the buffer nodes, events are reconstructed based on time tags, archived for storage, and optionally analyzed in real-time using a data-driven trigger system. Thus, the DAQ system encompasses the FEBs, DCMs, and buffer nodes.

The NOνA trigger system is divided into two main categories: clock-based and data-driven triggers. Clock-based triggers receive information about the NuMI beam spill and select data from a specific time window during the beam spill at Fermilab. This process primarily helps eliminate cosmic ray events in the far detector. Data-driven triggers analyze topologies in the data stream and make selections based on

specific criteria. One example is the supernova trigger, which detects intense bursts of neutrinos not associated with the NuMI beam.

Triggered readout windows are organized into runs and sub-runs. A run represents a period during which the detector configuration remains constant. A run ends under any of the following conditions:

- Completion of 64 sub-runs.
- Total run duration reaches 24 hours.
- Detector stops taking data.

Sub-runs are further segmented based on specific criteria:

- For the FD:
  - Sub-run duration is 1 hour.
  - File size reaches 1 GB.
  - Detector stops taking data.
- For the ND:
  - Sub-run duration is 3 hours.
  - Sub-run file sizes are approximately 10-15 minutes of data.

The timing system plays a crucial role in correlating interactions observed at the near and far detectors with the NuMI beam spill information. This synchronization is achieved through a timing and synchronization system. Timing data is distributed from the DCMs to the FEBs. The set of 64 FEBs ensures the readout and digitization of signals from the detector cells.

2.3.5 Near Detector

The NOνA Near Detector is located 105 meters underground in a cavern at Fermilab, adjacent to the MINOS access tunnel, and positioned 1,015 meters from the NuMI beam target hall. The detector is positioned at an offset of 14.6 milliradians relative to the beam axis, with the neutrino beam entering at a downward inclination of 3°.

Figure 2.9: The NOvA Near Detector located at Fermilab, Illinois.

It has dimensions of 3.8 m × 3.8 m × 16 m and a total mass of around 300 tons. This includes 193 tons of active detector components, comprising 45% liquid scintillator and 27% steel within the muon catcher. Its underground location provides shielding from cosmic rays. The detector consists of 20,192 cells arranged in planes that alternate between horizontal and vertical orientations, with a timing resolution of 5 ns.

The NOνA ND comprises of two parts: a 12.5-meter active detector volume and a 2-meter muon catcher. The muon catcher is designed to identify muons from ν_μ charged-current (CC) interactions, enhancing the precision of muon energy reconstruction. It consists of two planes of PVC modules (oriented vertically and horizontally) interspersed with 10 cm thick steel plates [52]. The ND has been operational since August 2014.

2.3.6 Far Detector

The NOνA Far Detector, shown in Figure 2.10, is located at Ash River in northern Minnesota, near the Canadian border. It has the same design as the Near Detector

but is much larger, with a total mass of around 14 kilotons, 62% of which is liquid scintillator. Similar to the Near Detector, neutrinos enter the Far Detector at an upward angle of approximately 3°. The Far Detector has dimensions of 15.6 m in width, 15.6 m in height, and extends 60 m along the beam direction. It consists of 896 planes, grouped in sets of 64 called diblocks, and contains a total of 344,064 cells. The electronics for readout are organized into diblocks, each containing 12 DCMs, with each DCM housing 64 FEBs.

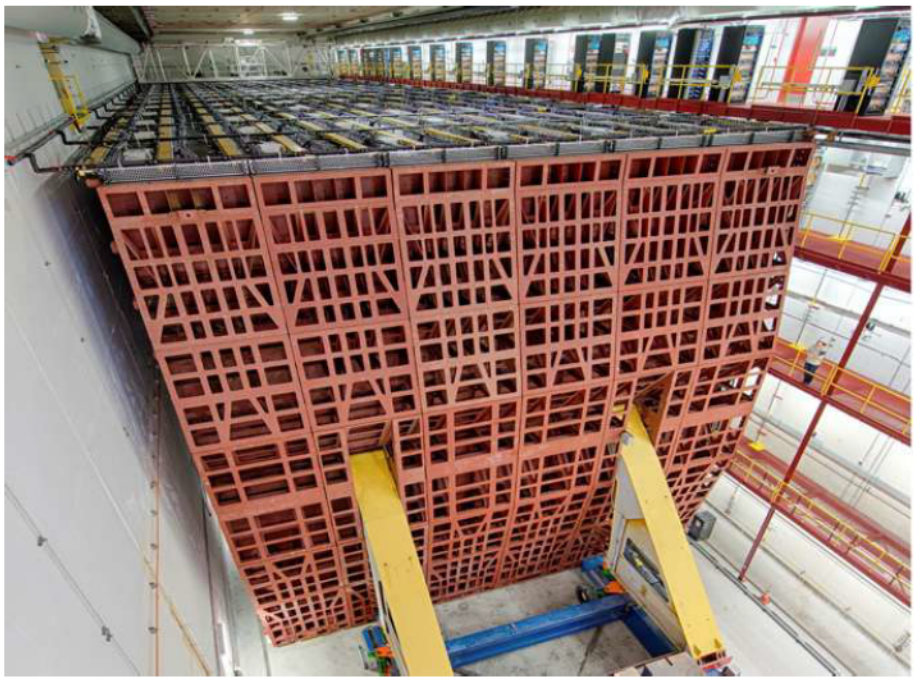

Figure 2.10: A view of the NOνA FD. Note the individual standing on the catwalk to the right, providing a clear sense of the detector's scale.

Situated above the Earth's surface, the Far Detector is shielded with 122 cm of concrete and 15 cm of barite to reduce cosmic ray interference. Approximately one-sixth of the detector is located above ground, while the remaining five-sixths are underground. This configuration offers around 12 radiation lengths of shielding, effectively reducing photon background.

Accurate timing of the readout electronics is crucial to reduce cosmogenic background, as the NuMI beam operates in 10 μs spills. The Far Detector has a timing resolution of 15 ns, slightly higher than the Near Detector, due to the FEBs sampling

the APDs at four times the rate compared to the Near Detector, which experiences a higher neutrino flux closer to the source. The Far Detector has been taking data since October 2013.

2.3.7 Neutrino Interactions and Event Display

The different neutrino interactions in NOνA can be distinguished by the signatures left by the final state particles in the detector. Charged current muon neutrino interactions (top of Figure 2.11) are characterized by a long muon track and a shorter final state nucleon track that deposits its energy much quicker compared to the electron. Charged current electron neutrino interactions (middle of Figure 2.11) show a shorter, less defined electron track, due to stronger electromagnetic interactions than muons because of their lower mass. Neutral current interactions (bottom of Figure 2.11), cannot distinguish between neutrino flavours, and are identified by characteristic hadronic showers and a single pion track, instead of two long tracks created by ν_μ CC event. NOνA detects a small number of tau neutrino events as well, with a threshold of 3.4 GeV, at the upper end of its energy range. Due to the short lifetime of tau particles, only their decay products (pions, electrons, and muons) are observable in the detector.

An event display is a useful tool for visualizing neutrino interactions and other raw data events in graphical form. It shows hit information collected by the detectors, arranged according to the physical layout. The top rectangle displays the X-Z view, while the bottom shows the Y-Z view. Hits are colored by signal intensity (charge) or time. The display also includes the time and charge distributions of hits. Figure 2.12 shows a ν_μ CC event, with the muon track clearly visible in both views.

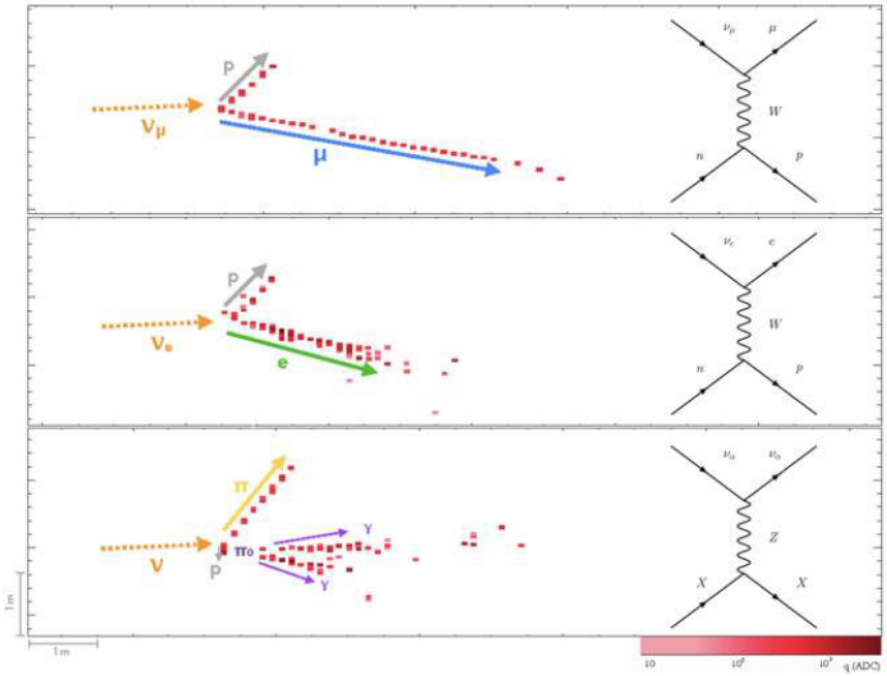

Figure 2.11: Examples of the three types of neutrino interactions in NOνA: ν_μ CC, ν_e CC, and NC, showing the distinct signals produced in the detectors.

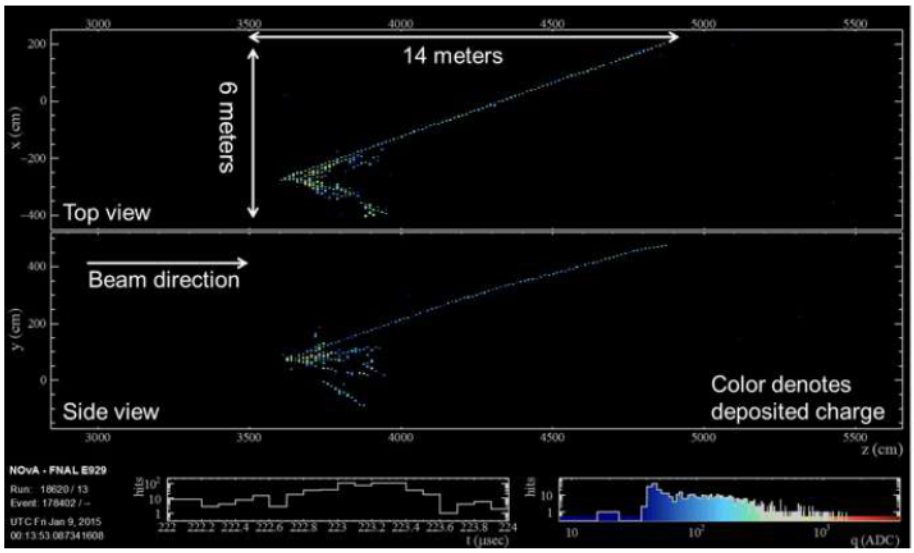

Figure 2.12: The NOνA event display shows a charged current muon neutrino interaction. The 14-meter-long track corresponds to a muon produced during the neutrino collision. A cluster of shorter tracks near the vertex represents the particles generated from the atomic nucleus struck by the incoming neutrino.

2.4 Contributions to the ND Refurbishment Effort

As part of the NOvA Near Detector (ND) refurbishment team, efforts were made to enhance detector performance and ensure the reliability of future data. A central focus of the project was replacing all baked Avalanche Photodiodes (APDs), a critical step to improve data quality while mitigating risks to detector longevity [53].

The refurbishment plan involved vacuum testing and reassembly of APDs to identify and repair defective units [54]. The APD reassembly process involved the following key steps:

1. **Inspection and Cleaning**: Dry-gas elbows were checked for looseness, and APD bases were examined for damage or excess glue. Damaged units or those with scratches affecting O-ring seals were excluded. Surfaces were cleaned with isopropanol to ensure a proper seal.
2. **Reassembly**: O-rings were placed, thermal paste was applied, and APD and Thermoelectric Cooler (TEC) units were assembled. Care was taken to avoid overtightening screws to prevent damage to spacer frames.
3. **Vacuum and Flow Testing**: Assembled APDs underwent vacuum tests to detect leaks or assembly issues. Adjustments were made for units showing minor leaks, while failing APDs were documented, repaired, or disassembled for parts.
4. **Final Quality Control**: APDs that passed vacuum tests were further tested for flow performance. Additional thermal paste was applied when necessary, followed by retesting. Finally, passing units were packed for installation.
5. **Underground Installation**: After reassembly and testing, refurbished APDs were installed underground in the ND, with adherence to safety protocols to minimize disruption.

This refurbishment effort contributed to extending the operational lifespan of

the detector and improving the quality of data collected for NOνA.

2.5 Setting up of ROC-India

ROC stands for Remote Operations Center for an experiment. Any ROC performs the following functions:

- 24x7 data acquisition of the experiment
- Real-time and secure operations
- Monitoring, visualization, and control of detector operations

In the NOνA experiment, data acquisition must be continuously monitored every minute of the day. To achieve this, supervision shifts are shared among collaboration members. Initially, the experiment was supervised exclusively at ROC-West, Fermilab . However, it soon became apparent that remote operation centers should also be established. Currently, there are 26 ROCs worldwide monitoring the NOνA experiment.

ROC-India has been officially validated by successfully passing two access tests conducted by the NOνA collaboration. It is the only ROC of its kind in the Asian subcontinent, and thus in India. This center can control the windows inside the Virtual Network Computing (VNC) sessions from thousands of miles away from the experiment. A dedicated Kerberos keytab has been assigned to ROC-India to facilitate secure access. ROC-India allows members of the India NOνA collaboration to participate in NOνA detector operation shifts without the inconvenience and expense of traveling to Fermilab.

The hardware of ROC-India includes five PCs and ten monitors, as shown in Figure 2.13. This setup is located at the Department of Physics, Panjab University, Chandigarh, India. It provides onsite shift experience for all Indian collaborators in the NOνA experiment. ROC-India can display five VNC sessions, each with a resolution of 2560 x 2880, across two medium-sized ultra-HD (4K) monitors, each with a resolution of 2560 x 1440, arranged vertically. The systems run on Ubuntu

Linux.

ROC-India has been officially added to the NOνA Blue Sheet. I have been serving as the ROC-India Liaison since its inception in February 2022.

Additionally, a website for ROC-India is hosted on the Department of Physics, Panjab University server. Indian collaborators can use this website to request shifts at ROC-India by filling out a form. The website address is `http://puhep.org/roc-india/`. Figure 2.13 shows a snapshot of the website's homepage, where shifters can book shifts by navigating to the "Shifts > Book Shifts" section.

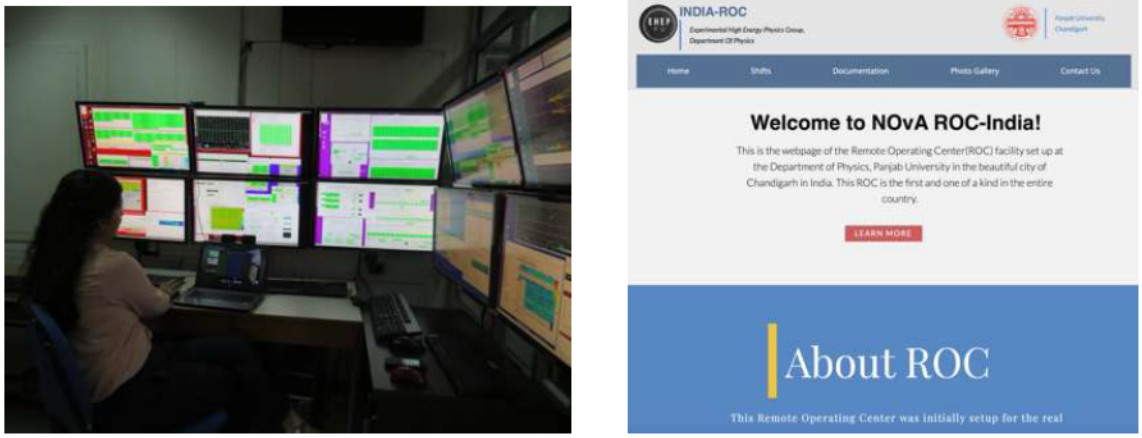

Figure 2.13: (Left) ROC-India setup showing five systems and ten monitors, with a shifter taking a remote NOνA shift. (Right) Snapshot of the ROC-India website.

2.6 Summary

This chapter provided an overview of the NOνA experiment, detailing the NuMI beamline components, focusing horns, and decay pipe, as well as the NOνA detectors and their data acquisition methods. The successful establishment of ROC-India was also highlighted, showcasing its role in remote detector operations and shift-taking.

A crucial aspect of neutrino experiments is the accurate prediction of the neutrino flux reaching the detectors. While the physical infrastructure described in this chapter enables neutrino production and detection, a detailed understanding of the neutrino beam requires sophisticated simulations. The next chapter focuses on modeling the NuMI beamline and predicting the neutrino flux using Monte Carlo

simulations. These simulations are essential for estimating systematic uncertainties and improving flux predictions, which are critical for interpreting NOνA's physics results.

Chapter 3

NuMI Beamline Simulation and Flux Predictions

Simulations play a vital role in enhancing our understanding of the physics of underlying particle detectors. NOνA employs sophisticated computational tools to model the NuMI beamline, neutrino interactions, and particle movement within the detector and beamline elements. These simulations utilize Monte Carlo (MC) techniques to account for the stochastic behavior of particle interactions. The MC simulations act as a virtual counterpart to experimental data, forming a foundation for analysis. They are indispensable for developing and validating analysis techniques, estimating systematic uncertainties, and predicting event distributions within the detectors. Accurate simulations ensure the reliability and precision of NOνA's findings.

This chapter describes the NuMI beam simulations performed for the NOνA experiment. Thus, the NOνA simulation proceeds in three stages:

1. **Beam Simulation**: The NuMI beamline geometry is simulated using GEANT4. The interaction of 120 GeV protons with the graphite target, the focusing of secondary hadrons, and their decay into neutrinos are modeled. PPFX applies event weights to correct for hadron production mis-modeling. Flux files containing neutrino properties are the primary output of this stage.
2. **Neutrino Interaction Simulation**: Neutrino interactions are simulated us-

ing an improved GENIE model. Cosmic ray backgrounds in FD events are accounted for using the CRY package. Flux files from the beam simulation are input into GENIE and CRY to generate a list of particles from neutrino interactions.

3. **Detector Simulation**: The particle list from the neutrino interaction simulation is passed through a GEANT4-based detector simulation to model energy deposits in the detector. These deposits are converted into scintillation light, captured by wavelength-shifting fibers, and digitized by avalanche photodiodes (APDs) to produce waveforms.

This chapter concludes with studies of the on-axis and off-axis spectra, beam transport uncertainties, and comparisons of the old and new GEANT4 flux simulations. Additionally, it presents flux studies using virtual detectors placed downstream of the target and Horn 1 in the NuMI beamline (see Figure 2.3 in Chapter 2). The impact of varying the virtual detector plane positions on the flux is analyzed, including comparisons between horn-on and horn-off configurations. Furthermore, transverse momentum and energy distributions are also examined at different virtual detector plane positions.

3.1 Software Frameworks

3.1.1 G4NuMI

The neutrino flux from the NuMI beam is predicted using a Monte Carlo (MC) beamline simulation package called G4NuMI, which is based entirely on GEANT4 [55]. This simulation incorporates the geometry and physics of the NuMI beamline, leveraging GEANT4 for its flexibility, including customizable physics models and processes.

The origin of the simulation coordinate system (MCZERO) is defined at the front face of Horn 1, following the trajectory of the primary proton beam. A right-handed Cartesian coordinate system is employed, where the Z-axis extends along

the beamline, and the Y-axis represents the vertical direction.

The process begins with a proton beam of 120 GeV energy, characterized by a Gaussian transverse distribution with a standard deviation of 1.1 mm. Upon entering the target region, protons interact to produce secondary particles, whose properties are tracked. This tracking allows linking a produced neutrino to its parent particle at the target. Key NuMI beamline components such as the Target Hall, decay pipe, and absorbers are modeled, with particular focus on the target and horns due to their significant impact on flux predictions.

The GEANT4 FTFP_BERT [56] hadronic model is employed, combining the FRITIOF model for high-energy processes (>4 GeV) and the Bertini cascade model for low-energy interactions (<5 GeV). This simulation ends with neutrino production, outputting data in a ROOT-based n-tuple format.

Neutrino interactions are modeled using the GENIE [57] package, which determines interaction probabilities and produces 4-vectors for resulting particles. GENIE's default models are corrected based on NOνA's measurements, external data, and observed discrepancies with the data.

G4NuMI determines the likelihood of neutrino production in a specific direction by analyzing the kinematics of the parent particle. Adjusting the neutrino's direction changes its energy, and the corresponding probability is stored as a weight for efficient flux calculations at specific points. For distant detectors, this flux calculation approximates the point-source flux. For nearby detectors, it provides a rough estimate, useful for systematic studies and quick evaluations.

3.1.2 Flux Reader

The output of the G4NuMI simulation is an n-tuple ROOT file. This file contains detailed information about neutrinos and their parent particles (hadrons and muons), which are the end products of the beamline simulation.

FluxReader [58] is a C++ framework built on the ROOT Data Analysis Framework to process these output G4NuMI flux files and generate spectra. It outputs

distributions for specified variables, categorized by neutrino flavor, parent species, applied cross section, and detector location. Users can configure flavors, parents, cross sections, detectors, binning, labels, variables, and weights to customize the output. FluxReader produces event spectra for the Near Detector (ND) and Far Detector (FD) under forward and reverse horn current configurations.

GENIE simulations are used to model neutrino interactions, providing essential inputs for event rate distributions. Event rates are computed as:

$$\text{Event Rate} = \text{Flux} \times \text{Cross Section} \times \text{Number of Targets},$$

where the number of targets is derived from standard molar mass assumptions for a single-material detector. Event rates are output in units of events per kiloton.

FluxReader outputs are not scaled to a specific number of protons on target (POT). Instead, the number of POT used to generate the distributions is stored in a histogram called `TotalPOT`, allowing users to scale to a desired POT value using the ratio:

$$\frac{\text{User-defined scale}}{\texttt{TotalPOT}}$$

3.1.3 PPFX

PPFX (Package to Predict the FluX) [31] is an experiment-independent neutrino flux determination package developed to correct hadron production mismodeling and propagate uncertainties within the NuMI beamline. It adjusts the simulated neutrino flux based on experimental hadron production data, ensuring accurate modeling of hadron production and neutrino flux.

PPFX models the reduction in particle flux as they traverse essential elements of the NuMI beamline, including the target, Budal monitors, magnetic horn inner conductors, and decay pipe. It employs the multi-universe method to propagate uncertainties, incorporating both correlated and uncorrelated components. This ensures the refinement of the beamline simulation and accurate modeling of hadron production for more precise predictions of neutrino flux.

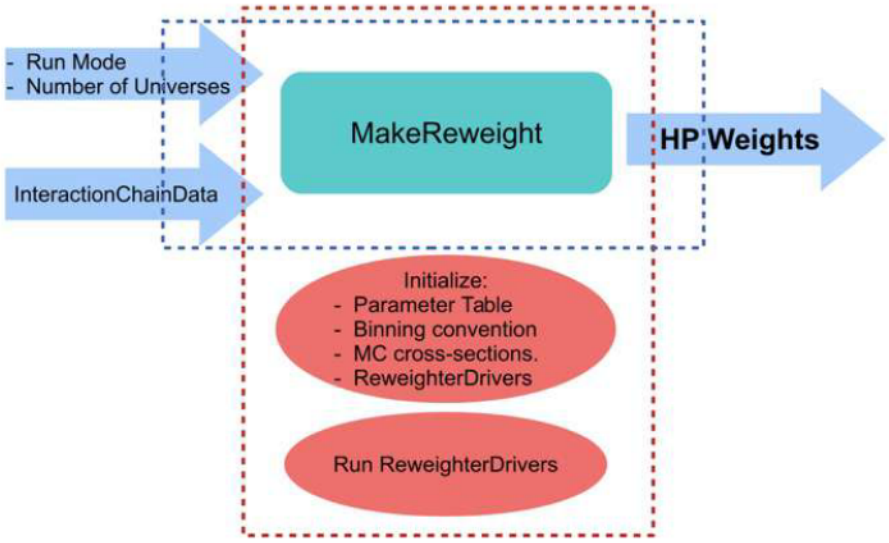

Figure 3.1: PPFX Flowchart [31]

3.2 NuMI Fluxes

The NuMI beamline is designed to be adaptable, enabling the generation of varying neutrino energy spectra and intensities. This flexibility is achieved by modifying the strength and orientation of the magnetic field, along with adjusting the relative placements of the target, Horn 1, and Horn 2. Such modifications allow precise focusing of particles originating from specific kinematic regions, thereby providing control over the beam energy. This tunability is a crucial aspect of the NuMI beamline, supporting studies on neutrino oscillations across different Δm^2 values.

NuMI operates primarily in two modes: **Low Energy (LE)** and **Medium Energy (ME)**.

Low Energy Beam Configuration

During the Low Energy (LE) phase, the focusing horns remained stationary while the target's position was adjustable remotely, enabling modifications to the neutrino energy spectrum. The target, along with the Budal monitors and baffle, was mounted on a shared carrier system, allowing smooth adjustments. The naming format for LE configurations follows the pattern "LEXXXzYYYi," where:

- `XXX`: Position (in cm) upstream from $z = 0$, which corresponds to the target being fully inserted into Horn 1 without causing electrical discharge.
- `YYYi`: Approximate current magnitude (in kA) applied during the setup.

For instance, in the "LE000z" configuration, the target is positioned at $z = 0$, its closest physical position to Horn 1.

Medium Energy Beam Mode

In ME mode, the target is moved upstream to increase the on-axis neutrino flux's peak energy and the second horn has been relocated further downstream from the first horn. This is more efficient when combined with increasing the distance between Horn 1 and Horn 2. By capturing more energetic pions with minimal transverse momentum, the horns reduce particle divergence, improving flux efficiency. Moving Horn 2 downstream from Horn 1, in conjunction with repositioning the target, results in an approximately 30% higher flux spectrum compared to the LE100z200i configuration.

Forward and Reverse Horn Current Modes

The current direction pulsed through the horn conductors determines whether hadrons with a specific charge are focused or defocused:

- **Forward Horn Current (FHC)**: Focuses π^+ and K^+, enhancing the muon neutrino component of the flux.
- **Reverse Horn Current (RHC)**: Focuses π^- and K^-, enhancing the muon antineutrino component.

Beam Components

Neutrino Parents

The main decay processes contributing to neutrino generation are listed in Table 3.1. Muon neutrinos are primarily produced by the decays of charged pions and kaons,

with a minor fraction of electron neutrinos also being generated. Muons produced in these decays also contribute to the electron neutrino flux, but this contribution is minimal as most muons are absorbed before decaying.

Decay Channel	Reaction	Branching Ratio (%)
1	$\pi^{\pm} \rightarrow \mu^{\pm} + \nu_{\mu}(\bar{\nu}_{\mu})$	99.9877
2	$\pi^{\pm} \rightarrow e^{\pm} + \nu_{e}(\bar{\nu}_{e})$	0.0123
3	$K^{\pm} \rightarrow \mu^{\pm} + \nu_{\mu}(\bar{\nu}_{\mu})$	63.55
4	$K^{\pm} \rightarrow \pi^{0} + e^{\pm} + \nu_{e}(\bar{\nu}_{e})$	5.07
5	$K^{\pm} \rightarrow \pi^{0} + \mu^{\pm} + \nu_{\mu}(\bar{\nu}_{\mu})$	3.353
6	$K^{0}_{L} \rightarrow \pi^{\pm} + e^{\mp} + \nu_{e}$	40.55
7	$K^{0}_{L} \rightarrow \pi^{\pm} + \mu^{\mp} + \nu_{\mu}$	27.04
8	$\mu^{\pm} \rightarrow e^{\pm} + \nu_{e}(\bar{\nu}_{e}) + \bar{\nu}_{\mu}(\nu_{\mu})$	100.0

Table 3.1: Decay channels and their corresponding branching ratios.

Flux Composition

Figure 3.2 shows the flux composition for the NOνA Near Detector (ND) and Far Detector (FD) in both Forward Horn Current (FHC) and Reverse Horn Current (RHC) modes. In Forward Horn Current (FHC) mode, the beam primarily consists of muon neutrinos, with a minor contribution from unfocused muon antineutrinos. These antineutrinos originate from mesons that are either produced beyond the target region or selectively focused by the second horn. At higher energies (> 10 GeV), the muon neutrino contribution becomes dominant due to the production and focusing of positively charged mesons such as π^{+} and K^{+}.

3.3 Beam Transport Uncertainties

Beam transport involves numerous uncertainties, arising from a variety of sources that can impact the neutrino flux. Some of the key sources of these uncertainties include:

- Shifts in the Horn Current relative to its nominal value.
- Positional shifts of Horn 1 and Horn 2 in both the X and Y directions relative

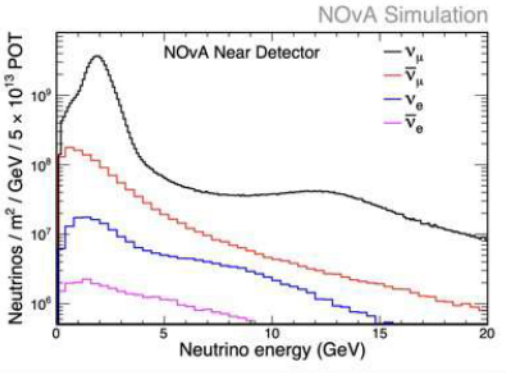

(a) Composition of the NuMI beam at the NOνA Near Detector for neutrino (FHC) mode.

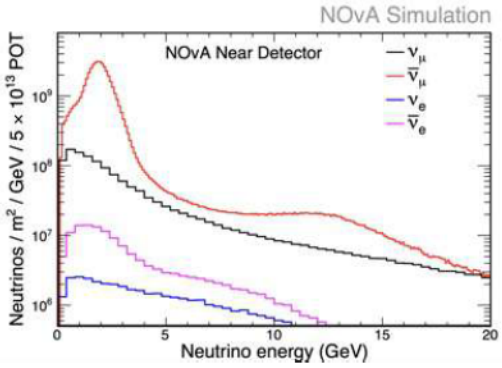

(b) Composition of the NuMI beam at the NOνA Near Detector for antineutrino (RHC) mode.

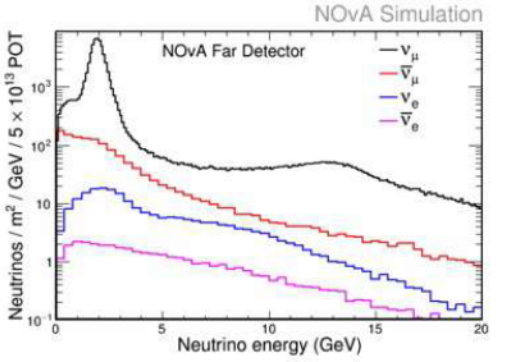

(c) Composition of the NuMI beam at the NOνA Far Detector for neutrino (FHC) mode.

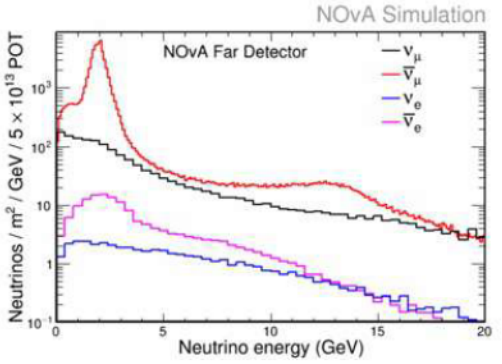

(d) Composition of the NuMI beam at the NOνA Far Detector for antineutrino (RHC) mode.

Figure 3.2: Flux components for the NuMI beam at the NOνA Near and Far Detectors for FHC and RHC configurations.[59]

to their nominal positions.

- Variations in the magnetic field distribution within the horn skin, such as transitioning to an exponential magnetic field distribution.
- Beam position shifts on the target in both the X and Y directions.
- Changes in the beam spot size in both X and Y directions.
- Shifts in the target position relative to its nominal value.
- Comparisons between different versions of the G4NuMI simulation framework.

The standard approach consists of adjusting each parameter by ± 1, ± 2, and ± 3 from its nominal value and evaluating the corresponding variations in the neutrino flux. This approach enables a systematic understanding of how individual uncer-

tainties influence the beam transport. While there are many potential sources of uncertainty, this study focuses on two specific cases:

1. Horn Position Uncertainty Study: This examines the impact of positional shifts of the horns on the neutrino flux.
2. Geant4 Version Comparison Study: This involves comparing neutrino flux predictions between Geant4.9.2 and Geant4.10.04 to evaluate discrepancies arising from software updates.

To investigate these uncertainties, the FluxReader framework is utilized to generate neutrino fluxes at both the Near Detector (ND) and Far Detector (FD). The neutrino flux (Φ) is defined as the number of neutrinos per square centimeter (ν/cm^2) for all Protons on Target (POT).

Understanding a beam transport uncertainty entails quantifying its effect on the neutrino flux when the associated parameter is varied. For this study, the goal is to identify and analyze the specific changes in flux caused by the horn position shifts and the differences between Geant4 simulation versions.

3.3.1 Horn Position Uncertainties Study

The position of the horns in the beamline plays a critical role in determining the nominal neutrino spectrum. Misalignments in the beamline elements, particularly the horns, affect the focusing of secondary particles, which in turn influences the geometric ray tracing of pions and kaons through the horns. Ultimately, these misalignments result in deviations in the neutrino spectrum at both the Near Detector and Far Detector.

The position of the horns was measured with an estimated error of ± 3 mm. The nominal beamline conditions used are as follows:

- Beam Spot Size: 1.5 mm in both X and Y directions.
- Horn Current: +200 kA for Forward Horn Current (FHC) mode.
- Water Layer on Horns: 1 mm.

- Target Position (z): -143.3 cm.
- Protons on Target (POT): 5×10^8.

For this study, the following horn position shifts were considered in G4NuMI simulations:

- Horn 1 shifted by ± 3 mm in X and Y directions separately.
- Horn 2 shifted by ± 3 mm in X and Y directions separately.

The FluxReader framework was used to produce flux predictions at both ND and FD. In total, 8 different simulations (8000 jobs) were performed, along with the corresponding FluxReader jobs, to obtain the neutrino spectrum. Please note that these plots are for the Forward Horn Current (FHC) configuration only.

3.3.1.1 Horn 1 Position Uncertainties

Misalignment of Horn 1 affects the focusing of secondary particles, which modifies the neutrino flux at ND and FD. For a ± 3 mm variation in Horn 1 position (X and Y directions), the Figures 3.3 illustrate these effects, showing both the neutrino flux and the flux ratio for variations in Horn 1 position.

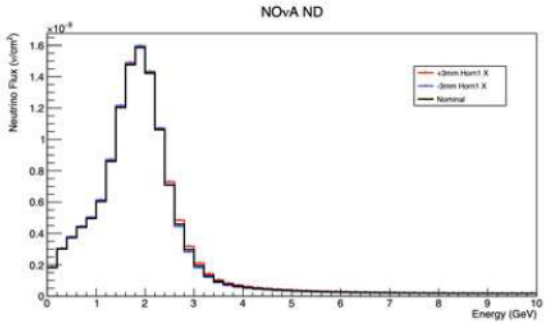

(a) Neutrino Flux at ND for FHC Horn 1X ±3 mm.

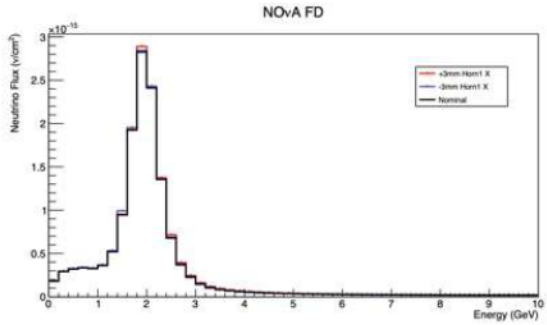

(b) Neutrino Flux at FD for FHC Horn 1X ±3 mm.

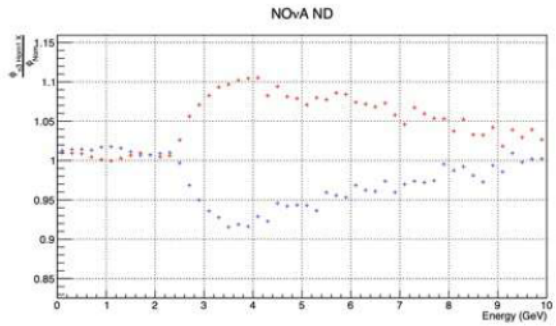

(c) Ratio of FHC Horn 1X ±3 mm flux to nominal flux at ND.

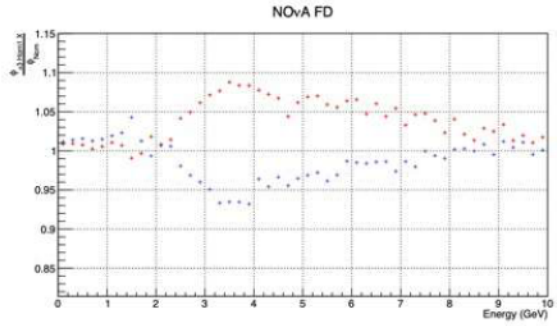

(d) Ratio of FHC Horn 1X ±3 mm flux to nominal flux at FD.

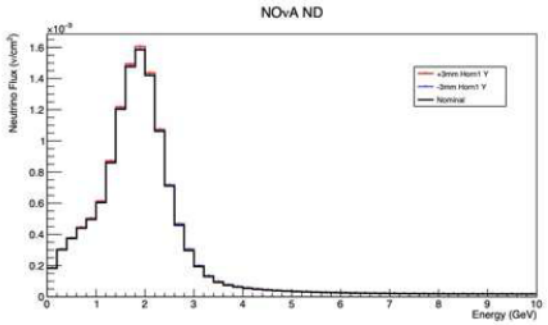

(e) Neutrino Flux at ND for FHC Horn 1Y ±3 mm.

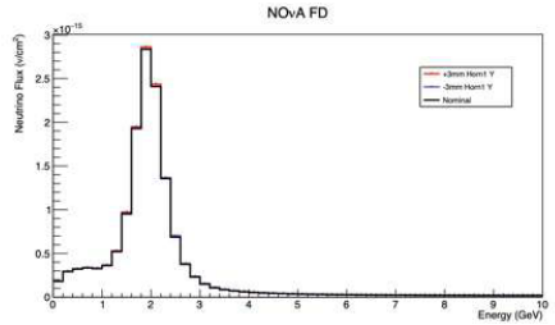

(f) Neutrino Flux at FD for FHC Horn 1Y ±3 mm.

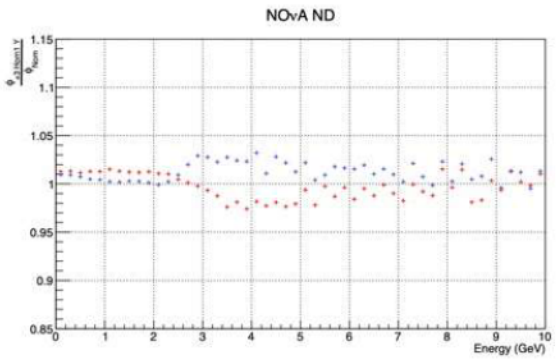

(g) Ratio of FHC Horn 1Y ±3 mm flux to nominal flux at ND.

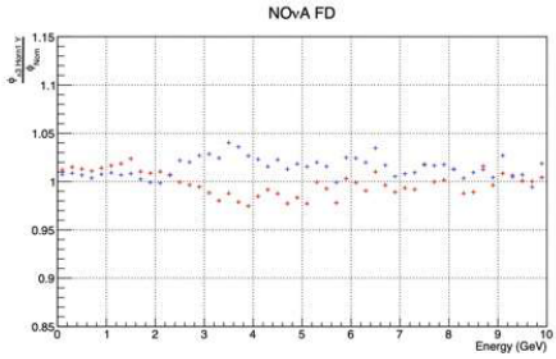

(h) Ratio of FHC Horn 1Y ±3 mm flux to nominal flux at FD.

Figure 3.3: Figures showing the impact of horn 1 position shifts on neutrino flux and their ratios to the nominal flux. Black represents the nominal flux, while red and blue correspond to position shifts of $x = \pm 3$ mm, respectively.

3.3.1.2 Horn 2 Position Uncertainties

Similarly, misalignment of Horn 2 impacts the focusing of secondary particles and the neutrino spectrum. For a ±3 mm variation in Horn 2 position (X and Y directions), the Figures 3.4 illustrate these effects for Horn 2 position variations.

3.3.1.3 Results and Observations

The results of this study, including the discrepancies observed in the flux for each simulation, are summarized in Table ??. The largest observed shift in flux occurs at ∼ 4 GeV, with a discrepancy of approximately 11% due to Horn 1X ±3 mm position uncertainty.

Horn Position Shift	**Energy at ND (GeV)**	**Largest Flux Shift at ND**	**Energy at FD (GeV)**	**Largest Flux Shift at FD**
Horn 1X ±3 mm	∼ 4	11%	∼3.5	10%
Horn 1Y ±3 mm	∼ 4	4%	∼ 3.5	4%
Horn 2X ±3 mm	∼ 3	3%	∼ 2.5	7%
Horn 2Y ±3 mm	∼ 3	3%	∼ 2.5	3.5%

Table 3.2: Discrepancies in Neutrino Flux Due to Horn Position Uncertainties at ND and FD

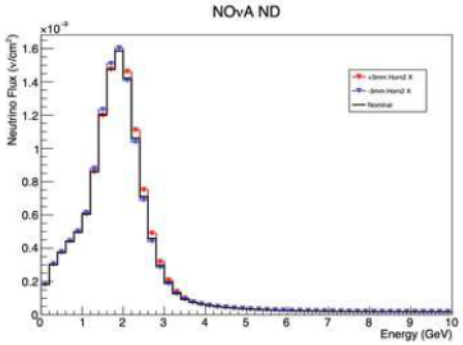

(a) Neutrino Flux at ND for FHC Horn 2X ±3 mm.

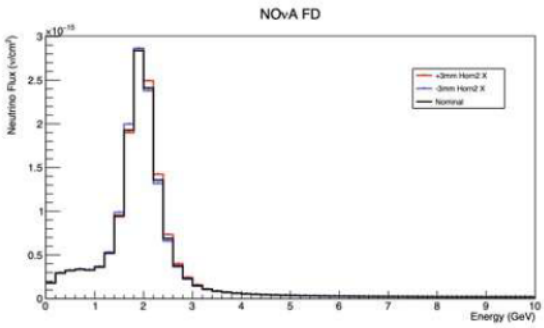

(b) Neutrino Flux at FD for FHC Horn 2X ±3 mm.

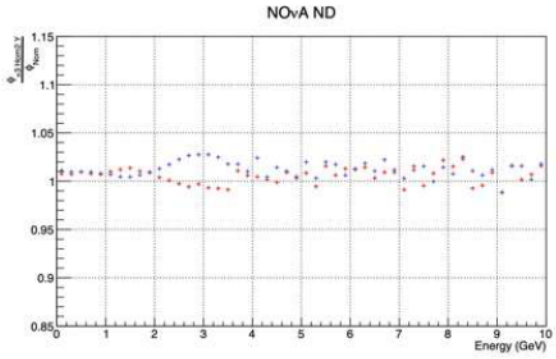

(c) Ratio of FHC Horn 2X ±3 mm flux to nominal flux at ND.

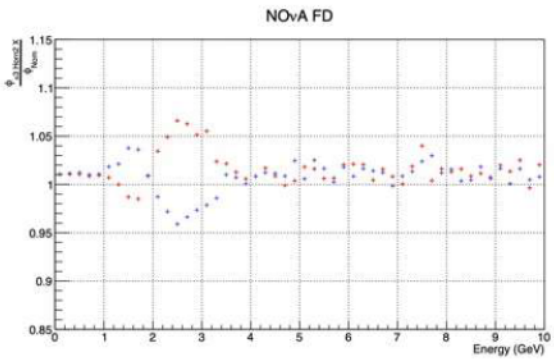

(d) Ratio of FHC Horn 2X ±3 mm flux to nominal flux at FD.

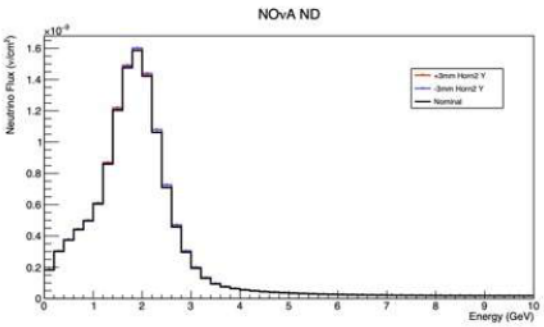

(e) Neutrino Flux at ND for FHC Horn 2Y ±3 mm.

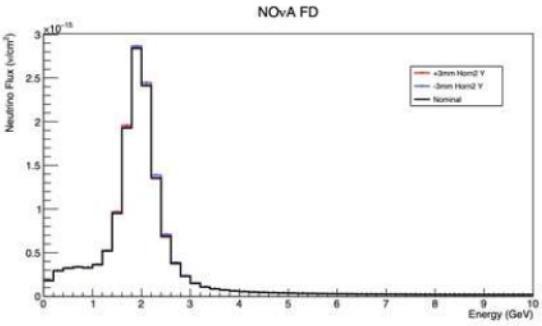

(f) Neutrino Flux at FD for FHC Horn 2Y ±3 mm.

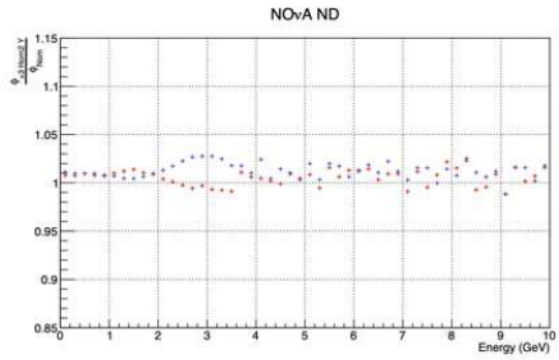

(g) Ratio of FHC Horn 2Y ±3 mm flux to nominal flux at ND.

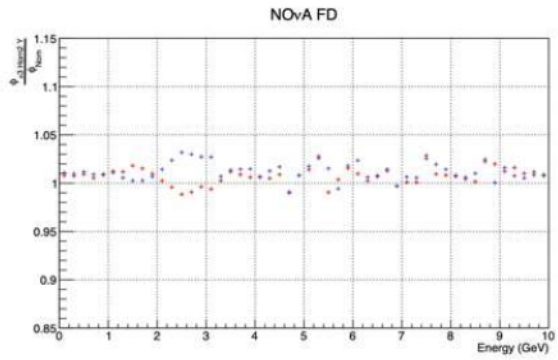

(h) Ratio of FHC Horn 2Y ±3 mm flux to nominal flux at FD.

Figure 3.4: Figures showing the impact of horn 2 position shifts on neutrino flux and their ratios to the nominal flux. Black represents the nominal flux, while red and blue correspond to position shifts of $x = \pm 3$ mm, respectively.

3.3.2 Geant4.9.2 vs. Geant4.10.04 Flux Comparison Studies

This study compares the neutrino flux predictions generated using two versions of the G4NuMI simulation framework: the older **G4NuMI** (Geant4.9.2.p03) and the newer **main_modern_g4** branch (Geant4.10.04.p02b). Simulations were performed with standard parameters: **500,000 POT** distributed across **500 jobs**, corresponding to 2.5×10^8 total POT, using the **old NuMI target**.

The modern G4 branch introduces several improvements over the previous version, enhancing compatibility with PPFX studies, expanding physics list options, integrating external Dk2Nu data structures, and restoring support for GDML output generation.

Detailed instructions for building and running the new branch are available on Fermilab Redmine, while instructions for the older branch can be found here.

Old (G4.9.2)	**New (G4.10.04)**
Geant4-09-02-patch-03 (29-January-2010)	Geant4-10-04-patch-02b (04-February-2019)
Geant4 Physics List simulation engine: FTFP_BERT 1.0	Geant4 Physics List simulation engine: FTFP_BERT 2.0
Depends on an internal (ancient) copy for the Dk2Nu data structures.	Depends on the dk2nudata UPS product for the Dk2Nu data structures.
Cannot write an output a GDML file	Can write an output a GDML file

Table 3.3: Differences between Old g4numi (G4.9.2) and New g4numi (G4.10.04)

The following plots show various comparisons of flux spectra, ND/FD ratios, and neutrino parent distributions for both Forward Horn Current (FHC) and Reverse Horn Current (RHC) configurations. These plots include the off-axis configuration of the NOνA experiment and the on-axis configuration like of MINOS experiment, allowing us to compare the effects of the old and new G4NuMI models both on-axis and off-axis.

From these plots, we observe that in the Off-Axis Near Detector, there is approx-

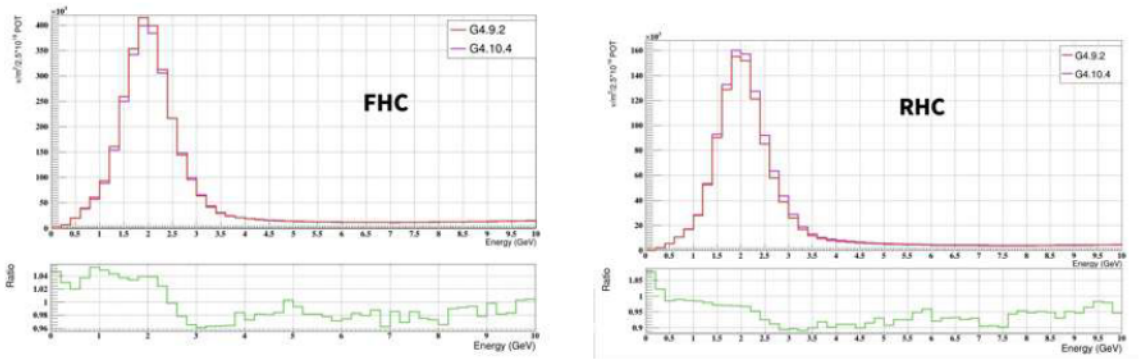

(a) FHC (b) RHC

Figure 3.5: Off-Axis ND Flux Spectra of Old and New G4NuMI in FHC and RHC.

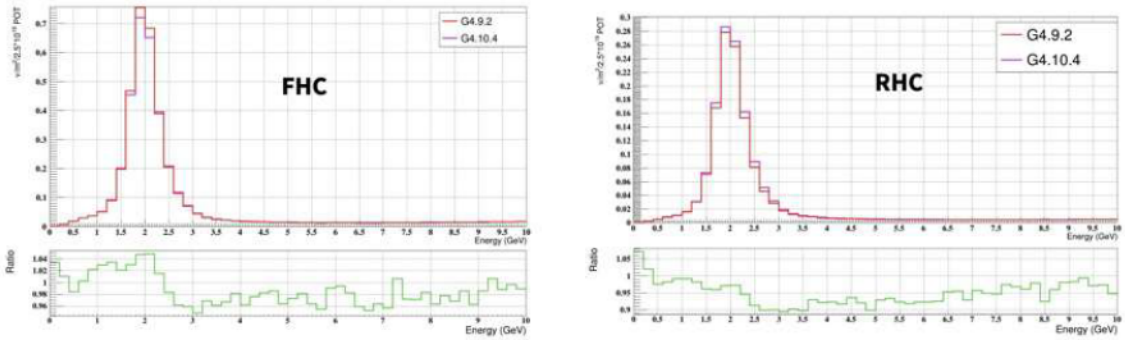

(a) FHC (b) RHC

Figure 3.6: Off-Axis FD Flux Spectra of Old and New G4NuMI in FHC and RHC.

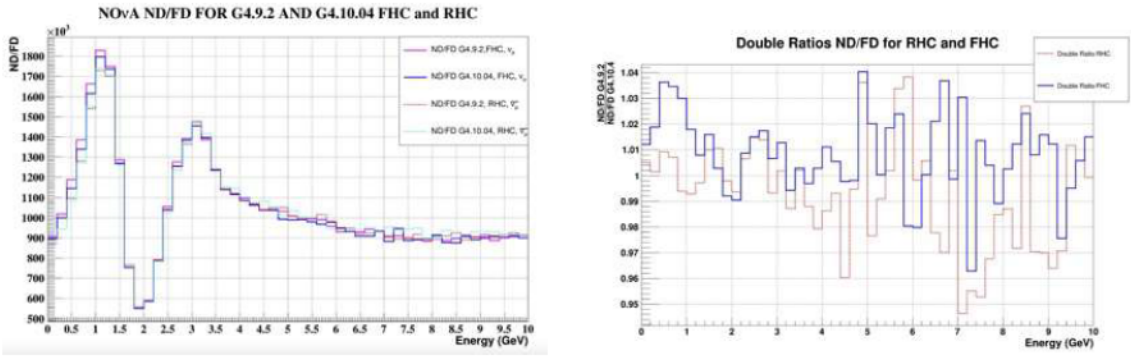

(a) ND/FD Ratio (FHC and RHC) (b) ND/FD Double Ratio (FHC and RHC)

Figure 3.7: Comparison of ND/FD Ratio and ND/FD Double Ratio for Old and New G4NuMI in FHC and RHC.

imately a 5% flux variation for ν_μ (FHC) and about 10% for $\overline{\nu_\mu}$ (RHC) within the 1–3 GeV range. For the On-Axis Near Detector flux, a discrepancy of approximately 4–5% is observed for ν_μ (FHC) in the 1–3 GeV range, while a smaller variation of

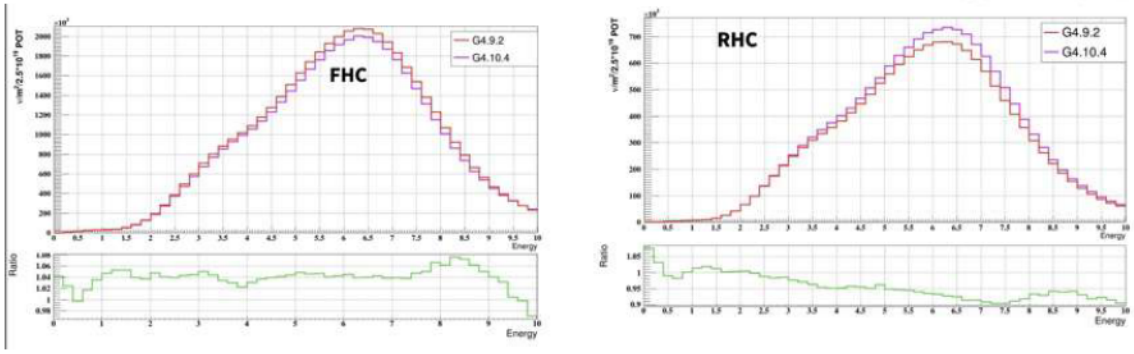

(a) On-Axis (MINOS) ND Flux (FHC) (b) On-Axis (MINOS) ND Flux (RHC)

Figure 3.8: On-Axis ND Flux Spectra in FHC and RHC.

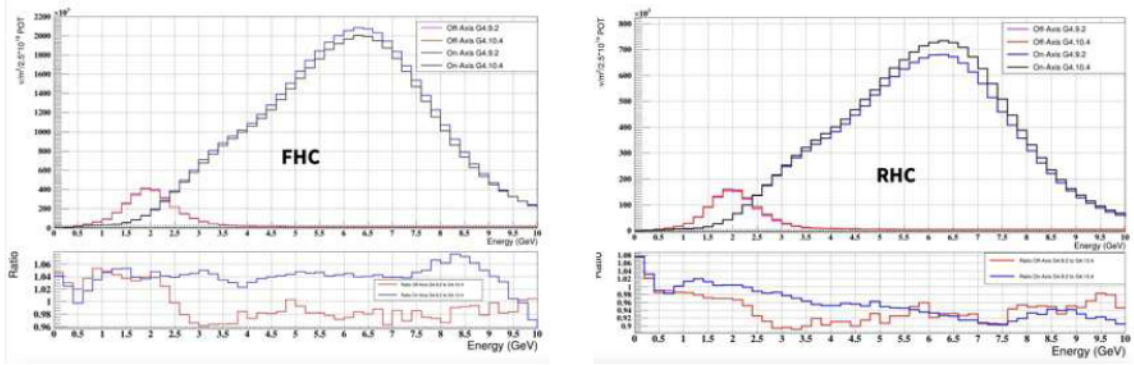

(a) On/Off-Axis Flux (FHC) (b) On/Off-Axis Flux (RHC)

Figure 3.9: Comparison of On-Axis and Off-Axis Flux Spectra for FHC and RHC, with ratios below each canvas.

around 2% is observed for $\overline{\nu_\mu}$ (RHC) within the same energy range.

For the neutrino parent flux comparisons under FHC configurations, the following plots are included:

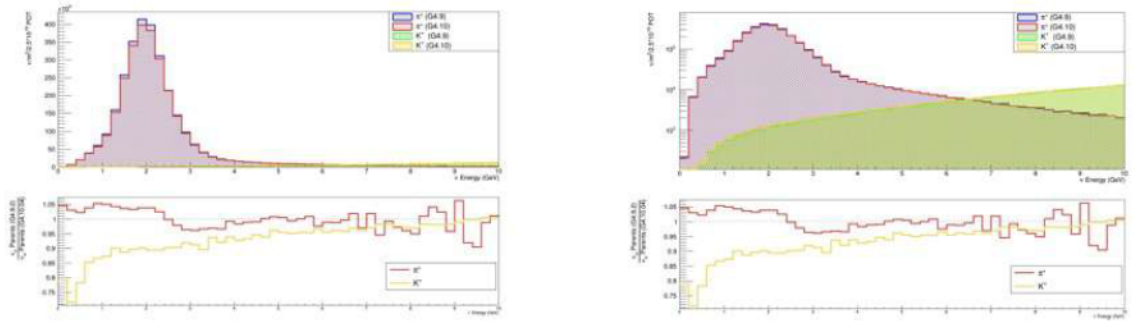

(a) Linear Scale (b) Log Scale

Figure 3.10: FHC Off-Axis (NOνA ND) Flux Spectra in Linear and Log Scales.

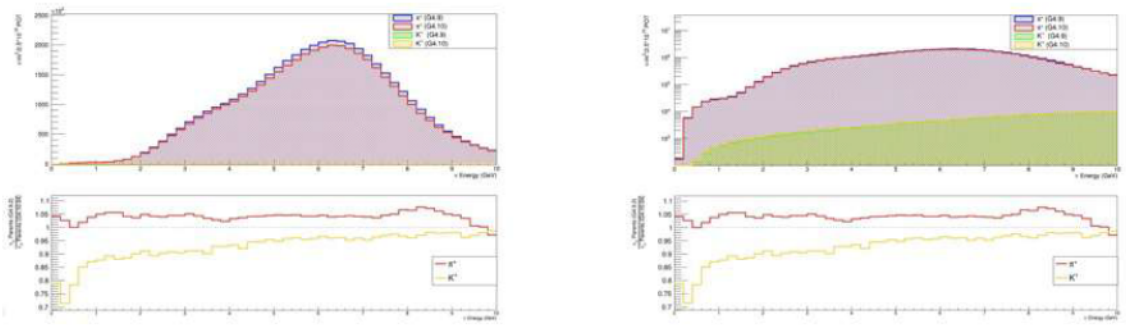

(a) Linear Scale (b) Log Scale

Figure 3.11: FHC On-Axis (MINOS ND) Flux Spectra in Linear and Log Scales.

For the neutrino parent flux comparisons under RHC configurations, the following plots are included:

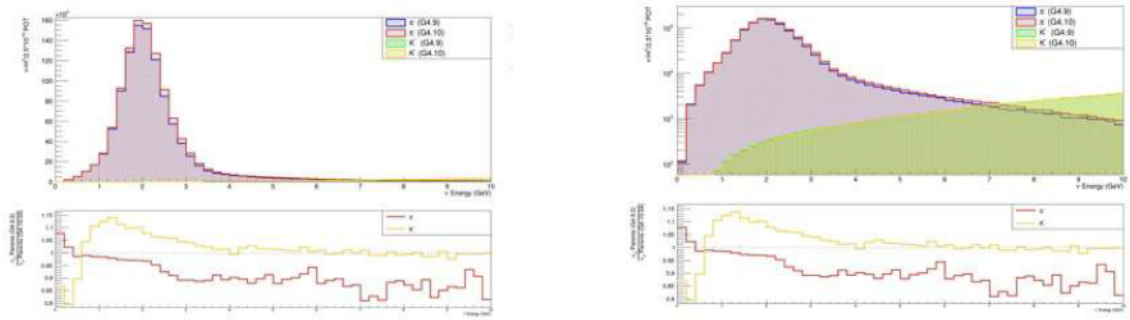

(a) Linear Scale (b) Log Scale

Figure 3.12: RHC Off-Axis (NOνA ND) Flux Spectra in Linear and Log Scales.

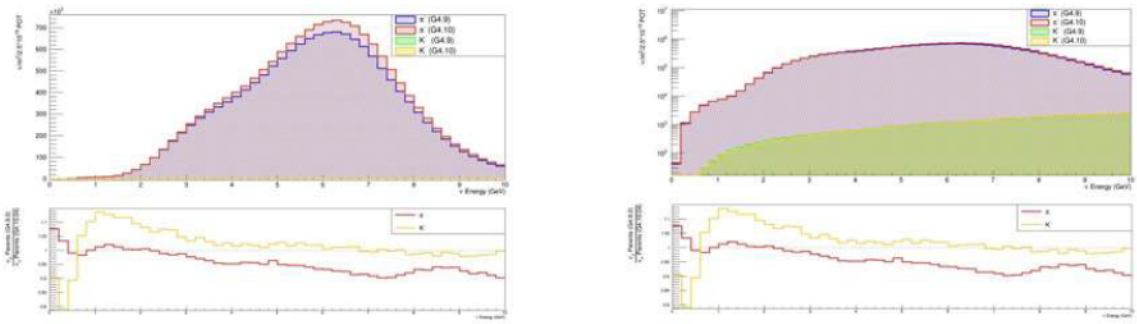

(a) Linear Scale (b) Log Scale

Figure 3.13: RHC On-Axis (MINOS ND) Flux Spectra in Linear and Log Scales.

Table 3.4 summarizing the flux discrepancies in FHC and RHC for on-axis and off-axis configurations, based on the different configurations of the figures plotted above.

Mode	Configuration	Flux	Discrepancy (%)
FHC (1-3 GeV)	On-Axis (MINOS)	ν_μ	$\sim 4-5$
		Parents (π^+)	~ 5
	Off-Axis (NOνA)	ν_μ	~ 5 (with sudden dip at 3 GeV)
		Parents (π^+)	~ 5 (with sudden dip at 3 GeV)
RHC (1-3 GeV)	On-Axis (MINOS)	$\overline{\nu}_\mu$	~ 2
		Parents (π^-)	~ 2
	Off-Axis (NOνA)	$\overline{\nu}_\mu$	~ 10 (with sudden dip at 3 GeV)
		Parents (π^-)	~ 8 (with sudden dip at 3 GeV)

Table 3.4: Summary of Flux Discrepancies in FHC and RHC for On-axis and Off-axis Configurations

Figure 3.14: Beamline output GDML file generated with the latest G4NuMI version, showing the target and Horn 1 enclosure.

The discrepancy in ν_μ flux appears to be almost proportional to the discrepancy in the parent π flux, likely due to differences between the RHC FTFP BERT 1.0 and FTFP_BERT 2.0 hadron production models. Additionally, the 9-year gap between these versions may contribute to further differences in more intricate aspects.

The output GDML file of the beamline, generated using this new G4NuMI version, is shown in Figure 3.14. This image is one of the outputs possible with the new Geant4 version, highlighting one of its advantages. In the figure, the first enclosure has the target, and the second enclosure contains Horn 1. A more detailed image generated with this version is presented in the next section.

3.4 Studies with Virtual Detectors Downstream of Target and Horn1

This study focuses on the region downstream of the Target and Horn 1, utilizing the latest version of G4NuMI as described earlier.

3.4.1 Introduction

The NuMI (Neutrinos at the Main Injector) Beamline at Fermilab is a vital component of the Fermilab accelerator complex, producing a high-intensity 120 GeV proton beam through the Main Injector. This powerful proton beam enables a wide range of on-axis and off-axis experiments, such as MINOS, MINERνA, NOνA, and in future, the EMPHATIC(Experiment to Measure the Production of Hadrons at a Testbeam in Chicagoland) during its second-phase run. The second phase of EMPHATIC will operate with the NuMI Beamline in the Target and Horn 1 (Off) configuration.

In this study, the flux, energy, and momentum distributions of particles are analyzed at five different locations downstream of Horn 1 to examine the impact of distance on these distributions. Additionally, the same distributions are compared to those obtained with the Horn Off configuration to evaluate the effect of horn focusing and the resulting differences in beam spread at these five locations.

3.4.2 Motivation

The motivation behind this study aligns with the broader goal of understanding neutrino flux uncertainties, as outlined in Chapter 1. Precise neutrino flux determination is essential for reducing systematic uncertainties in neutrino oscillation measurements. As discussed in Section 1.6, achieving this precision requires a detailed understanding of hadron production and the interactions occurring within the beamline.

In addition to these overarching goals, this study specifically focuses on the NuMI beamline downstream of Horn 1. Virtual detector planes are placed downstream of Horn 1 to analyze the characteristics of particles reaching these planes. By studying these distributions, we aim to gain deeper insight into hadron production and secondary interactions within the beamline, ultimately contributing to improved neutrino flux predictions.

Virtual detector planes downstream of Horn 1 are placed and the characteris-

tics of particles reaching that specific plane are recorded. The study presents flux, energy, and momentum spectra at five distinct locations along these planes. By examining different setups with the the Horn on (Forward Horn Current) and off, we seek to understand and illustrate the variations in particle distributions at each of these planes. The main goal is to understand how particle flux is distributed at various locations at the end of Horn 1. The significance of this study lies in its potential to identify the optimal location for recording particles/events, a crucial aspect for experiments like EMPHATIC, as discussed further in Chapter 4. As EMPHATIC prepares for Phase 2 of its run, utilizing the NuMI Target and Horn, insights from this study could guide the strategic placement of detectors. This contribution enhances the efficiency and precision of EMPHATIC, which aims to reduce neutrino flux prediction uncertainties. The experiment's data will also benefit the broader scientific community relying on hadron interaction modeling.

3.4.3 Virtual Detector Plane

The Virtual Detector Plane that is 1mm thick and has an area of 1m*1m is placed at various distances downstream of the Numi Horn 1. The virtual detector is made of air and the particles are recorded and killed at the location of the virtual detector plane and the information is saved in the form of ntuples in a separate tree inside a separate file. As the Horn1 ends at ~332 cm from the start of the coordinate axis in which the 0 is the start of Horn1, The distances where the virtual detector would be placed are given in Table 3.5.

Z (cm)	Distance from Horn 1 (cm)
350	18
382	50
432	100
482	150
532	200

Table 3.5: Placements of the Virtual Detector Plane placed downstream of NuMI Horn 1

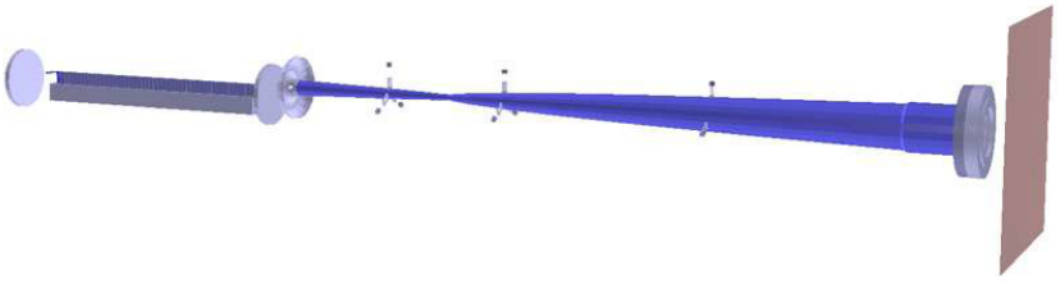

Figure 3.15: Virtual Detector placed at z= 350 cm along the NuMI Beamline ((From the left) Figure shows Target, Horn 1 and the Virtual Detector Plane)

3.4.4 Parameters used for the study

Following parameters were used for this study:

- G4numi Branch: main_h1TrackingPlane
- Protons on Target (PoTs): 1000000
- Physics List: FTFP_BERT
- Horn Current: 0 kA(Horn off) and 200 kA(Horn on)
- Importance Weights : Off
- Kill Tracking Threshold: 2MeV
- Target: New Medium Energy NOνA Target

Also this is an exhaustive list of all the Particles that are recorded on the Plane with the corresponding Numi Particle codes:

Particle Type	Particle Code
Electron (e^-)	2
Positron (e^+)	3
Gamma (γ)	4
Muon Plus (μ^+)	5
Muon Minus (μ^-)	6
Pion Neutral (π^0)	7
Pion Plus (π^+)	8
Pion Minus (π^-)	9
Kaon Long (K^0_L)	10
Kaon Plus (K^+)	11
Kaon Minus (K^-)	12
Neutron (n)	13
Proton (p)	14
Anti-Proton ($\bar{p}$)	15
Kaon Short (K^0_S)	16
Eta (η)	17
Lambda (Λ)	18
Sigma Plus (Σ^+)	19

(a) Numi Particle Codes 2-19

Particle Type	Particle Code
Sigma Neutral (Σ^0)	20
Sigma Minus (Σ^-)	21
Xi Neutral (Ξ^0)	22
Xi Minus (Ξ^-)	23
Omega Minus (Ω^-)	24
Anti-Neutron ($\bar{n}$)	25
Anti-Lambda ($\bar{\Lambda}$)	26
Anti-Sigma Minus ($\bar{\Sigma}^-$)	27
Anti-Sigma Neutral ($\bar{\Sigma}^0$)	28
Anti-Sigma Plus ($\bar{\Sigma}^+$)	29
Anti-Xi Neutral ($\bar{\Xi}^0$)	30
Anti-Xi Minus ($\bar{\Xi}^-$)	31
Electron Anti-Neutrino ($\bar{\nu}_e$)	52
Electron Neutrino (ν_e)	53
Muon Anti-Neutrino ($\bar{\nu}_\mu$)	55
Muon Neutrino (ν_μ)	56
Other	99
Default	99

(b) Numi Particle codes from 20-99

Figure 3.16: Particle Codes for all Particles recorded at H1 Tracking Plane

Details regarding the code development for the `main_h1TrackingPlane` branch, including implementation specifics and modifications, are provided in Appendix A.1.

3.4.5 Particle Production Vertices

Below is a side view (YZ plane) of the particle production vertices to show where the particles that are recorded on the virtual detector planes are originally produced.

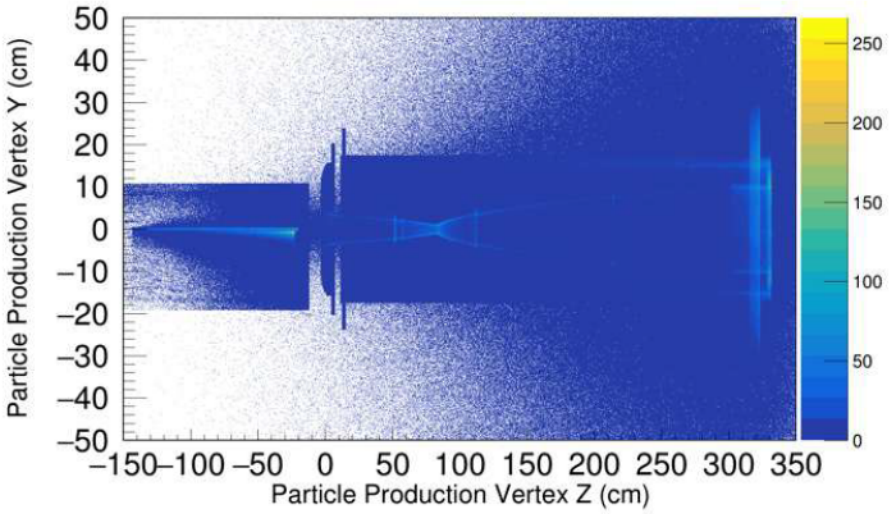

Figure 3.17: Side view of Particle Production vertices

3.4.6 Horn off Configuration

Additional plots for charged and neutral particles, as well as backgrounds (electrons, positrons, and gammas), showing flux and longitudinal vs. transverse momenta, are provided in Appendix A.1.

Flux

All Particles, Pions and Kaons

(Up to down: 18cm, 50 cm 100 cm , 150 cm and 200 cm from Horn 1)

(Left to Right: All Particles, Pions and Kaons)

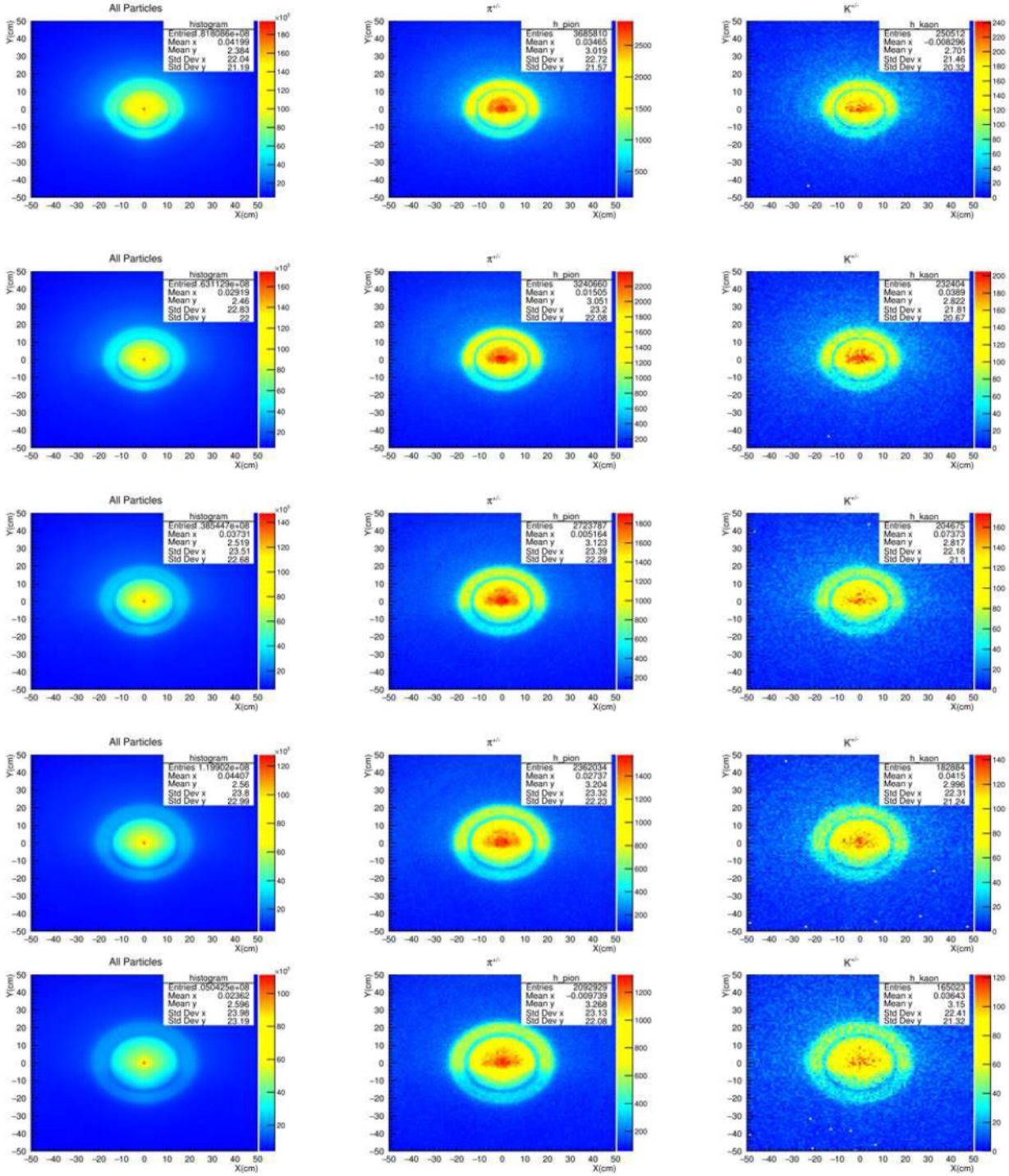

Longitudnal v/s Transverse Momenta

All Particles, Pions and Kaons

(Up to down: 18cm, 50 cm,100 cm , 150 cm and 200 cm from Horn 1)

(Left to Right: All Particles, Pions and Kaons)

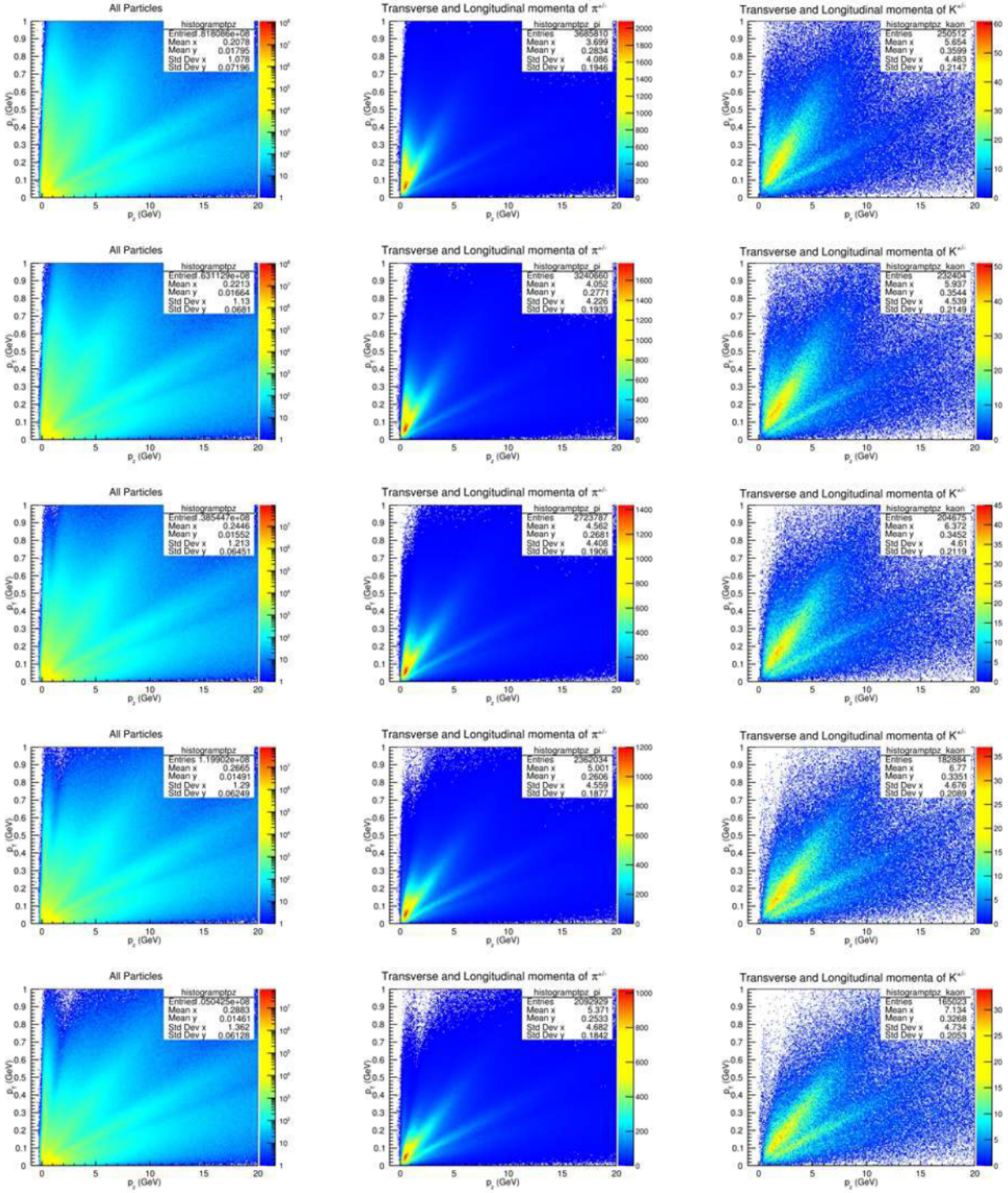

Energy Spectra

(Up to down: 18cm, 50 cm,100 cm , 150 cm and 200 cm from Horn 1)

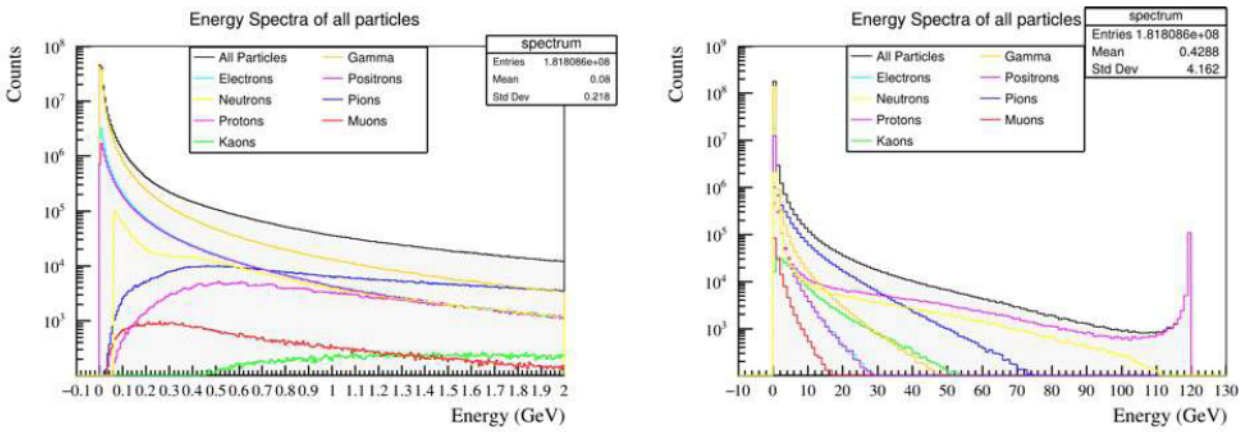

Figure 3.18: (From Left)0 to 2GeV and 0 to 120GeV at 18 cm from the end of Horn 1

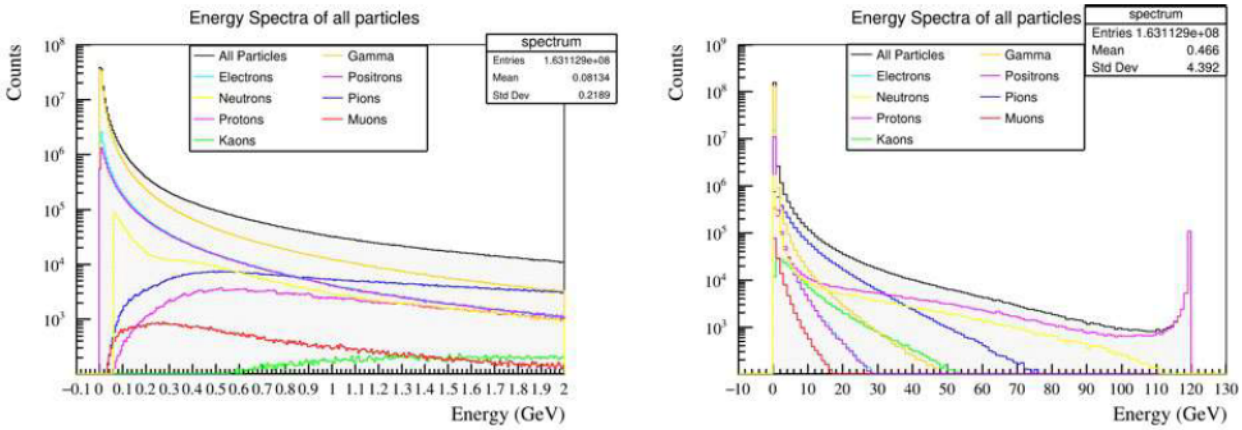

Figure 3.19: (From Left)0 to 2GeV and 0 to 120GeV at 50 cm from the end of Horn 1

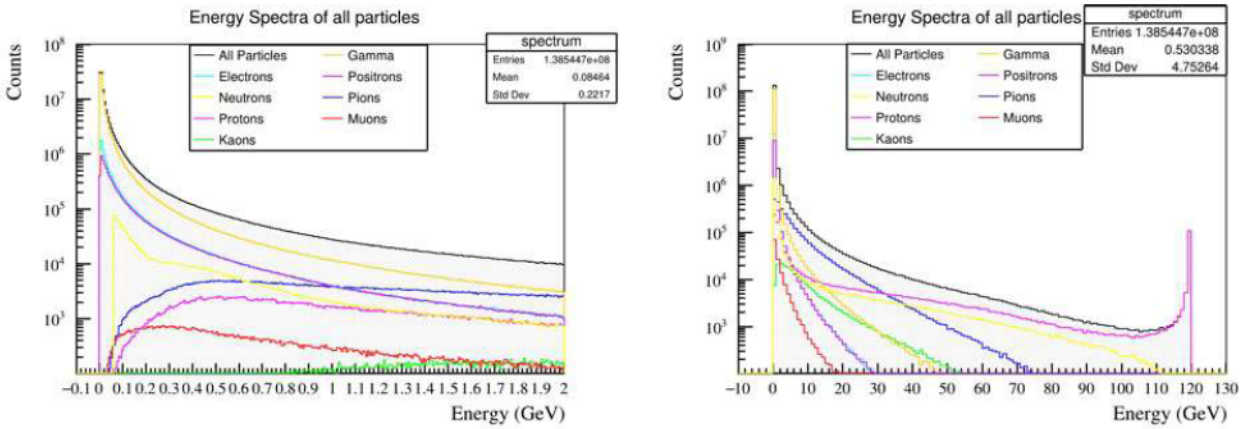

Figure 3.20: (From Left)0 to 2GeV and 0 to 120GeV at 100 cm from the end of Horn 1

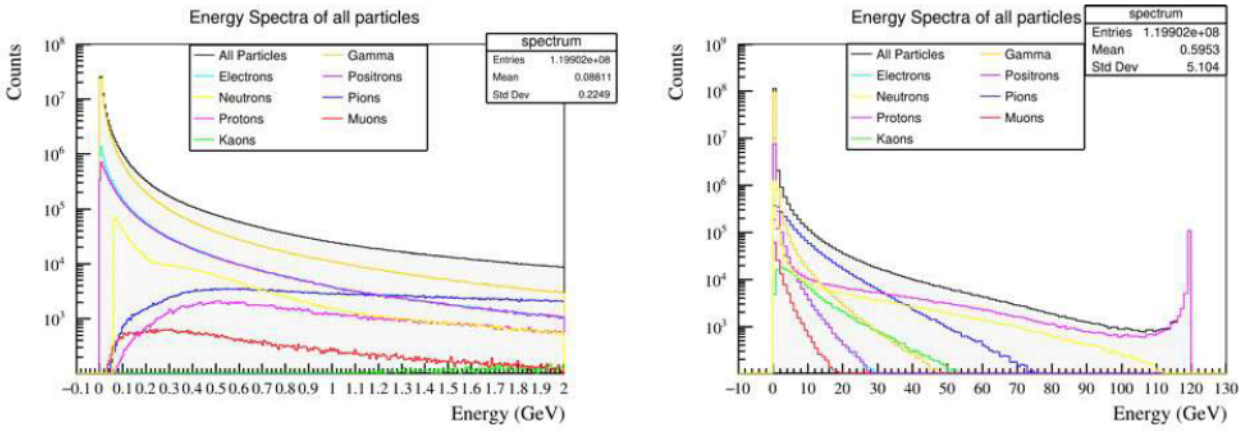

Figure 3.21: (From Left)0 to 2GeV and 0 to 120GeV at 150 cm from the end of Horn 1

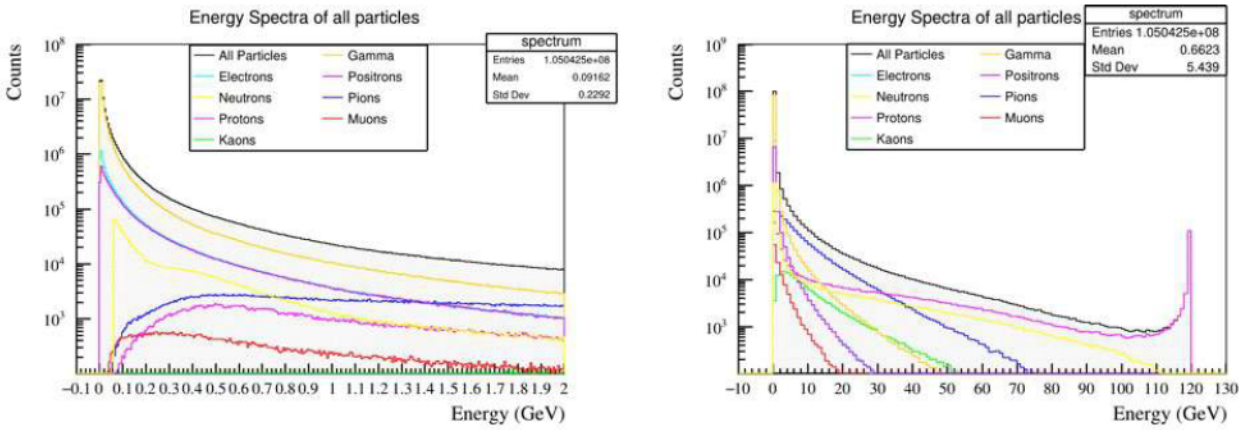

Figure 3.22: (From Left)0 to 2GeV and 0 to 120GeV at 200 cm from the end of Horn 1

3.4.3 Horn On Configuration

Additional plots for charged and neutral particles, as well as backgrounds (electrons, positrons, and gammas), showing flux and longitudinal vs. transverse momenta, are provided in Appendix A.2.

Flux

All Particles, Pions and Kaons

(Up to down: 18cm, 50 cm 100 cm , 150 cm and 200 cm from Horn 1)

(Left to Right: All Particles, Pions and Kaons)

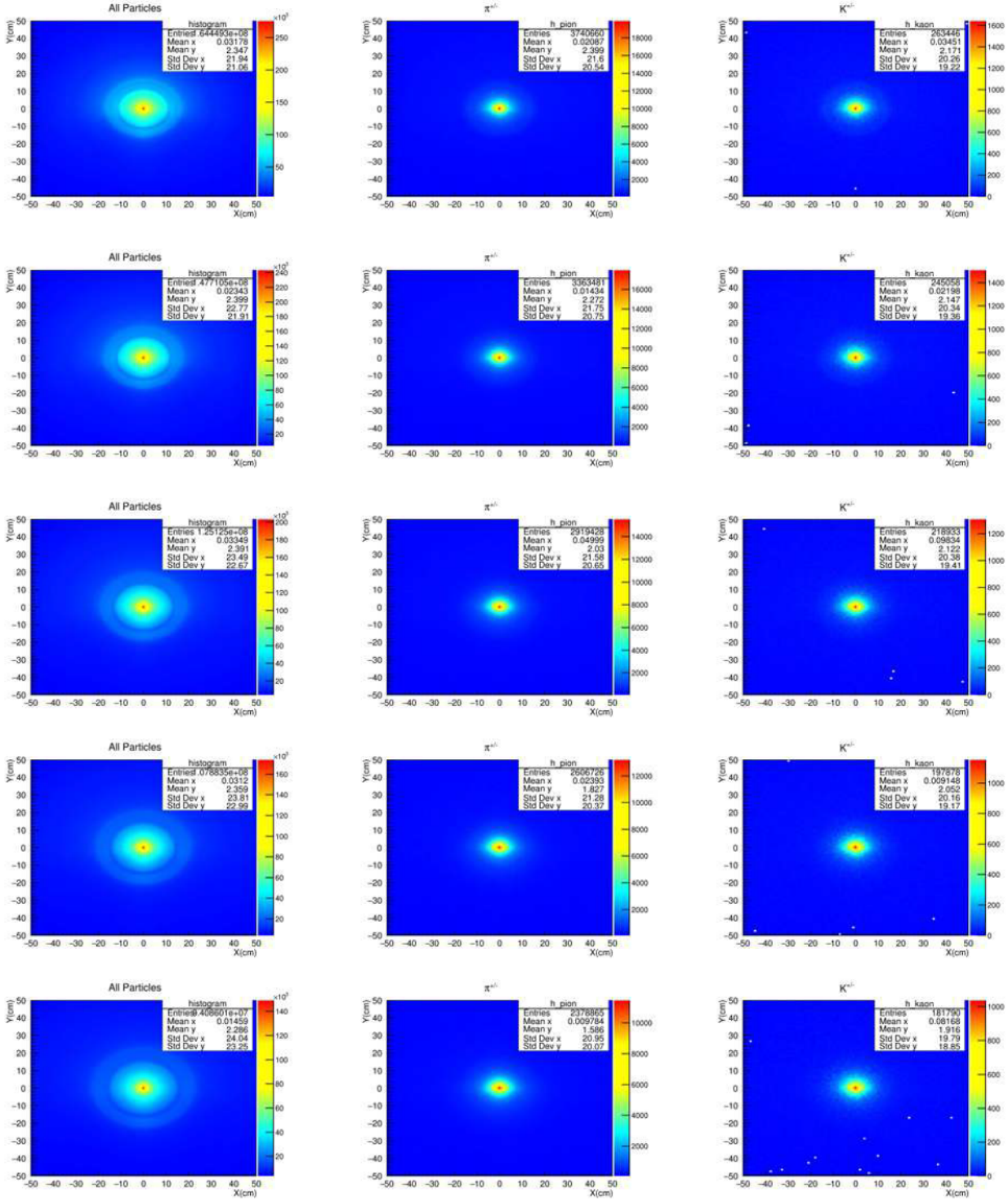

Longitudnal v/s Transverse Momenta

All Particles, Pions and Kaons

(Up to down: 18cm, 50 cm 100 cm , 150 cm and 200 cm from Horn 1)

(Left to Right: All Particles, Pions and Kaons)

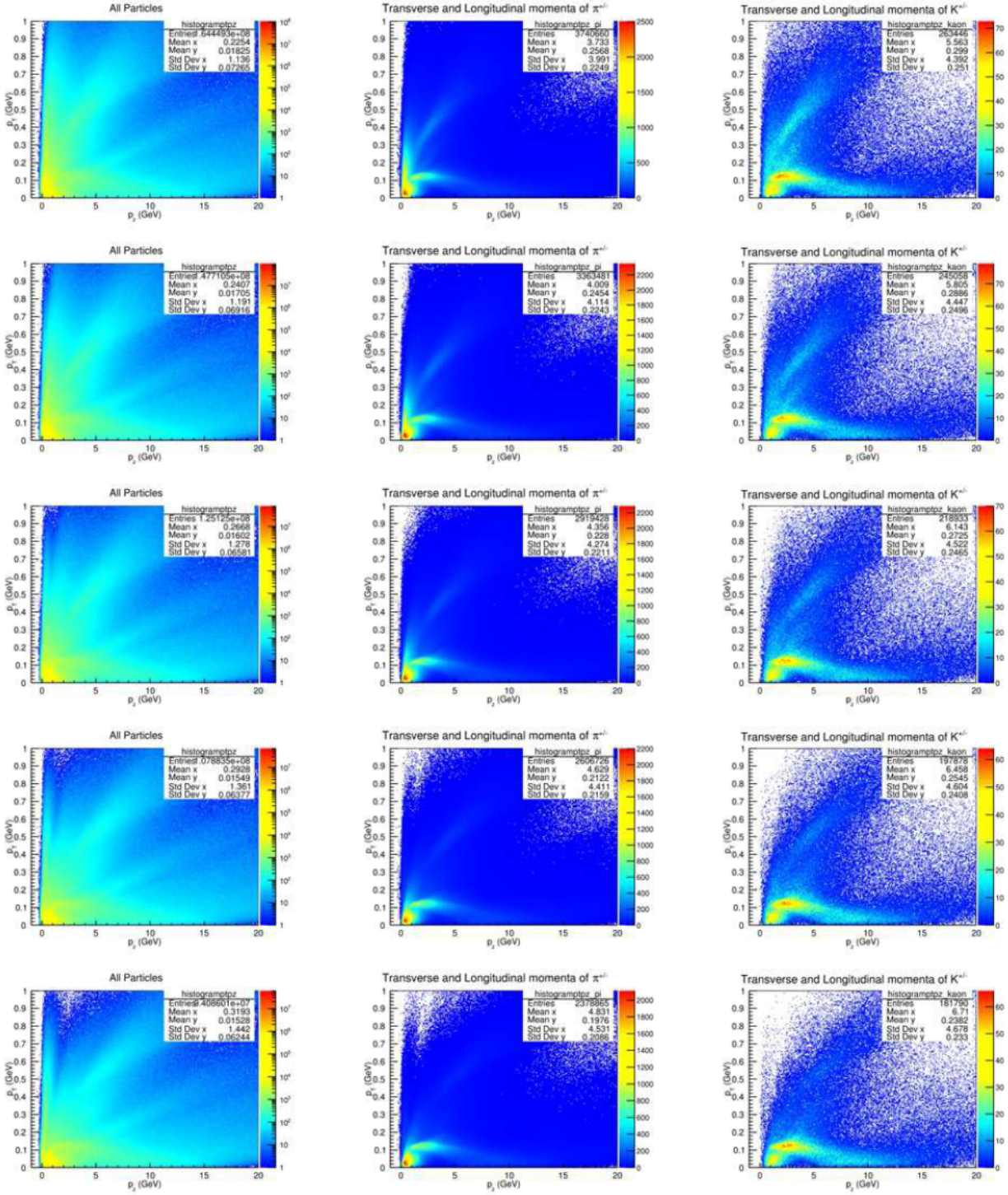

3.4.3.1 Energy Spectra

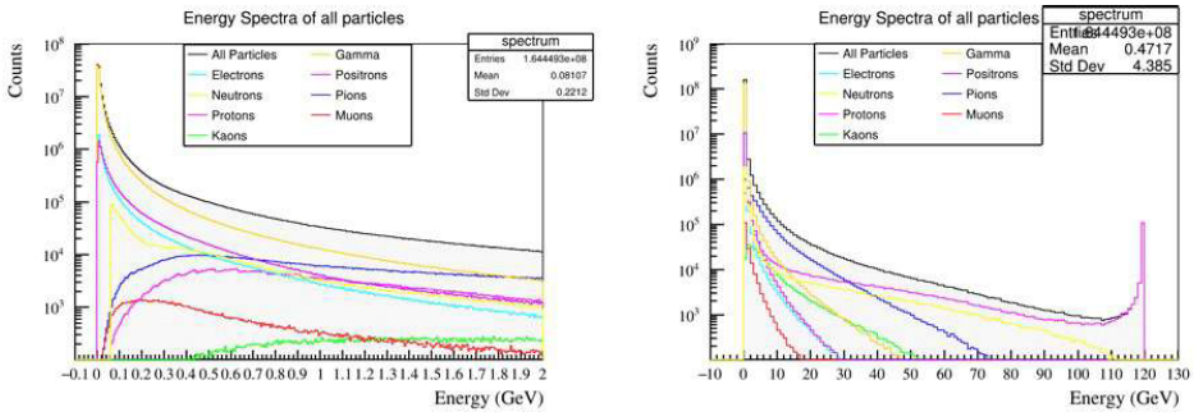

Figure 3.23: (From Left)0 to 2GeV and 0 to 120GeV at 18 cm from the end of Horn 1

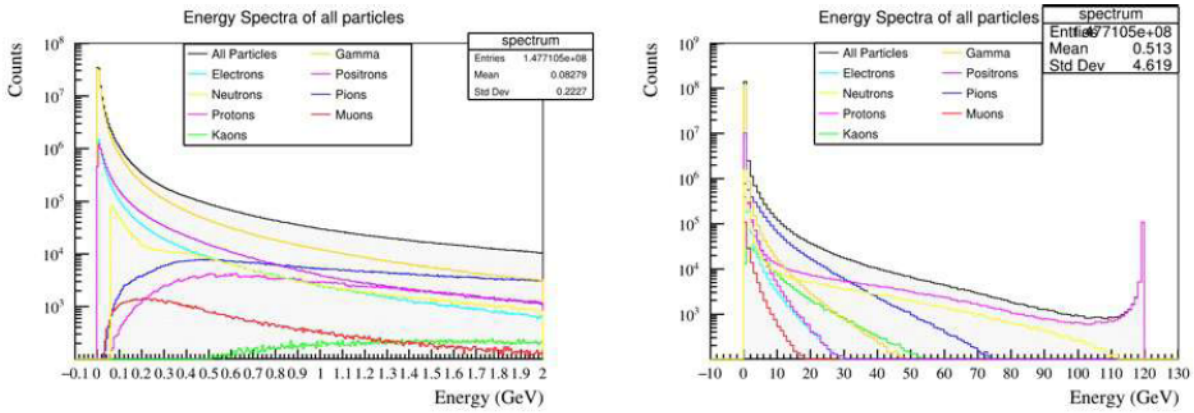

Figure 3.24: (From Left)0 to 2GeV and 0 to 120GeV at 50 cm from the end of Horn 1

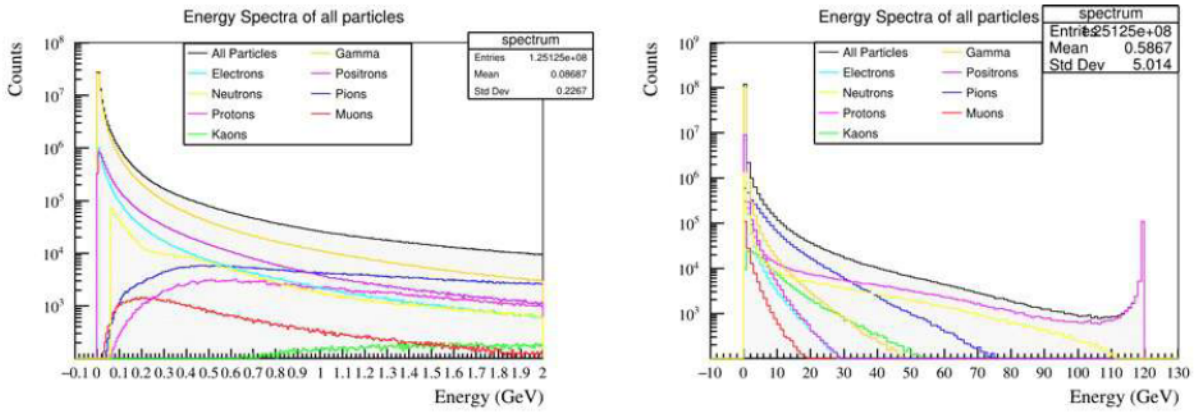

Figure 3.25: (From Left)0 to 2GeV and 0 to 120GeV at 100 cm from the end of Horn 1

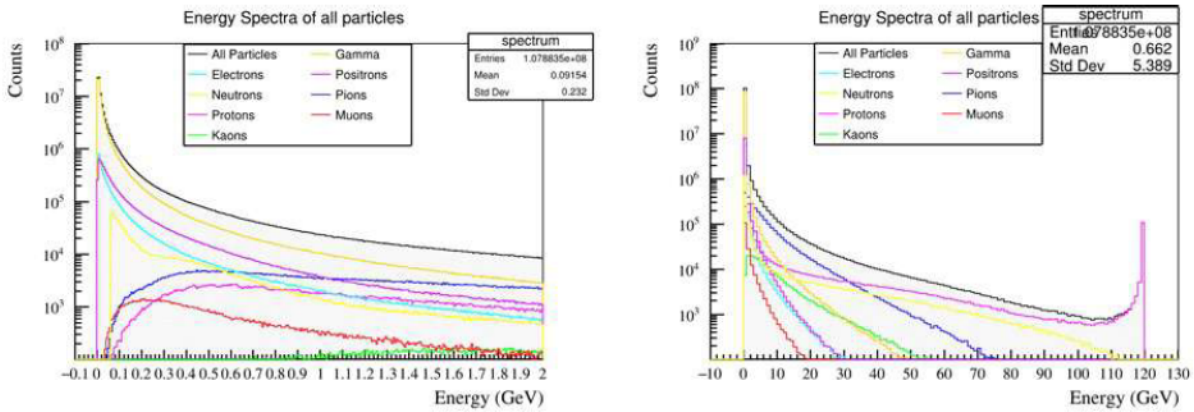

Figure 3.26: (From Left)0 to 2GeV and 0 to 120GeV at 150 cm from the end of Horn 1

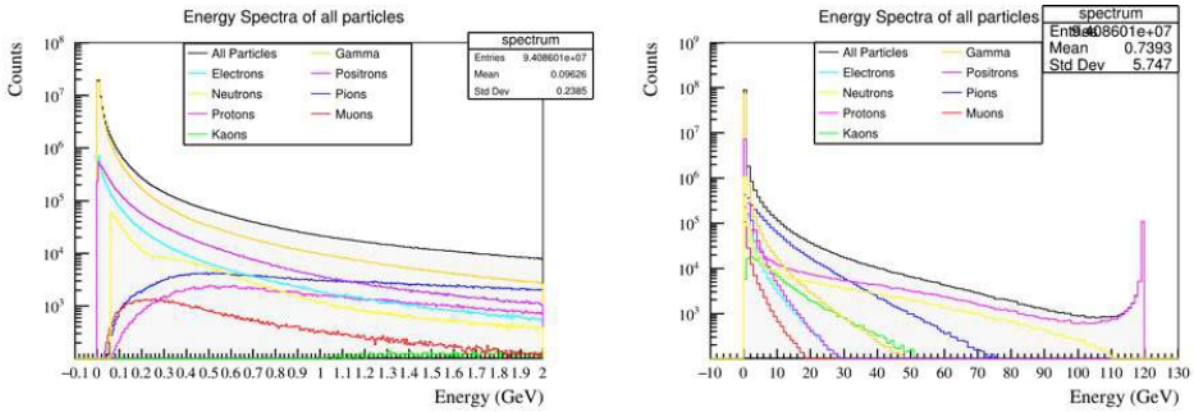

Figure 3.27: (From Left)0 to 2GeV and 0 to 120GeV at 200 cm from the end of Horn 1

Conclusions

From the plots of Flux, we conclude that:

1. **Horn-On Configuration**
    - **Focused Flux:** The magnetic horn focuses charged particles (pions, kaons), directing them along the beamline and increasing neutrinos in the desired energy range.
    - **Higher Neutrino Flux:** More parent particles enter the decay pipe, producing higher neutrino flux at the detector.
    - **Narrower Energy Spectrum:** A more collimated beam.
2. **Horn-Off Configuration**
    - **Defocused Flux:** Without the horn, charged particles spread out, creating a less collimated beam.
    - **Lower Neutrino Flux:** Fewer parent particles reach the decay pipe, reducing neutrino flux.
    - **Wider Energy Spectrum:** The beam is less focused, producing a broader energy spectrum with more low- and high-energy neutrinos.

Also, we can compare the plots of transverse vs. longitudinal momenta in the horn-on and horn-off configurations. In the horn-on plots, a sharp, high-density region appears along the p_z axis with low p_T, while in the horn-off configuration, the distribution is more scattered, with particles occupying a larger range in both p_T and p_z. A better comparison is shown below:

1. **Horn-On Configuration**
    - **Focusing Effect:** The magnetic horn focuses charged particles (e.g., pions and kaons), particularly those aligned with the beam axis (z-direction), resulting in:
        - Higher longitudinal momentum (p_z) for many particles.
        - A denser concentration of particles near the beamline.

- **Narrower Transverse Momentum Distribution (p_T):**
  - The horn reduces the transverse spread, leading to smaller p_T values.
  - Particles appear closer to the $p_T = 0$ axis.
- **Increased Density:** The plots show higher density in regions of high p_z and low p_T.

2. **Horn-Off Configuration**
   - **No Focusing:** Without the horn, charged particles spread isotropically, leading to:
     - Lower longitudinal momentum (p_z).
     - A broader spread of particles in transverse momentum (p_T).
   - **Wider Transverse Momentum Distribution (p_T):**
     - Particles are distributed more uniformly across the p_T axis.
     - A larger range of p_T values is observed.
   - **Lower Density:** The overall density of particles is lower, especially at high p_z.

Thus, the study of particle recordings at five positions of the virtual detector downstream of Horn 1 provides valuable insights into the flux, momenta, and energy spectra under both horn-on and horn-off configurations. This allows for a better understanding of the neutrino flux downstream of Horn 1 on the NuMI beamline. The results can be utilized by various experiments that use the NuMI beamline, helping to determine optimal locations for future detectors. Furthermore, given the budgetary constraints of running experiments with the horn on, studies like this can assess the impact of switching to a horn-off configuration on flux, momenta, and energy. As EMPHATIC prepares for Phase 2, insights from this study will guide the strategic placement of detectors, thereby enhancing the efficiency and precision of the experiment while reducing uncertainties in neutrino flux predictions as discussed in Chapter 4.

Future plans include integrating the above flux, energy, and momentum spectra,

along with related information, into the EMPHATIC software framework to prepare for Phase 2 simulations of EMPHATIC.

Thus, the insights gained from the studies discussed in this chapter are valuable for experiments utilizing the NuMI beamline, including EMPHATIC. The following chapter introduces the EMPHATIC experiment, detailing its motivation, experimental setup, and initial data collection efforts, which will benefit from improved flux predictions and detector optimization strategies discussed in this chapter.

Chapter 4

The EMPHATIC Experiment

Accurately modeling neutrino production in accelerator-based and atmospheric neutrino experiments requires precise measurements of hadron interactions for incident particle momenta ranging from 1 to 100 GeV/c. As discussed in Chapter 1, hadron production experiments, provide essential data to refine hadronic interaction generators and improve Monte Carlo-based neutrino flux predictions. The neutrino flux uncertainty dominate many neutrino measurements, including cross-section studies, sterile neutrino searches, and CP violation measurements. With upcoming long-baseline experiments like Hyper-Kamiokande and DUNE entering a precision era, uncertainties in neutrino flux and cross-section energy dependence are most challenging systematics. Neutrinos arise from hadron decays in proton-nucleus interactions, because directly measuring neutrino flux as a function of energy is challenging, Monte Carlo simulations relying on hadron interactions are utilized. However, sparse data and errors in hadron interaction models introduce uncertainties, which can be reduced by directly measuring hadron interactions to constrain or refine the models for more accurate neutrino flux predictions. The need for improved hadron interaction measurements was highlighted in Chapter 3 in the context of optimizing particle detection strategies for experiments like EMPHATIC.

The majority of hadron interaction data used for GeV-energy neutrino flux predictions were gathered in the 20th century; however, they are limited in precision and

lack well-defined error covariances. Recent experiments like NA61/SHINE, HARP, and MIPP have improved data quality with targeted cross-section and hadron production measurements. Despite this, current accelerator-based neutrino experiments face 5–15% flux uncertainty due to limited phase space coverage and systematic errors.

Neutrino flux uncertainty directly affects single-detector measurements as far-to-near detector cancellation is not possible and impacts CP violation studies in neutrino oscillations. Reducing flux uncertainty, especially the ν_e/ν_μ ratio and measuring ν_e cross-section, is critical for Hyper-Kamiokande and DUNE experiments, requiring levels below 3%. Atmospheric neutrino CP violation measurements are similarly constrained by flux uncertainties from sub-20 GeV/c cosmic ray interactions.

Minimizing uncertainties in neutrino flux necessitates addressing gaps in data, including:

1. Hadron production in pion and kaon interactions below 10 GeV on targets such as carbon, aluminum, titanium, and iron.
2. Hadron production from proton interactions with air (or equivalent targets) at energies below 20 GeV.
3. Coherent elastic and quasi-elastic interactions of hadrons with carbon, aluminum, titanium, and iron over a momentum range of 1–120 GeV/c.
4. Production of strange hadrons in proton-carbon collisions to cross-check existing experimental data.

4.1 Introduction

EMPHATIC at Fermilab's Test Beam Facility, studies 2–120 GeV/c hadron interactions to improve neutrino flux predictions for future long-baseline experiments. Its compact spectrometer uses silicon strip detectors (SSDs) ($\sim$10 μm resolution), a custom Halbach dipole magnet (0.25 Tm B.dl), gas/aerogel Cherenkov detectors for

beam particle identification, time-of-flight RPC measurements and measurement of Cherenkov angle in aerogel ring imaging detector (ARICH) based on the Belle-II design for secondary particle identification. A lead calorimeter separates electrons, muons, and hadrons. The total spectrometer length is ~2 m.

A test-beam experiment conducted in January 2018 [60] utilized SSDs to track particle trajectories without incorporating a magnet or secondary particle identification detectors. The study measured differential cross-sections for $p + C \to X^{\pm}$ at momenta of 20, 30, and 120 GeV/c, where $X^{\pm}$ represents a charged particle within a 20 mrad acceptance determined by the tracking detectors. This approach enabled the investigation of forward scattering, including coherent elastic and quasi-elastic interactions. The observed event topology, characterized by a single forward-moving charged particle, includes contributions from coherent elastic, quasi-elastic, and certain inelastic interactions. In coherent elastic scattering, the entire nucleus remains intact, while quasi-elastic interactions involve the fragmentation of the target nucleus. Inelastic interactions produce at least one new meson.

The new data from EMPHATIC will reduce uncertainties and improve flux predictions, benefiting all GeV-scale neutrino experiments. Conservative estimates show reductions in key uncertainties:

- K absorption ($p < 4$ GeV/c): 60–90% $\to$ 10%.
- Quasi-elastic interactions: 40% $\to$ 10%.
- $p + X$: 40% $\to$ 10%.
- $K + X$: 40% $\to$ 20%.

EMPHATIC aims to achieve better than 10% measurements.

4.2 Experimental Setup

EMPHATIC will undergo multiple phases throughout its lifetime; currently, Phase 1 is complete, and preparations for Phase 2 are underway. Unless stated otherwise, the experimental setup described here pertains to Phase 1. A schematic of the

EMPHATIC layout is given in Figure 4.1.

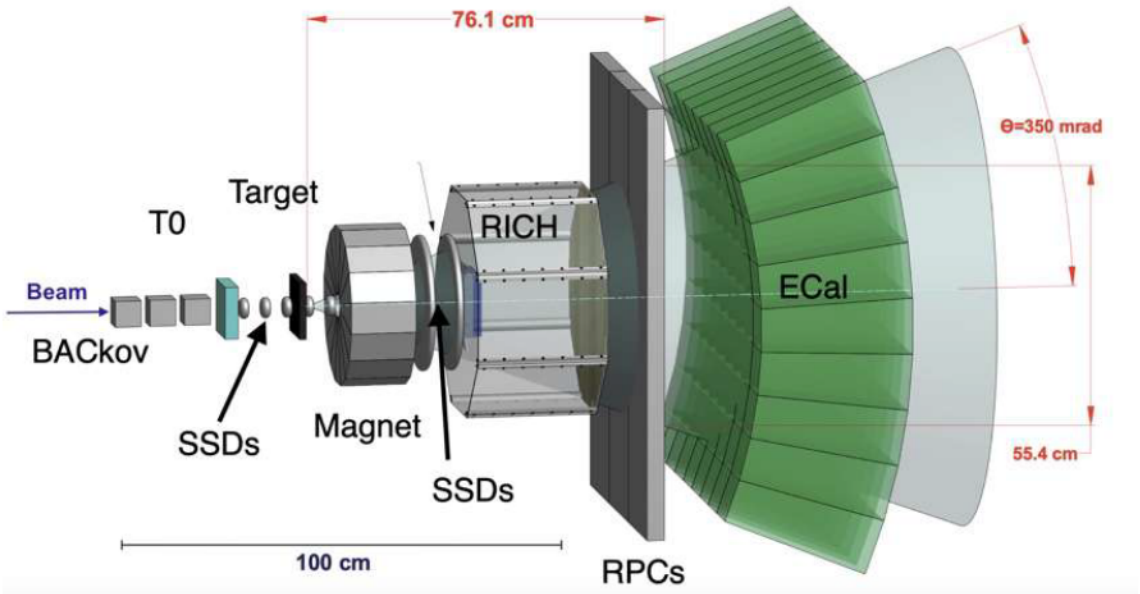

Figure 4.1: Top view of the EMPHATIC detector layout. Note that smaller versions of the Magnet, RICH, and ECal were used in Phase 1, providing ≤100 mrad acceptance and PID up to 8 GeV/c.

EMPHATIC test-beam measurements took place at the FTBF, where a 120 GeV/c proton beam from the Main Injector or a secondary beam with momentum exceeding 2 GeV/c was utilized. The beam is delivered in 4-second spills each minute, with an adjustable intensity ranging from 1 kHz to 100 kHz and a typical spot size of $2\,\mathrm{cm}^2$.

The secondary beam achieves a momentum resolution of 2% ($\Delta p/p$). Particle identification in the FTBF secondary beam is carried out using gas threshold Cherenkov detectors, which identify pions at energies above 5 GeV/c and kaons above 18 GeV/c. The first Cherenkov detector was adjusted to detect positrons, muons, and pions, with a trigger setup that used an anti-coincidence signal with two scintillators to exclude all particles except kaons and protons. The second Cherenkov detector was optimized for kaons, enabling their distinction from protons during data analysis.

The FTBF is equipped with silicon strip detectors (SSDs) that feature an active area of $3.8 \times 3.8\,\mathrm{cm}^2$ and a strip pitch of $60\,\mu$m. Each detector consists of two planes

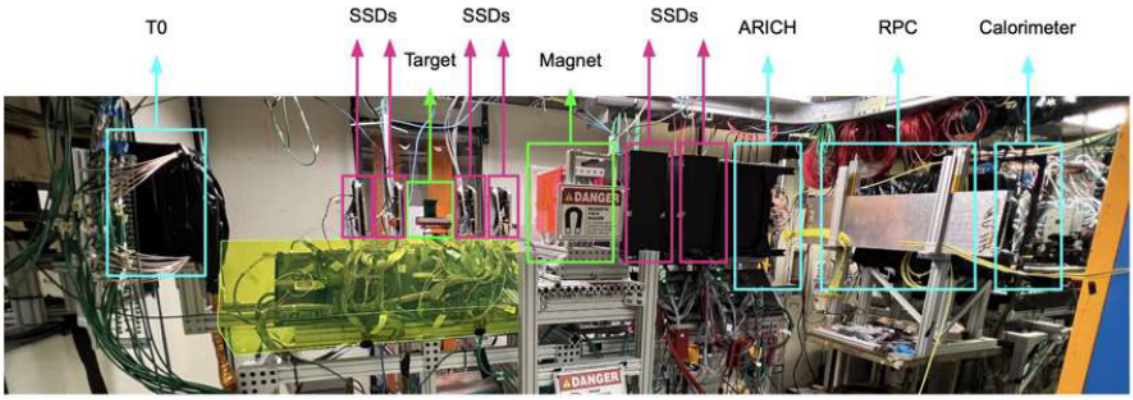

Figure 4.2: Phase 1 experimental setup illustrating the complete spectrometer layout, with all detectors distinctly marked.

of silicon strips, allowing for independent two-dimensional measurements. In the EMPHATIC beam test setup, four SSDs were installed upstream of the target and three downstream. Additionally, an eight-plane silicon pixel telescope was placed between the upstream SSDs and the target. Four of these planes had a sensitive area of $3.24 \times 1.62\,\mathrm{cm}^2$, while the remaining four measured $1.62 \times 2.43\,\mathrm{cm}^2$. Due to inefficiencies and limited coverage, pixel data were excluded from the measurement. Instead, the pixel telescope was considered passive material, with energy losses accounted for in the data corrections.

The target is composed of Toyo Tanso IG-43 graphite, the same material used in T2K and NA61/SHINE. It has a thickness of 2 cm, corresponding to roughly 5% of an interaction length, with a measured density of $1.83 \pm 0.04\,\mathrm{g/cm}^3$.

The following subsections describe the beam, particle identification, spectrometer, and secondary particle identification systems of the experiment in detail.

4.2.1 Beam Characterization

Particle identification (PID) is a crucial part of the experiment, and several detectors are used to achieve this. The FTBF provides PID through different techniques, including gas Cherenkov and aerogel Cherenkov detectors.

Gas Cherenkov: The gas Cherenkov detectors at the FTBF use nitrogen as the

filling gas, with pressure adjusted to optimize particle separation. These detectors enable pion identification at 5 GeV, but kaon-proton separation is only possible at energies above approximately 18 GeV. The facility's Cherenkov detector consists of inner and outer mirrors and is filled with CO_2, with pressure variations depending on the beam momentum. These detectors provide upstream PID for the experiment.

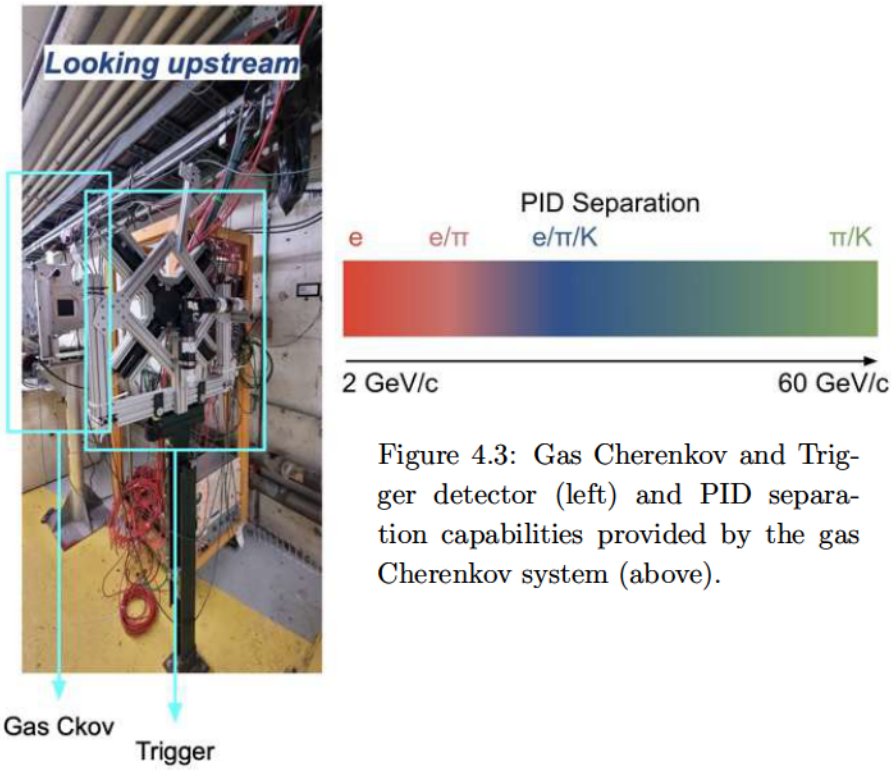

Figure 4.3: Gas Cherenkov and Trigger detector (left) and PID separation capabilities provided by the gas Cherenkov system (above).

Beam Aerogel Cherenkov (BACkov): The BACkov system enhances upstream particle identification for lower momentum ranges. Positioned between the gas Cherenkov detectors and the EMPHATIC spectrometer, it comprises an array of threshold Cherenkov counters. These counters utilize silica aerogels as radiators, enabling efficient particle identification at reduced energies.

4.2.2 Silicon Strip Detectors (SSDs)

Silicon strip detectors (SSDs) track the motion of charged particles by capturing their digitized paths in real-time, both before and after they interact with the target. These detectors provide tracking for charged particles in these regions, offering a spatial resolution of approximately 17.3 μm with a 60 μm pitch.

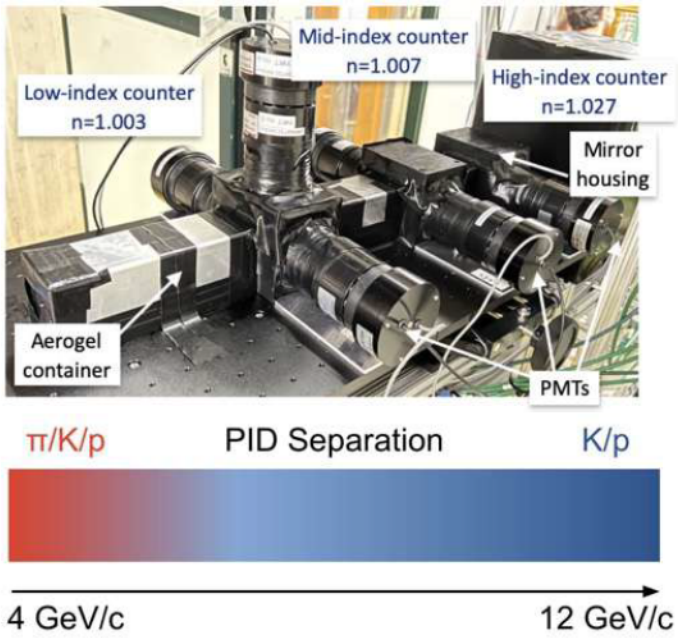

Figure 4.4: BACkov detector (above) and PID capabilities achievable with BACkov (below).

To increase the acceptance, two SSDs are placed side by side at downstream stations, resulting in an acceptance of approximately 100 mrad for Phase 1 of the experiment. Proper alignment of these SSDs is crucial for accurate tracking, and our group at Panjab University is tasked with ensuring their precise alignment.

4.2.3 Magnet

The magnet used in this experiment is a compact Halbach array magnet. It is constructed using N52-grade Neodymium permanent magnet segments, which generate a dipole magnetic field. A 3D map of the magnetic field has been measured, with a maximum field strength of $B_{\text{max}} = 1.44\,\text{T}$. The integrated magnetic field along a path is $B \cdot \text{dl} = 1.2\,\text{Tm}$. Further details about the magnet and precise map are provided in the next chapter.

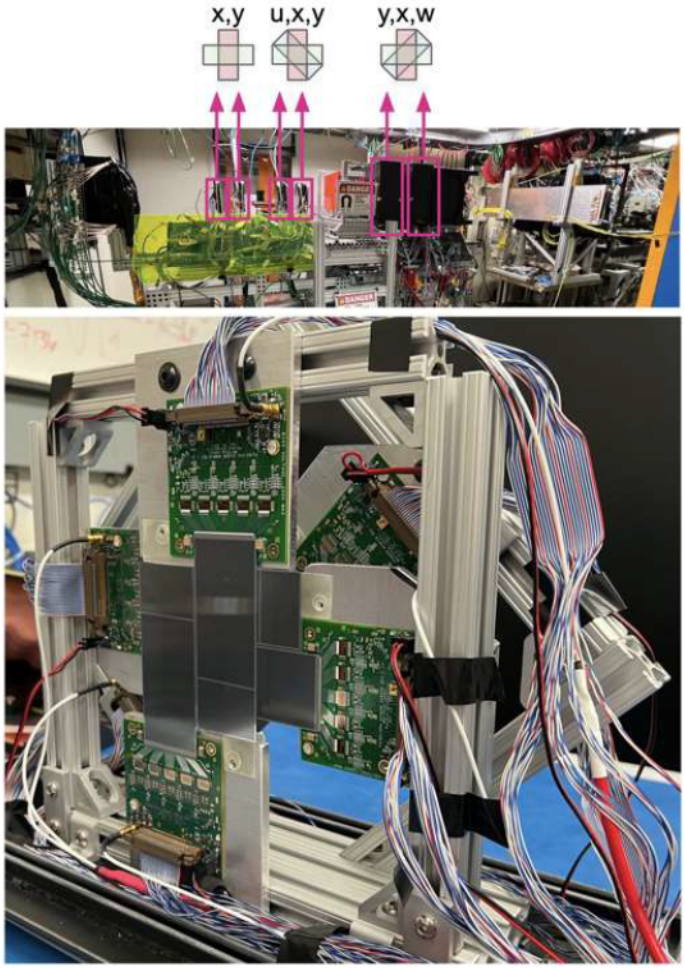

Figure 4.5: The SSDs in the EMPHATIC setup.

4.2.4 Aerogel Ring Imaging CHerenkov (ARICH)

The downstream Aerogel Ring Imaging Cherenkov (ARICH) detector is designed to identify forward-moving particles with momenta exceeding 2 GeV/c. Utilizing an aerogel-based proximity-focusing technique, this detector plays a crucial role in particle identification for the Belle II experiment, particularly in its endcap region.

The ARICH detector consists of two layers of aerogel, developed by Chiba University for Belle II, with aerogels featuring low indices of refraction (n1 = 1.02, n2 = 1.03) and good transmittance. The detector is expected to achieve better than 2σ pion/kaon separation at 7 GeV/c, and it can provide a 2σ separation of pions and kaons below 7 GeV/c, as well as a 2σ separation of protons and pions below 13 GeV/c.

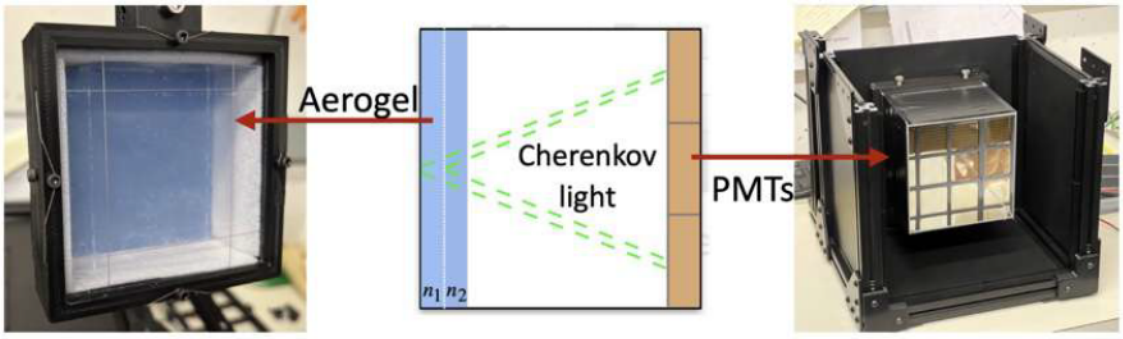

Figure 4.6: A charged particle passing through aerogel emits Cherenkov light, which is detected by PMTs for particle identification.

The Phase 1 detector's prototype is designed with a 150 mrad acceptance, and Cherenkov light emitted by charged particles passing through the aerogel is detected by photomultiplier tubes (PMTs) for particle identification, as shown in Figure 4.6.

4.2.5 Time-of-Flight (ToF) System

The Time-of-Flight (ToF) system measures the timing of beam particles (T0) before they hit the target and secondary particles downstream. It comprises two detectors: the T0 detector and a downstream Resistive Plate Chamber (RPC). Both detectors achieve timing resolutions below 100 ps (rms) to handle high particle rates efficiently. The system has a combined resolution of approximately 70 ps, enabling particle separation up to momenta of 1.5 GeV/c.

The T0 detector uses an X-shaped acrylic Cherenkov radiator coupled to Multi-Pixel Photon Counters (MPPCs) with enhanced quantum efficiency. The acrylic radiator, cut to dimensions of 3 mm × 3 mm × 150 mm, reflects Cherenkov light internally to MPPCs attached at both ends. The radiators are oriented at a 45° angle to the beam axis, ensuring efficient light collection. Each MPPC has a timing resolution of approximately 200 ps (FWHM) for single photoelectrons, with a light yield of ∼50 photoelectrons at the center for particles with $\beta \sim 1$. To suppress accidental signals caused by the MPPC's high dark current rate (∼1 MHz), the time window is restricted to 10 ns. Signal readout utilizes a shaping amplifier with a fast operational amplifier (AD8000) and a pole-zero cancellation resistance for

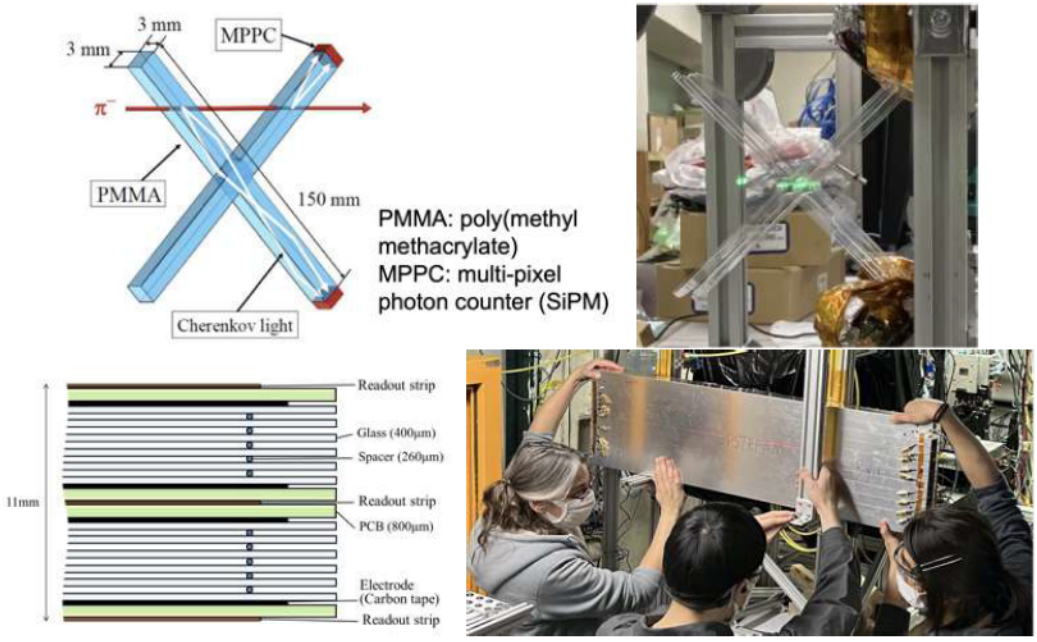

Figure 4.7: Images of the T0 detector (top) and RPC installation (bottom).

optimal performance.

The RPC detects the timing of downstream secondary particles. Timing and pulse height information are processed using the DRS4 module, which incorporates a high-resolution FPGA-based TDC (HR-TDC). This allows precise time measurements with discriminator signals.

4.2.6 Target

The target is positioned between the two upstream SSD stations. A variety of target materials have been utilized in the experiment, including graphite, CH_2, aluminum, and iron. These targets have widths corresponding to approximately 5% of an interaction length, enabling efficient data collection while minimizing unnecessary interactions.

Figure 4.8 shows of the graphite, beryllium, and water targets used in the experiment.

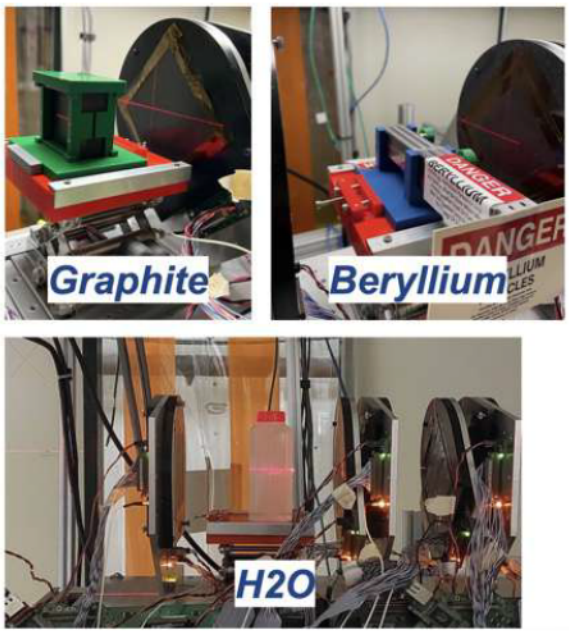

Figure 4.8: Examples of target materials used in the experiment.

4.3 Proof of Principle Test

Forward differential cross-sections for proton-carbon interactions [60] were measured at 20, 30, and 120 GeV/c using silicon strip detectors. This method combines transmission measurements with the optical theorem. Empty target data were used for alignment and background estimation, achieving sub-micron positional and sub-0.01 mrad angular misalignment.

A Geant4-based simulation (FTFP_BERT, QGSP_BERT) modeled detector inefficiencies, acceptance, and reconstruction errors. The forward differential cross-section was extracted using:

$$\left(\frac{d\sigma}{d(p_b^2\theta^2)}\right)_i = \frac{N_i}{N_{\text{pot}} \cdot nd \cdot \Delta(p_b^2\theta^2)_i} \tag{4.1}$$

where N_i is the corrected number of events, and nd is the target number density. Model predictions differ from data by 0–40%.

4.4 Phase 1

Over six weeks, more than 250 million triggers were recorded. Data collection occurred in two sub-phases:

- **Phase 1a (Jan-Feb 2022)**: Beam momenta ranged from ±2 to 120 GeV/c for graphite, CH_2, aluminum, and iron targets.
- **Phase 1b (Jun-Jul 2022)**: Similar range, including beryllium and H_2O targets.

4.4.1 Preliminary Results

A first look at the Phase 1 data reveals several key findings. We observed bending tracks through the magnet, which suggests the expected behavior of charged particles in the magnetic field. Additionally, Cherenkov rings were detected by the ARICH detector, providing further validation of the experimental setup.

4.4.2 Simulation and Analysis Efforts

As part of the ongoing analysis, the collaboration is focused on several critical aspects of the experiment:

- **Magnetic Field Mapping:** An extensive map of the magnetic field region of the spectrometer was developed, which is discussed in detail in the next chapter.
- **Detector Alignment and Calibration:** Efforts were made to ensure the precision of the detector setup, including alignment procedures to minimize systematic errors.
- **Particle Identification (PID) Algorithm Development:** Work is ongoing to develop algorithms for particle identification, particularly with the ARICH detector.
- **Analysis Infrastructure:** The development of analysis infrastructure, including the creation of CAFs (Common Analysis Frameworks), is underway

to streamline data analysis.

These initial results and ongoing efforts provide a strong foundation for future phases of the experiment, with continued focus on improving detector calibration, simulation accuracy, and data analysis capabilities. The first results of this phase are expected to be published soon.

4.5 Future Measurements

EMPHATIC provides a novel, table-top approach to significantly reducing hadron production uncertainties by at least a factor of two. This is achieved through measurements using both thin and thick targets, offering complementary insights to existing efforts like NA61/SHINE, which also aims to improve flux predictions through comprehensive hadron production data.

Preparations for future measurements, i.e., Phase 2, are actively progressing with several key goals. The primary objective is to achieve the first-ever measurement of the charged-particle spectrum downstream of a target using an unpowered NuMI horn. Additionally, more thin-target measurements will be conducted.

The spectrometer will be mounted on a motion table for improved horn acceptance, and beam characterization will be enhanced with LAPPD-based ToF technology for particle identification up to 25 GeV/c. Additionally, a new magnet will strengthen the experimental setup, with preparations underway for relocation to the FNAL MCenter.

As EMPHATIC prepares for Phase 2, insights from the study discussed in Chapter 3, which examines the flux, momentum, and energy spectra downstream of the NuMI target and Horn 1, will guide the strategic placement of detectors. This will enhance the efficiency and precision of the experiment while reducing uncertainties in neutrino flux predictions for the Phase 2 setup, where the NuMI target and Horn 1 are positioned in front of the EMPHATIC setup, as shown in Figure 4.10. Additionally, the high-resolution 1 mm magnetic field map developed in the study,

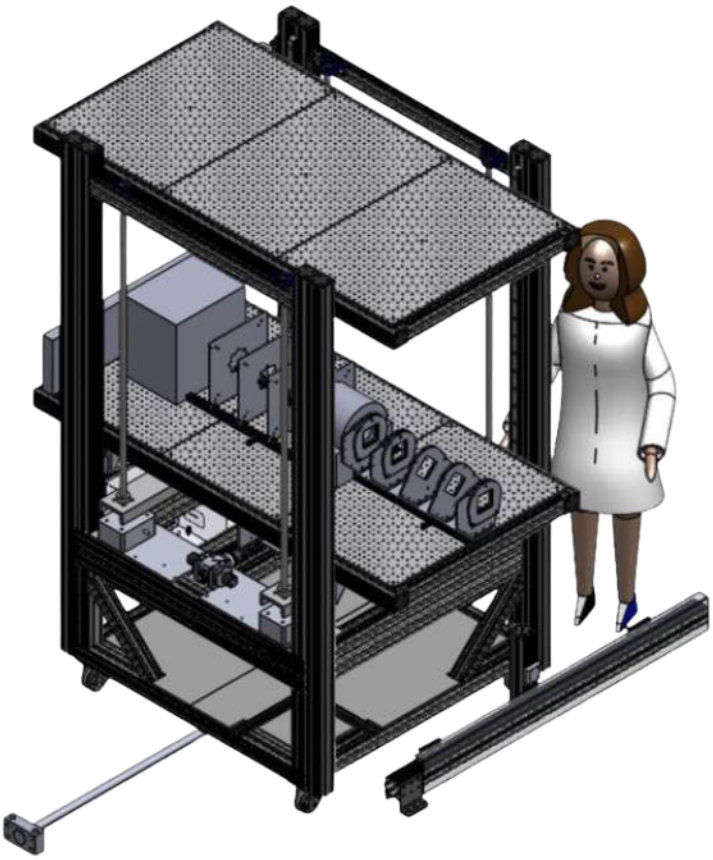

Figure 4.9: Phase 2 setup mounted on a motion table [61].

discussed extensively in the next chapter for the Phase 1 Halbach array magnet, will be extended to the Phase 2 magnet, ensuring continued improvements in magnetic field mapping.

4.6 EMPHATIC Phase 1 Magnet and Concept

EMPHATIC utilizes a compact cylindrical Halbach array configuration magnet, which is a unique arrangement of permanent magnets known for producing a nearly uniform magnetic field on one side while canceling the field on the opposite side. Unless otherwise stated, any reference to the 'magnet' hereafter refers to the Phase 1 Halbach array cylindrical magnet.

EMPHATIC employs two key Halbach array magnets across its different phases.

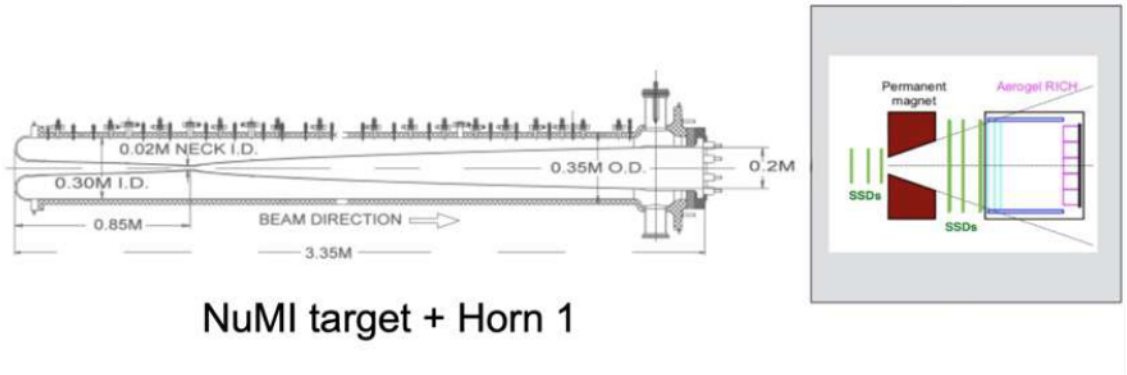

Figure 4.10: Schematic representation of the NuMI target and horn 1 in front of EMPHATIC setup for Phase 2.

The Phase 1 magnet is a 3-layer cylindrical Halbach dipole consisting of 48 N52 Neodymium magnets, arranged with 16 magnets per layer. This magnet, procured from China Magnets Source Materials Limited [62], was delivered to TRIUMF in January 2020 and now has been returned to TRIUMF. The Phase 2 magnet, featuring the same design as Phase 1, was purchased from SABR Enterprises [63] by Fermilab in 2023. While this chapter and the next focus on the Phase 1 magnet, the methods described will also be applied to the Phase 2 magnet for precise mapping.

4.7 EMPHATIC Phase 1 Magnet and Concept

4.7.1 Planar Halbach Array

Planar halbach array also called Linear or 1-D array is a configuration that involves a series of permanent magnets arranged in such a way that their flux cancels on one side while enhancing it on the other, resulting in a unidirectional magnetic field.

The one-dimensional magnetization pattern along the x-axis can be described by the following equation:

$$\vec{M}(x) = \begin{pmatrix} M_x \\ M_y \\ M_z \end{pmatrix} = M_0 \begin{pmatrix} \sin(k'x) \\ \cos(k'x) \\ 0 \end{pmatrix} \quad \text{with} \quad k' = \frac{2\pi}{\lambda}, \tag{4.2}$$

Here, k' represents the wave number, which corresponds to the spatial frequency, while λ denotes the wavelength associated with the magnetization pattern.

The magnetic field produced by such a structure above the surface ($y > 0$) of thickness d (and infinite length in the z direction) is given by:

$$\vec{B}(x,y) = \begin{pmatrix} B_x \\ B_y \end{pmatrix} = B_R \left(1 - e^{-k'd}\right) e^{-k'y} \begin{pmatrix} \sin(k'x) \\ \cos(k'x) \end{pmatrix}, \tag{4.3}$$

where B_R is the remanence of the magnetic material. Outside the magnet material, the magnetic field components, B_x and B_y, exhibit harmonic behavior. As a result, their sinusoidal variation along the horizontal direction is accompanied by an exponential decay in the vertical direction [64].

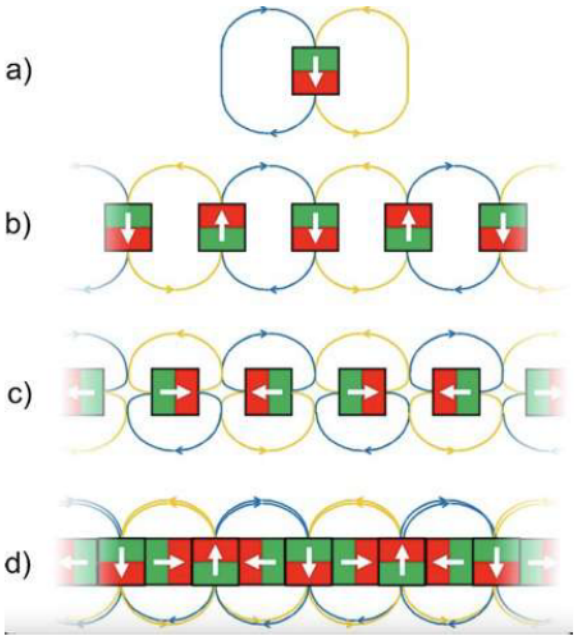

Figure 4.11: Diagram illustrating the arrangement of magnets to achieve a unidirectional magnetic flux.

a) A single magnet with downward magnetization, shown by the white arrow. The red and green shading indicate the north and south poles. The dipolar magnetic field is represented by two field lines of equal strength but opposite directions (blue = clockwise, gold = counterclockwise).

b) Multiple magnets, similar to the one in (a), arranged in an alternating vertical magnetization pattern with uniform gaps.

c) Similar to (b), but with alternating horizontal magnetization.

d) A combination of (b) and (c) forms a basic planar Halbach array, demonstrating flux cancellation below and enhancement above the array.
Adapted from [64].

Figure 4.11 shows different one dimensional arrangements of magnets to achieve

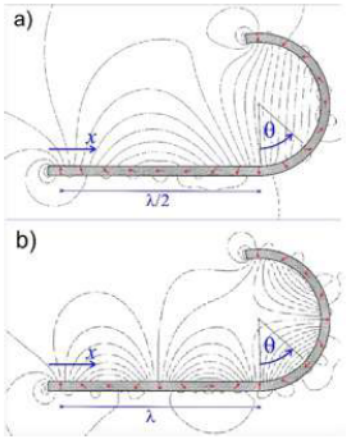

Figure 4.12: Diagram illustrating how a planar Halbach array can be converted into a cylindrical Halbach ring by rolling it.
a) Rolling a single wavelength λ around an imaginary cylinder with a radius of $\lambda/2\pi$ creates a uniform dipole field.
b) A quadrupole field is generated when 2λ is wrapped around the cylinder.

single-sided magnetic flux.

Halbach later expanded this concept to cylindrical and spherical configurations, allowing for the generation of multipolar magnetic fields.

4.7.2 Cylindrical Halbach Multipoles

When a planar Halbach array with a length of λ is curved around a cylindrical surface, the spatial variable x in equation 4.2 transforms into an angular position given by $\theta = \frac{x}{\lambda}$, or equivalently, $x = \theta\lambda/(2\pi)$. Consequently, the magnetization within the cylindrical structure becomes a function of θ. Wrapping one full wavelength around the cylinder generates a uniform dipolar magnetic field, while wrapping two wavelengths results in a quadrupole field, and so on. Figure 4.12 demonstrates the transition from a planar Halbach array to a Halbach ring.

By rolling planar Halbach arrays of length $k\lambda$, multipolar fields are generated with polarity $p = 2|k|$, where $|k| = 1$ corresponds to a dipole, $|k| = 2$ to a quadrupole, and so on. Figure 4.13 illustrates this concept, where the coordinate system has been modified so that $\theta = 0$ lies along the x-axis. The figure depicts an idealized magnet in the shape of an infinitely long hollow cylinder or ring with continuously changing magnetization direction. The magnetization angle φ varies with the position angle θ as follows:

$$\varphi = (k+1)\theta \quad \text{with} \quad k \in Z. \tag{4.4}$$

Thus, we can say that for Halbach arrays, the magnetic field can be directed inside or outside depending on the configuration:

- For $k > 0$: the field is directed inside the cylinder.
- For $k < 0$: the field is directed outside the cylinder.
- For $k = 0$: only an axial field is produced.

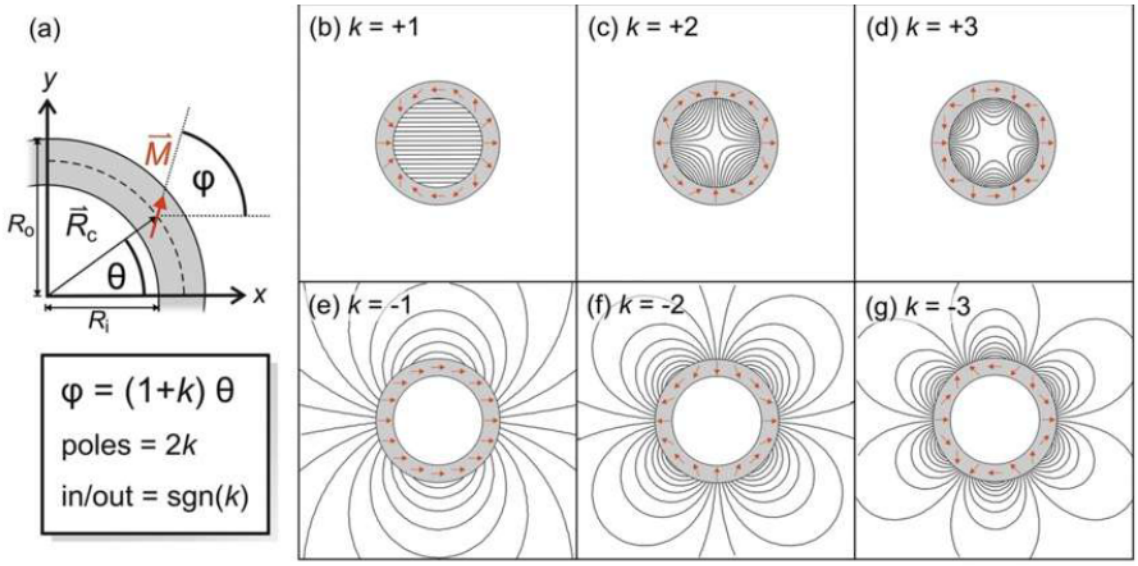

Figure 4.13: Schematic representation of the formation of cylindrical ideal Halbach multipoles:
a) The magnet (gray) forms a hollow cylindrical shape. Its magnetization $\boldsymbol{M}$ (red arrow) varies continuously with the position vector $\boldsymbol{R}_c$ (defined on a central circle of radius $|R_c| = R_c = (R_o + R_i)/2$). When the position angle with respect to the x-axis is θ, the magnetization angle is rotated by φ. This angle φ is a multiple of θ, depending on the polarity and whether the magnetic field is internal or external (as determined by the index k in Eq. (4.4)).
The polarity increases from left to right: **b, e** show dipolar fields ($|k| = 1$), **c, f** show quadrupolar fields ($|k| = 2$), and **d, g** show hexapolar fields ($|k| = 3$).
For $k > 0$, the magnetic field is confined inside the cylinder **(b, c, d)**, with zero field outside.
In contrast, for $k < 0$, the field is outside the cylinder. When $k = 0$, the magnetization is radially oriented, producing only an axial field along the z-axis (no transverse field).

4.7.3 EMPHATIC Phase 1 Magnet

The EMPHATIC Phase 1 magnet is a 3-layer cylindrical Halbach dipole designed to enhance the magnetic flux on one side while nearly cancelling it on the other. A Halbach array achieves this effect using a spatially oscillating magnetization pattern in permanent magnets, such as the N52 Neodymium (NdFeB) magnets used in this design. The magnet consists of 48 N52 Neodymium magnets arranged in three layers, with 16 magnets per layer. Each layer is 50 mm thick and encased with 5 mm steel cladding on both sides. The diameter of the magnet increases with each layer: the first layer has an inner diameter of 46 mm, the second layer has an inner diameter of 62 mm, and the third layer has an inner diameter of 80 mm. A schematic drawing of the EMPHATIC Phase 1 magnet is shown in Figure 4.14. Figure 4.16 shows a sectional view of the magnet model, clearly revealing the three layers with varying diameters.

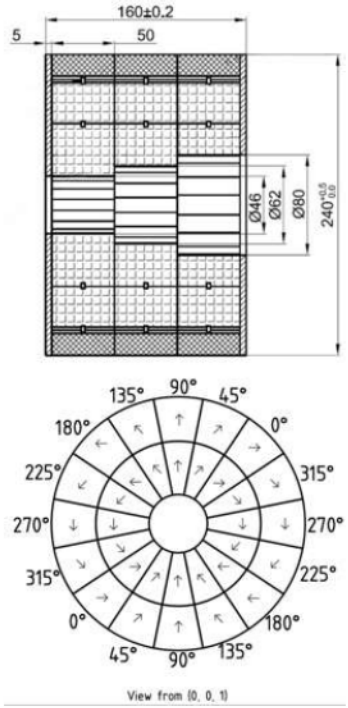

Figure 4.14: **(a)** Schematic drawing of the EMPHATIC Phase 1 magnet showing the 3 layers and their increasing diameters

(b) Magnetisation directions of the 16 neodynium magnet components in each of the three layers shown from the (0,0,1)

The magnetic field strength within the NdFeB material is 1.44 T, and the integrated magnetic field $\int \mathbf{B} \cdot d\mathbf{l}$ is 0.2 Tm [65]. The coordinate system for this magnet

inside the EMPHATIC setup is such that the magnet's length spans from coordinates (0,0,0) mm to (0,0,160) mm as shown in Figure 4.15. Please note that the coordinate system is defined such that it begins at the surface of the 5 mm steel cladding.

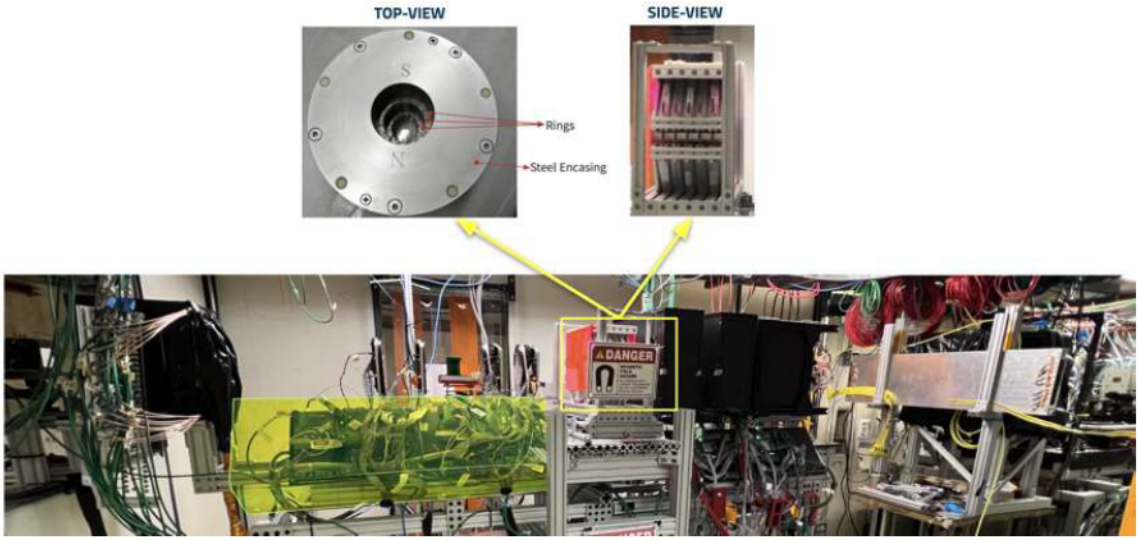

Figure 4.15: Images of the EMPHATIC Phase 1 magnet from the top and side views within the EMPHATIC Phase 1 run setup.

4.8 Magnetic Field Mapping: Data

4.8.1 Measurement Setup and Data Collection

The magnetic field measurements were conducted by the Applied Physics and Superconducting Technology Directorate (AP-STD) at Fermilab in March 2023. The measurement apparatus included a SENIS F3A-03A05F-A02T2K5J 3-axis Hall probe with $5V/T$ sensitivity, a $\pm$2T range, and 0.1% accuracy. The probe features a fully integrated CMOS 3-axis sensor with high spatial resolution, negligible planar Hall effect, and a broad bandwidth (DC–25 kHz). Manufacturer calibration was used without additional corrections.

During the AP-STD data-taking, data points were recorded with a spatial resolution of 5 mm across the magnet's field. The measurement grid spanned from -15 mm to +15 mm in both the x and y directions and from -140 mm to 310 mm

in the z direction. It should be noted that some of the raw data points near the edges recorded a magnetic field value of 0 T. These values were removed in the post-processing phase, leaving the final 4095 data points used in the analysis.

The yellow cylinder in Figure 4.16 shows the measurement radius of the magnet spanning from -140 to 310mm. Also shown are the mapped data points on one of the xy planes.

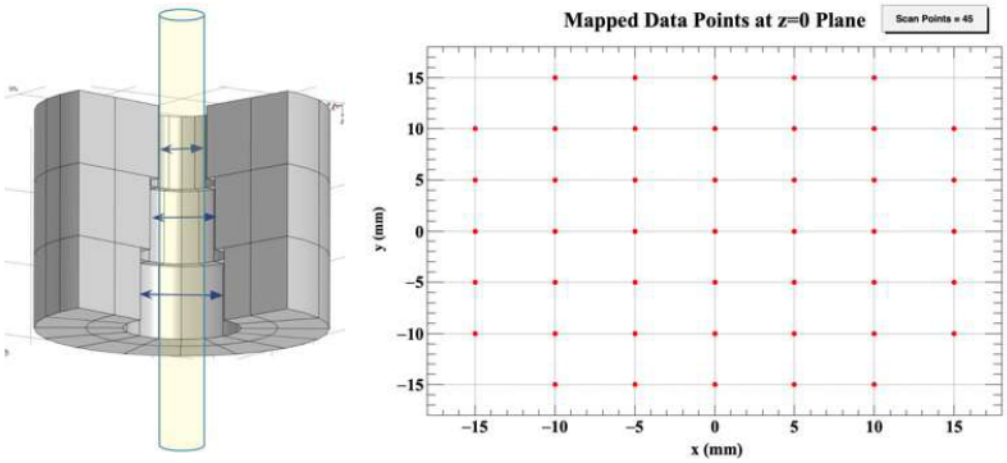

Figure 4.16: **(Left)** Mapped cylinder of the measurements and **(Right)** Distribution of magnet scan points in the z=0 plane

4.8.2 Interpreting the Data

Figure 4.17 field plots show the components of the magnetic field (Bx, By, Bz) along the z-axis at the central location of the field map (x=0, y=0). These data points provide a snapshot of the magnetic field distribution down the central bore of the magnet. The peak magnetic field along the central axis is measured to be $1.50601T$ at $z = 45mm$ as can be seen in Figure 4.17.

Similar field maps were generated at all 45 scan locations across the magnet. The results indicate no sharp discontinuities, although some asymmetries are observed in regions that should theoretically be symmetric.

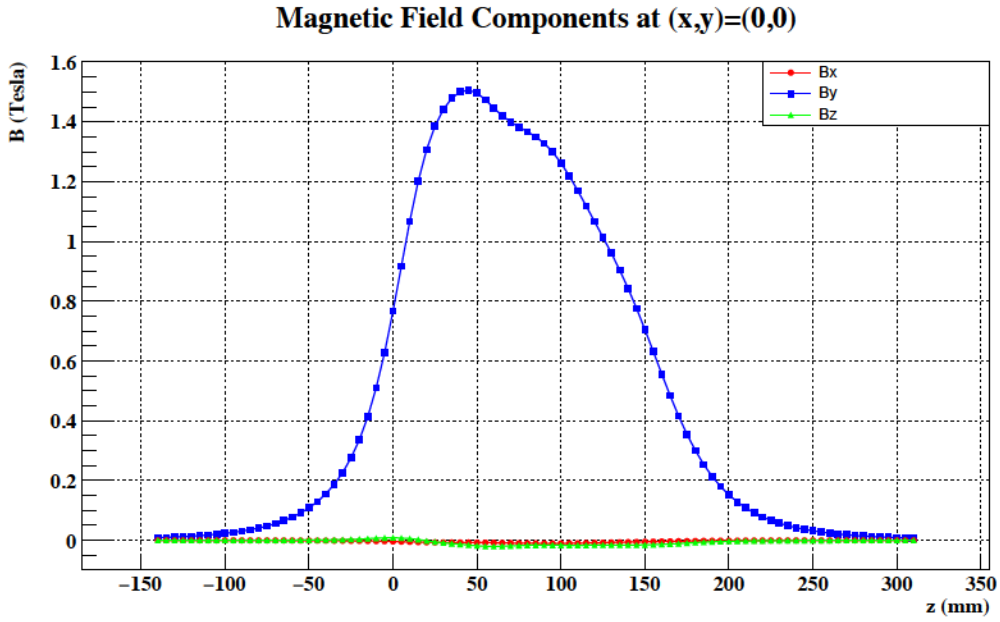

Figure 4.17: Magnetic field components (Bx, By, Bz) along the z-axis at (x, y = 0,0)

4.8.2.1 Magnetic Field Magnitude in the (x, y) Planes

The plots in Figure 4.18 show the magnetic field magnitude in the (x, y) planes at four distinct z-positions within the magnet. These positions are the upstream aperture plane at $z \approx 0\,\text{mm}$, the transition between the smallest ring of the Halbach array and the middle ring at $z \approx 55\,\text{mm}$, the middle ring of the array and the largest ring at $z \approx 105\,\text{mm}$, and the downstream aperture plane at $z \approx 160\,\text{mm}$. Ideally, these plots would display symmetry along both horizontal and vertical axes; however, slight asymmetries are noticeable.

4.8.2.2 Vector Plot of the Magnetic Field

The vector plot shown in Figure 4.19 depicts the magnetic field components (Bx, By) across the same (x, y) planes as above. The length of the arrows denotes the magnitude of the magnetic field , while the direction indicates the orientation of the field. Together, the length and direction provide a clear representation of both the strength and orientation of the magnetic field across the plotted plane. As seen in Figure 4.19, the plots should maintain symmetry about the vertical axis, but some

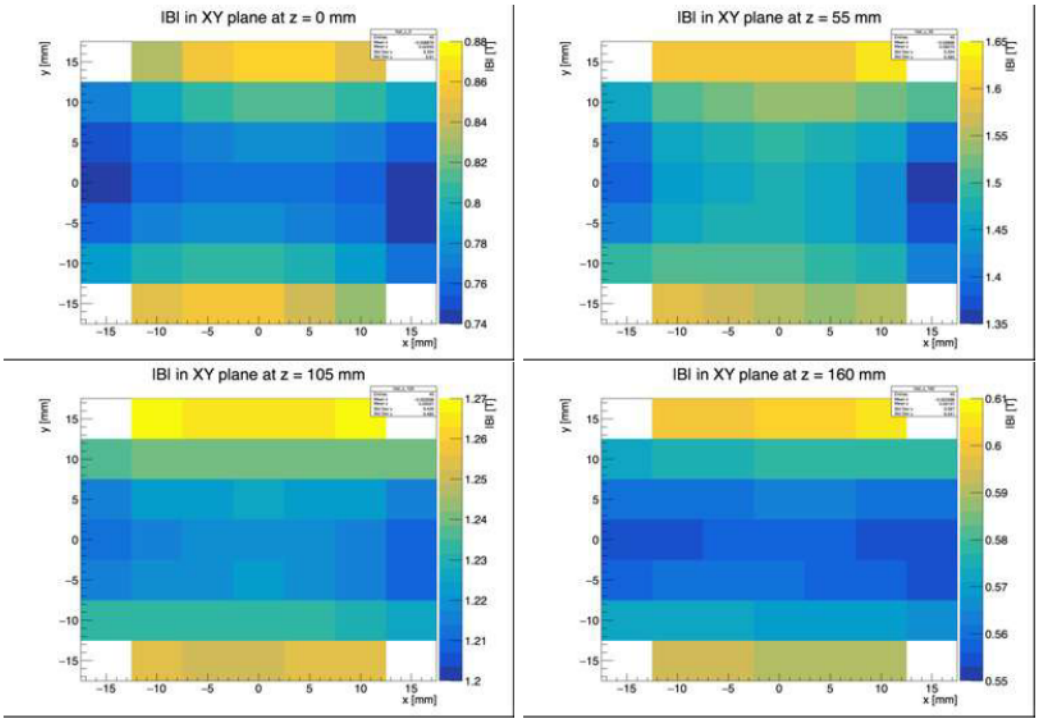

Figure 4.18: Magnitude of the magnetic field in (x, y) planes at various z-locations along the magnet.

asymmetry is present, particularly in regions close to the edges of the magnet.

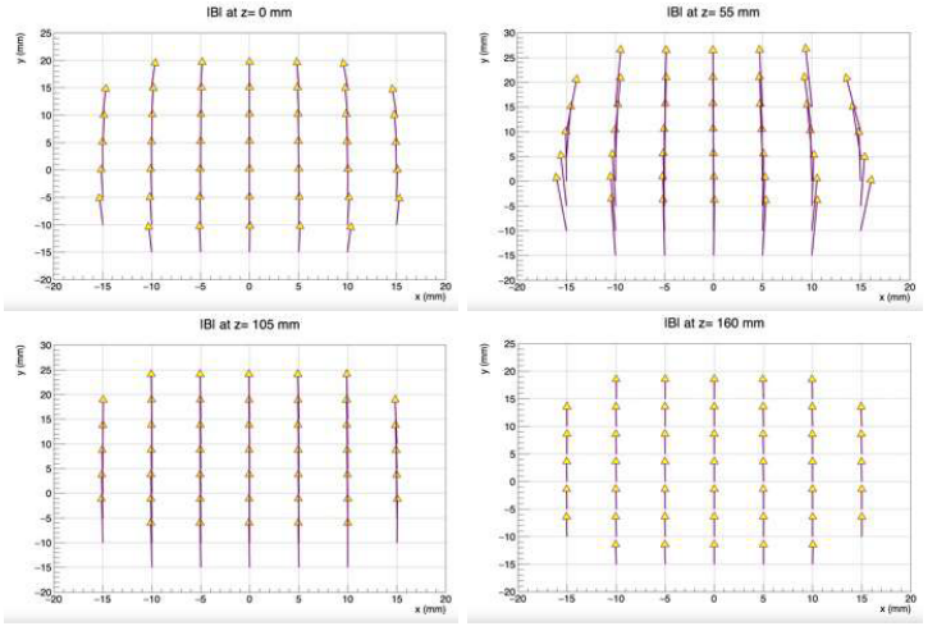

Figure 4.19: Vector plot of the magnetic field (Bx, By) in (x, y) planes at various z-locations along the magnet.

4.9 Summary

Thus, the successful mapping of the magnetic field in EMPHATIC Phase 1 has provided crucial data for validating and refining our understanding of the Halbach array magnet's performance. However, to fully leverage these measurements, it is essential to develop an accurate computational model that not only replicates the observed field but also enables optimization for future configurations.

In the next chapter, we model the magnet using COMSOL, establishing a numerical framework to simulate and compare the magnetic field with measurements. We define fit parameters, refine model hierarchies, and optimize for the best-fit field representation. A high-resolution 1 mm field map will improve momentum and angle resolution, enhance spectrometer accuracy, and expand detector acceptance, while also covering regions inaccessible to the Hall probe.

Chapter 5

Magnetic Field Modeling and Fit

5.1 Introduction

As discussed in Chapter 4, EMPHATIC uses a compact cylindrical Halbach array magnet, generating a uniform field on one side while canceling it on the other. The Phase 1 magnet is a 3-layer dipole with 48 N52 Neodymium magnets, a design retained for Phase 2. The magnetic field map for the Phase 1 magnet was measured by AP-STD [66] in March 2023 with a resolution of 5 mm. To improve upon this, we employed a detailed model of the magnet using COMSOL Multiphysics, which allowed us not only to enhance the map's resolution to 1 mm, but also to perform accurate modeling and fitting to the measured data. COMSOL's simulation capabilities enable precise modeling and optimization of magnetic fields in complex geometries such as the Halbach array.

In this chapter, we will present the 1 mm resolution magnetic field map generated through COMSOL modeling and fitting to the measured data.

5.2 Modelling the Magnet with COMSOL

COMSOL Multiphysics [67] is a versatile simulation software widely used for modeling complex physical phenomena, including electromagnetics, structural mechanics,

and fluid dynamics. Its flexibility makes it a valuable tool for researchers working on detailed simulations and optimizations, such as magnetic field modeling. COMSOL enables the development of parameterized models with powerful visualization and post-processing tools, using .mph files for storing configurations and results. This study utilizes COMSOL version 6.1, with licenses provided by Fermilab (Network License) and the University of Notre Dame (Class-Kit License). Additionally, COMSOL offers various modules to extend its core functionality, including the AC/DC Module for electromagnetic simulations, as well as mechanical, fluid flow, chemical, and interfacing modules for integration with other software.

5.2.1 COMSOL Model Hierarchy

The hierarchy of a COMSOL model is structured within the *Model Builder*, which organizes various components into a tree-based system, guiding the user through the modeling and simulation process.

- **Global Definitions**
  - **Parameters**: Define constants (e.g., physical dimensions, field strengths) for easy adjustment.
  - **Variables**: Set up user-defined expressions and functions for custom calculations.
  - **Materials**: Define materials and assign properties (e.g., density, thermal conductivity) relevant to the study.
- **Component**
  - **Geometry**: Draw or import shapes, then specify dimensions to create the model's structure.
  - **Selections**: Group parts of the geometry to simplify the setup of physics and boundary conditions.
  - **Coordinate Systems**: Add custom coordinate systems for complex geometries.

- **Physics Interfaces**
  - Define the physical phenomena to simulate (e.g., electromagnetic fields, heat transfer, fluid flow).
  - **Domains**: Assign physics to specific parts of the model.
  - **Boundaries, Edges, and Points**: Apply conditions like heat flux, electrical insulation, and source terms.
- **Mesh**
  - Divide the geometry into smaller elements (mesh) suitable for numerical calculations.
  - Adjust mesh size and distribution based on required accuracy and computational resources.
- **Study**
  - Defines the type of simulation and analysis (e.g., stationary, time-dependent, eigenfrequency).
  - Each study step solves equations relevant to a specific physics interface.
- **Solver**
  - COMSOL automatically sets up solvers based on the study but allows manual adjustments for convergence, iterative solutions, and accuracy.
- **Results**
  - **Plots**: Create 1D, 2D, or 3D plots to display fields, vectors, or surfaces.
  - **Derived Values**: Calculate integrals, averages, or other quantitative results.
  - **Export**: Save results in various formats for reporting or further analysis.

Figure 5.1 illustrates the standard model hierarchy.

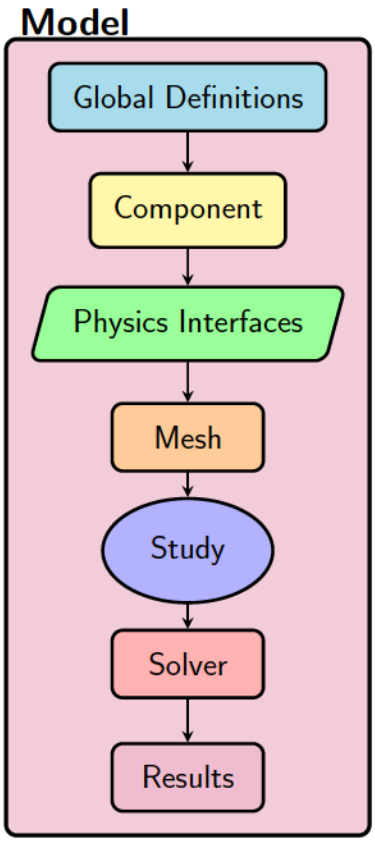

Figure 5.1: Hierarchy of components in COMSOL Model Builder

5.2.1.1 Magnet Model Hierarchy

For our magnet model, the primary nodes used include the Global Definitions, Component, Study, and Results nodes. The Global Definitions node contains parameters and variables defined in our case. The Component node encompasses Geometry, Materials, and MFNC (Magnetic Fields, No Currents) interfaces. The geometry is a COMSOL geometry (No separate CAD module license required). A custom implementation, referred to as the `move` sub-node, is included to adjust the magnet's position within the model. The Study node defines the type of simulation which is stationary in case of our model. The Results node enables visualization of magnetic field data through sub-nodes like Flux Density Norm and Magnetic Scalar Potential. It also includes tools for detailed post-processing, such as 1D, 2D, and 3D plots, quantitative analyses via derived values, and data export options.

Figure 5.2 provides screenshots of the model setup and mesh configurations in

both 3D and YZ views.

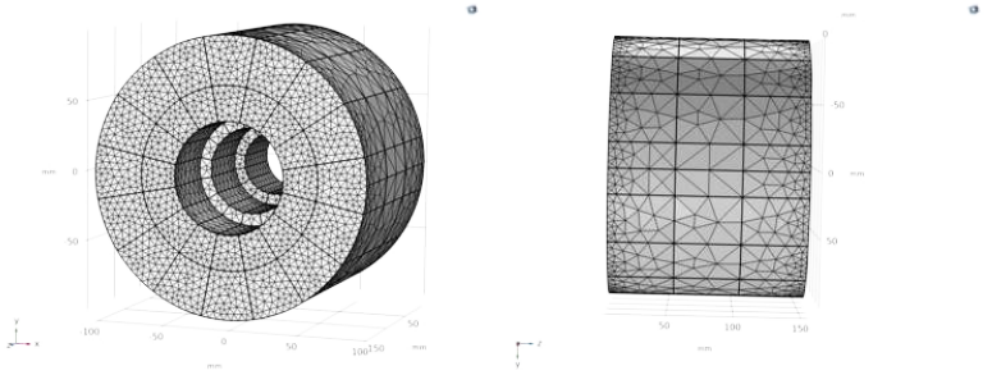

Figure 5.2: COMSOL Model geometry views of the magnet.

5.2.2 Configuration

The configuration details of the magnet model are summarized in Table 5.1. Specific settings were used to achieve high precision in simulating the magnet's behavior, including an extra-fine mesh for accuracy.

Configuration Item	Setting/Description
Mesh	Extra Fine Mesh
Interface	Magnetic Fields, No Currents (MFNC)
Materials Defined	Air, NdFeB, Steel 304
Magnetization Parameters	144 parameters, with 3 per component for each layer
Offsets	X(=0 mm), Y(=0 mm), Z(=80 mm) offsets
Initial Magnetic Field Strength	1.44 Tesla for each component
Center of Magnet	(0, 0, 80) mm

Table 5.1: Configuration details for the magnet model in COMSOL

5.2.3 Fit Parameters

A total of 147 parameters were defined for the magnet model, including 144 parameters corresponding to the 3 components of magnetization of the 48 pieces of

Neodymium across three layers. Each parameter name is structured to capture key information:

- **Naming Convention and Parameter Changes**: The parameter naming convention follows a structured format to distinguish magnetization components, angles, and layers within the magnet. A complete table of parameter names, their meanings, and nominal values is provided in Appendix B.1.
- **Initial Magnetization**: Each component has an initial magnetization of 1.44 Tesla. The vector components for `ex`, `ey`, and `ez` are calculated based on this magnitude and the directions shown in Figure 4.14 in Chapter 4.
- **Angle Progression**: Magnetization vector directions change by 45° between successive components, ensuring that the Halbach array has the intended magnetic field orientation.
- **Units**: Magnetization values are measured in Tesla, while offsets in x, y, and z are measured in millimeters.

5.2.4 Batch Mode Execution

COMSOL's batch mode is useful for automated simulations or parameter sweeps across multiple configurations. It allows users to run simulations without the GUI, using predefined input and parameter files. A detailed explanation of the batch mode execution process, including command syntax and input file format, is provided in Appendix B.2.

5.2.5 Comparing Nominal Model with Data

First we compare the nominal COMSOL model with the measurement data using several plots in Figure 5.3. These plots can be compared with the data plots in Figure 4.18, and the descriptions follow a similar logic. The plots in Figure 5.3 show the magnitude of the magnetic field in the (x, y) planes at four distinct z-positions along the magnet. These locations are the upstream aperture plane at $z \approx 0\,\text{mm}$, the transition between the smallest ring of the Halbach array and the

middle ring at $z \approx 55\,\text{mm}$, the interface between the middle ring and the largest ring at $z \approx 105\,\text{mm}$, and the downstream aperture plane at $z \approx 160\,\text{mm}$.

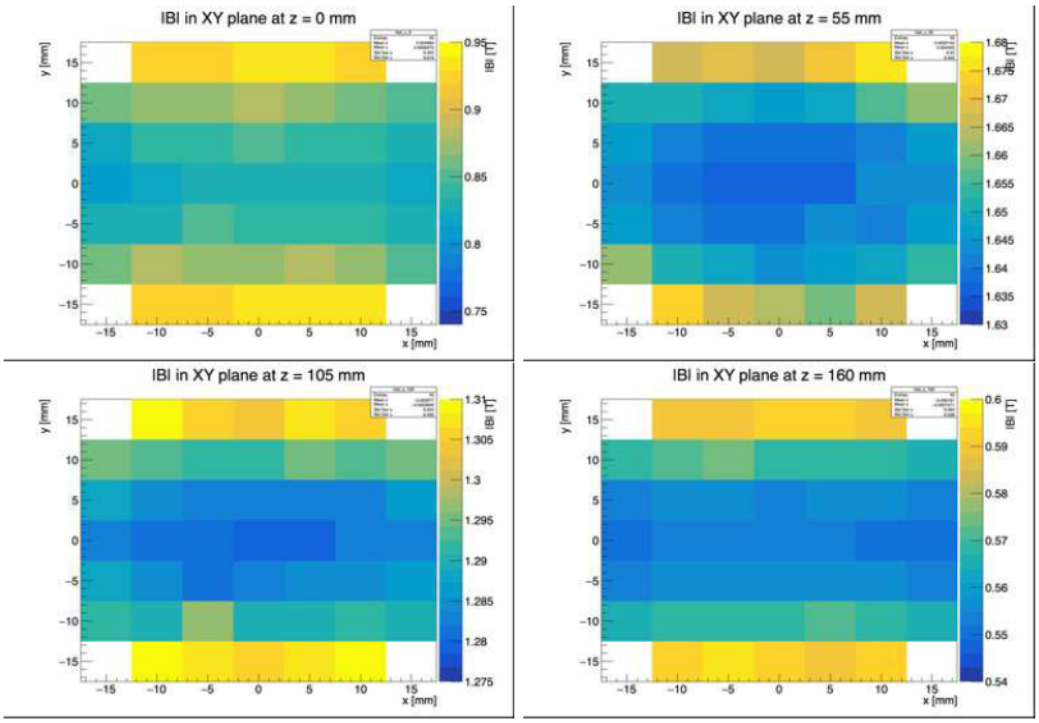

Figure 5.3: Magnitude of the magnetic field in the (x, y) planes at various z-locations along the magnet for the nominal COMSOL model. Compare with Figure 4.18.

For further comparison, as shown in Figure 5.4, the central field (at $x, y = 0, 0$) of the nominal COMSOL model and measurement data are plotted together. The green band indicates a 0.01% uncertainty in B_y. We can clearly see the difference in the magnetic field B_y of the data and the nominal model.

To provide a more comprehensive understanding of how data and the nominal model differ, Figure 5.5 shows the positions used in the measurement grid, represented on a circular plane for visualization and ratio plots have been plotted in these distances. Each set of colors i.e. red, green, violet, and blue correspond to measurement distances 0 mm, 10 mm, $10\sqrt{2}$ mm and 15 mm, respectively . While 13 data points are shown, only four positions are used for the ratio plots, representing all 13 distances.

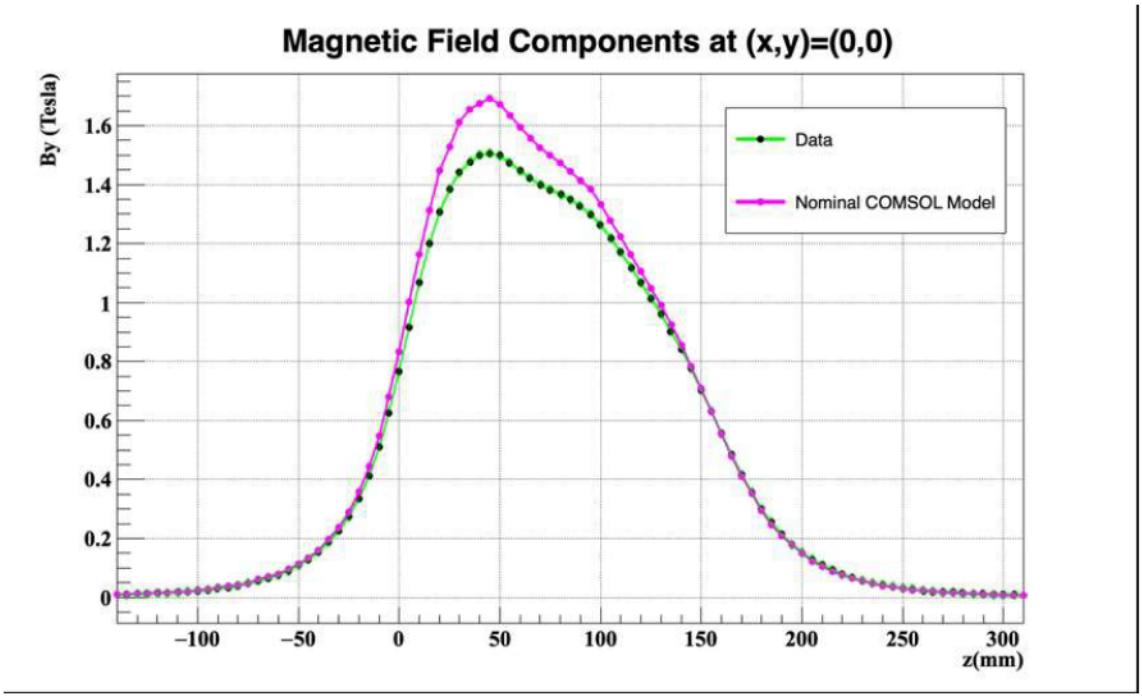

Figure 5.4: Comparison of the COMSOL model and measurement data at the central position $(x, y = 0, 0)$, with a 0.01% uncertainty band in green.

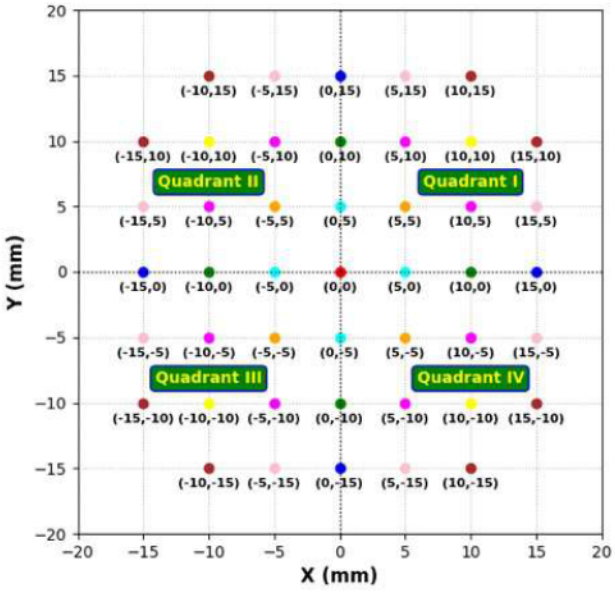

Figure 5.5: Measurement grid with positions where the ratios between the nominal COMSOL model and measurement data have been plotted.

The grid is divided into four quadrants, and a separate ratio plot will be made for each quadrant.

In Figure 5.6, the ratio plots for the 12 positions in Quadrant 1 of the grid (shown in Figure 5.5) are displayed. These positions are: (0,0), (5,0), (10,0), (15,0), (15,5), (10,5), (5,5), (15,10), (10,10), (5,10), (10,15), and (5,15). Similarly, in Figure 5.7, the ratio plots for the 11 positions in Quadrant 2 of the grid are shown. These positions are: (0,5), (0,10), (0,15), (-5,5), (-5,10), (-5,15), (-10,15), (-15,10), (-10,10), (-15,5), and (-10,5).

In Figure 5.8, the ratio plots correspond to the 11 positions in Quadrant 3 of the grid. These positions are: (-15,0), (-10,0), (-5,0), (-15,-5), (-10,-5), (-5,-5), (-15,-10), (-10,-10), (-5,-10), (-10,-15), and (-5,-15). Finally, for Quadrant 4 of the grid, as shown in Figure 5.9, the 11 positions plotted are: (0,-5), (0,-10), (0,-15), (5,-5), (5,-10), (5,-15), (10,-5), (10,-10), (10,-15), (15,-5), and (15,-10).

In total, there are 45 positions on the grid, which represent all the points where data was recorded on a 5 mm grid.

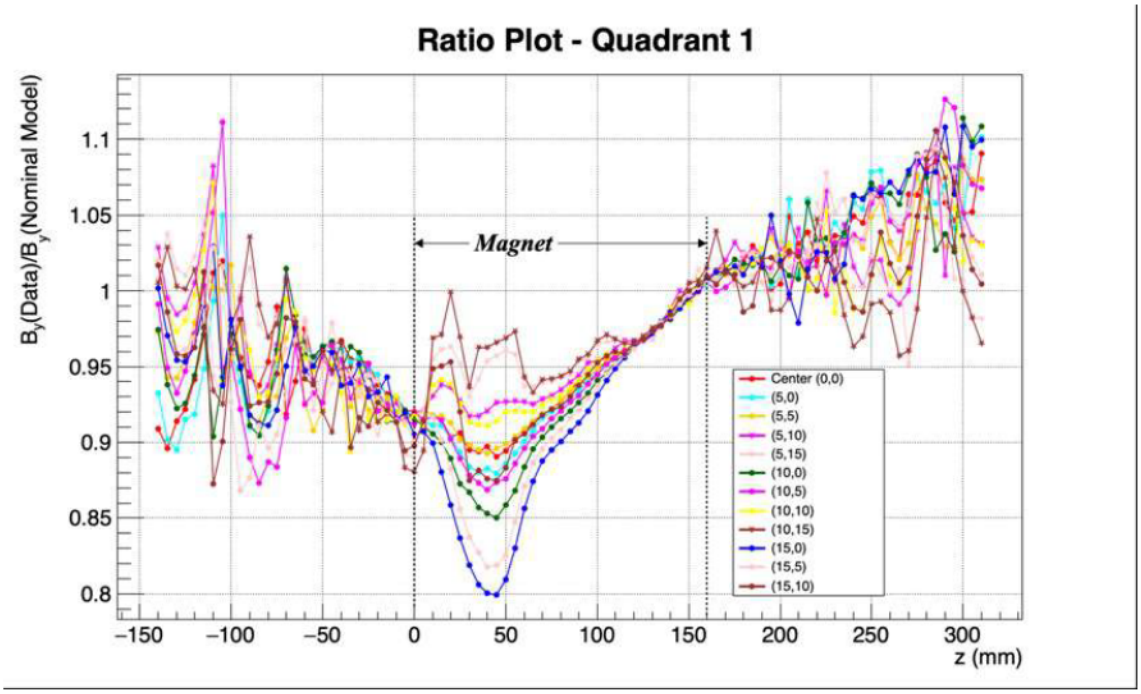

Figure 5.6: Ratio plot of the data and the COMSOL model at 12 positions in Quadrant 1 of the 5 mm measurement grid.

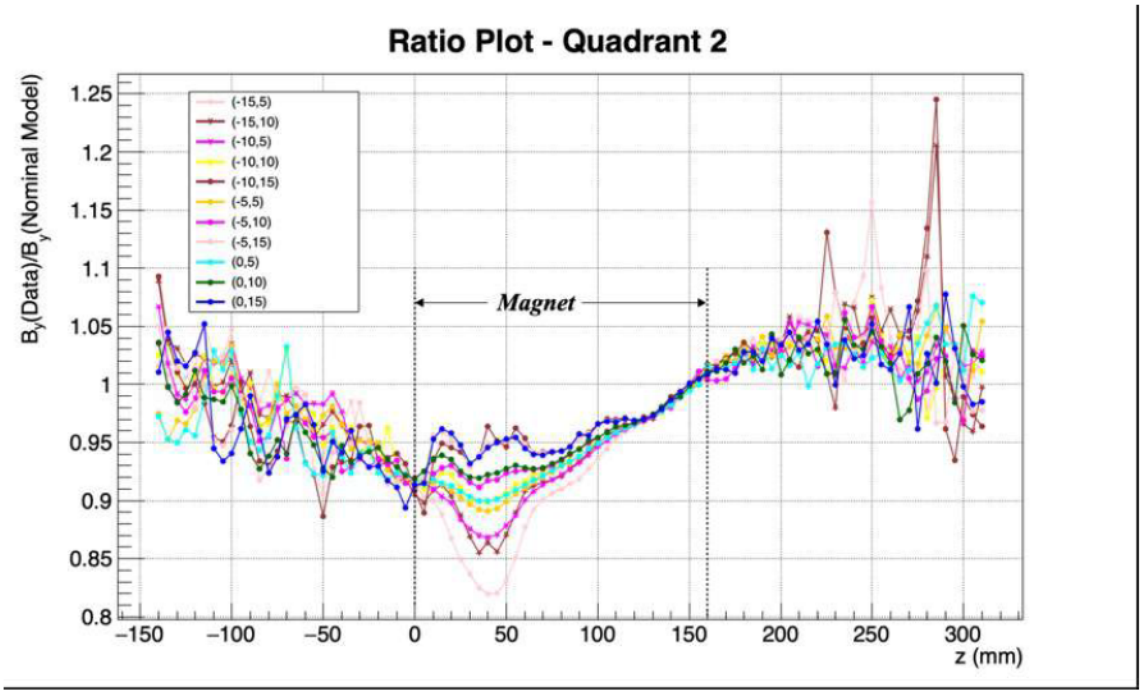

Figure 5.7: Ratio plot of the data and the COMSOL model at 11 positions in Quadrant 2 of the 5 mm measurement grid.

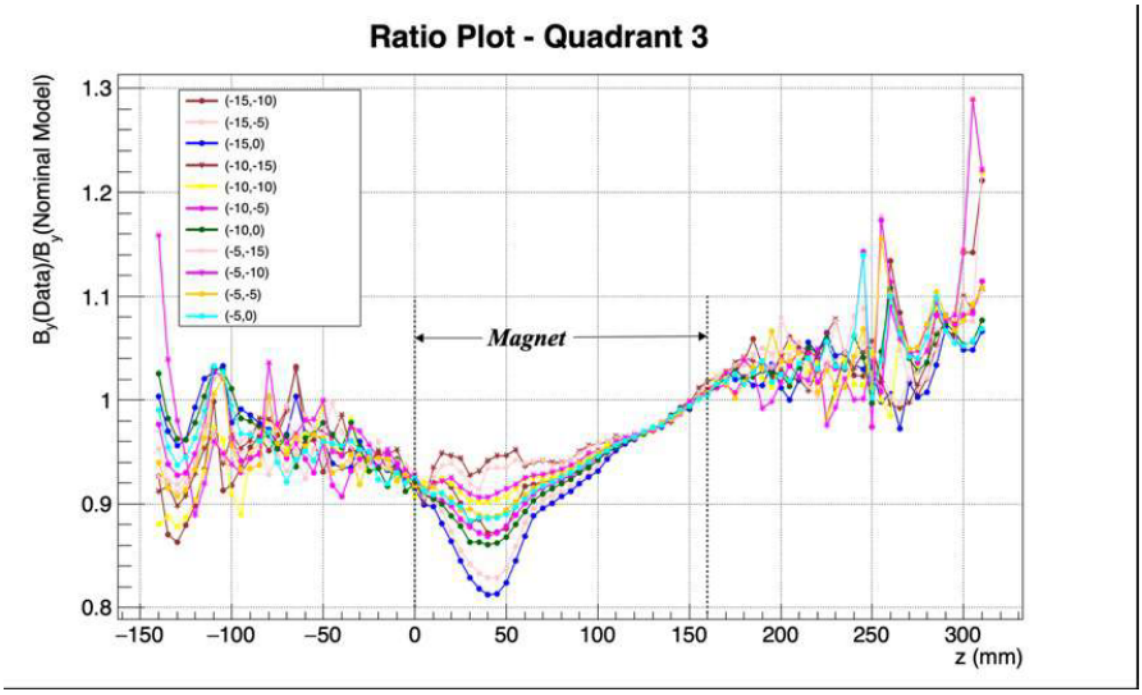

Figure 5.8: Ratio plot of the data and the COMSOL model at 11 positions in Quadrant 3 of the 5 mm measurement grid.

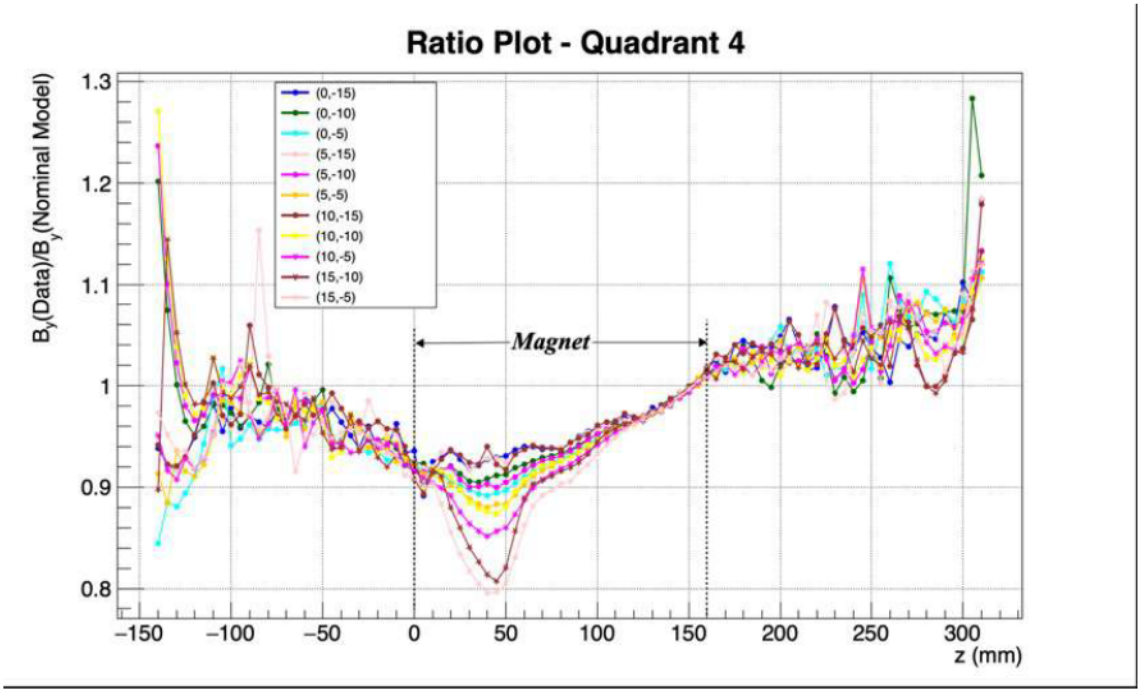

Figure 5.9: Ratio plot of the data and the COMSOL model at 11 positions in Quadrant 4 of the 5 mm measurement grid.

From Figures 5.6, 5.7, 5.8, and 5.9, it is evident that the greatest variation or discrepancy inside the magnet, across all positions on the xy-plane in the plot, occurs at the edges, such as at (15,0) and (15,-5), with a discrepancy of approximately 21%. At the center, represented by the red curve, the maximum discrepancy is around 12%.

5.3 Fitting

Fitting, in our case, refers to the optimization of the magnetization of the neodymium pieces in the nominal COMSOL model to ensure that the resulting map from the model best represents the set of measured data points. The goal is to find the 147 model parameters, defined in Table 1, that minimize the discrepancy between the mapped data and the model's predictions. Once a reasonable fit is obtained, we can interpolate and extrapolate the magnetic field map according to our needs. This is discussed further in Section 5.4.4.

This section provides a detailed explanation of the objective function being minimized, the programming framework developed for this minimization, and how the workflow was automated to enable the algorithm to iteratively run on the COMSOL model until a reasonable fit is achieved. Finally, the magnetic field maps of the nominal, data, and fitted models are compared to evaluate the improvements.

5.3.1 Objective Function

In our case, the objective function being minimized by the algorithm is a chi-squared (χ^2) function. The chi-squared function is defined as:

$$\chi^2 = \sum_{i=1}^{N_{\text{DataPoints}}} \left(\frac{(b_{x,i} - b_{x,\text{pred},i})^2}{\sigma^2} + \frac{(b_{y,i} - b_{y,\text{pred},i})^2}{\sigma^2} + \frac{(b_{z,i} - b_{z,\text{pred},i})^2}{\sigma^2} \right),$$

where:

- $b_{x,i}, b_{y,i}, b_{z,i}$ are the observed(measured) components of the magnetic field,
- $b_{x,\text{pred},i}, b_{y,\text{pred},i}, b_{z,\text{pred},i}$ are the corresponding predicted(COMSOL) components,
- σ is the constant uncertainty, set to 0.01 T,
- $\sum_{i=1}^{N_{\text{DataPoints}}} = 4095$, i.e., the total number of data points in the AP-STD measured map.

An important thing to note here is that in our analysis, we set the constant uncertainty, σ, to 0.01 T. While this value is larger than the measurement accuracy of the Hall Probe used, it was chosen to facilitate convergence of the optimization process, given the large number of unconstrained parameters in the fit. This means that the reported χ^2 value does not strictly represent a statistical measure of goodness-of-fit based on the true experimental uncertainties. Instead, it served as a practical tool to guide the fitting process.

The challenges with convergence stem from the complexity of the model and the high dimensionality of the parameter space. Despite these challenges, the final fit achieved satisfactory agreement with the data. However, readers should be cautious in interpreting the χ^2 value and view it primarily as a means to optimize the fit rather than a definitive statistical metric.

5.3.2 Programming Framework and Implementation

This subsection describes the programming framework used for the optimization process. The optimization workflow we designed is iterative and follows a systematic approach to minimize the differences between the COMSOL model and the experimental data. Figure 5.10 illustrates the general workflow of the program designed to perform the optimization.

The flowchart provides an overview of the sequential steps involved in the optimization process, which are then translated into code to automate the process. Each step is explained in detail in the following subsections, including its implementation and role in the overall framework.

5.3.2.1 Input Parameters

The first step in the workflow is the process of providing initial input parameters. These parameters are prepared in a specific file format to ensure compatibility with COMSOL. The required file format is a `.dat` file, where the first row contains the names of the 147 parameters, and the second row contains their corresponding val-

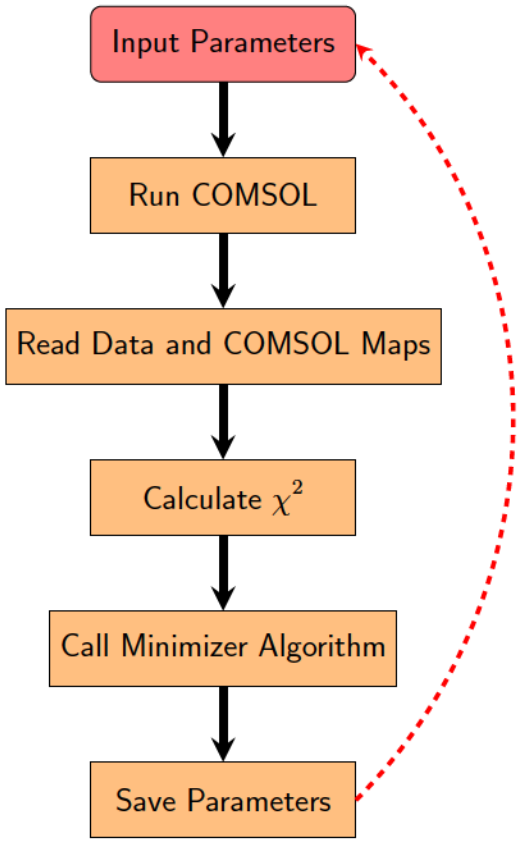

Figure 5.10: Flowchart of the programming framework used for iterative minimization of the COMSOL model to fit the experimental data.

ues, strictly separated by spaces.

The initial parameters used in this process are the nominal values in the COMSOL model before the fitting procedure begins. As the fitting process progresses, the parameter file is continuously updated. After each iteration, the new, optimized parameter values are saved to a file. This updated file then serves as the initial parameter file for the subsequent COMSOL run in the iterative fitting process.

5.3.2.2 Run COMSOL

The next step in this workflow involves running COMSOL using the parameter file prepared in the previous step. The output magnetic field map generated from this COMSOL batch mode run serves as the input for the next step in the optimization process.

It is worth noting that the time required for a single COMSOL run in batch mode typically ranges from 30 to 60 seconds per iteration.

5.3.2.3 Read Data and COMSOL Maps

The next step involves reading the measured data map file and the map generated by COMSOL in the previous step.

5.3.2.4 Calculate χ^2

Once the data and COMSOL maps are loaded, the χ^2 statistic is calculated to evaluate the goodness of fit between the two. The calculation follows the formula described in Section 5.3.1. The implementation of the χ^2 calculation follows a standard approach, where residuals between data and predictions are computed and weighted by the inverse of the variance. A detailed code snippet demonstrating this implementation is provided in **Appendix B.3**.

This χ^2 value serves as the objective function to minimize during the iterative optimization process.

5.3.2.5 Call Minimizer Algorithm

After calculating the χ^2, the next step is to minimize it. For this, we utilize the "SCAN" algorithm from the Minuit2 framework provided by CERN ROOT. This algorithm scans the objective function by varying one parameter at a time.

The step size for the SCAN algorithm is a crucial parameter and was experimented with values ranging from 0.01 T to 0.1 T during the minimization process. The number of points (`npoints`) in the scan is set to 40 by default and cannot exceed 100. In this implementation, the default value of 40 was used.

After each scan, if a new minimum χ^2 value is found, the corresponding parameter values are retained as starting values for subsequent scans or further minimizations. The uncertainty in the parameter values is set to a constant value of

0.01 T.

Figure 5.11 illustrates examples of χ^2 minimization across different iterations of the SCAN algorithm. Each curve represents the evolution of χ^2 as the parameter space is explored. The dips in the curves correspond to new minima being identified, where the best-fit parameter values are updated.

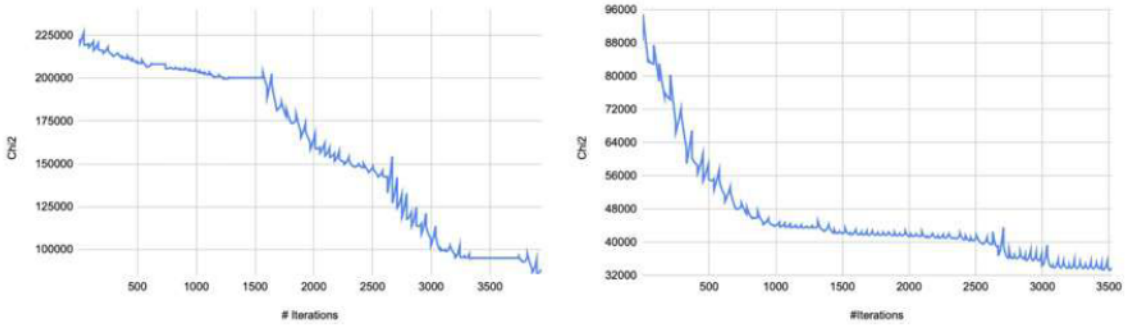

Figure 5.11: Examples of χ^2 minimization with extensive parameter space exploration. Each curve shows the evolution of χ^2 as parameters are varied.

5.3.2.6 Save Parameters

Once the SCAN algorithm identifies the minimum χ^2 value, the corresponding parameter values are saved back into the original input parameter file in the `.dat` format. This updated file replaces the previous input parameter file and serves as the starting point for the next iteration.

5.3.2.7 Closing the Loop

As shown in Figure 5.10, the loop is closed by updating the saved parameters, which are then used as input for the next iteration. The input parameter file is continuously updated, and the process repeats until the χ^2 is minimized to an acceptable value, indicating that the COMSOL model has reached a satisfactory fit to the data. Once the desired fit is achieved, the final parameter file is saved as the fitted parameters file. The fitted parameters file is then provided to the COMSOL model, and a 1mm map is extracted from the fitted model.

5.4 Results and Discussions

5.4.1 Comparing Magnetic Field Maps: Nominal vs. Fitted Model

In this section, we compare the magnetic field maps of the nominal COMSOL model with those of the fitted COMSOL model. The following figures show comparison plots between the nominal and fitted models. On the left-hand side of each figure are the magnetic field maps from the nominal COMSOL model, while on the right-hand side are the maps from the fitted model.

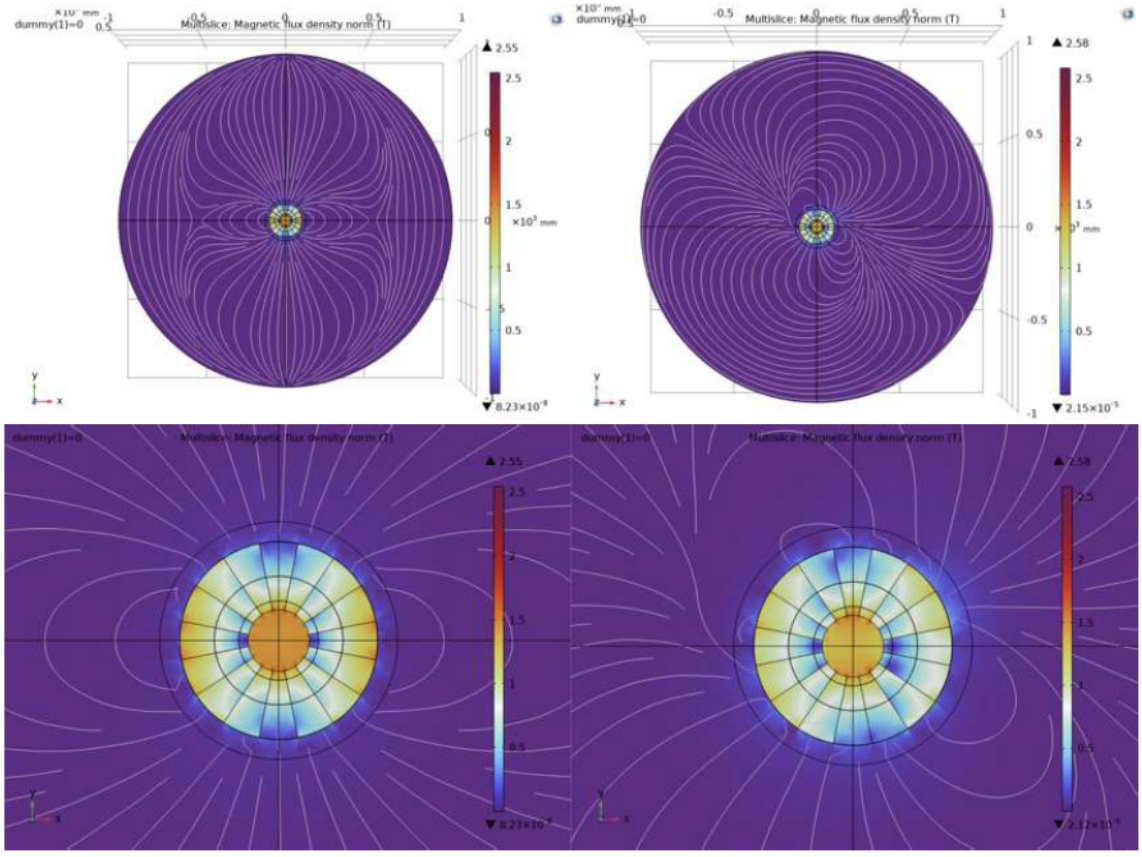

Figure 5.12: Magnetic Field Maps generated by COMSOL before (Left) and after (Right) fitting in the XY plane, along with their magnified versions below each.

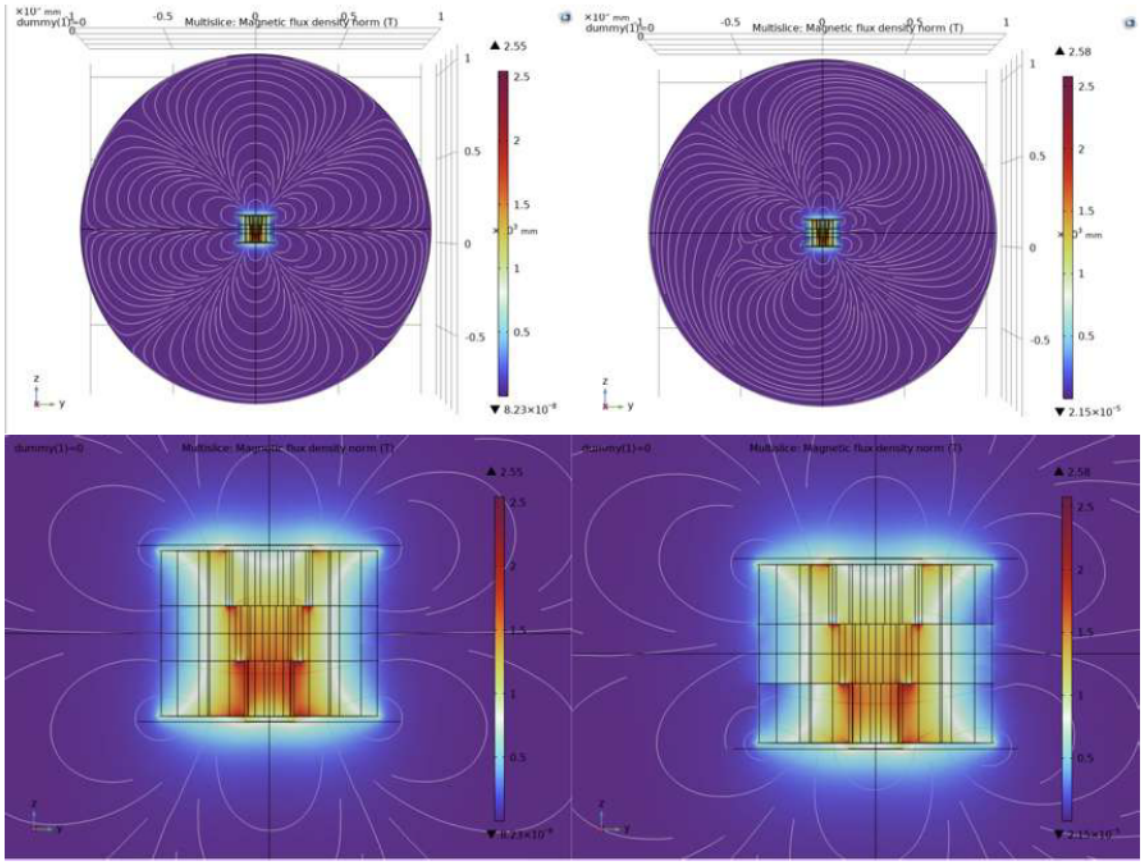

Figure 5.13: Magnetic Field Maps generated by COMSOL before (Left) and after (Right) fitting in the YZ plane, along with their magnified versions below each.

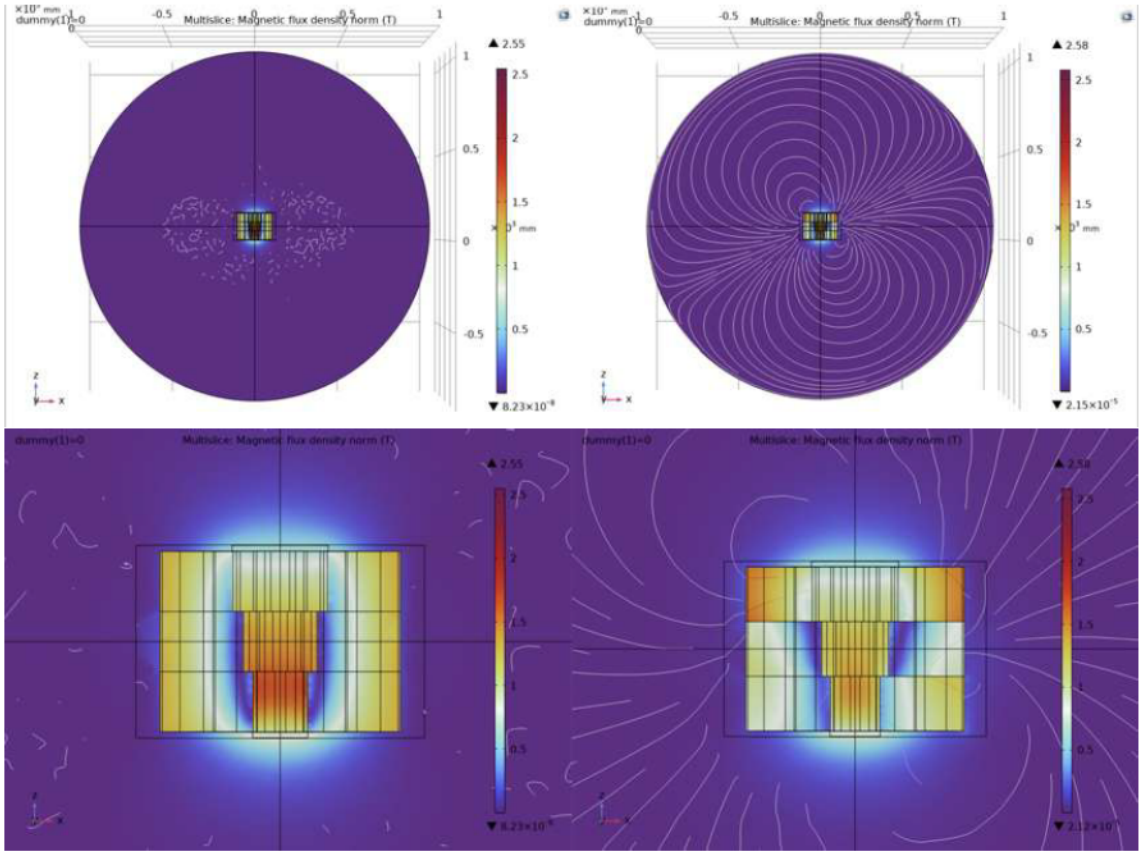

Figure 5.14: Magnetic Field Maps generated by COMSOL before (Left) and after (Right) fitting in the XZ plane, along with their magnified versions below each.

5.4.2 Comparison Plots: Data vs. Fit

First, we compare the fitted COMSOL model to the measured data down the central bore $(x, y = 0, 0)$. Figure 5.15 shows the magnetic field data on the upper panel and the corresponding ratio in the lower panel of the canvas. Within the magnet, along the central bore (i.e., at $(x, y) = (0, 0)$), we observe excellent agreement between the data and the model.

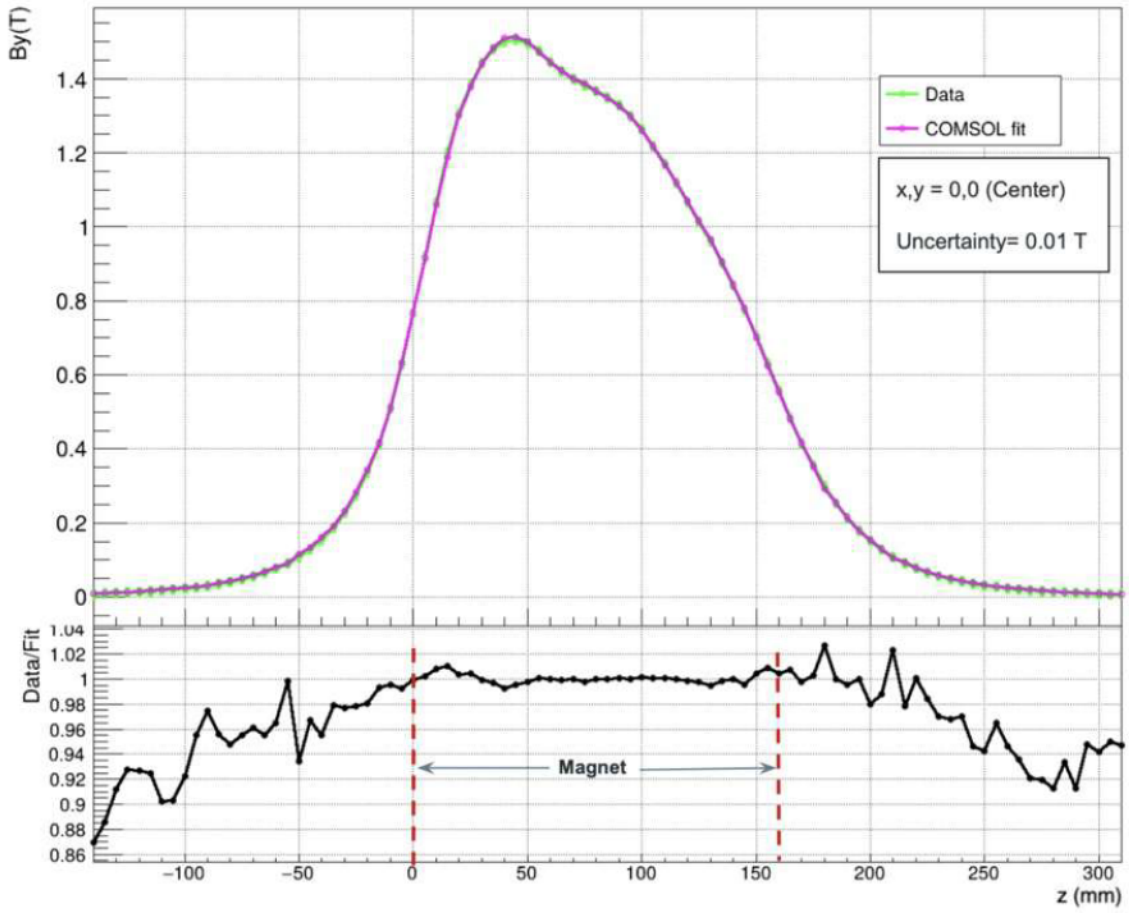

Figure 5.15: Comparison of the **fitted** COMSOL model and measurement data at the central position $(x, y = 0, 0)$, with a 0.01% uncertainty band in green.

Next, we evaluate the fitted COMSOL model and the measured data using a ratio plot. Figures 5.16, 5.17, 5.18 and 5.19 illustrate the ratio of the data to the fitted model in 4 quadrants as shown on the grid in Figure 5.5.

In Figure 5.16, the ratio plots for the 12 positions in Quadrant 1 of the grid (shown in Figure 5.5) are displayed. These positions are: (0,0), (5,0), (10,0), (15,0),

(15,5), (10,5), (5,5), (15,10), (10,10), (5,10), (10,15), and (5,15). Similarly, in Figure 5.17, the ratio plots for the 11 positions in Quadrant 2 of the grid are shown. These positions are: (0,5), (0,10), (0,15), (-5,5), (-5,10), (-5,15), (-10,15), (-15,10), (-10,10), (-15,5), and (-10,5).

In Figure 5.18, the ratio plots correspond to the 11 positions in Quadrant 3 of the grid. These positions are: (-15,0), (-10,0), (-5,0), (-15,-5), (-10,-5), (-5,-5), (-15,-10), (-10,-10), (-5,-10), (-10,-15), and (-5,-15). Finally, for Quadrant 4 of the grid, as shown in Figure 5.19, the 11 positions plotted are: (0,-5), (0,-10), (0,-15), (5,-5), (5,-10), (5,-15), (10,-5), (10,-10), (10,-15), (15,-5), and (15,-10).

Comparing this plot with Figures 5.6, 5.7, 5.8 and 5.9, it is evident that the model now fits the data significantly better.

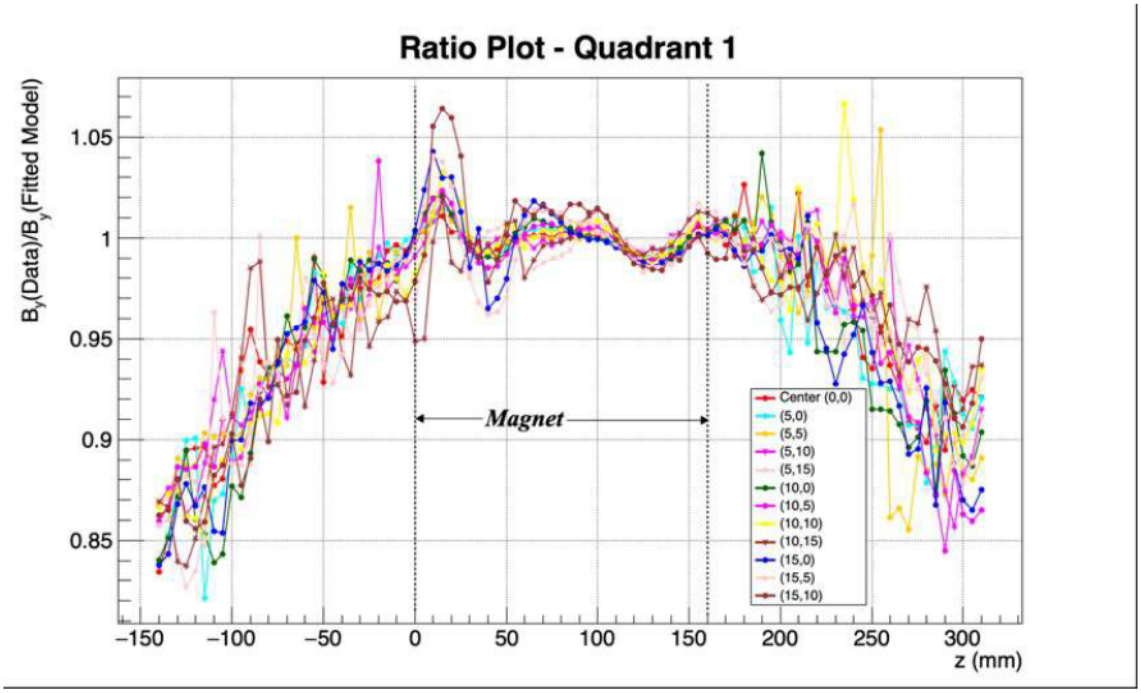

Figure 5.16: Ratio plot of the Data and the **fitted** COMSOL model at 12 positions in Quadrant 1 of the 5 mm measurement grid.

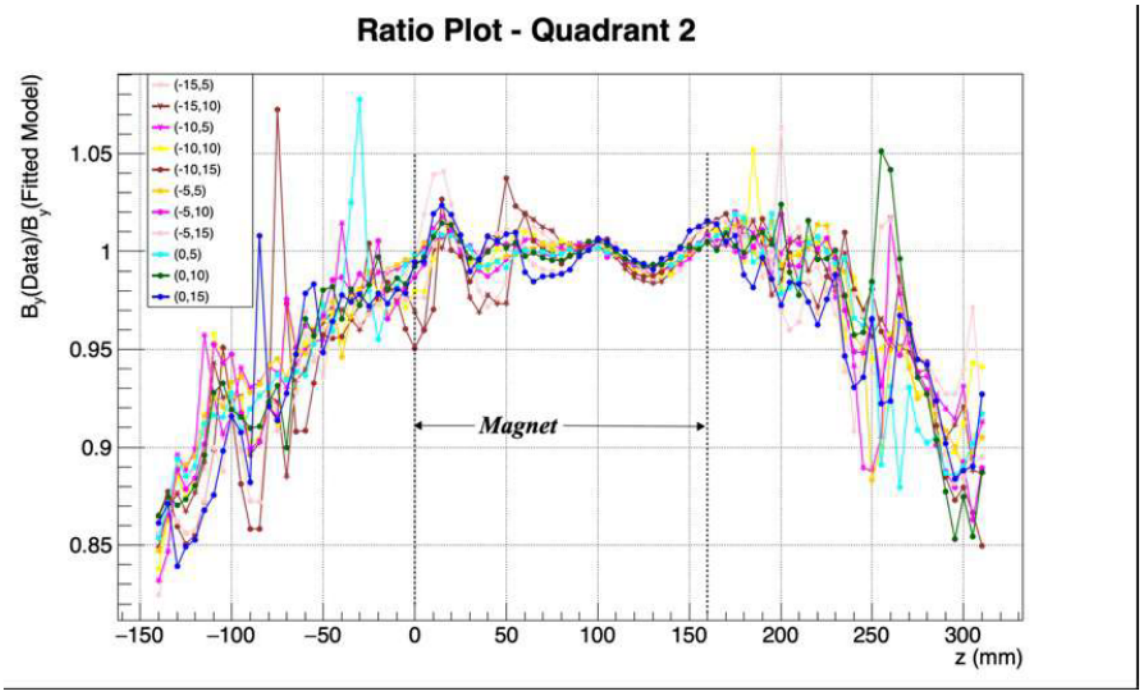

Figure 5.17: Ratio plot of the Data and the **fitted** COMSOL model at 11 positions in Quadrant 2 of the 5 mm measurement grid.

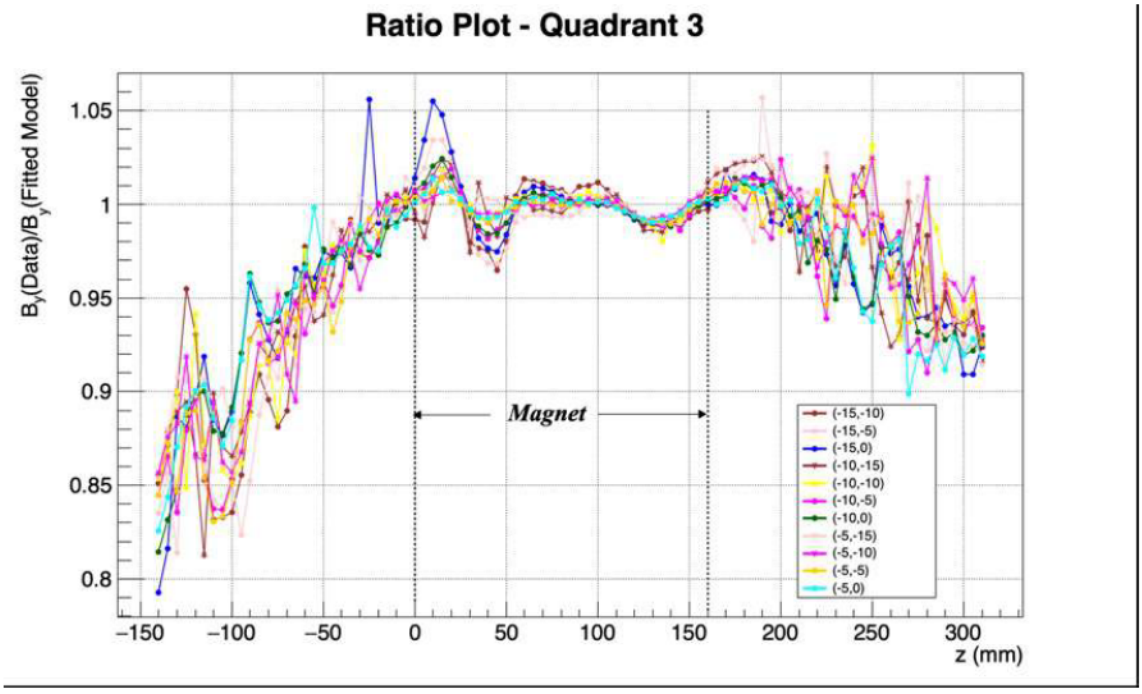

Figure 5.18: Ratio plot of the Data and the **fitted** COMSOL model at 12 positions in Quadrant 3 of the 5 mm measurement grid.

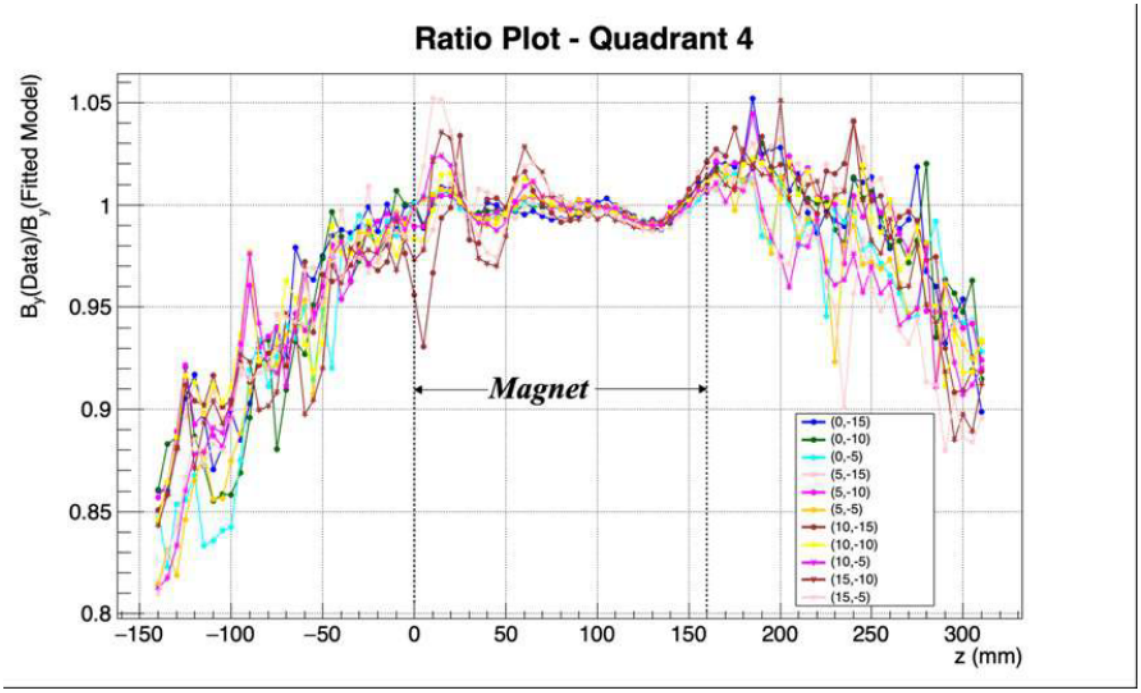

Figure 5.19: Ratio plot of the Data and the **fitted** COMSOL model at 12 positions in Quadrant 4 of the 5 mm measurement grid.

Interpretations: As observed in the ratio plots (compare Figures 5.6, 5.7, 5.8, 5.9, and Figures 5.16, 5.17, 5.18, 5.19), the discrepancy within the magnet has decreased significantly after optimization. Along the edges, the maximum discrepancy has reduced from approximately 21% to 6%, while along the central axis, it has decreased from approximately 12% to 1%.

To track changes in the fitted parameter values relative to their nominal values, we analyzed the **relative percentage change** in the resultant magnetic field ($\vec{B}$) for each magnet segment. This comparison helps identify segments with significant deviations, potentially indicating manufacturing errors. The relative percentage change for each segment was calculated as:

$$\%\,\text{Relative Change} = \frac{\text{Nominal Resultant MF Value} - \text{Fitted Resultant MF Value}}{\text{Nominal Resultant MF Value}} \times 100$$

The resultant magnetic field $\vec{B}$ for a given segment is computed as the magnitude of the field vector:

$$|\vec{B}| = \sqrt{B_x^2 + B_y^2 + B_z^2}$$

Here, B_x, B_y, and B_z are the magnetization components in the x-, y-, and z-directions, respectively.

Table 5.2 lists the segment numbers and their corresponding relative percentage changes.

#	% Relative Change	#	% Relative Change	#	% Relative Change
1	-0.3644	17	-17.5721	33	-25.1365
2	2.5134	18	5.6797	34	0.3284
3	9.0318	19	-2.8942	35	0.9668
4	-2.0125	20	9.5143	36	10.2259
5	-2.5293	21	3.6365	37	15.2729
6	3.8306	22	4.4440	38	9.0735
7	-20.1591	23	26.7711	39	32.1000
8	-14.3	24	9.5951	40	12.3430
9	5.7784	25	-4.8873	41	4.7825
10	0.7168	26	-6.4388	42	10.0314
11	-3.5181	27	-0.8176	43	17.5887
12	3.2802	28	1.2539	44	0.2614
13	5.3655	29	6.1514	45	-13.4574
14	-15.3676	30	36.6114	46	13.1856
15	-13.5856	31	39.3752	47	11.4878
16	-18.5257	32	7.0100	48	4.7776

Table 5.2: Relative percentage change in the resultant magnetic field for each of the 48 magnet segments. For detailed visualization, refer to Figure 5.20.

Figure 5.20 provides a geometric visualization of the segments. Green represents minor variations ($< 10\%$), blue indicates moderate shifts (10–20%), and red highlights significant deviations ($> 20\%$).

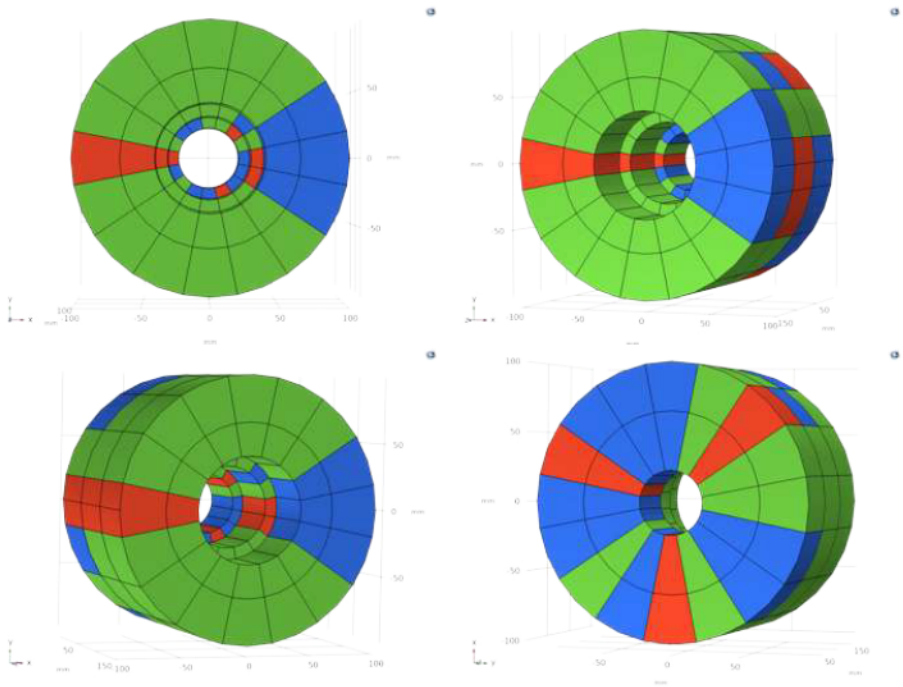

Figure 5.20: Visualization of the relative percentage changes across magnet segments. The axis orientation is shown in the lower-left corner. Colors represent relative variation: Green (< 10%), Blue (10–20%), and Red (> 20%). See Table 5.2 for exact values.

5.4.3 Final Fit Parameters

The final fit parameters are obtained by iteratively minimizing the χ^2 function. Once the fit converges, the parameter values deemed reasonable are saved. A detailed table listing the final fit parameters is provided in Appendix B.4.

5.4.4 Final Fitted 1mm Map

After achieving the desired fit to the experimental data, we utilized the fitted parameters to generate high-resolution magnetic field maps. This was accomplished by inputting the list of 147 optimized parameters into the COMSOL model and subsequently triggering the creation of a map with a 1 mm spatial resolution.

We know that the measurement data by AP-STD was a coarser 5 mm resolution map, where the x, y coordinates ranged from -15 mm to $+15$ mm, resulting in a total of 4095 nodes.

To achieve a finer resolution and extend the field map coverage needed for detailed analysis, we expanded the range of x, y coordinates to -45 mm to $+45$ mm and interpolated the field values to a 1 mm resolution. This increase in resolution resulted in a significant rise in the total number of nodes, reaching approximately 3 million. The extended map not only captures intricate field variations but also provides a robust dataset for further analysis and simulations. Additionally, values inside the neodymium magnet segments themselves were retained in the map, even though they will not be needed for any tracking analysis down the line.

Table 5.3 summarizes the key differences between the initial 5 mm map and the higher resolution 1 mm map, highlighting the improvements in resolution, range, and node count.

Parameter	**Measured (AP-STD)**	**COMSOL Fitted**
Map Resolution	5 mm	1 mm
Total Data Points/Nodes	4,095	3,734,731
x, y **Range**	-15 mm to $+15$ mm; No $(\pm 15, \pm 15)$ mm points	-45 mm to $+45$ mm
z **Range**	-140 mm to $+310$ mm	-140 mm to $+310$ mm

Table 5.3: Comparison of magnetic field map parameters between measured data (AP-STD) and COMSOL-fitted data.

Next, we present the plots in Figure 5.21 (comparable to Figure 4.18 and Figure 5.3) that illustrate the magnitude of the magnetic field in the (x, y) planes at four distinct z-positions along the magnet. These positions correspond to the upstream aperture at $z \approx 0\,\text{mm}$, the transitions between Halbach array rings at $z \approx 55\,\text{mm}$ and $z \approx 105\,\text{mm}$, and the downstream aperture at $z \approx 160\,\text{mm}$. Due to the high-resolution map, the magnet segments are clearly visible at $z = 55\,\text{mm}$ and $z = 105\,\text{mm}$.

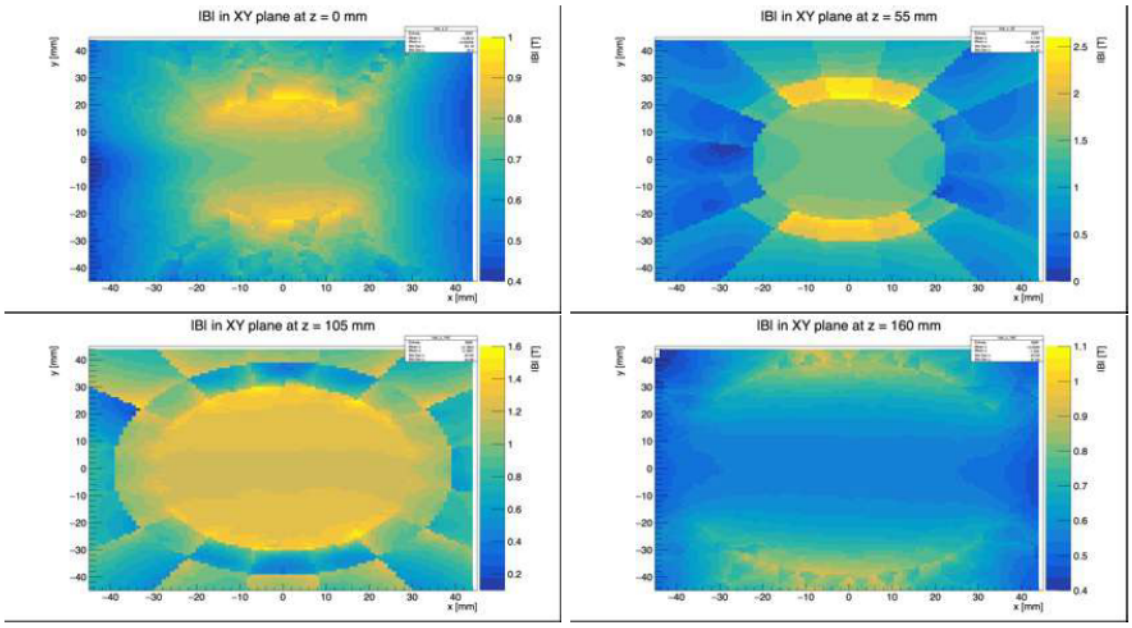

Figure 5.21: Magnitude of the magnetic field in the (x, y) planes at various z-locations along the magnet for the fitted COMSOL model. Compare with Figure 4.18 and Figure 5.3.

Finally, we present vector plots for the same z-locations. The vector plots in Figure 5.22 and 5.23 depict the magnetic field components B_x and B_y across the (x, y) planes. The arrow length represents the magnetic field magnitude, while their direction shows its orientation. The high resolution of the 1 mm fitted map allows detailed visualization of the vector directions and magnitudes, not only inside the magnet but also within individual segments. For instance, at $z = 55\,\text{mm}$ and $z = 105\,\text{mm}$, the vector directions and magnitudes within each segment are distinctly visible. These plots can be compared to Figure 4.19.

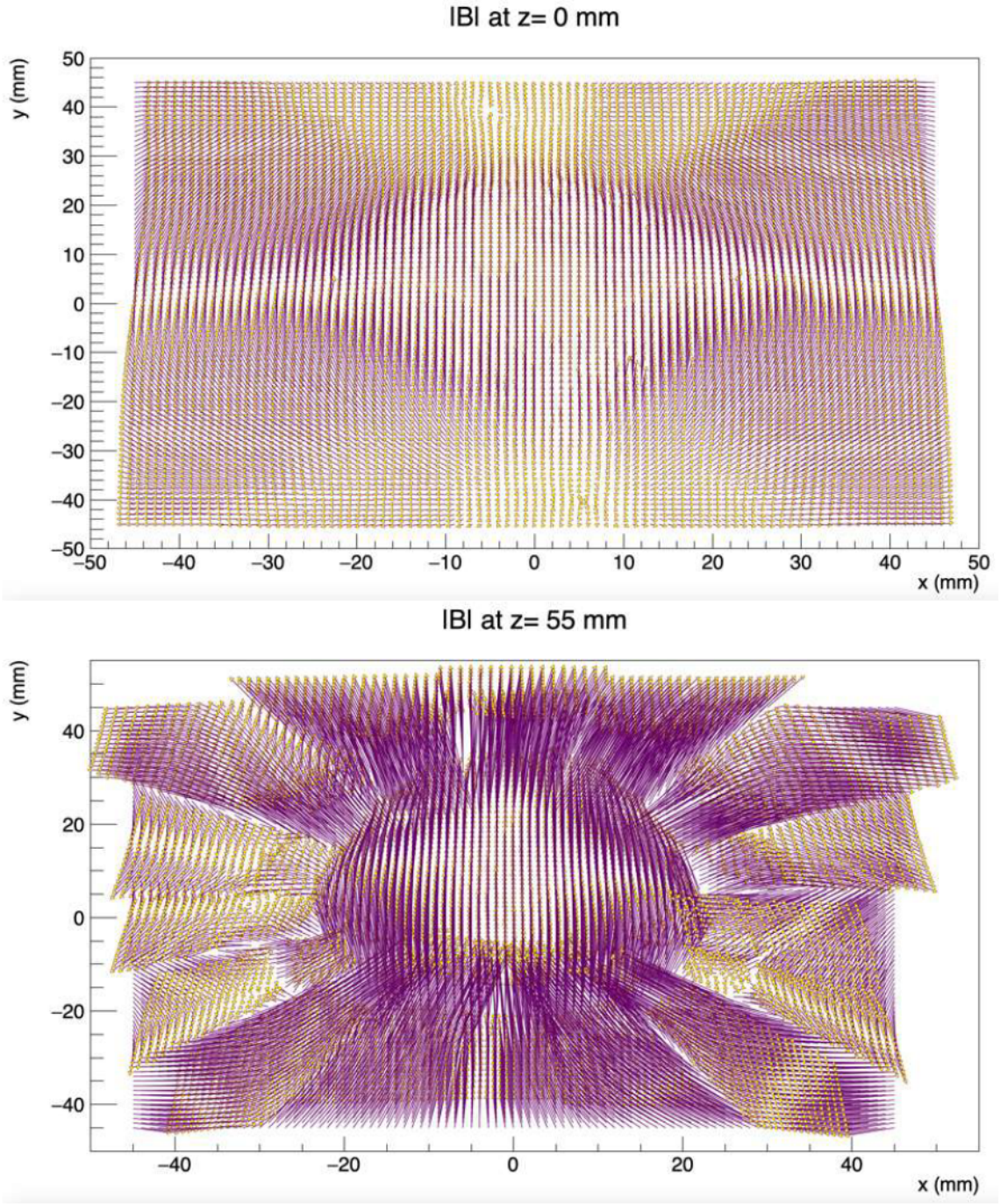

Figure 5.22: Vector plots of the magnetic field components B_x and B_y at $z = 0$ and $z = 55$ mm.

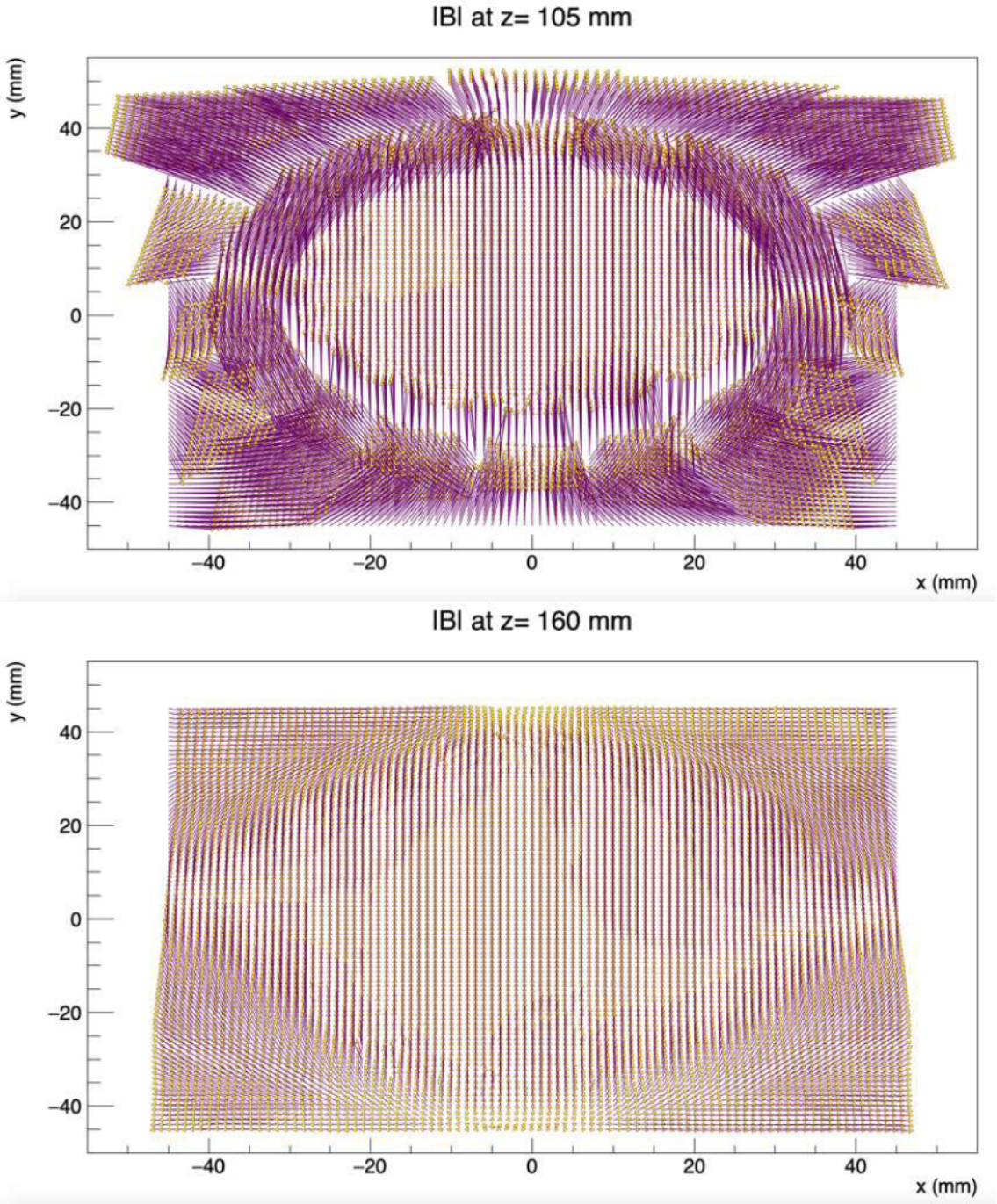

Figure 5.23: Vector plots of the magnetic field components B_x and B_y at $z = 105$ and $z = 160$ mm.

5.4.4.1 Interpolated Maps

The interpolated maps are generated at a resolution of 1 mm. To evaluate the effectiveness of the interpolation, we compare the magnetic field values at all 45 positions in the 5 mm measurement grid, as shown in Figure 5.5. These visual comparisons highlight how the interpolated data captures the expected field variations and smooth transitions, even at finer resolutions. All these plots are presented in Appendix A.

5.4.4.2 Extrapolated Maps

With the extrapolation, we can extend the magnetic field map beyond the measured volume. This capability is particularly valuable as it allows us to generate data for areas where the probe was unable to take measurements. The extended field map now spans a larger range, from -45 mm to $+45$ mm in both x and y, while maintaining the original z range of -140 mm to $+310$ mm, as outlined in Table 5.3.

For a visual comparison, refer to Figure 4.16 (Left), which highlights the original measurement area. Observe how it contrasts with the extrapolated area shown in Figure 5.24, extending beyond the measured regions to provide a broader field map coverage.

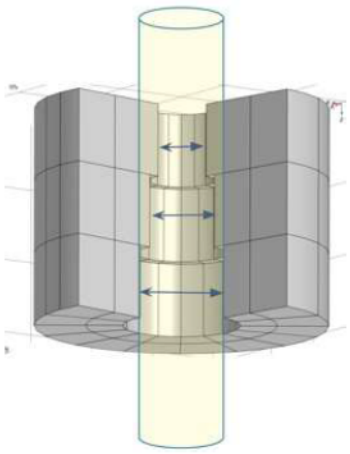

Figure 5.24: The yellow cylindrical region represents the magnet volume for which the 1 mm map has been extrapolated.

Figure 5.25 provides an example of an extrapolated magnetic field map at $x = 0, y = 22$.

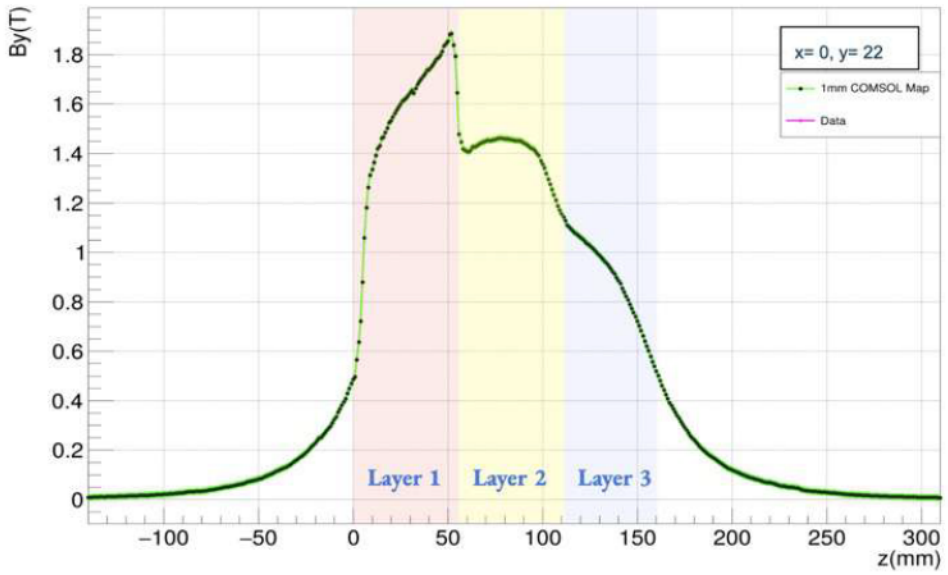

Figure 5.25: Extrapolated magnetic field map at $x = 0, y = 22$. This map shows the extended field beyond the original measurement region. The red, yellow, and blue shaded regions represent the three layers of the Halbach array magnet.

5.5 Conclusions and Future Work

This study has developed a high-resolution 1 mm magnetic field map for the Phase 1 Halbach array magnet used in the EMPHATIC experiment. The map was created using COMSOL Multiphysics by fitting and optimizing data from the initial 5 mm hall probe measurements conducted by AP-STD.

The study has improved the precision of magnetic field mapping, enabling better momentum and angle resolution, enhanced spectrometer accuracy, and expanded detector acceptance. The refined map also provides full coverage of the magnet, including areas not accessible to hall probe.

This work will be extended to the Phase 2 magnet, which has a similar design, ensuring continued improvements in magnetic field mapping for future phases of the EMPHATIC experiment. These advancements will significantly contribute to achieving the experiment's goals.

The EMPHATIC data will be used to improve flux predictions either by con-

straining Monte Carlo models— by incorporating the data into a flux prediction package such as PPFX (discussed in Chapter 3, Section 3.1.3)—or by directly applying it to the NOvA cross-section and particle yield calculations. Additionally, this approach can be extended to future experiments. One such experiment is the upcoming DUNE, where our contribution focuses on developing detector technologies for tracking and energy loss (dE/dx) measurements using specialized straw-like tubes, known as the Straw Tube Tracker (STT), which will be discussed in the next chapter.

Chapter 6

Straw Tube Tracker for DUNE

6.1 Introduction

Straw tubes are drift chambers consisting of a gas-filled conducting cylinder acting as the cathode and a wire stretched along the cylinder's axis serving as the anode. These tubes form the basis of Straw Tube Trackers (STTs), which are low-mass tracking systems offering exceptional vertex, momentum, angular, and time resolution, along with particle identification capabilities. STT-based tracking detectors are proposed for the System for on-Axis Neutrino Detection (SAND), one of the Near Detectors in the long-baseline neutrino experiment, Deep Underground Neutrino Experiment (DUNE) at Fermilab. The SAND is permanently located on-axis to monitor the neutrino beam's stability and to measure the absolute flux of four neutrino flavors (ν_μ, $\bar{\nu}_\mu$, ν_e, and $\bar{\nu}_e$). For accurate flux calculations, a precise tracking system is essential, and the straw tube trackers play a critical role in this process.

As part of the DUNE-India-ND collaboration, progress has been made at Panjab University toward the assembly and testing of the SAND STT modules. A test bench has been developed and is being actively operated for setting up readout and characterization facilities. Additionally, a prototype module measuring 1.8 m $\times$ 50 cm has been designed. This prototype includes newly fabricated straw tubes and associated gas chambers.

Studies are being conducted to ensure the reliability and performance of these components. Gas leak tests and characterization of the straw tubes under various conditions are underway. Furthermore, simulation studies using GARFIELD++, a C++-based framework for modeling tracking detectors, are being performed to evaluate the dimensions and properties of the assembled straw tubes with different gas mixtures.

6.2 Overview of DUNE

A schematic of the DUNE experiment setup is shown in Figure 6.1. The experiment features a far detector located 1.5 km underground at the Sanford Underground Research Facility (SURF), 1,300 km from the neutrino source. The far detector consists of four modules using LArTPC technology, each containing 17 kt of liquid argon (with a fiducial mass of at least 10 kt), totaling nearly 70 kt. The near detector, placed 574 meters from the source, includes a flexible LArTPC, a magnetized gaseous argon TPC, and a large magnetized beam monitor. The Long-Baseline Neutrino Facility (LBNF) beamline [9] will deliver the world's most intense neutrino beam to the near and far detectors in an on-axis configuration.

The primary objectives of the experiment are to:

- Measure neutrino oscillations, including the appearance of electron neutrinos (ν_e) from a muon neutrino (ν_μ) beam, as well as measurements of the charge-parity phase and determination of the neutrino mass hierarchy.
- Search for proton decay.
- Detect electron neutrinos from core-collapse supernovae.

The DUNE Near Detector (ND) includes three main components, two of which are capable of moving off the beam axis. Each component plays a crucial and complementary role in achieving the overall objectives of the ND. Due to their distinct features, the DUNE ND is often described as a suite of detectors with varying capabilities. Figure 6.2 illustrates the DUNE ND components in the detector hall,

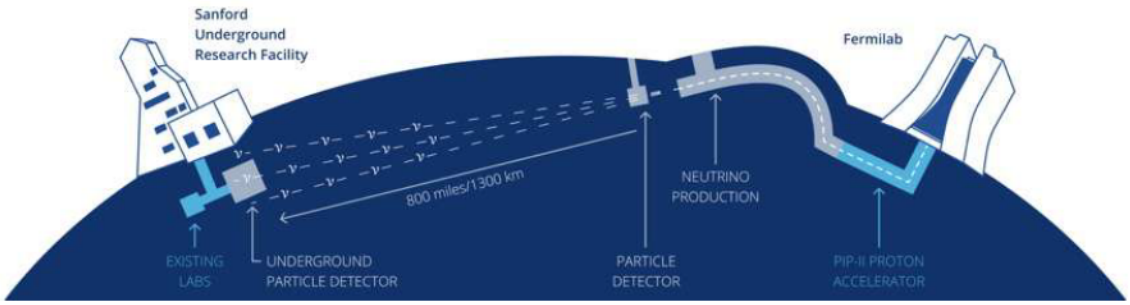

Figure 6.1: A diagram of the DUNE experiment setup, where neutrinos produced at Fermilab travel 1300 km through a near detector to reach the far detector at the Sanford Underground Research Facility.[68]

showing on-axis configuration. The three components are: ND-LAr (Liquid Argon), ND-GAr (Gaseous Argon), and SAND (System for on-Axis Neutrino Detection).

The SAND design focuses on refurbishing the superconducting magnet and electromagnetic calorimeter from the KLOE experiment[69]. The calorimeter is made from lead and scintillating fibers. Other components of SAND include an inner tracker and a potential liquid argon component known as GRanular Argon for Interaction of Neutrinos (GRAIN). The inner tracker consists of orthogonal straw tube trackers that enhance particle identification and provide carbon nuclear targets for neutrino interactions.

6.3 Straw Tube Tracker

Straw tubes are gaseous drift detectors that work in proportional operation mode. It is a cylindrical conducting tube filled with gas and a wire that is tensioned along the axis of the tube. The main purpose of the straw tube is to detect charged particles passing through it. When a charged particle passes the tube, an electromagnetic interaction takes place between the charged particle and the atoms and molecules of the gas. Due to these Coulomb interactions, electron-ion pairs are created along the trajectory of the charged particle. The applied electric field between the wire (given positive voltage of few kV) and the tube results in the drifting of electrons and ions through the gas. The anode wire collects the electrons while the ions drift towards

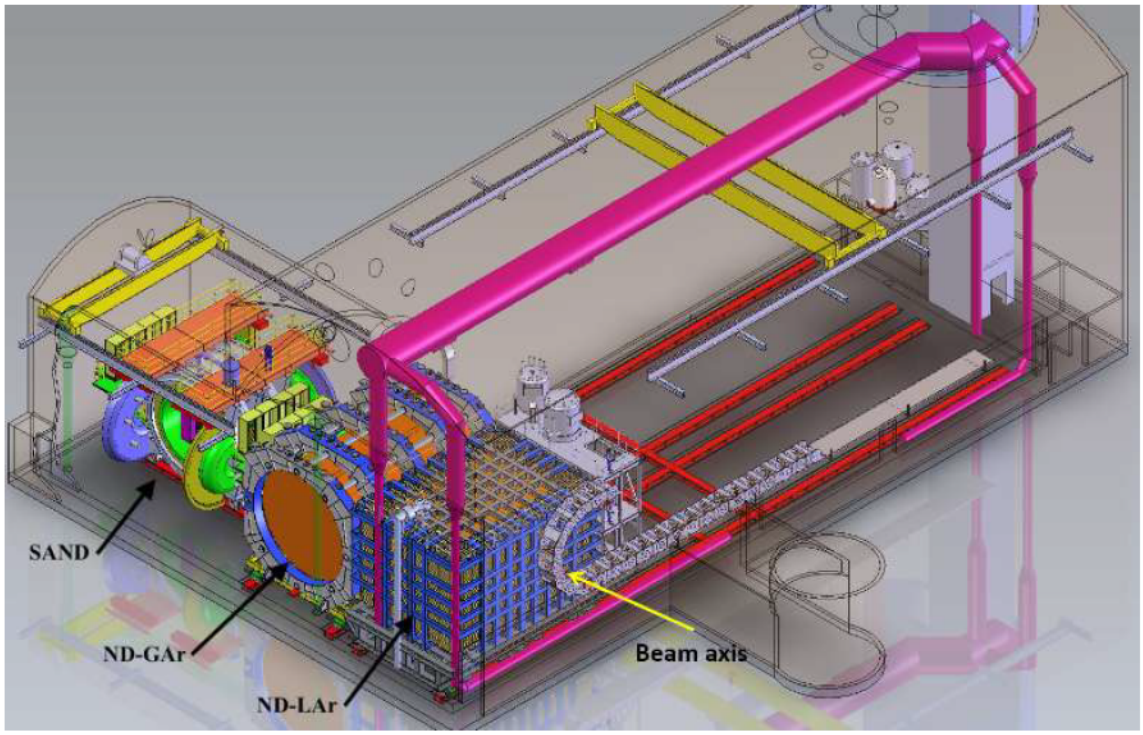

Figure 6.2: A schematic of the DUNE ND hall is shown with all component detectors in the on-axis configuration, and the SAND detector positioned on the beam axis. [21]

the straw tube wall (cathode). As the electric field is strong near the anode wire, the primary electrons formed drift to produce electron-ion pairs via the secondary ionization in the gas eventually forming an avalanche. Near the anode, the strong electric field (increasing as r^{-1}) enables gas amplification, where secondary ionization produces an electron avalanche, amplifying signals by 10^4–10^6. This avalanche when reaches the anode wire is large enough to produce a measurable signal that can be recorded by the readout electronics. As the straw tubes work in the proportional region, the size of the signal is proportional to the deposited primary charge.

The tracking of the charged particles traversing the straw tube is done by the drift time measurement of the anode wire i.e. the arrival time of the signal defines the drift radius, and the charge collected is proportional to the particle energy lost by ionization. The minimal distance between the wire and the trajectory of the charged particle is determined from the drift time of the ionized particles and this distance is the main information obtained using straw tube detectors for charged

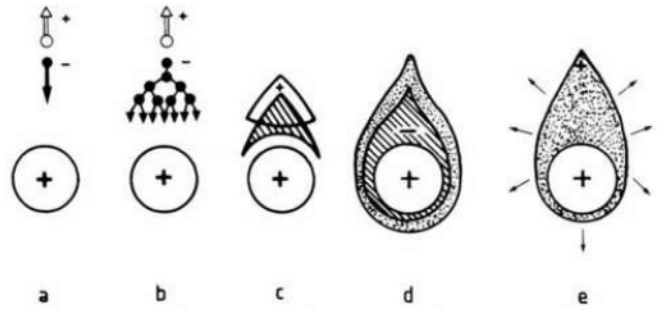

Figure 6.3: Time development of an avalanche in the Straw tube

particles. Thus, by measuring electron drift times, the particle's track and its closest approach to the anode wire can be reconstructed, providing coordinate information as a "cylinder of closest approach". Sketch of a straw tube is shown in Figure 6.4

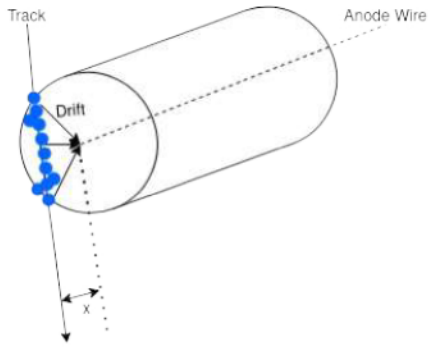

Figure 6.4: Drawing of a straw tube for charged particle tracking. Distance of closest approach of charged particle track to the anode wire is denoted by x.

6.4 STT for SAND

The System for on-Axis Neutrino Detection (SAND) is part of the DUNE Near Detector complex at Fermilab, with its first data-taking expected in the second quarter of 2031. SAND is designed to provide high precision measurements and address systematic uncertainties in long-baseline oscillation analyses, as well as contribute to short-baseline physics programs. [70]

6.4.1 Key Features of the STT Design

- **Detector Configuration:** The system consists of 86 modules, containing approximately 220,000 straws. The average straw length is 3.2 meters, with a maximum length of 3.8 meters. The internal gas volume of the detector is 14 m^3, operating at a nominal pressure of approximately 2 bar. The gas mixtures used in the system are Xe/CO_2 and Ar/CO_2, with a 70/30 ratio.
- **Target and Tracking Design:**
  - The detector includes about 80-100 thin($\sim 1.5\% X_0$) passive targets, each separated from the active straw layers. These targets have high chemical purity (around 97% of the mass), and a low density of $\rho \leq 0.17 g/cm^3$, optimized for tracking efficiency.
  - The system provides high track sampling with an average of 0.15% X_0 for perpendicular tracks and 0.36% X_0 for parallel tracks, with the total detector dimension approximately $1X_0$.
  - A "solid" hydrogen target is created through a subtraction of CH_2 and C targets. The design allows for replacement of individual targets with planar targets of desired material and thickness.

6.4.2 Performance and Capabilities

- **Precision Measurements:** The STT is designed to offer precise control over neutrino-target interactions, similar to $e^{\pm}$ fixed-target experiments. It is fully tunable and configurable during data-taking, ensuring flexibility in different experimental conditions.
- **Tracking and Particle Identification:**
  - *Tracking Efficiency:* The STT features combined particle identification and tracking across its entire volume. For instance:
    - Electron identification using Transition Radiation (TR) and dE/dx, with a π/e discrimination factor of approximately 10^{-3}.

    * 4π Detection of π^0s from γ conversions (about 49%) within the STT volume.
    * Identification of pions, kaons, and protons using dE/dx, range, and time-of-flight measurements in the surrounding calorimeter.
  - *High-Performance Readout:* The readout system provides both drift time and charge measurements, with a dynamic range of 10^3 for O(100k) straws.
- **Kinematic Reconstruction:** The STT allows for the accurate reconstruction of transverse plane kinematics from particle four-momenta, providing momentum resolution of approximately 3% and angular resolution of 1-2 mrad.

6.4.3 Detector Integration and Design

- **Lightweight and Self-Supporting Modules:** The STT tracking modules are designed to minimize thickness (28 mm for 4 XXYY layers, including the frame) and mass (straws with $\leq$ 19 μm walls, light carbon-fiber frame). The closely packed straw layers are operated under a 2 bar absolute pressure, contributing to high tracking efficiency.
- **Robust and Flexible Design:** The STT is designed with high integration and operational robustness:
  - Low-power integrated readout and self-cooling system.
  - Each STT half-module (XX or YY layers) is functionally independent, with both gas and electrical connections that can be disconnected without affecting the rest of the detector.
  - The design minimizes operational risks and allows for easy module reconfiguration.

6.4.4 Optimized for Mass Production

The STT modules are optimized for mass production, with a self-alignment mechanism for the straws during assembly. The use of pre-tension from overpressure and precise self-centering of the wires ensures minimal misalignment during assembly. This results in uncompromised performance, reduced costs, and simplified assembly procedures.

Item Description	Default STT	Reduced STT
Number of straws	219,334	136,192
Total straw length (km)	700	430
Straw outer diameter (mm)	5	5
Average straw length (m)	3.19	3.16
Maximal straw length (m)	3.75	3.75
Total straw film area (m^2)	10,990	6,751
Total straw internal volume (m^3)	14	8
Total detector length (mm)	2,998	2,998
Average density (g/cm^3)	0.17	0.11
Average radiation length X_0 (m)	2.8	4.3
Fiducial (20 cm) C mass (t)	0.544	0.544
Fiducial (20 cm) CH_2 mass (t)	3.863	2.334
Total number of modules	86	54
Number of modules with CH_2 target & radiator	48	39
Number of modules with CH_2 target only	23	0
Number of modules with graphite target	8	8
Number of tracking modules (no target)	7	7
Number of straw planes	344	232
Number of modules per super-module	10	6
Number of super-modules	8+1	8+1
Number of FE boards	3,427	2,128
Modularity of FE boards (channels)	64	64
Number of HV channels	172	108
Number of LV channels	190	126
Number of DAQ/DTS interface boards	18	18
Number of LV distribution boards	18	18

Table 6.1: Summary of key numbers for the default and reduced STT configurations in SAND

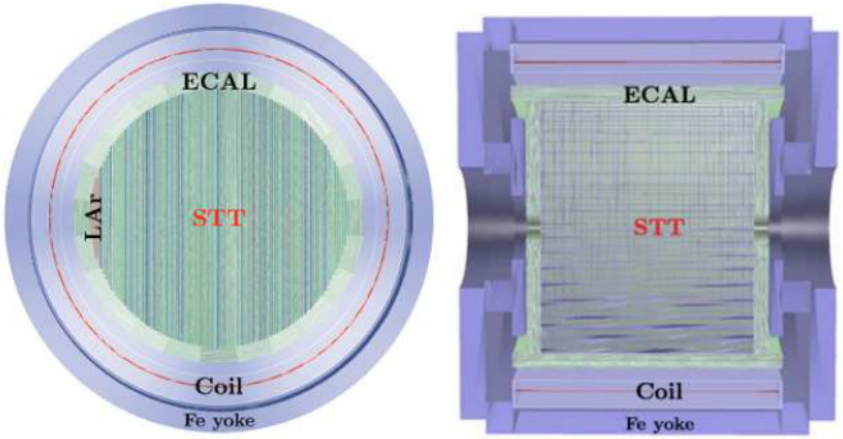

Figure 6.5: Geometry of the STT-only configuration for the SAND inner target/-tracker. The different STT modules are visible in the YZ view on the left: the blue modules are equipped with graphite targets, interleaved with standard CH_2 modules shown in green. [70]

6.5 STT R&D at Panjab University

6.5.1 Studies with Straw Tube Chamber Prototype

At Panjab University, a test ST Chamber procured from JINR, Dubna, Russia, is operational. The setup includes 50 straws (1.8 m length, 9.53 mm diameter) from Lamina Dielectrics Ltd., UK, and a 20 μm gold-plated tungsten wire from Luma Metall AB, Sweden. A leak test setup consisting of a gas sniffer, manometer, and pressure gauge has been established. The gas mixture used is Ar/CO_2 in an 80/20 volume ratio. A $6' \times 4'$ optical bench has been prepared for straw fabrication, and a single-channel preamplifier (provided with the test chamber) is available. [71]

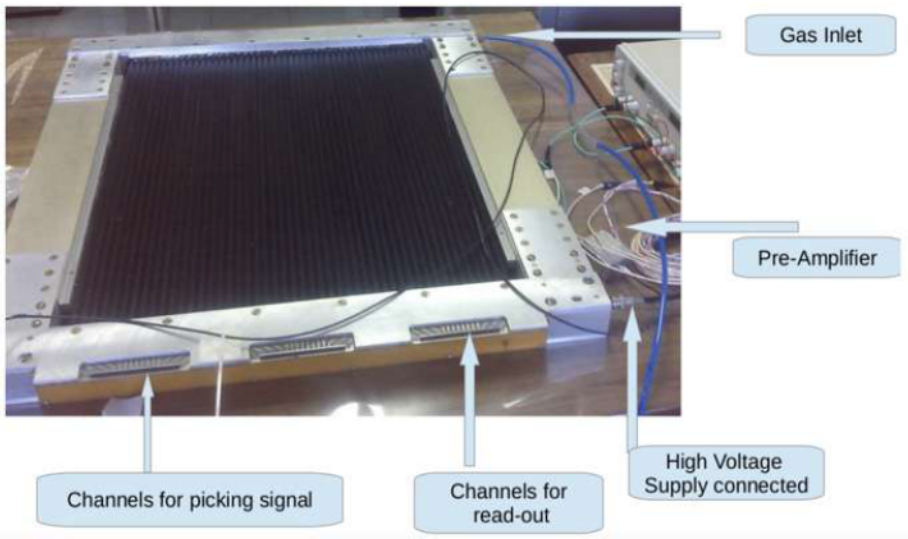

Figure 6.6: Straw Tube Chamber Prototype, JINR, Dubna

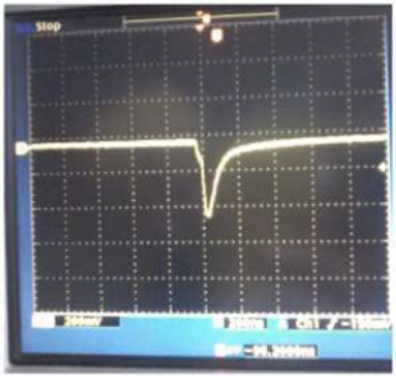

Figure 6.7: Signal pulse shape observed on the CRO with an anode high voltage of 1.95 kV, an amplitude of 220 mV, and a rise time of 25 ns.

Gas is supplied to test the chamber from a gas cylinder with the help of a regulator, maintaining a pressure of 0.3 bar. A dual voltage supply is connected to the pre-amplifier. The input of the pre-amplifier is connected to the channels (to be read out) via connectors, and the output is connected to the CRO (Cathode Ray Oscilloscope). A high voltage supply (1.75–2.00 kV) is provided to the anode. Each straw corresponds to two channels: one for the anode and one for the cathode. The signal is taken from the anode with respect to ground. The entire apparatus is grounded for safety and signal integrity.

Signals were recorded for all 48 straws using cosmic muons as the source. Abnormal behavior in the signal shape was observed in straws numbered 1 and 12. For the remaining 46 straws, negative pulses were recorded. The signal was measured from the anode with respect to ground. Each individual straw was tested by varying the anode high voltage from 1.75 to 2.00 kV. Amplitude values were observed for all straws at different voltages.

To verify the proportional behavior of the straws, we plotted V-A (Voltage vs. signal amplitude) curves for 5 randomly selected straws as shown in Figure 6.8. Additionally, we plotted the V-averaged signal amplitude curve to study the overall behavior as can be seen in Figure 6.10.

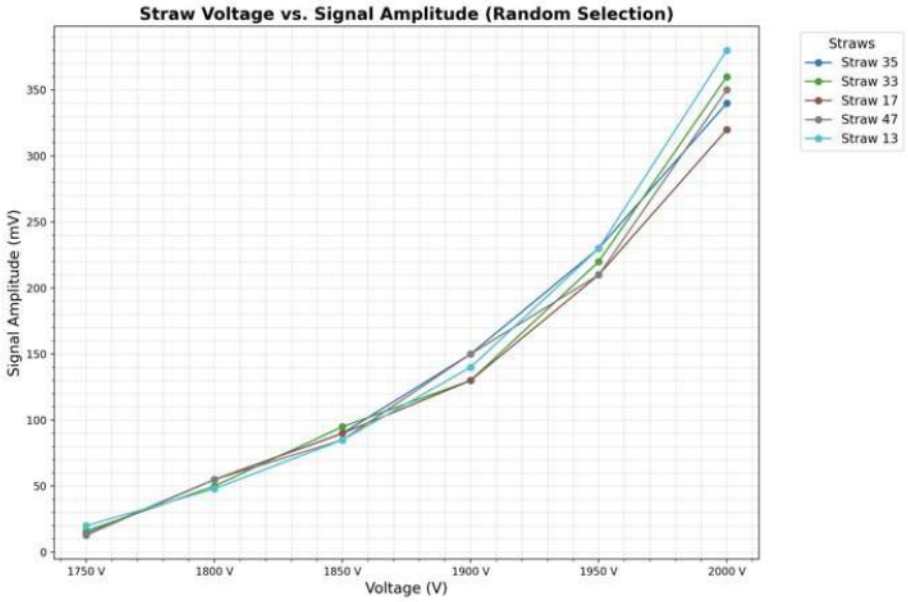

Figure 6.8: Plot of Voltage vs. Signal Amplitude for 5 randomly selected straws out of the 48, demonstrating proportional behavior with increasing voltage in the straw tube tracker.

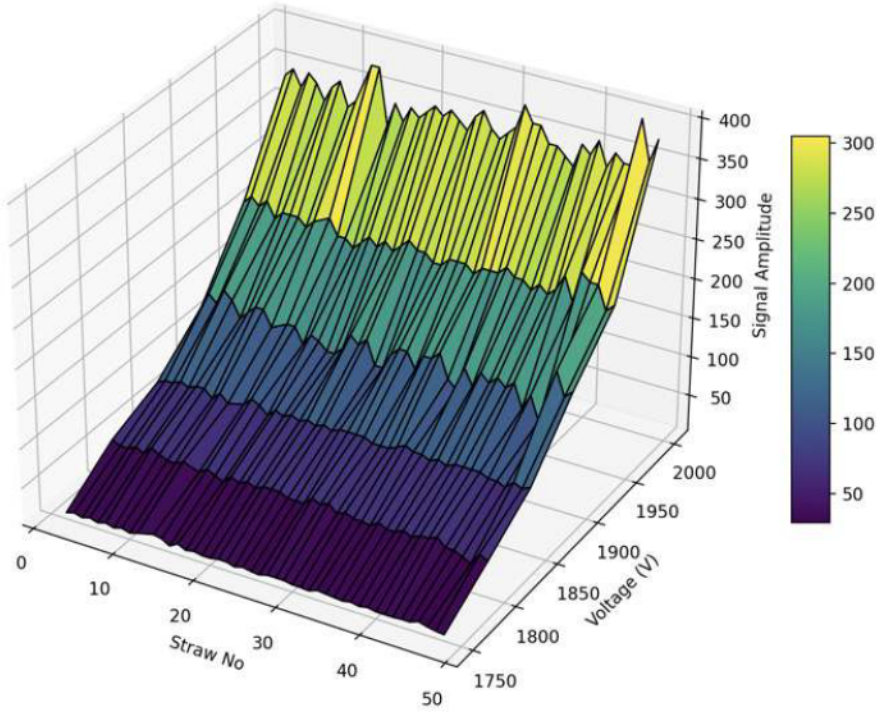

Figure 6.9: 3D Surface Plot of Signal Amplitudes vs. Straw Number and Voltage.

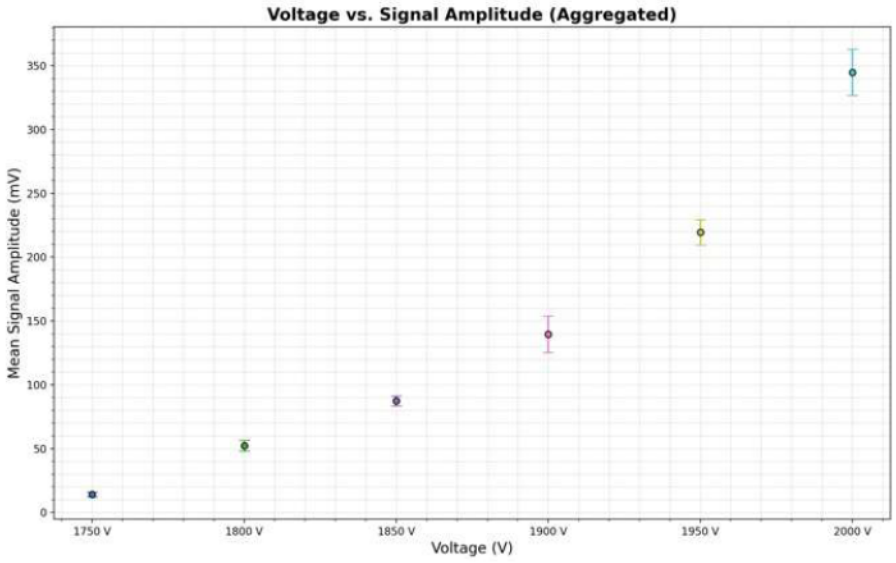

Figure 6.10: Voltage versus the mean signal amplitude averaged over all 48 straws.

6.5.2 Prototype Development and Assembly

The assembly of a single straw tube has been completed, and a perspex gas chamber has been prepared for it. Wire tension tests have been conducted using a sonometer setup. For the test stand setup, we are using 10 mm straws. The proposed SAND STT will use 5 mm straws, which are currently under production.

Wire Tension Test

The wire tension was measured with a sonometer setup (Figure 6.11). Resonant frequencies were observed for varying masses, with results summarized in Table 6.3. The properties of the wire are given in Table 6.2. The wire demonstrated a maximum tension capacity of 60 grams.

Type	Gold-plated Tungsten
Thickness	20 μm
Density	19.22 g/cc
Specific Resistance	0.092 Ω-mm^2/m
Length (between 2 bridges)	75 cm

Table 6.2: Properties of the Wire

Mass (g)	Observed Frequency (Hz)	Theoretical Frequency (Hz)	Percentage Error (%)
20	124	120	3.33
30	145	147	1.36
40	162	169	4.14
50	188	189	0.53
60	201	204	1.47

Table 6.3: Wire Tension Measurement with Sonometer

Figure 6.11: Wire Tension Measurement Setup at Panjab University

Assembly

A single straw tube prototype has been assembled. As shown in Figure 6.12, components include aluminium-coated Mylar straws, crimping pins, spacers, and end plugs. The Straw tube used is an aluminium coated Mylar tube. It is 181 cm long and has a diameter of 9.53 mm . A gold plated tungsten wire is used as anode and the cylindrical straw tube is the cathode. A spacer is placed in the middle of the straw tube and the wire is crimped with a crimping pin, after giving it the required tension. This setup is then glued to an endcap using Araldite glue leaving space for the passage of gas. The weight of the Straw Tube before assembly was 5.81 g and after the assembly was 9.76 g. The performance study of the assembled single straw tube is ongoing.

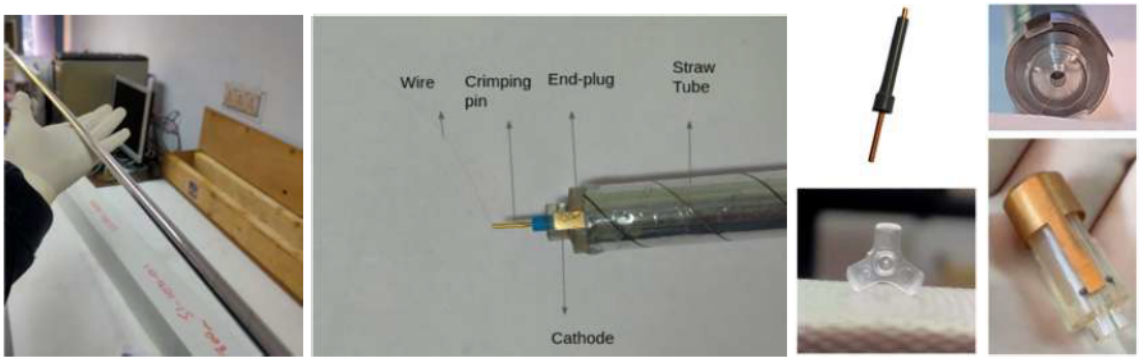

Figure 6.12: (a) Aluminium-coated Mylar Straw Tube (b) Assembled Straw Tube (c) Crimping Pin (above) and Spacer (below) (d) End Plug

Ongoing Efforts and Future Plans

The group at Panjab University is working on the prototype shown in Figure 6.13, which is being designed for the study of an assembled single straw tube. Gas chambers will be fixed at both ends of the straw tube, and the straw tube holders (shown in yellow) will be placed beneath the straw tube. The inlet and outlet of the gas in the Perspex chambers are also depicted. A PCB will be mounted on one side of the gas chamber. The gas to be passed through the system will be a mixture of Ar/CO_2 in the ratio 80/20. The connection to the high voltage (HV) for the straw wire is illustrated in Figure 6.14. Since the proposed SAND STT will use 5 mm straws and we are currently using 10 mm straws for the test bench stand, the R&D performed with the 10 mm straws will be repeated for the 5 mm straws once they become available. Additionally, comparisons with other types of anode wires will be initiated in the future after the procurement of the 5 mm straws.

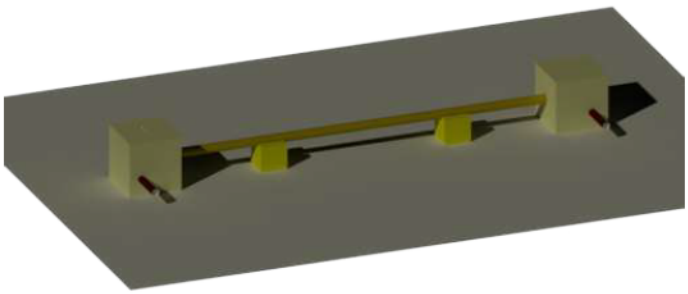

Figure 6.13: Prototype designed for a single straw tube study.

A prototype chamber, shown in Figure 6.15, has also been proposed with dimensions of 1.8 m $\times$ 50 cm.

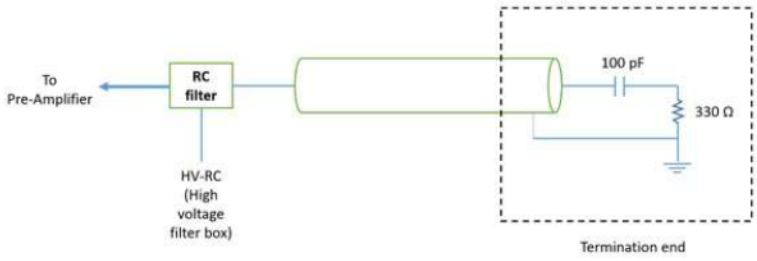

Figure 6.14: Simplified schematic circuit of one detector channel for the straw tube.

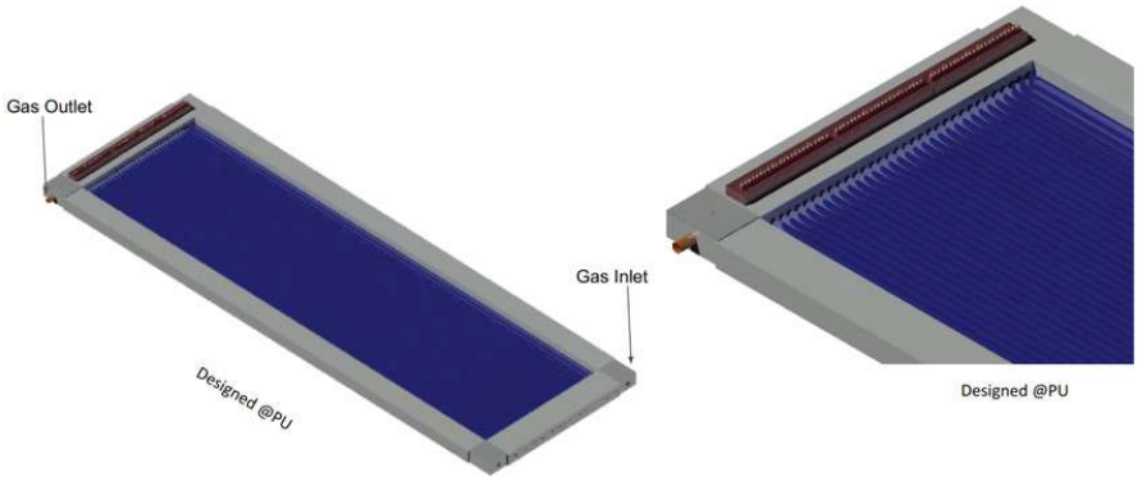

Figure 6.15: 3D CAD model of the proposed prototype straw tube chamber.

6.6 Simulation Studies with Garfield++

Garfield++ [72] is an object-oriented toolkit designed for the detailed simulation of particle detectors that utilize a gas mixture or semiconductor material as the sensitive medium. It builds upon many concepts and techniques from the Fortran-based program **Garfield**, which has been widely used for simulating gas-based detectors. Development of the C++ version began around 2011.

Primary Ionisation

The energy loss of relativistic charged particles is accurately described by the **PAI model** (Photo Absorption Ionisation). Garfield++ includes an interface with **Heed** (developed by I. Smirnov), which implements an extended version of this model. Heed simulates atomic relaxation and delta-electron transport, providing the coor-

dinates of all low-energy electrons and ions (or holes) produced along a particle's track.

Electric Fields

For devices composed of thin wires, planes, and tubes, Garfield++ includes pre-implemented two-dimensional analytic solutions (ported from the classic Garfield toolkit). For more complex geometries, such as **Micropattern Gas Detectors**, field maps calculated using external finite-element solvers like **Ansys**, **Elmer**, or **Comsol** can be imported for simulation.

The performance of a gaseous detector is strongly influenced by the choice of gas mixture, which can be optimized based on several factors:

- *Stability:* Resistance to unintended discharges.
- *Detection Efficiency and Amplification:* Ability to reliably detect and amplify signals.
- *Drift Velocity:* Tuned for either slow speeds (enhancing positional accuracy) or fast speeds (minimizing dead time).
- *Safety:* Use of non-flammable gases.
- *Low Diffusion:* Improves time and spatial resolution.
- *Durability:* Minimizing aging effects to extend the detector's operational lifespan.

The following plots illustrate the results from straw tube simulations performed using Garfield++. These simulations provide valuable insights into the behavior of gas mixtures and the impact of wire sag on detector performance.

In Figure 6.16, the drift velocity of electrons is shown for various Argon-based gas mixtures with different percentages of quencher gases. The 80:20 Ar/CO_2 mixture demonstrates a high drift velocity ($\sim$ 10 cm/μs), making it ideal for applications requiring rapid signal collection. The saturation of drift velocity at high electric

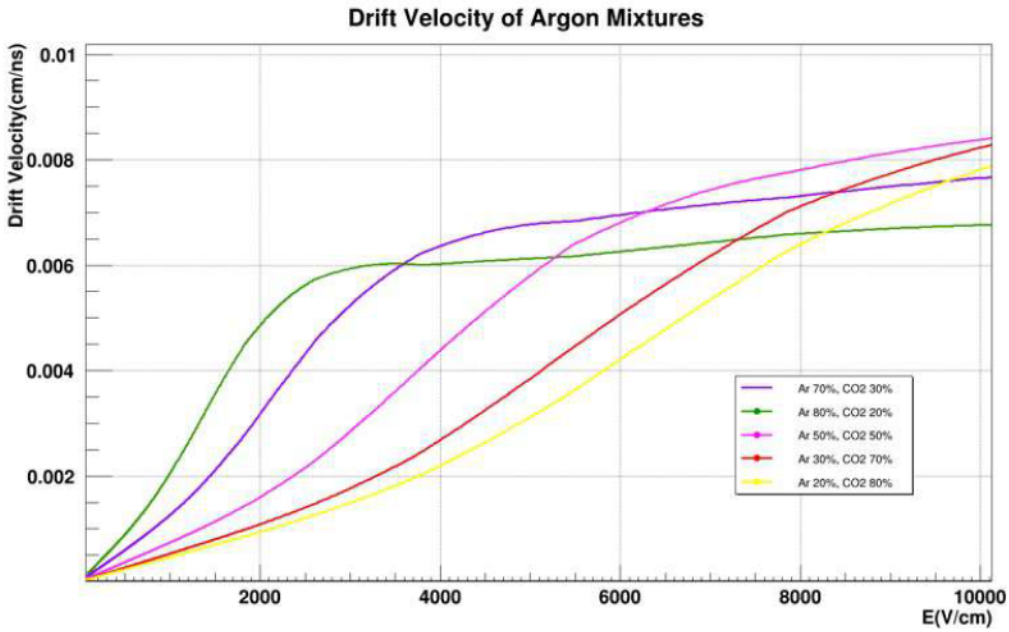

Figure 6.16: Drift velocity of Argon mixtures for different percentages.

field strengths further enhances its suitability for precise particle tracking.

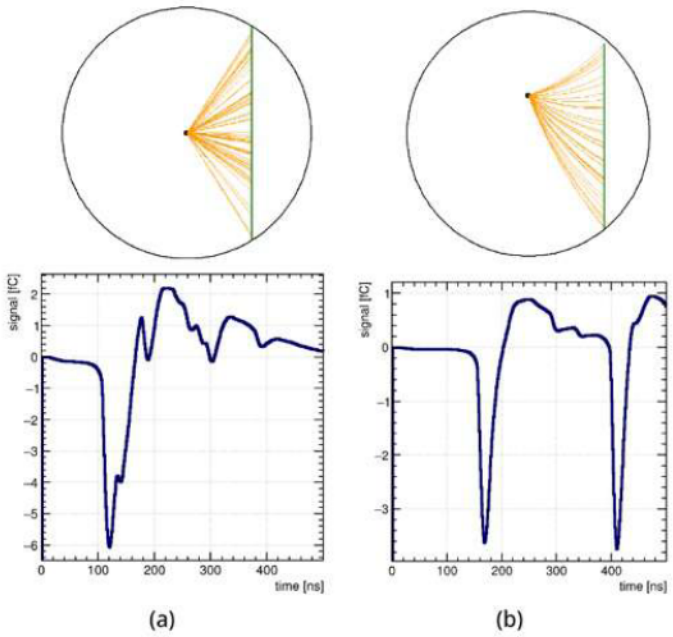

Figure 6.17: Signal from a straw tube with a 10mm diameter for a 170 GeV muon, comparing (i) no wire sag and (ii) 1.5 mm wire sag from the center.

Figure 6.17 compares the signal output of a straw tube detector for two cases: one

with no wire sag and the other with a 1.5 mm sag at the center of the wire due to gravitational effects. Wire sag significantly distorts the electric field ($\vec{E}$), altering the trajectory of electrons and ions and leading to a degradation in signal quality. These effects emphasize the need for meticulous wire tensioning to ensure optimal detector performance.

Conclusions

The studies highlight the following key points:

- For tracking and triggering applications requiring high electric fields ($\vec{E}$), the 80:20 Ar/CO_2 gas mixture is ideal due to its high drift velocity and saturation properties.
- Gravitational wire sag introduces distortions in the electric field and the paths of electrons and ions, adversely affecting signal quality and track reconstruction accuracy.

Future work will focus on:

1. Conducting gas leak tests using an 80:20 Ar/CO_2 mixture to evaluate its containment and stability.
2. Studying the transport properties of various gas mixtures to identify alternatives or improvements.
3. Developing methods to precisely estimate and mitigate wire sag to enhance track reconstruction accuracy.

These studies on the Straw Tube Tracker not only contribute to the development of precision tracking for neutrino interactions but also support broader detector advancements in high-energy physics experiments. The insights gained from these efforts help refine experimental techniques and improve data quality for future neutrino experiments.

The next chapter summarizes the key findings of this thesis, highlighting the advancements in neutrino flux determination, detector development, and optimiza-

tion techniques that contribute to reducing uncertainties in long-baseline neutrino experiments.

Chapter 7

Summary and Conclusions

7.1 Summary

This thesis presents a comprehensive study of neutrino flux determination and the reduction of related uncertainties. Accurate flux predictions are crucial for the success of long-baseline neutrino experiments, as uncertainties in the flux significantly impact the measurements and interpretation of neutrino interactions. These uncertainties are primarily driven by hadronic interactions, and reducing them would advance the physics goals of such experiments.

Neutrino physics, including neutrino interactions, oscillations, and mixing in two- and three-flavor frameworks, is discussed in Chapter 1. It highlights the importance of precise neutrino flux determination and the role of direct hadron production measurements in reducing uncertainties. Additionally, it reviews past hadron production studies and outlines the structure of the thesis. The NOνA experiment, detailed in Chapter 2, includes a discussion on the NuMI beamline, its components, and the off-axis beam concept. It describes the NOνA detectors, including their scintillator-based design, wavelength-shifting fibers, and avalanche photodiodes. Furthermore, it highlights key contributions, such as the Near Detector refurbishment effort and the establishment of ROC-India.

NuMI beam simulations for the NOνA experiment, covering on-axis and off-

axis spectra, beam transport uncertainties, and comparisons between old and new Geant4 flux simulations are described in Chapter 3. It also presents flux studies using virtual detectors downstream of the target and Horn 1, analyzing the impact of detector plane positions on flux, including horn-on and horn-off configurations. Additionally, transverse momentum and energy distributions at various detector positions are examined. A new branch, main_h1TrackingPlane, was developed for these studies.

Improving flux precision through direct hadron production measurements, with a focus on the EMPHATIC experiment, enhances hadron production data for better flux predictions, as detailed in Chapter 4. A detailed study of the EMPHATIC Halbach array magnet, modeled using COMSOL, is presented in Chapter 5. A numerical framework was established to simulate and compare the magnetic field with measurements, defining fit parameters, refining model hierarchies, and optimizing for the best-fit field representation. A total of 147 parameters were fitted to the mapped data, producing a high-resolution 1 mm field map.

In chapter 6 we discuss a future experiment DUNE where the detectors are being tailored for better flux handling and this can be done by developing systems like Straw Tube Trackers (STTs) for the System for on-Axis Neutrino Detection (SAND), a Near Detector in the Deep Underground Neutrino Experiment (DUNE) at Fermilab. This chapter covers the assembly and characterization efforts at Panjab University as part of the DUNE-India-ND collaboration. Key topics include the fabrication of straw tubes, prototype module design, gas leak tests, and performance characterization. Additionally, simulation studies using GARFIELD++ being conducted to optimize detector performance with different gas mixtures were discussed.

Thus, the work described in this thesis focuses on reducing flux uncertainties in accelerator-based neutrino experiments like NOνA, which is actively collecting data. Additionally, hadron production experiments like EMPHATIC aim to reduce systematics arising from secondary particle production, benefiting NOνA as well as

other similar present and future experiments.

7.2 Conclusions

This thesis has focused on reducing uncertainties in accelerator-based neutrino experiments through simulation studies, hardware contributions, and detector development. The key findings and their implications are summarized below.

Simulation studies on horn position misalignment in the NOνA experiment demonstrated that a misalignment of horn 1 by ± 3 mm can lead to significant flux shifts, with a maximum discrepancy of approximately 11% at ~ 4 GeV. These results highlight the importance of precise horn alignment in minimizing systematic uncertainties in neutrino flux predictions.

Further investigations into flux discrepancies between older and newer versions of simulations revealed notable differences in the off-axis configurations for both neutrino and antineutrino fluxes. In the Reverse Horn Current (RHC) mode, a maximum discrepancy of 10% was observed in the off-axis antineutrino flux, while the Forward Horn Current (FHC) mode exhibited a 5% discrepancy in the neutrino flux. These discrepancies were found to be closely related to variations in the parent pion flux, emphasizing the need for improved hadron production modeling. The results are crucial for any experiment utilizing the NuMI beamline, including NOνA and future efforts such as EMPHATIC, as they inform detector placement and enhance the accuracy of flux predictions.

A major outcome of this work is the improved fitted magnetic field model, which significantly reduced discrepancies in the data. Edge-region discrepancies decreased from approximately 21% to 6%, while central-axis discrepancies were reduced from 12% to 1%. Additionally, the interpolated field map, now refined to 1 mm resolution and extended beyond measured regions, provides a more precise representation of the magnetic field. These improvements enhance tracking precision, momentum resolution and detector acceptance, directly benefiting experiments like EMPHATIC.

On the hardware front, contributions to the NOνA Near Detector (ND) refurbishment have extended the detector's operational lifespan and improved data quality. The replacement of baked avalanche photodiodes in the underground detector ensures continued functionality. Additionally, the establishment of the Remote Operations Center (ROC) at Panjab University marks a significant milestone, enabling 24/7 data acquisition and supporting global collaboration in NOνA.

As part of the DUNE-India collaboration, this thesis has contributed to the development of the Straw Tube Tracker (STT) prototype for the DUNE SAND detector. Simulation studies using Garfield++ identified the 80/20 Ar/CO_2 gas mixture as the most suitable for tracking.

Overall, the findings presented in this thesis contribute to improving the precision of neutrino flux predictions, enhancing detector performance, and supporting the development of next-generation neutrino experiments. These advancements will play a crucial role in reducing systematic uncertainties in long-baseline neutrino oscillation studies and hadron production experiments, paving the way for more accurate and reliable measurements in the field of neutrino physics.

Looking forward, the continued advancements in detector technologies and simulation frameworks as discussed in the thesis will play a pivotal role in reducing uncertainties in flux modeling. The analysis of particle recordings at virtual detector positions downstream of Horn 1 will aid present and future NuMI beamline experiments in optimizing detector placement, enhancing experimental efficiency, and reducing uncertainties in neutrino flux predictions. The high-resolution 1 mm magnetic field map for the Phase 1 Halbach array magnet will be extended to the similarly designed Phase 2 magnet, ensuring ongoing improvements in magnetic field mapping for future EMPHATIC phases. The establishment of the Remote Operations Center (ROC) at Panjab University serves as a model for effective remote monitoring and control, offering valuable guidance for future long-baseline neutrino experiments and lessons to inform strategies for detector maintenance, operational efficiency, and remote data acquisition. Finally, the ongoing efforts in the

future DUNE experiment—particularly through the development of the Straw Tube Tracker—will further refine particle tracking technologies. These advancements are expected to significantly improve event reconstruction capabilities in the DUNE, ultimately enhancing the experiment's sensitivity and precision in studying neutrino interactions.

APPENDIX A

Supplementary material for Chapter 3

A.1 Code Development: main h1TrackingPlane branch

To checkout the code, checkout the branch `main_h1TrackingPlane` out of the main branch of g4numi. This is the link to the branch:
`https://cdcvs.fnal.gov/redmine/projects/numi-beam-sim/repository/g4numi?rev=main_h1TrackingPlane`

There are two files:
`build_instructions.txt` and `README_h1trackingplane.md`

The `build_instructions.txt` contains necessary instructions to build the branch, and the `README_h1trackingplane.md` file contains instructions to run the code and produce the output file containing the h1trackingPlane data TTree. Please note that this branch of g4numi also records electrons, positrons, and gammas, which are otherwise not recorded in the main g4numi branch. These are important

for background studies.

A.1.1 Source Code Modifications

The main changes made in each of the source codes are as follows:

- **NumiDetectorConstruction.cc/hh**: The tracking plane construction is implemented here. The function `ConstructNumiHorn1TrackingPlane` is written in this script to construct the tracking plane. The thickness and area of the tracking plane can be modified in this function. The distance of the virtual detector can be adjusted by editing the variable `z`.
- **NumiSteppingAction.cc/hh**: The rules for storing particle information are set here. The function `CheckInTrackingDetectorH1Plane` is implemented in this script. The `G4Step` class is used to track the transition of particles from some volume to the tracking plane.
- **NumiAnalysis.cc/hh**: The function `FillH1Ntuple` is implemented here. A new TFile is created in which ntuples are filled and stored in a TTree. The parameters defined in the output TTree are:

Variable	**Description**
job	Job ID or event ID number
tvx, tvy, tvz	Recorded particle vertices at the plane
tpx, tpy, tpz	Particle momenta at the plane
tptype	Particle Type
ppvx, ppvy, ppvz	Particle production vertices where recorded particles are originally created

Figure 1: The structure of the output TTree

A.2 Flux and Momentum Plots

- Plots showing flux and longitudinal vs. transverse momenta for:
  - Charged particles
  - Neutral particles
  - Backgrounds (electrons, positrons, and gammas)
- Plots are provided for the following configurations:
  - Horn-off
  - Horn-on

A.3 Horn Off Configuration

A.3.1 Flux

Positive Particles, Negative Particles, Neutral Particles (Neutron, π^0, K_L^0, K_S^0)

(Up to down: 18cm, 50 cm,100 cm , 150 cm and 200 cm from Horn 1)

(Left to Right:Positive Particles, Negative Particles, Neutral Particles)

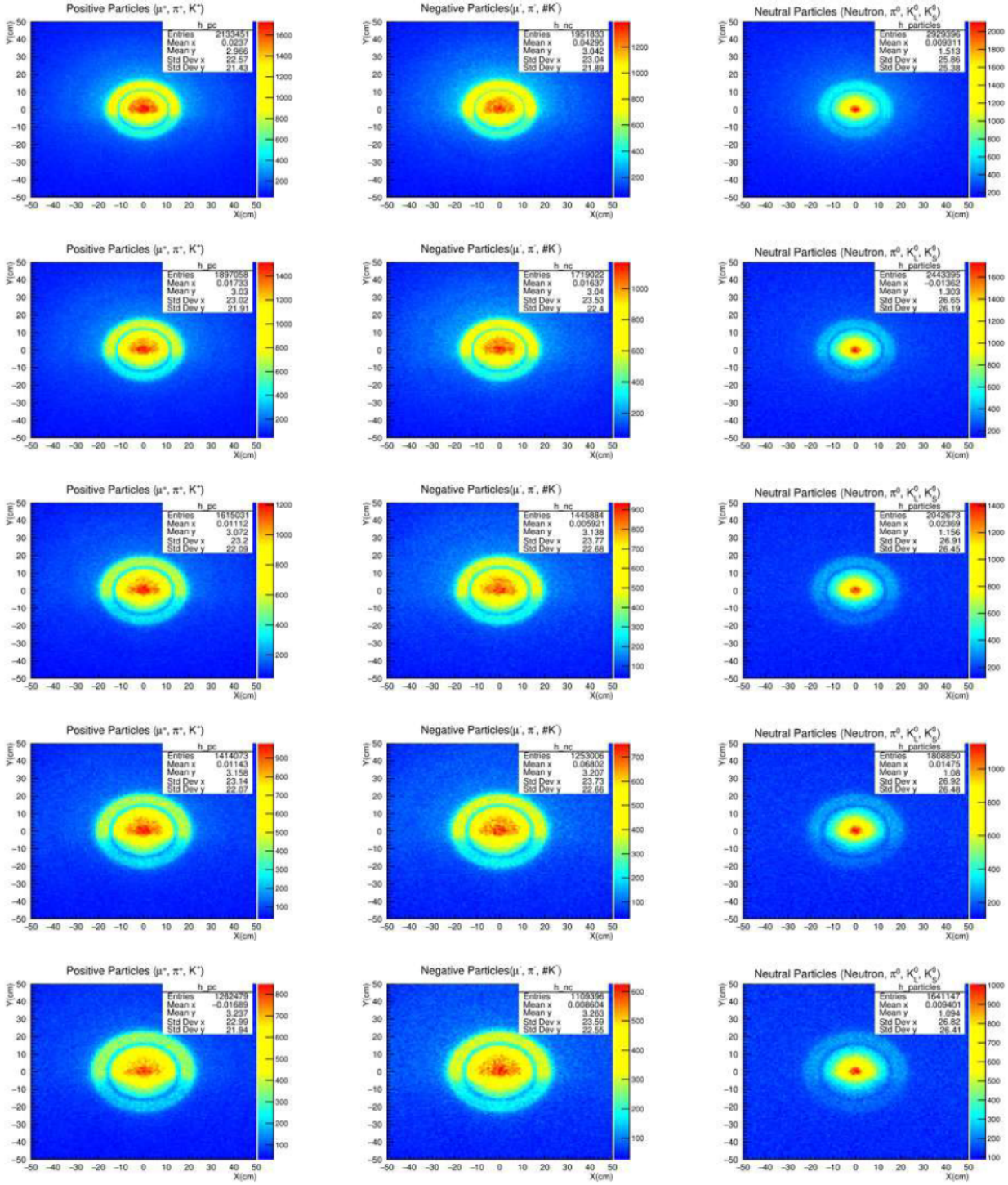

Backgrounds(Electrons, Positrons and Gammas)

(Up to down: 18cm, 50 cm,100 cm , 150 cm and 200 cm from Horn 1)

(Left to Right: Electrons, Positrons and Gammas)

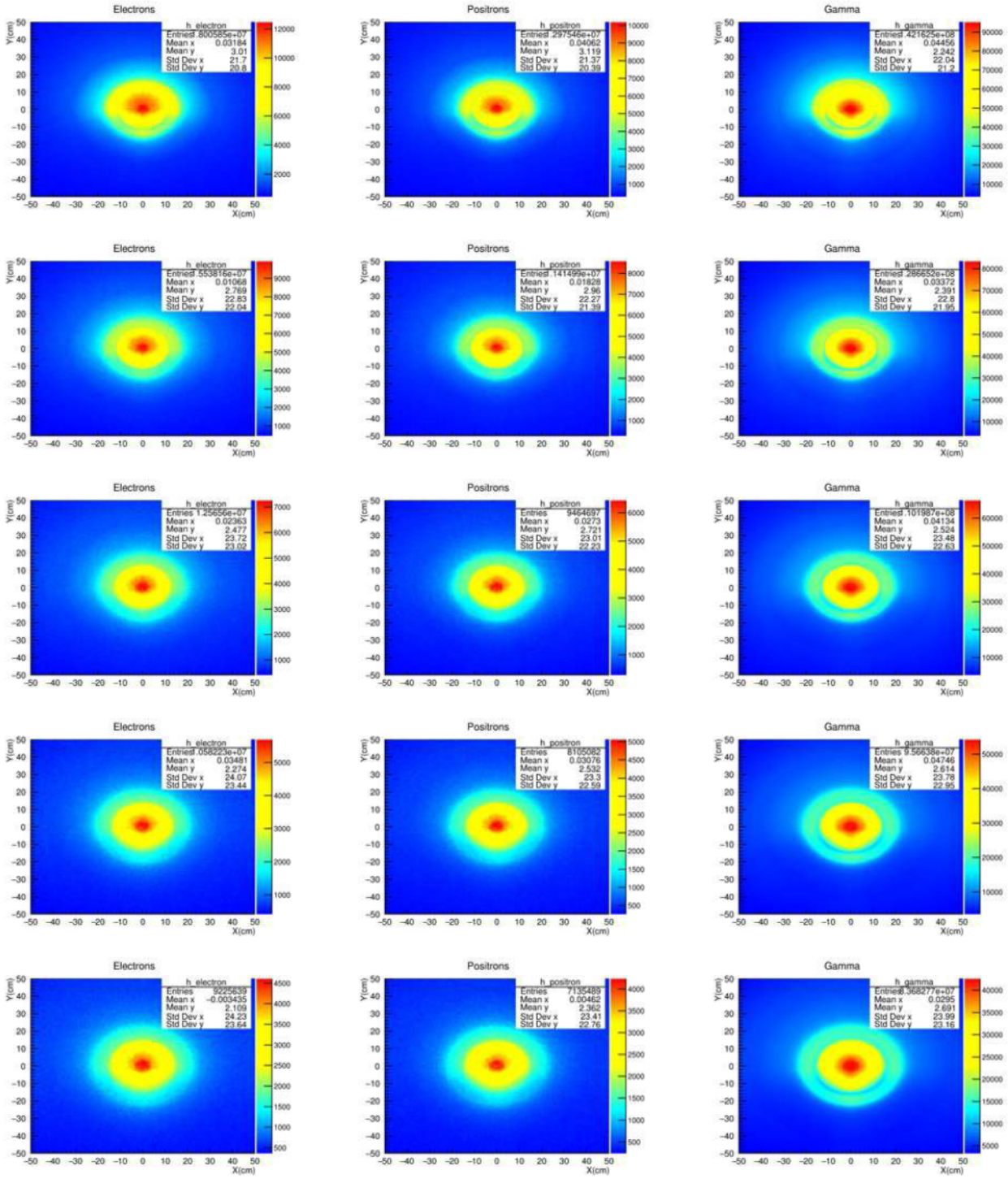

A.3.2 Longitudnal v/s Transverse Momenta

Positive Particles, Negative Particles , Neutral Particles

(Up to down: 18cm, 50 cm,100 cm , 150 cm and 200 cm from Horn 1)

(Left to Right: Positive Particles, Negative Particles , Neutral Particles)

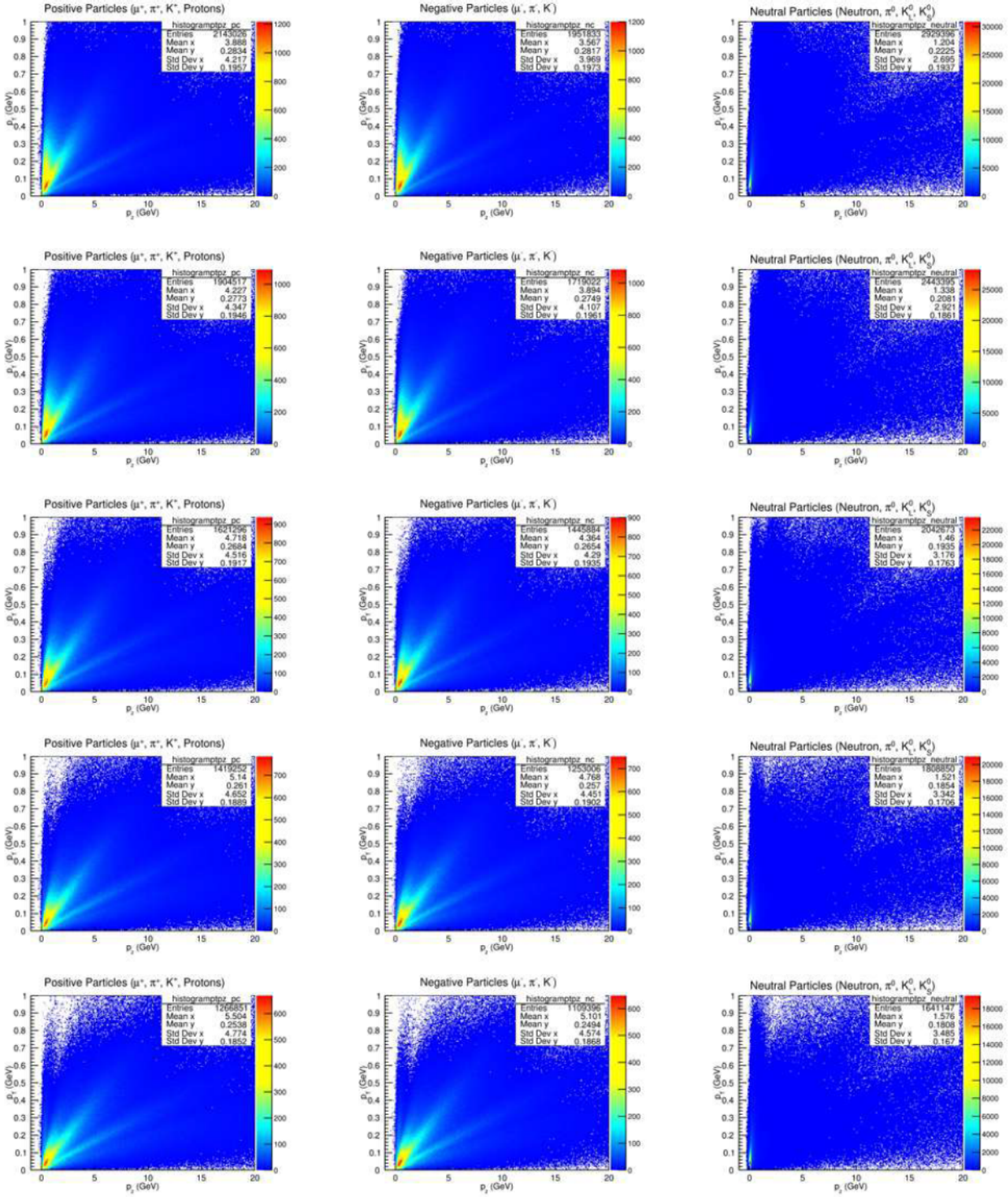

Backgrounds(Electrons, Positrons and Gammas)

(Up to down: 18cm, 50 cm,100 cm , 150 cm and 200 cm from Horn 1)

(Left to Right: Backgrounds(Electrons, Positrons and Gammas))

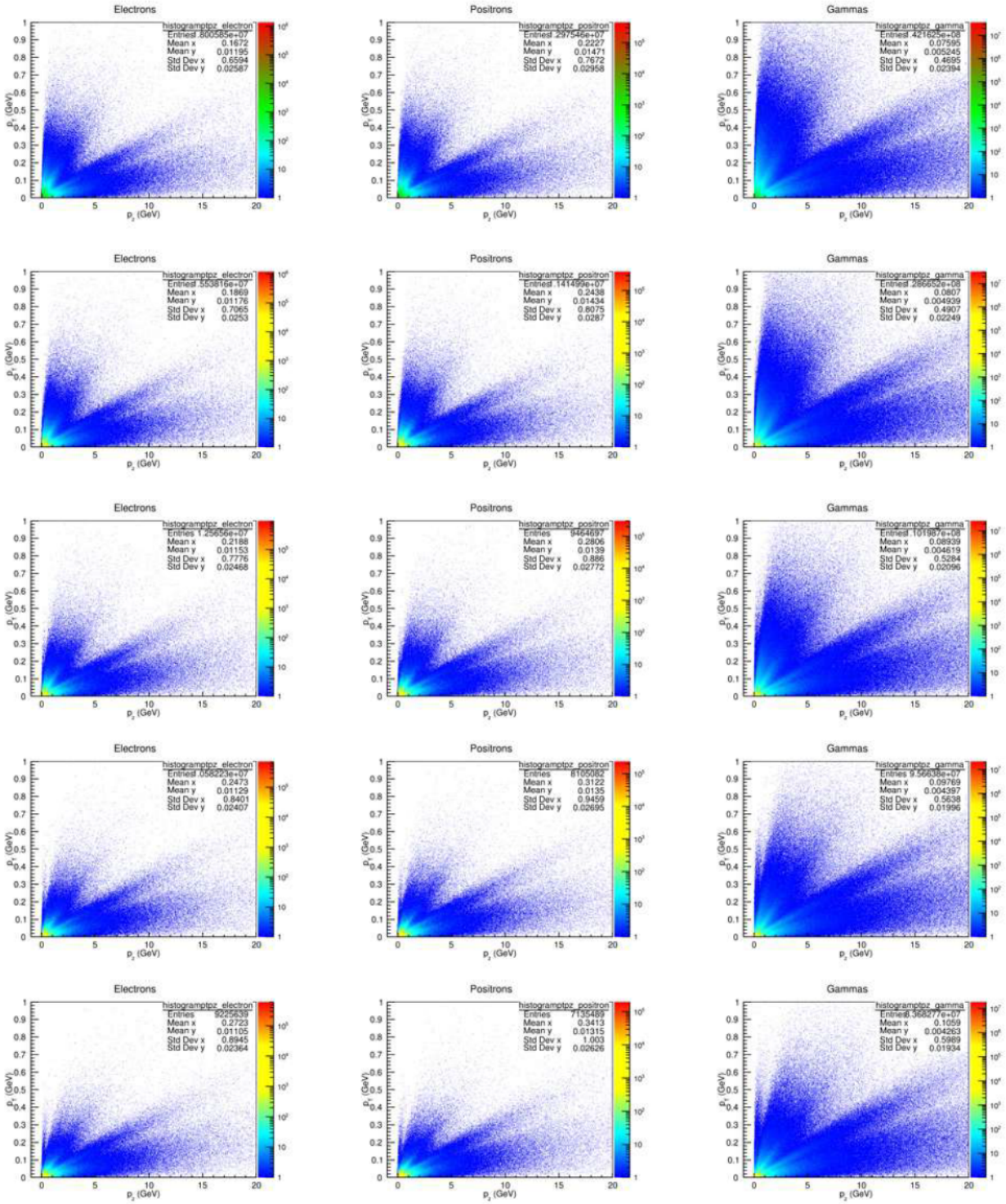

A.4 Horn On Configuration

A.4.1 Flux

Positive Particles, Negative Particles, Neutral Particles (Neutron, π^0, K^0_L, K^0_S)

(Up to down: 18cm, 50 cm 100 cm , 150 cm and 200 cm from Horn 1)

(Left to Right: Positive Particles, Negative Particles, Neutral Particles)

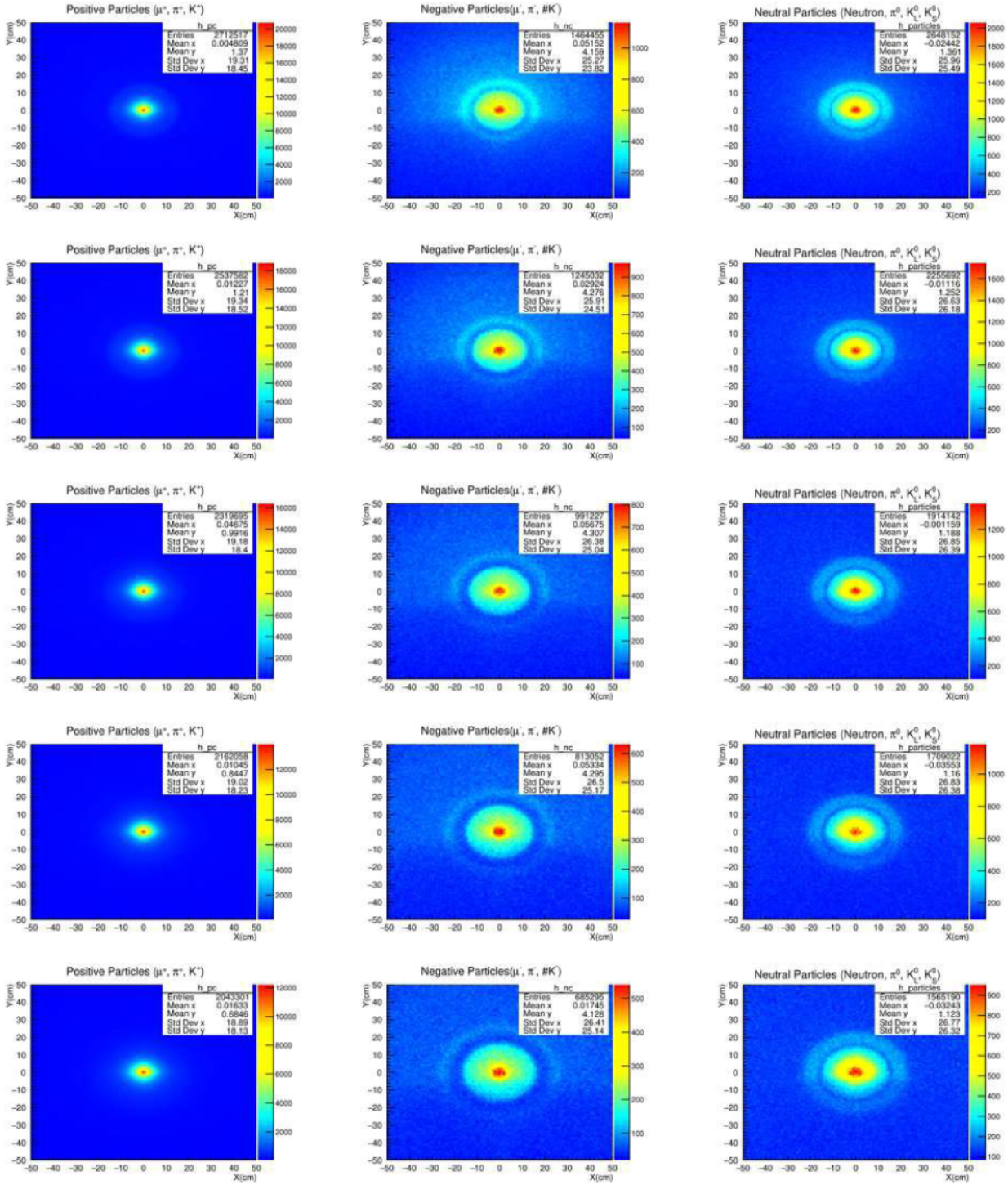

Backgrounds (Electrons, Positrons and Gammas)

(Up to down: 18cm, 50 cm 100 cm , 150 cm and 200 cm from Horn 1)

(Left to Right: Electrons, Positrons and Gammas)

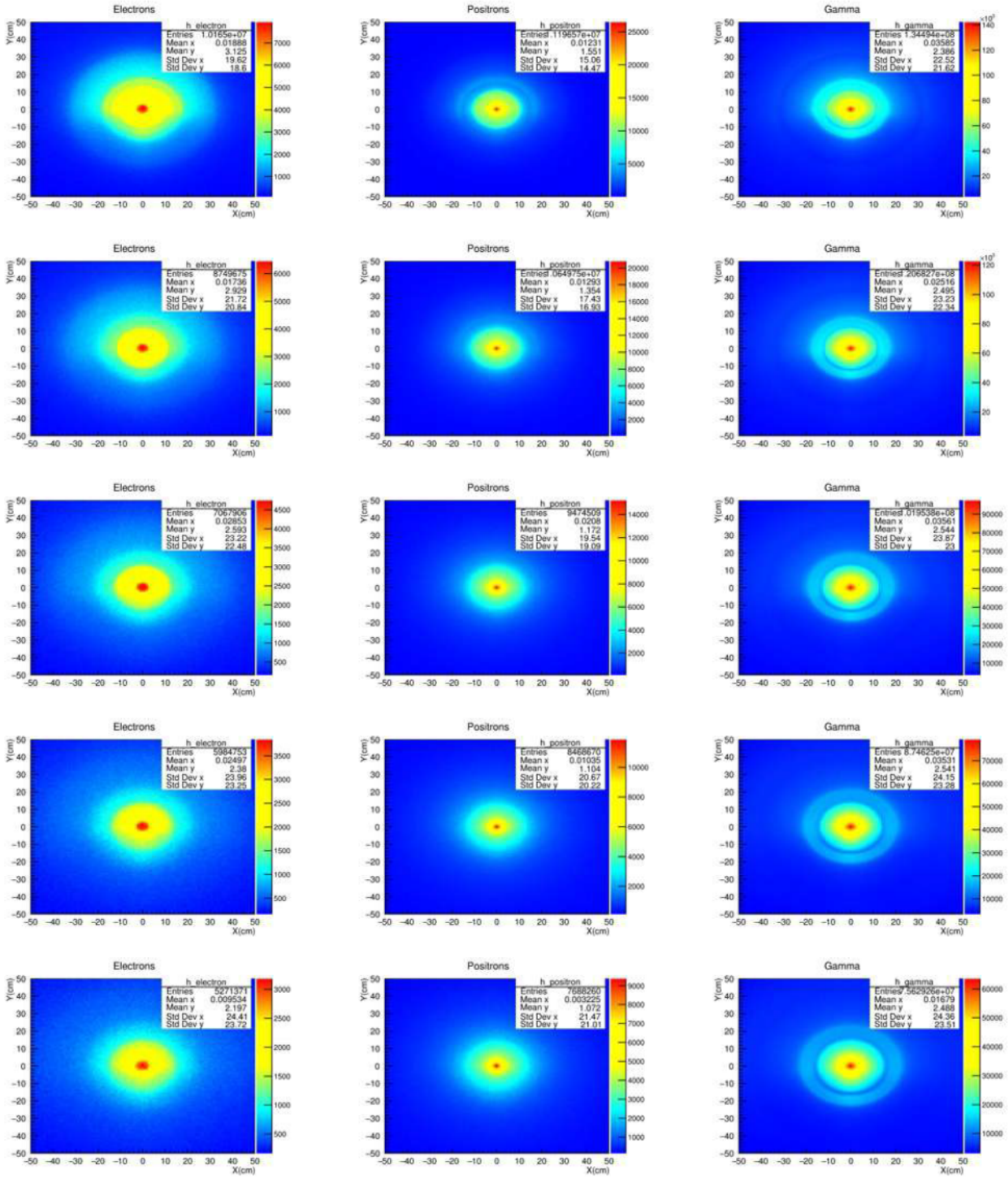

A.4.2 Longitudnal v/s Transverse Momenta

Positive Particles, Negative Particles , Neutral Particles

(Up to down: 18cm, 50 cm,100 cm , 150 cm and 200 cm from Horn 1)

(Left to Right: Positive Particles, Negative Particles , Neutral Particles)

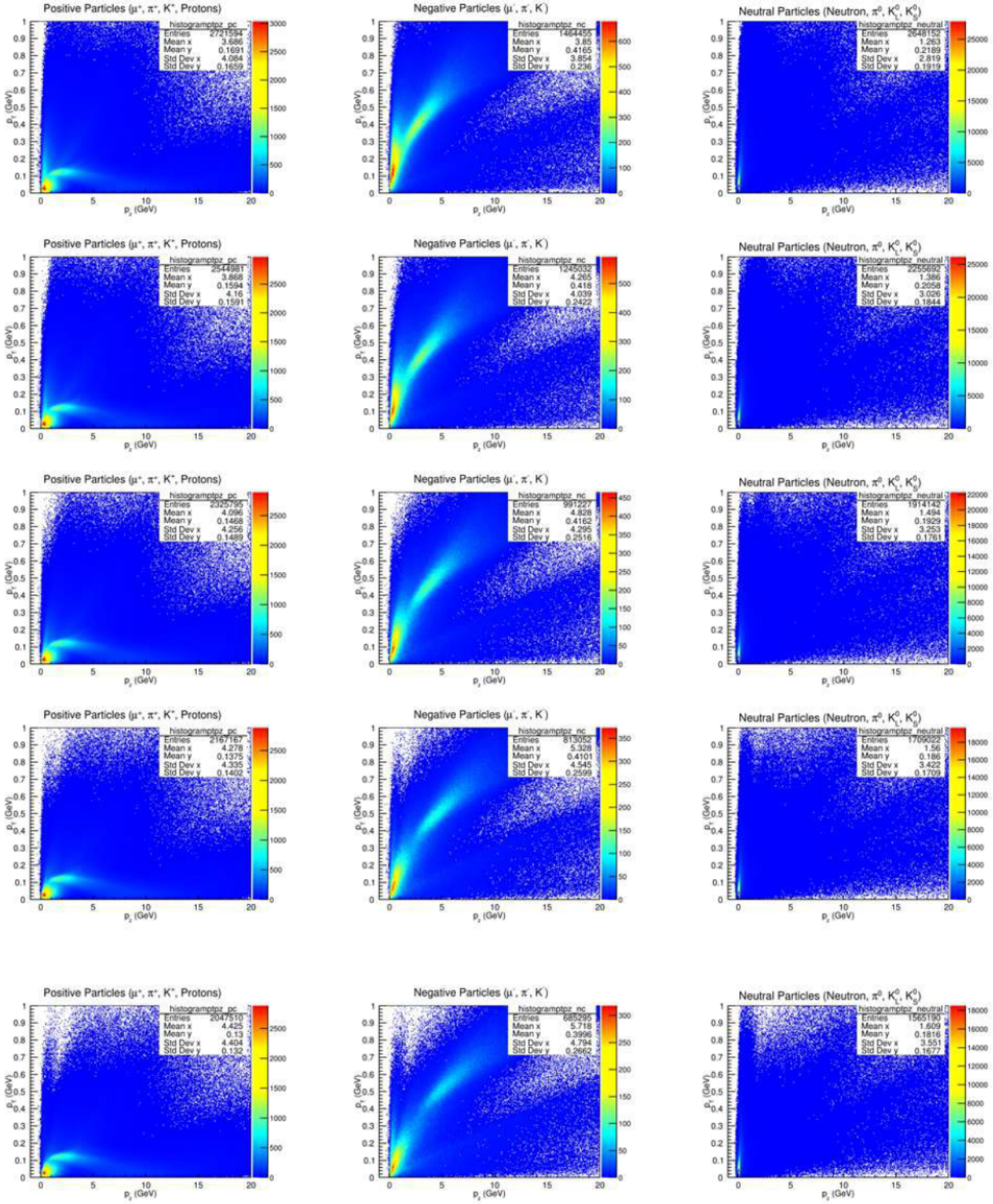

Backgrounds(Electrons, Positrons and Gammas)

(Up to down: 18cm, 50 cm, 100 cm , 150 cm and 200 cm from Horn 1)

(Left to Right: Backgrounds(Electrons, Positrons and Gammas))

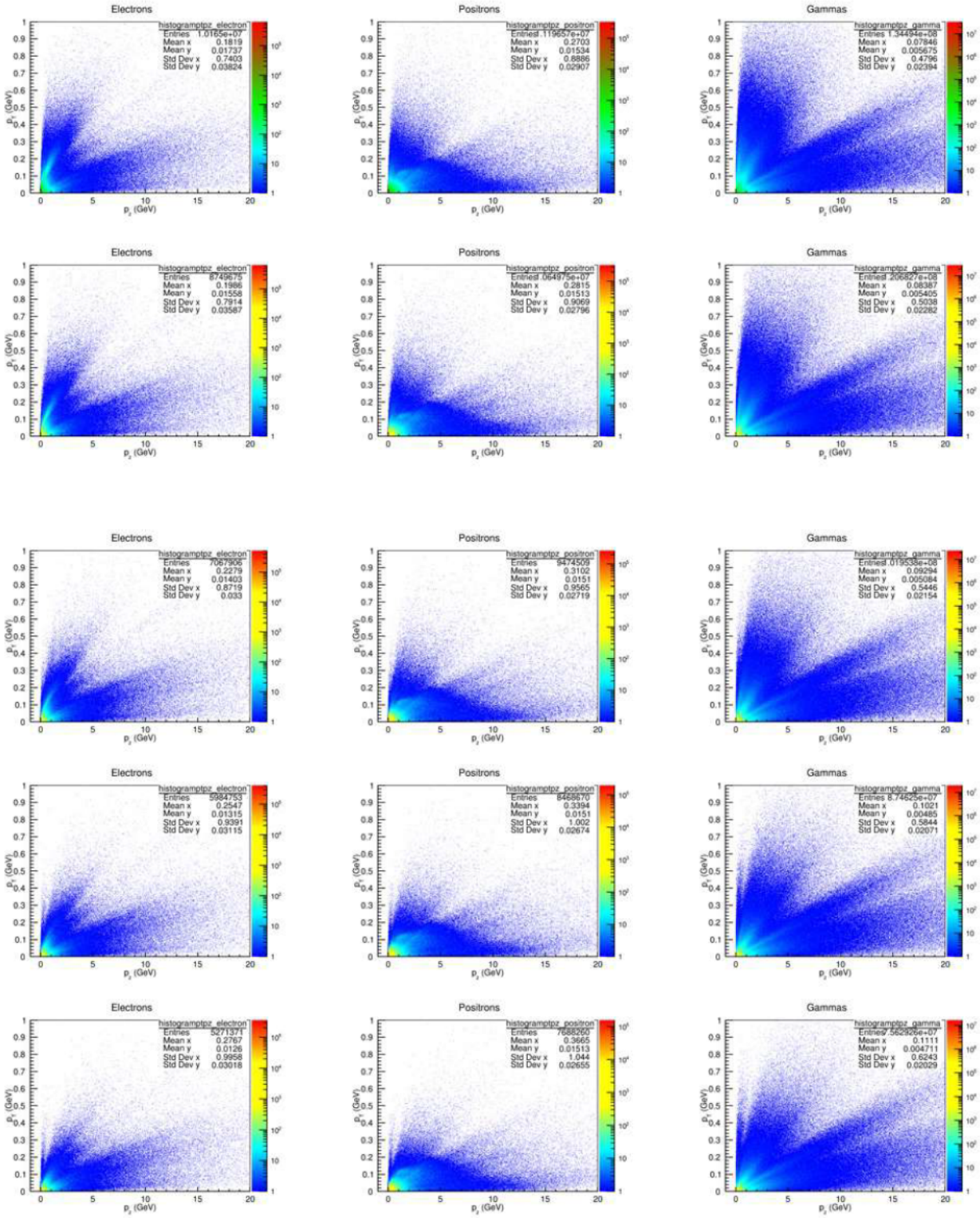

Appendix B

Supplementary material for Chapter 5

B.1 Parameter Naming and Organization

Naming Convention: For instance, the parameter name `$ex_0Deg_layer1_1$` specifies the following:

- `ex`: The magnetization component in the x direction.
- `0Deg`: The magnetization angle for this component.
- `layer1`: The layer within the magnet (layer 1, layer 2, or layer 3).
- `1`: The index, distinguishing it from other components in the same direction and layer, incrementing up to 144.

Parameter Changes: As we go through Table 1, the names follow a pattern where the component (`ex`, `ey`, `ez`), layer (`layer1`, `layer2`, `layer3`), and component numbers vary, covering all necessary directions and layers for the array.

Parameter name	Value	Parameter name	Value	Parameter name	Value
ex_0Deg_layer1_1	1.44	ey_0Deg_layer1_2	0	ez_0Deg_layer1_3	0
ex_45Deg_layer1_4	1.018233765	ey_45Deg_layer1_5	1.018233765	ez_45Deg_layer1_6	0
ex_90Deg_layer1_7	0	ey_90Deg_layer1_8	1.44	ez_90Deg_layer1_9	0
ex_135Deg_layer1_10	-1.018233765	ey_135Deg_layer1_11	1.018233765	ez_135Deg_layer1_12	0
ex_180Deg_layer1_13	-1.44	ey_180Deg_layer1_14	0	ez_180Deg_layer1_15	0
ex_225Deg_layer1_16	-1.018233765	ey_225Deg_layer1_17	-1.018233765	ez_225Deg_layer1_18	0
ex_270Deg_layer1_19	0	ey_270Deg_layer1_20	-1.44	ez_270Deg_layer1_21	0
ex_315Deg_layer1_22	1.018233765	ey_315Deg_layer1_23	-1.018233765	ez_315Deg_layer1_24	0
ex_0Deg_layer2_25	1.44	ey_0Deg_layer2_26	0	ez_0Deg_layer2_27	0
ex_45Deg_layer2_28	1.018233765	ey_45Deg_layer2_29	1.018233765	ez_45Deg_layer2_30	0
ex_90Deg_layer2_31	0	ey_90Deg_layer2_32	1.44	ez_90Deg_layer2_33	0
ex_135Deg_layer2_34	-1.018233765	ey_135Deg_layer2_35	1.018233765	ez_135Deg_layer2_36	0
ex_180Deg_layer2_37	-1.44	ey_180Deg_layer2_38	0	ez_180Deg_layer2_39	0
ex_225Deg_layer2_40	-1.018233765	ey_225Deg_layer2_41	-1.018233765	ez_225Deg_layer2_42	0
ex_270Deg_layer2_43	0	ey_270Deg_layer2_44	-1.44	ez_270Deg_layer2_45	0
ex_315Deg_layer2_46	1.018233765	ey_315Deg_layer2_47	-1.018233765	ez_315Deg_layer2_48	0
ex_0Deg_layer3_49	1.44	ey_0Deg_layer3_50	0	ez_0Deg_layer3_51	0
ex_45Deg_layer3_52	1.018233765	ey_45Deg_layer3_53	1.018233765	ez_45Deg_layer3_54	0
ex_90Deg_layer3_55	0	ey_90Deg_layer3_56	1.44	ez_90Deg_layer3_57	0
ex_135Deg_layer3_58	-1.018233765	ey_135Deg_layer3_59	1.018233765	ez_135Deg_layer3_60	0
ex_180Deg_layer3_61	-1.44	ey_180Deg_layer3_62	0	ez_180Deg_layer3_63	0
ex_225Deg_layer3_64	-1.018233765	ey_225Deg_layer3_65	-1.018233765	ez_225Deg_layer3_66	0
ex_270Deg_layer3_67	0	ey_270Deg_layer3_68	-1.44	ez_270Deg_layer3_69	0
ex_315Deg_layer3_70	1.018233765	ey_315Deg_layer3_71	-1.018233765	ez_315Deg_layer3_72	0
ex_0Deg_layer4_73	1.44	ey_0Deg_layer4_74	0	ez_0Deg_layer4_75	0
ex_45Deg_layer4_76	1.018233765	ey_45Deg_layer4_77	1.018233765	ez_45Deg_layer4_78	0
ex_90Deg_layer4_79	0	ey_90Deg_layer4_80	1.44	ez_90Deg_layer4_81	0
ex_135Deg_layer4_82	-1.018233765	ey_135Deg_layer4_83	1.018233765	ez_135Deg_layer4_84	0
ex_180Deg_layer4_85	-1.44	ey_180Deg_layer4_86	0	ez_180Deg_layer4_87	0
ex_225Deg_layer4_88	-1.018233765	ey_225Deg_layer4_89	-1.018233765	ez_225Deg_layer4_90	0
ex_270Deg_layer4_91	0	ey_270Deg_layer4_92	-1.44	ez_270Deg_layer4_93	0
ex_315Deg_layer4_94	1.018233765	ey_315Deg_layer4_95	-1.018233765	ez_315Deg_layer4_96	0
ex_0Deg_layer5_97	1.44	ey_0Deg_layer5_98	0	ez_0Deg_layer5_99	0
ex_45Deg_layer5_100	1.018233765	ey_45Deg_layer5_101	1.018233765	ez_45Deg_layer5_102	0
ex_90Deg_layer5_103	0	ey_90Deg_layer5_104	1.44	ez_90Deg_layer5_105	0
ex_135Deg_layer5_106	-1.018233765	ey_135Deg_layer5_107	1.018233765	ez_135Deg_layer5_108	0
ex_180Deg_layer5_109	-1.44	ey_180Deg_layer5_110	0	ez_180Deg_layer5_111	0
ex_225Deg_layer5_112	-1.018233765	ey_225Deg_layer5_113	-1.018233765	ez_225Deg_layer5_114	0
ex_270Deg_layer5_115	0	ey_270Deg_layer5_116	-1.44	ez_270Deg_layer5_117	0
ex_315Deg_layer5_118	1.018233765	ey_315Deg_layer5_119	-1.018233765	ez_315Deg_layer5_120	0
ex_0Deg_layer6_121	1.44	ey_0Deg_layer6_122	0	ez_0Deg_layer6_123	0
ex_45Deg_layer6_124	1.018233765	ey_45Deg_layer6_125	1.018233765	ez_45Deg_layer6_126	0
ex_90Deg_layer6_127	0	ey_90Deg_layer6_128	1.44	ez_90Deg_layer6_129	0
ex_135Deg_layer6_130	-1.018233765	ey_135Deg_layer6_131	1.018233765	ez_135Deg_layer6_132	0
ex_180Deg_layer6_133	-1.44	ey_180Deg_layer6_134	0	ez_180Deg_layer6_135	0
ex_225Deg_layer6_136	-1.018233765	ey_225Deg_layer6_137	-1.018233765	ez_225Deg_layer6_138	0
ex_270Deg_layer6_139	0	ey_270Deg_layer6_140	-1.44	ez_270Deg_layer6_141	0
ex_315Deg_layer6_142	1.018233765	ey_315Deg_layer6_143	-1.018233765	ez_315Deg_layer6_144	0
x_o	0	y_o	0	z_o	80

Table 1: Table of initial ex, ey, ez components at different angles and layers as defined in the COMSOL Model

B.2 Batch Mode Execution

Batch mode in COMSOL is particularly useful for automated simulations or parameter sweeps across multiple configurations. To submit a job in batch mode, the command format is as follows:

B.1 COMSOL Batch Mode Command

```
comsol batch -inputfile full/path/to/input/mph/model/file.mph
-paramfile full/path/to/parameters/file.dat -nosave -study std1
-batchlog full/path/to/output/log/file.txt
```

The input parameter file should follow a specific format:

- The first row should contain parameter names separated by spaces.
- The second row should contain the corresponding values separated by spaces.

For example, a file defining 144 parameters would consist of two rows and 144 columns, with the first row for parameter names and the second for their values.

B.3 χ^2 Calculation Code

Below is a code snippet that demonstrates the implementation of the χ^2 calculation:

B.2 Code Snippet: χ^2 Calculation

```
double chi2 = 0.0;
// Precompute 1/sigma^2
const double inv_sigma_squared = 1.0 / (0.01 * 0.01);

for (int iEntry = 0; iEntry < dataTree->GetEntries(); ++iEntry) {
    dataTree->GetEntry(iEntry);
    predictionsTree->GetEntry(iEntry);

    double residual_bx = bxData - bxPredictions;
    double residual_by = byData - byPredictions;
    double residual_bz = bzData - bzPredictions;

    chi2 += (residual_bx * residual_bx +
             residual_by * residual_by +
             residual_bz * residual_bz) * inv_sigma_squared;
}
```

B.4 Final Fit Parameters

Parameter	Value	Parameter	Value	Parameter	Value
ex_0Deg_layer1_1	1.42989	ey_0Deg_layer1_2	0.175869	ez_0Deg_layer1_3	0.115
ex_45Deg_layer1_4	1.01189	ey_45Deg_layer1_5	0.971727	ez_45Deg_layer1_6	-0.05
ex_90Deg_layer1_7	0.187181	ey_90Deg_layer1_8	1.29139	ez_90Deg_layer1_9	-0.115
ex_135Deg_layer1_10	-1.1974	ey_135Deg_layer1_11	0.849772	ez_135Deg_layer1_12	0.045
ex_180Deg_layer1_13	-1.43171	ey_180Deg_layer1_14	0.320632	ez_180Deg_layer1_15	0.165
ex_225Deg_layer1_16	-0.809285	ey_225Deg_layer1_17	-1.12375	ez_225Deg_layer1_18	-0.005
ex_270Deg_layer1_19	0.160998	ey_270Deg_layer1_20	-1.72174	ez_270Deg_layer1_21	0.06
ex_315Deg_layer1_22	0.93248	ey_315Deg_layer1_23	-1.35569	ez_315Deg_layer1_24	1.73E-18
ex_0Deg_layer1_25	1.3519	ey_0Deg_layer1_26	0.00473318	ez_0Deg_layer1_27	0.115
ex_45Deg_layer1_28	0.921345	ey_45Deg_layer1_29	1.06765	ez_45Deg_layer1_30	0.235005
ex_90Deg_layer1_31	0.0058654	ey_90Deg_layer1_32	1.48406	ez_90Deg_layer1_33	0.140005
ex_135Deg_layer1_34	-1.01073	ey_135Deg_layer1_35	0.957599	ez_135Deg_layer1_36	0.035
ex_180Deg_layer1_37	-1.36238	ey_180Deg_layer1_38	0.027321	ez_180Deg_layer1_39	-0.015
ex_225Deg_layer1_40	-1.02423	ey_225Deg_layer1_41	-1.30513	ez_225Deg_layer1_42	-0.0865005
ex_270Deg_layer1_43	-0.0975102	ey_270Deg_layer1_44	-1.631	ez_270Deg_layer1_45	0.075
ex_315Deg_layer1_46	1.10023	ey_315Deg_layer1_47	-1.30059	ez_315Deg_layer1_48	0.105
ex_0Deg_layer2_49	1.65565	ey_0Deg_layer2_50	-0.307532	ez_0Deg_layer2_51	-0.175
ex_45Deg_layer2_52	1.0348	ey_45Deg_layer2_53	0.876087	ez_45Deg_layer2_54	0.08
ex_90Deg_layer2_55	0.234388	ey_90Deg_layer2_56	1.45809	ez_90Deg_layer2_57	0.12
ex_135Deg_layer2_58	-0.889016	ey_135Deg_layer2_59	0.949234	ez_135Deg_layer2_60	0.08
ex_180Deg_layer2_61	-1.352	ey_180Deg_layer2_62	-0.305612	ez_180Deg_layer2_63	-0.065
ex_225Deg_layer2_64	-1.01023	ey_225Deg_layer2_65	-0.934039	ez_225Deg_layer2_66	-0.02
ex_270Deg_layer2_67	0.0307472	ey_270Deg_layer2_68	-1.054	ez_270Deg_layer2_69	0.01
ex_315Deg_layer2_70	0.959036	ey_315Deg_layer2_71	-0.876234	ez_315Deg_layer2_72	0.085
ex_0Deg_layer2_73	1.5055	ey_0Deg_layer2_74	-0.102388	ez_0Deg_layer2_75	0.065
ex_45Deg_layer2_76	1.18489	ey_45Deg_layer2_77	0.972234	ez_45Deg_layer2_78	0.005
ex_90Deg_layer2_79	0.15	ey_90Deg_layer2_80	1.4415	ez_90Deg_layer2_81	-0.085
ex_135Deg_layer2_82	-0.654377	ey_135Deg_layer2_83	1.26075	ez_135Deg_layer2_84	-0.065
ex_180Deg_layer2_85	-1.35088	ey_180Deg_layer2_86	0.037888	ez_180Deg_layer2_87	-0.005
ex_225Deg_layer2_88	-0.56572	ey_225Deg_layer2_89	-0.702536	ez_225Deg_layer2_90	0.14
ex_270Deg_layer2_91	0.0796122	ey_270Deg_layer2_92	-0.869	ez_270Deg_layer2_93	0.025
ex_315Deg_layer2_94	1.13023	ey_315Deg_layer2_95	-0.717234	ez_315Deg_layer2_96	-0.035
ex_0Deg_layer3_97	1.69876	ey_0Deg_layer3_98	-0.517946	ez_0Deg_layer3_99	0.305
ex_45Deg_layer3_100	1.00999	ey_45Deg_layer3_101	0.981986	ez_45Deg_layer3_102	-0.275
ex_90Deg_layer3_103	0.17998	ey_90Deg_layer3_104	1.41212	ez_90Deg_layer3_105	-0.085
ex_135Deg_layer3_106	-0.826532	ey_135Deg_layer3_107	0.992479	ez_135Deg_layer3_108	-0.055
ex_180Deg_layer3_109	-1.17119	ey_180Deg_layer3_110	-0.120355	ez_180Deg_layer3_111	0.32
ex_225Deg_layer3_112	-0.536023	ey_225Deg_layer3_113	-1.14666	ez_225Deg_layer3_114	0.335
ex_270Deg_layer3_115	-0.117612	ey_270Deg_layer3_116	-0.959	ez_270Deg_layer3_117	-0.15
ex_315Deg_layer3_118	0.689424	ey_315Deg_layer3_119	-1.0223	ez_315Deg_layer3_120	-0.27
ex_0Deg_layer3_121	1.34354	ey_0Deg_layer3_122	-0.201687	ez_0Deg_layer3_123	-0.185
ex_45Deg_layer3_124	0.860862	ey_45Deg_layer3_125	0.937955	ez_45Deg_layer3_126	0.24
ex_90Deg_layer3_127	-0.165029	ey_90Deg_layer3_128	1.16905	ez_90Deg_layer3_129	0.12
ex_135Deg_layer3_130	-1.16263	ey_135Deg_layer3_131	0.843113	ez_135Deg_layer3_132	0.015
ex_180Deg_layer3_133	-1.54163	ey_180Deg_layer3_134	-0.347	ez_180Deg_layer3_135	-0.415
ex_225Deg_layer3_136	-0.467816	ey_225Deg_layer3_137	-1.09697	ez_225Deg_layer3_138	-0.375
ex_270Deg_layer3_139	-0.326369	ey_270Deg_layer3_140	-1.201	ez_270Deg_layer3_141	0.275
ex_315Deg_layer3_142	0.935205	ey_315Deg_layer3_143	-0.923845	ez_315Deg_layer3_144	0.39
x_o	0	y_o	0	z_o	80

Table 2: Final Fitted magnetic field parameters

B.5 Visualization of Interpolated Magnetic Field Maps

These plots display a random selection of the interpolated magnetic field maps from a few of the 45 positions where data was collected, covering the entire 5mm grid. These visual comparisons highlight how the interpolated data captures the expected field variations and smooth transitions, even at finer resolutions.

The some of the 45 points of the grid map that the plots are plotted is the grid shown in Figure 5.5.

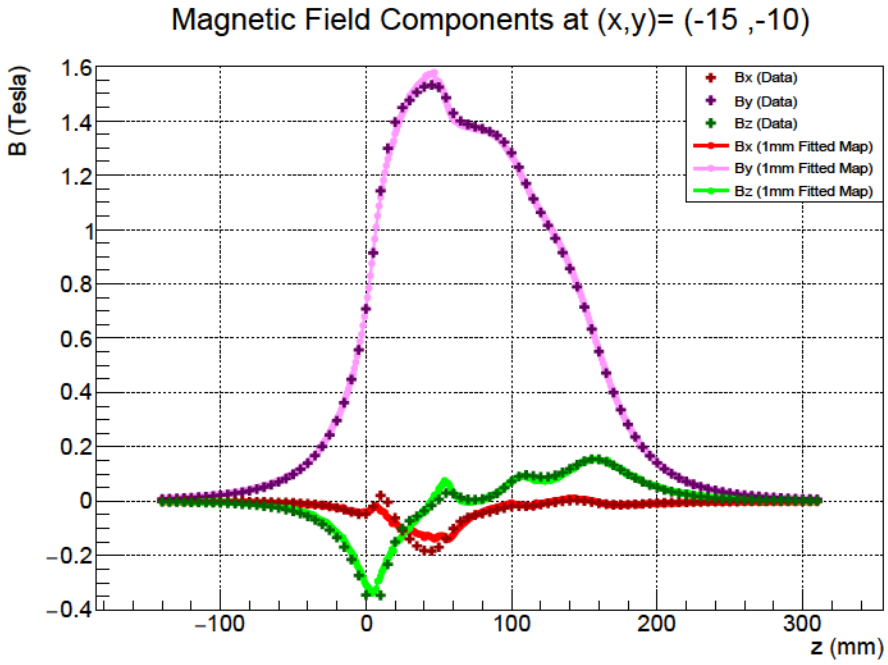

Figure 2: Interpolated magnetic field map for the 1 mm resolution data at (-15, -10)

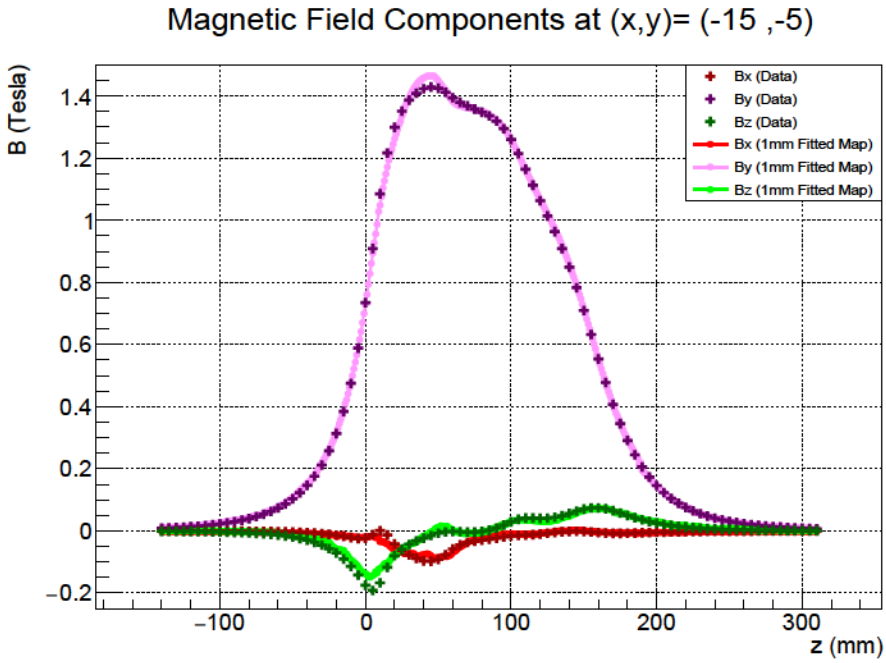

Figure 3: Interpolated magnetic field map for the 1 mm resolution data at (-15, -5)

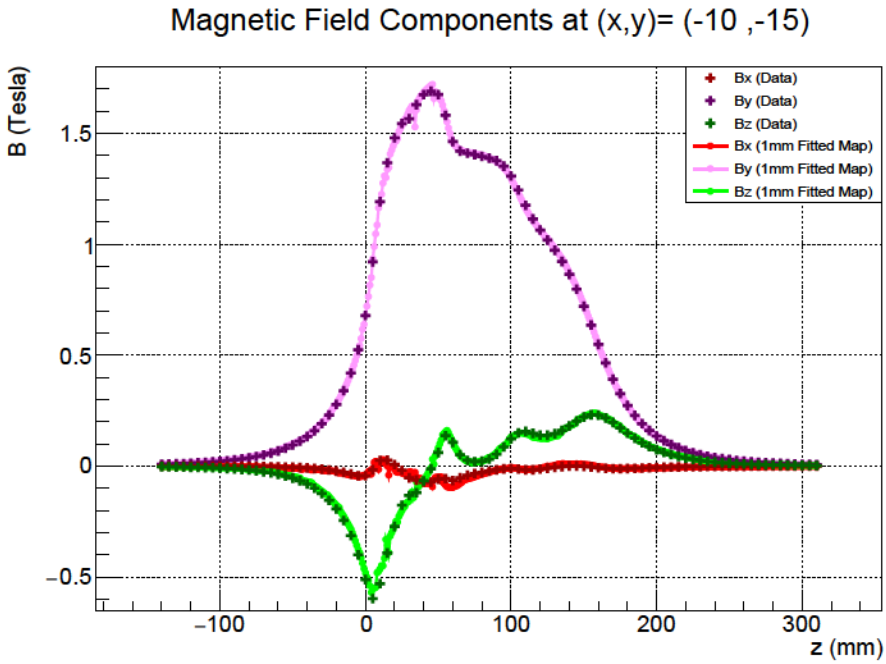

Figure 4: Interpolated magnetic field map for the 1 mm resolution data at (-10, -15)

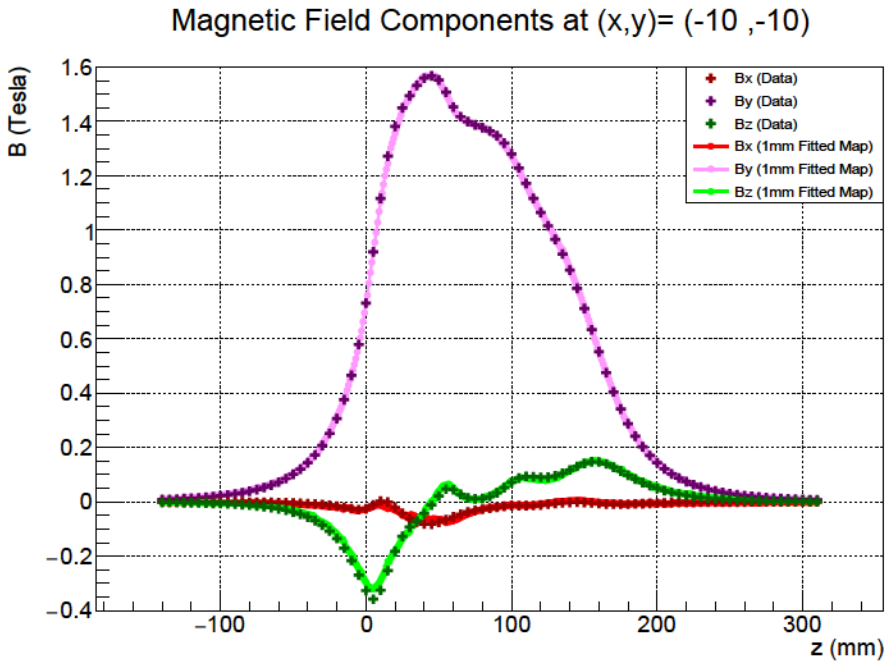

Figure 5: Interpolated magnetic field map for the 1 mm resolution data at (-10, -10)

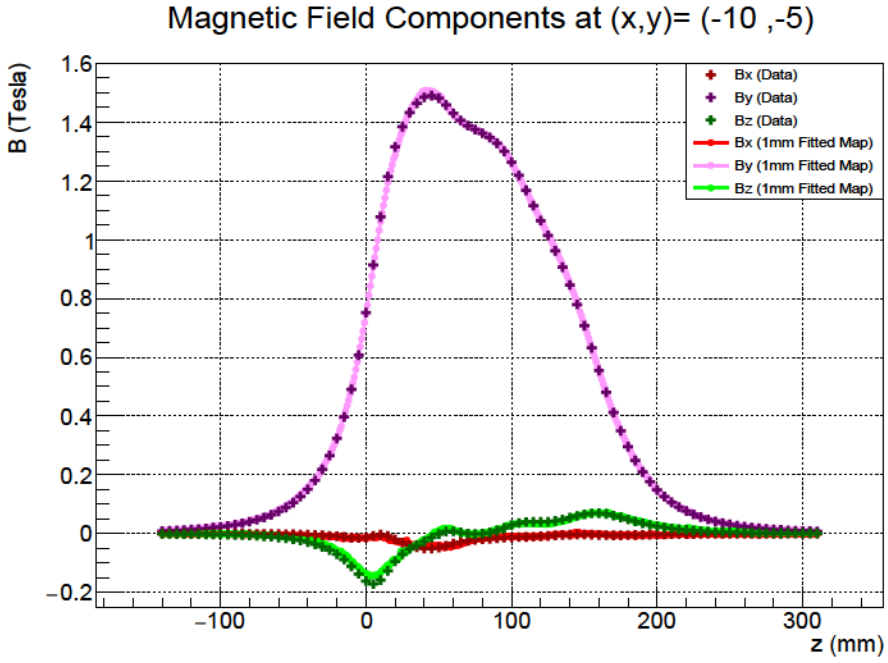

Figure 6: Interpolated magnetic field map for the 1 mm resolution data at (-10, -5)

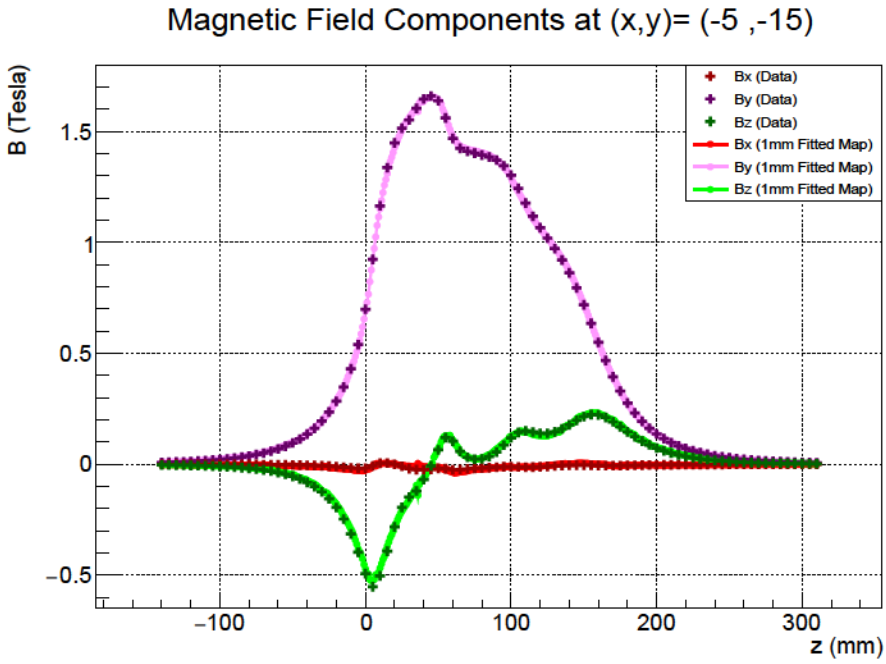

Figure 7: Interpolated magnetic field map for the 1 mm resolution data at (-5, -15)

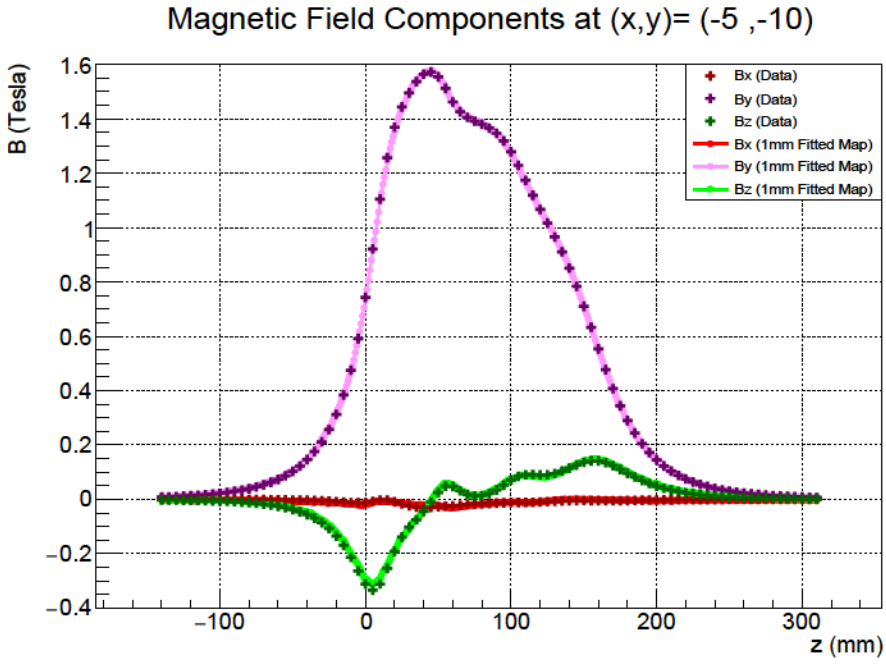

Figure 8: Interpolated magnetic field map for the 1 mm resolution data at (-5, -10)

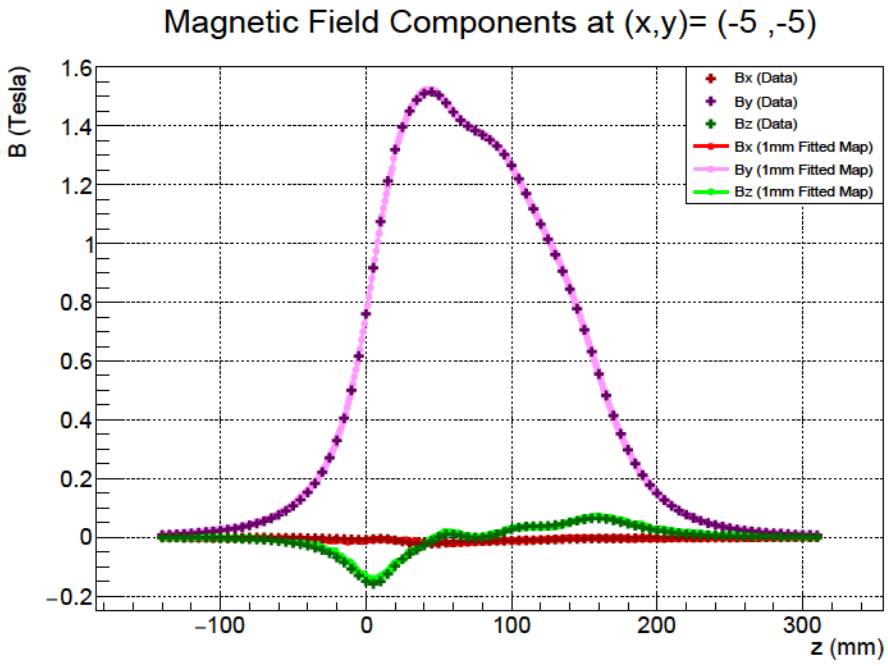

Figure 9: Interpolated magnetic field map for the 1 mm resolution data at (-5, -5)

Bibliography

[1] J. Chadwick. "The intensity distribution in the magnetic spectrum of beta particles from radium (B + C)". In: *Verh. Phys. Gesell.* 16 (1914), pp. 383–391.

[2] E. Fermi. "An attempt of a theory of beta radiation. I". In: *Z. Phys* 88 (1934), pp. 161–177. DOI: 10.1007/BF01351864.

[3] C. L. Cowan et al. "Detection of the Free Neutrino: a Confirmation". In: *Science* 124 (1956), pp. 103–104. DOI: 10.1126/science.124.3212.103.

[4] G. Danby et al. "Observation of High-Energy Neutrino Reactions and the Existence of Two Kinds of Neutrinos". In: *Phys. Rev. Lett.* 9 (1962), pp. 36–44. DOI: 10.1103/PhysRevLett.9.36.

[5] The Nobel Prize. *The Nobel Prize in Physics 1988*. [Accessed: 20-Jun-2024]. 1988. URL: https://www.nobelprize.org/prizes/physics/1988/summary/.

[6] Fermilab. *Physicists Find First Direct Evidence for Tau Neutrino at Fermilab*. Accessed: 2024-06-20. July 2000. URL: https://news.fnal.gov/2000/07/physicists-find-first-direct-evidence-tau-neutrino-fermilab/.

[7] P. Adamson et al. "The NuMI neutrino beam". In: *Nuclear Instruments and Methods in Physics Research Section A: Accelerators, Spectrometers, Detectors and Associated Equipment* 806 (Jan. 2016), pp. 279–306. ISSN: 0168-9002. DOI: 10.1016/j.nima.2015.08.063. URL: http://dx.doi.org/10.1016/j.nima.2015.08.063.

[8] K. Abe et al. "The T2K experiment". In: *Nuclear Instruments and Methods in Physics Research Section A: Accelerators, Spectrometers, Detectors and Associated Equipment* 659.1 (Dec. 2011), pp. 106–135. ISSN: 0168-9002. DOI: 10.1016/j.nima.2011.06.067. URL: http://dx.doi.org/10.1016/j.nima.2011.06.067.

[9] V. Papadimitriou et al. *Design Of The LBNF Beamline*. 2017. arXiv: 1704.04471.

[10] Dave G. *Standard Model Standard Infographic*. Accessed: 2024-06-20. 2023. URL: https://daveg.medium.com/standard-model-standard-infographic-fbf9ad981b30.

[11] J. A. Formaggio and G. P. Zeller. "From eV to EeV: Neutrino cross sections across energy scales". In: *Reviews of Modern Physics* 84.3 (Sept. 2012), pp. 1307–1341. ISSN: 1539-0756. DOI: 10.1103/revmodphys.84.1307. URL: http://dx.doi.org/10.1103/RevModPhys.84.1307.

[12] S. T. Petcov. "The Nature of Massive Neutrinos". In: *Adv. High Energy Phys.* 2013 (2013), p. 852987. DOI: 10.1155/2013/852987. arXiv: 1303.5819 [hep-ph].

[13] John N. Bahcall and R. Davis. "Solar Neutrinos - a Scientific Puzzle". In: *Science* 191 (1976), pp. 264–267. DOI: 10.1126/science.191.4224.264.

[14] Carlo Giunti and Chung W. Kim. *Fundamentals of Neutrino Physics and Astrophysics*. 2007. ISBN: 978-0-19-850871-7.

[15] L. Wolfenstein. "Neutrino oscillations in matter". In: *Phys. Rev. D* 17 (9 May 1978), pp. 2369–2374. DOI: 10.1103/PhysRevD.17.2369. URL: https://link.aps.org/doi/10.1103/PhysRevD.17.2369.

[16] Y. Fukuda et al. "The Super-Kamiokande detector". In: *Nucl. Instrum. Meth. A* 501 (2003). Ed. by V. A. Ilyin, V. V. Korenkov, and D. Perret-Gallix, pp. 418–462. DOI: 10.1016/S0168-9002(03)00425-X.

[17] Geoffrey B. Mills. "Neutrino oscillation results from LSND". In: *Nucl. Phys. B Proc. Suppl.* 91 (2001). Ed. by J. Law, R. W. Ollerhead, and J. J. Simpson, pp. 198–202. DOI: 10.1016/S0920-5632(00)00941-5.

[18] Pedro A.N. Machado, Ornella Palamara, and David W. Schmitz. "The Short-Baseline Neutrino Program at Fermilab". In: *Annual Review of Nuclear and Particle Science* 69.1 (Oct. 2019), pp. 363–387. ISSN: 1545-4134. DOI: 10.1146/annurev-nucl-101917-020949. URL: http://dx.doi.org/10.1146/annurev-nucl-101917-020949.

[19] Justin Evans. *The MINOS experiment: results and prospects*. 2013. DOI: https://doi.org/10.1155/2013/182537. eprint: https://onlinelibrary.wiley.com/doi/pdf/10.1155/2013/182537. URL: https://onlinelibrary.wiley.com/doi/abs/10.1155/2013/182537.

[20] Ko Abe and Hide-Kazu Tanaka. "Hyper-Kamiokande construction status and prospects". In: *Frontiers in Physics* 12 (2024). ISSN: 2296-424X. DOI: 10.3389/fphy.2024.1378254. URL: https://www.frontiersin.org/journals/physics/articles/10.3389/fphy.2024.1378254.

[21] B. Abi et al. *Volume I. Introduction to DUNE*. Aug. 2020. DOI: 10.1088/1748-0221/15/08/T08008. URL: https://dx.doi.org/10.1088/1748-0221/15/08/T08008.

[22] M. Apollonio et al. "Search for neutrino oscillations on a long base-line at the CHOOZ nuclear power station". In: *Eur. Phys. J. C* 27 (Apr. 2003). Issue Date: April 2003, pp. 331–374. DOI: 10.1140/epjc/s2002-01127-9.

[23] Jun Cao and Kam-Biu Luk. "An overview of the Daya Bay reactor neutrino experiment". In: *Nuclear Physics B* 908 (July 2016), pp. 62–73. ISSN: 0550-3213. DOI: 10.1016/j.nuclphysb.2016.04.034. URL: http://dx.doi.org/10.1016/j.nuclphysb.2016.04.034.

[24] J. K. Ahn et al. "Observation of Reactor Electron Antineutrinos Disappearance in the RENO Experiment". In: *Phys. Rev. Lett.* 108 (19 May 2012), p. 191802. DOI: 10.1103/PhysRevLett.108.191802. URL: https://link.aps.org/doi/10.1103/PhysRevLett.108.191802.

[25] Y. Fukuda et al. "Solar neutrino data covering solar cycle 22". In: *Phys. Rev. Lett.* 77 (1996), pp. 1683–1686. DOI: 10.1103/PhysRevLett.77.1683.

[26] J. N. Abdurashitov, E. P. Veretenkin, V. M. Vermul, et al. "Solar neutrino flux measurements by the Soviet-American gallium experiment (SAGE) for half the 22-year solar cycle". In: *J. Exp. Theor. Phys.* 95 (2002), pp. 181–193. DOI: 10.1134/1.1506424.

[27] W. Hampel et al. "GALLEX solar neutrino observations: Results for GALLEX IV". In: *Phys. Lett. B* 447 (1999), pp. 127–133. DOI: 10.1016/S0370-2693(98)01579-2.

[28] S. van der Meer. "A Directive Device for Charged Particles and Its use in an Enhanced Neutrino Beam". In: (Feb. 1961). DOI: 10.5170/CERN-1961-007.

[29] P. Adamson et al. "The NuMI neutrino beam". In: *Nuclear Instruments and Methods in Physics Research Section A: Accelerators, Spectrometers, Detectors and Associated Equipment* 806 (Jan. 2016), pp. 279–306. ISSN: 0168-9002. DOI: 10.1016/j.nima.2015.08.063. URL: http://dx.doi.org/10.1016/j.nima.2015.08.063.

[30] Fermilab Test Beam Facility. *Fermilab Test Beam Facility*. 2018. URL: http://ftbf.fnal.gov.

[31] Leonidas Aliaga Soplin. "Neutrino Flux Prediction for the NuMI Beamline". PhD thesis. William-Mary Coll., 2016. DOI: 10.2172/1250884.

[32] S KOPP. "Accelerator neutrino beams". In: *Physics Reports* 439.3 (Feb. 2007), pp. 101–159. ISSN: 0370-1573. DOI: 10.1016/j.physrep.2006.11.004. URL: http://dx.doi.org/10.1016/j.physrep.2006.11.004.

[33] G. Ambrosini et al. "Measurement of charged particle production from 450-GeV/c protons on beryllium". In: *Eur. Phys. J. C* 10 (1999), pp. 605–627. DOI: 10.1007/s100520050601.

[34] M. G. Catanesi et al. "The HARP detector at the CERN PS". In: *Nucl. Instrum. Meth. A* 571 (2007), pp. 527–561. DOI: 10.1016/j.nima.2006.08.132.

[35] A. Rodriguez et al. "Measurement of single charged pion production in the charged-current interactions of neutrinos in a 1.3-GeV wide band beam". In: *Phys. Rev. D* 78 (2008), p. 032003. DOI: 10.1103/PhysRevD.78.032003.

[36] Alexis A. Aguilar-Arevalo. "The MiniBooNE Experiment". In: *eConf* C0406271 (2004). Ed. by Ulrich Heintz, MONP01. arXiv: hep-ex/0408074.

[37] K. Hiraide et al. "Search for Charged Current Coherent Pion Production on Carbon in a Few-GeV Neutrino Beam". In: *Phys. Rev. D* 78 (2008), p. 112004. DOI: 10.1103/PhysRevD.78.112004. arXiv: 0811.0369 [hep-ex].

[38] Rajendran Raja. "The Main Injector Particle Physics Experiment (MIPP FNAL E-907) at Fermilab – status and plans". In: *Nuclear Physics B - Proceedings Supplements* 175–176 (Jan. 2008), pp. 17–24. ISSN: 0920-5632. DOI: 10.1016/j.nuclphysbps.2007.10.003. URL: http://dx.doi.org/10.1016/j.nuclphysbps.2007.10.003.

[39] L. Aliaga et al. "Neutrino flux predictions for the NuMI beam". In: *Physical Review D* 94.9 (Nov. 2016). ISSN: 2470-0029. DOI: 10.1103/physrevd.94.092005. URL: http://dx.doi.org/10.1103/PhysRevD.94.092005.

[40] N Abgrall et al. "NA61/SHINE facility at the CERN SPS: beams and detector system". In: *Journal of Instrumentation* 9.06 (June 2014), P06005. DOI: 10.1088/1748-0221/9/06/P06005. URL: https://dx.doi.org/10.1088/1748-0221/9/06/P06005.

[41] F. Siklér et al. "Hadron production in nuclear collisions from the NA49 experiment at 158-GeV/c/A". In: *Nucl. Phys. A* 661 (1999). Ed. by L. Riccati, M. Masera, and E. Vercellin, pp. 45–54. DOI: 10.1016/S0375-9474(99)85007-6.

[42] L Fields and P Podlaski. *Report from the NA61/SHINE experiment at the CERN SPS*. Tech. rep. Geneva: CERN, 2020. URL: https://cds.cern.ch/record/2739340.

[43] T. Akaishi and et al. "EMPHATIC: A Proposed Experiment to Measure Hadron Scattering and Production Cross Sections for Improved Neutrino Flux Predictions". In: (Dec. 2019). URL: https://www.osti.gov/biblio/1594135.

[44] G. Bellettini et al. "Proton-nuclei cross sections at 20 GeV". In: *Nucl. Phys.* 79 (1966), pp. 609–624. DOI: 10.1016/0029-5582(66)90267-7.

[45] A. S. Carroll et al. "Absorption Cross-Sections of $\pi^{\pm}$, $K^{\pm}$, p and $\bar{p}$ on Nuclei Between 60 GeV/c and 280 GeV/c". In: *Phys. Lett. B* 80 (1979), pp. 319–322. DOI: 10.1016/0370-2693(79)90226-0.

[46] S. P. Denisov et al. "Absorption cross-sections for pions, kaons, protons and anti-protons on complex nuclei in the 6-GeV/c to 60-GeV/c momentum range". In: *Nucl. Phys. B* 61 (1973), pp. 62–76. DOI: 10.1016/0550-3213(73)90351-9.

[47] Fermi National Accelerator Laboratory. *NOvA experiment sees first long-distance neutrinos*. Accessed: 2024-07-18. 2014. URL: https://news.fnal.gov/2014/02/nova-experiment-sees-first-long-distance-neutrinos/.

[48] R. Acciarri et al. *Improved Limits on Millicharged Particles Using the ArgoNeuT Experiment at Fermilab*. Apr. 2020. DOI: 10.1103/PhysRevLett.124.131801. URL: https://link.aps.org/doi/10.1103/PhysRevLett.124.131801.

[49] L.H. Whitehead. "Neutrino oscillations with MINOS and MINOS+". In: *Nuclear Physics B* 908 (July 2016), pp. 130–150. ISSN: 0550-3213. DOI: 10.1016/j.nuclphysb.2016.03.004. URL: http://dx.doi.org/10.1016/j.nuclphysb.2016.03.004.

[50] S. van der Meer. "A Directive Device for Charged Particles and Its use in an Enhanced Neutrino Beam". In: (Feb. 1961). DOI: 10.5170/CERN-1961-007.

[51] T. G. Olson. "Measurement of $d^2\sigma/d$—$\vec{q}$—dE_{avail} and 2p2h contribution using charged current ν_μ interactions in the NOvA Near Detector". PhD thesis. Tufts University, Sept. 2021.

[52] D. S. Ayres et al. *The NOvA Technical Design Report*. Tech. rep. NOvA Collaboration, Oct. 2007. DOI: 10.2172/935497.

[53] Thomas Wieber. *Near Detector Swaps Summary*. Internal Document. https://nova-docdb.fnal.gov/cgi-bin/sso/ShowDocument?docid=60023. Fermilab, 2024.

[54] Teresa Lackey. *Proposed NearDet swaps for shutdown 2023*. Internal Document NOVA Document 59972-v1. https://nova-docdb.fnal.gov/cgi-bin/sso/ShowDocument?docid=59972. Fermilab, 2023.

[55] S. Agostinelli et al. "GEANT4 - A Simulation Toolkit". In: *Nucl. Instrum. Meth. A* 506 (2003), pp. 250–303. DOI: 10.1016/S0168-9002(03)01368-8.

[56] J. Allison et al. "Recent developments in Geant4". In: *Nuclear Instruments and Methods in Physics Research Section A: Accelerators, Spectrometers, Detectors and Associated Equipment* 835 (2016), pp. 186–225. ISSN: 0168-9002. DOI: https://doi.org/10.1016/j.nima.2016.06.125. URL: https://www.sciencedirect.com/science/article/pii/S0168900216306957.

[57] C. Andreopoulos et al. "The GENIE neutrino Monte Carlo generator". In: *Nuclear Instruments and Methods in Physics Research Section A: Accelerators, Spectrometers, Detectors and Associated Equipment* 614.1 (2010), pp. 87–104. ISSN: 0168-9002. DOI: https://doi.org/10.1016/j.nima.2009.12.009. URL: https://www.sciencedirect.com/science/article/pii/S0168900209023043.

[58] Fermilab Collaboration. *FluxReader Documentation*. https://cdcvs.fnal.gov/redmine/projects/fluxreader/wiki. Internal Document.

[59] Leonidas Aliaga Soplin. *2017-2018 Beam Plots*. NOVA Document 20843-v12. Internal Document. [NOvA DocDB Home]. 2017.

[60] M. Pavin et al. "Measurement of proton-carbon forward scattering in a proof-of-principle test of the EMPHATIC spectrometer". In: *Phys. Rev. D* 106 (11 Dec. 2022), p. 112008. DOI: 10.1103/PhysRevD.106.112008. URL: https://link.aps.org/doi/10.1103/PhysRevD.106.112008.

[61] Gavin S. Davies. "EMPHATIC". In: Fermi National Accelerator Laboratory (FNAL), Batavia, IL (United States). Oct. 2024. DOI: 10.2172/2474970. URL: https://www.osti.gov/biblio/2474970.

[62] Source Magnets. *Halbach Array Magnet*. Accessed: 2024-12-04. 2024. URL: https://sourcemagnets.com/products/halbach-array-magnet/.

[63] SABR Enterprises. *SABR Enterprises: Specialist in Advanced Business Resources*. Accessed: 2024-12-04. 2024. URL: https://sabrllc.net/#/.

[64] Peter Blümler and Helmut Soltner. "Practical Concepts for Design, Construction and Application of Halbach Magnets in Magnetic Resonance". In: *Applied Magnetic Resonance* 54 (2023), pp. 1701–1739. DOI: 10.1007/s00723-023-01602-2. URL: https://doi.org/10.1007/s00723-023-01602-2.

[65] Leo Bellantoni. *EMPHATIC-doc-1643-v13*. EMPHATIC Internal Document. Apr. 2024.

[66] Applied Physics and Superconducting Technology Directorate. *Fermilab: Applied Physics and Superconducting Technology Directorate*. Accessed: 2024-12-04. 2024. URL: https://td.fnal.gov.

[67] COMSOL AB. *COMSOL Multiphysics® v. 6.1*. COMSOL AB, Stockholm, Sweden. https://www.comsol.com. 2024.

[68] FermiLab. *DUNE at LBNF*. Last accessed on 2023-07-03. 2014. URL: https://lbnf-dune.fnal.gov/how-it-works/introduction/.

[69] M. Adinolfi et al. "The KLOE electromagnetic calorimeter". In: *Nuclear Instruments and Methods in Physics Research Section A: Accelerators, Spectrometers, Detectors and Associated Equipment* 482.1 (2002), pp. 364–386.

[70] A. Abed Abud et al. *Deep Underground Neutrino Experiment (DUNE) Near Detector Conceptual Design Report*. 2021. arXiv: 2103.13910 [physics.ins-det]. URL: https://arxiv.org/abs/2103.13910.

[71] Prachi Sharma et al. "Straw Tube Studies and Prototype Assembly for DUNE". In: *Springer Proc. Phys.* 282 (2023), pp. 67–73. DOI: 10.1007/978-3-031-19268-5_9.

[72] H. Schindler and R. Veenhof. " Garfield++ simulation of ionisation based tracking detectors". In: (2018).

List of Publications

Publications and Collaboration Technical Notes with Direct Contribution

1. P. Sharma, "*Precise Magnetic Field Mapping of the EMPHATIC Phase 1 Magnet with COMSOL*," Accepted in Journal of Instrumentation, *arXiv*: 2501.01979, Dec, 2024.
2. P. Sharma *et al.*, "*Experimental Properties of an Assembled Straw Tube and Simulation Studies with Garfield++*," *Springer Proc. Phys.*, vol. 304, pp. 1278–1280, 2024. doi:10.1007/978-981-97-0289-3_363.
3. P. Sharma *et al.*, "*Reducing Flux Uncertainties of NuMI Beamline*," *Springer Proc. Phys.*, vol. 304, pp. 1026–1028, 2024. doi:10.1007/978-981-97-0289-3_276.
4. P. Sharma *et al.*, "*Straw Tube Studies and Prototype Assembly for DUNE*," *Springer Proc. Phys.*, vol. 282, pp. 67–73, 2023. doi:10.1007/978-3-031-19268-5_9.
5. P. Sharma, "*Comparison of Flux, Energy and Momentum Spectra at Various Virtual Detector Planes Downstream of Horn 1 for Horn On and Off Configurations in the NuMI Beamline*," NOνA Internal Technical Note, `NOVA-doc-61106-v1`, Jan 28, 2024.
6. P. Sharma, "*Precise Magnetic Field Mapping of the EMPHATIC Phase 1 Magnet*," EMPHATIC Internal Note, `EMPHATIC Document 2054-v2`, Dec 09, 2024.

Presentations in Conferences and Workshops

1. P. Sharma, "*Precise Magnetic Field Mapping of the EMPHATIC Phase 1 Magnet with COMSOL*," presented at 13th International Workshop on Neutrino Beams and Instrumentation, AYA'S LABORATORY Quantum Beam Research Center (AQBRC), Ibaraki, Japan, Oct 7–10, 2024.
2. P. Sharma, "*Precise Magnetic Field Mapping of the EMPHATIC Phase 1 Magnet with COMSOL*," presented at NuFact 2024, the 25th International Workshop on Neutrinos from Accelerators, Argonne National Laboratory, USA, Sep 16, 2024.
3. P. Sharma, "*Experimental Study of Properties of an Assembled Single Straw Tube and Other Simulation Studies with GARFIELD++*," presented at the XXV DAE-BRNS High Energy Physics Symposium 2022, Panjab University, India.
4. P. Sharma, "Straw Tube Studies and Prototype Assembly for DUNE," presented at the Workshop on Advanced Radiation Detector and Instrumentation in Nuclear and Particle Physics (RAPID 2021), University of Jammu, Oct 25–29, 2021.
5. P. Sharma *et al.*, "*Reducing Flux Uncertainties of NuMI Beamline*," presented at the XXV DAE-BRNS High Energy Physics Symposium 2022, Panjab University, India.
6. P. Sharma, "Neutrino Detectors in Experimental Physics," presented at Chandigarh Science Congress (CHASCON 2020) , Dec 18, 2020.
7. P. Sharma *et al.*, "Principle of Off-Axis Neutrino Beam (Narrow Band Beam such as T2K, NOvA): Pros and Cons in Comparing to On-Axis Neutrino Beam," presented at the Vietnam School of Neutrinos, 16th Rencontres du Vietnam, Dec 7–18, 2020, awarded Best Presentation.

Publications as co-author with Collaborations

1. *NOνA Collaboration*, "Measurement of the double-differential cross section of muon-neutrino charged-current interactions with low hadronic energy in the NOvA Near Detector," FERMILAB-PUB-24-0654-PPD, *arXiv*: 2410.10222, Oct, 2024.
2. *NOνA Collaboration*, "Measurement of d2sigma/d—q—dEavail in charged current neutrino-nucleus interactions at $\langle E_\nu \rangle = 1.86\,\text{GeV}$ using the NOvA Near Detector," FERMILAB-PUB-24-0571-PPD, *arXiv*: 2410.05526, Oct, 2024.
3. *DUNE Collaboration*, "The track-length extension fitting algorithm for energy measurement of interacting particles in liquid argon TPCs and its performance with ProtoDUNE-SP data," FERMILAB-PUB-24-0561-LBNF-PPD, CERN-EP-2024-256, *arXiv*: 2409.18288, Sep, 2024.
4. *DUNE Collaboration*, "DUNE Phase II: scientific opportunities, detector concepts, technological solutions," FERMILAB-TM-2833-LBNF, *JINST* **19**, P12005 (2024), *arXiv*: 2408.12725, doi: 10.1088/1748-0221/19/12/P12005.
5. *DUNE Collaboration*, "First measurement of the total inelastic cross section of positively charged kaons on argon at energies between 5.0 and 7.5 GeV," *Phys. Rev. D* **110**, 092011 (2024), FERMILAB-PUB-24-0216-V, *arXiv*: 2408.00582, doi: 10.1103/PhysRevD.110.092011.
6. *DUNE Collaboration*, "Supernova Pointing Capabilities of DUNE," FERMILAB-PUB-24-0319-LBNF, *arXiv*: 2407.10339, Jul, 2024.
7. *NOνA Collaboration*, "Search for CP-Violating Neutrino Nonstandard Interactions with the NOvA Experiment," *Phys. Rev. Lett.* **133**, 201802 (2024), FERMILAB-PUB-24-0108-PPD, *arXiv*: 2403.07266, doi: 10.1103/PhysRevLett.133.201802.
8. *DUNE Collaboration*, "Performance of a Modular Ton-Scale Pixel-Readout Liquid Argon Time Projection Chamber," *Instruments* **8**, 41 (2024),

FERMILAB-PUB-24-0073-LBNF, *arXiv*: 2403.03212, doi: 10.3390/instruments8030041.

9. *DUNE Collaboration*, "Doping liquid argon with xenon in ProtoDUNE Single-Phase: effects on scintillation light," *JINST* **19**, P08005 (2024), FERMILAB-PUB-23-0819-LBNF, *arXiv*: 2402.01568, doi: 10.1088/1748-0221/19/08/P08005.

10. *DUNE Collaboration*, "The DUNE Far Detector Vertical Drift Technology. Technical Design Report," *JINST* **19**, T08004 (2024), FERMILAB-TM-2813-LBNF, *arXiv*: 2312.03130, doi: 10.1088/1748-0221/19/08/T08004.

11. *NOνA Collaboration*, "Expanding neutrino oscillation parameter measurements in NOvA using a Bayesian approach," *Phys. Rev. D* **110**, 012005 (2024), FERMILAB-PUB-23-667-AD-CSAID-ND, *arXiv*: 2311.07835, doi: 10.1103/PhysRevD.110.012005.

12. *NOνA Collaboration*, "The Profiled Feldman-Cousins technique for confidence interval construction in the presence of nuisance parameters," FERMILAB-PUB-22-476-ND, *arXiv*: 2207.14353 (2022).

Societal Impact

Neutrino physics plays a crucial role in understanding the universe, from the fundamental properties of matter to the origins of the cosmos. This thesis improves the precision of neutrino flux predictions, contributing to both scientific advancement and societal applications.

A major outcome of this research is the reduction of uncertainties in neutrino flux models. Experiments like NOνA and DUNE rely on accurate flux predictions to measure neutrino oscillations, which could help explain the universe's matter-antimatter asymmetry. By refining these predictions, this work strengthens the foundation for future discoveries in particle physics.

Beyond fundamental science, the computational and statistical tools used in this research have direct applications in data science and artificial intelligence (AI). The techniques developed in this thesis can be widely applicable to medical diagnostics, financial forecasting, climate modeling, and cybersecurity. These methodologies highlight how advances in physics directly contribute to modern AI-driven technologies.

Furthermore, neutrinos have strategic applications, particularly in earth tomography and nuclear monitoring. Natural neutrino flux can be used to detect underground structures, monitor nuclear reactors, and track fissile material production—essential for global security. The same data-driven techniques used in neutrino experiments are relevant to these applications, demonstrating the broader impact of this research.

The study of the magnetic field in the EMPHATIC experiment also has practi-

cal applications in applied physics. The optimization techniques developed for the Halbach array magnet can enhance the design of advanced magnetic systems used in MRI scanners, energy storage solutions, and particle accelerators—benefiting healthcare, clean energy, and industrial applications.

This research also emphasizes international collaboration and the development of remote monitoring infrastructure. The Remote Operations Center (ROC) established for the NOvA experiment in India demonstrates how such facilities can be used for large-scale monitoring in scientific research, industrial automation, and environmental observation. Establishing similar remote centers can improve global access to cutting-edge research and real-time data analysis, aligning with the growing need for interconnected, AI-assisted monitoring systems.

Finally, improvements in neutrino flux simulations and detector technology will directly benefit next-generation neutrino experiments. These advancements contribute to solving major scientific questions about the evolution of the universe. By reducing experimental uncertainties, this thesis accelerates progress toward groundbreaking discoveries in fundamental physics.

In summary, this research drives technological innovation with real-world impact. From AI and data science to nuclear security, medical imaging, and remote monitoring, the methodologies developed in this thesis demonstrate how fundamental research fuels progress across multiple disciplines, ultimately benefiting society as a whole.

DEPARTMENT OF PHYSICS

Centre of Advanced Study in Physics
PANJAB UNIVERSITY, CHANDIGARH- 160 014 (INDIA)
(Established under the Panjab University Act VII of 1947-enacted by the Govt. of India)

PHS 1601

Dated: 25/03/25

Tel. : +91-172-2541741
Fax : +91-172-2783336
E-mail: physics@pu.ac.in

To whom it may concern

This is to certify that research work entitled "**STUDY OF NEUTRINO OSCILLATIONS AND FLUX SYSTEMATICS IN THE NOνA EXPERIMENT AT FERMILAB**" is carried out by Prachi Sharma under the supervision of Prof. Vipin Bhatanagar in the Department of Physics is a original piece of work and no part of this work has been submitted for any other degree for this or any other University/Institute. It is further certified that the thesis has also been thoroughly checked using anti-plagiarism software and 9% similarity is found on similarity index. Nothing has been found that can be considered as plagiarized as per the Panjab University, Plagiarism Policy.

Prachi

(Prachi Sharma)
Signature & Name of
the candidate

Vipin Bhatnagar

(Prof. Vipin Bhatnagar)
Signature & Name of
the supervisor

S. K. Bhardwaj

Chairperson

Chairperson
Department of Physics
Panjab University
Chandigarh-160014

turnitin

Digital Receipt

This receipt acknowledges that Turnitin received your paper. Below you will find the receipt information regarding your submission.

The first page of your submissions is displayed below.

Submission author:	Prachi Sharma
Assignment title:	Quick Submit
Submission title:	Thesis_with_title_page
File name:	Prachi_Thesis_no_ref.pdf
File size:	14.09M
Page count:	168
Word count:	32,890
Character count:	171,049
Submission date:	21-Mar-2025 12:12PM (UTC+0530)
Submission ID:	2620836772

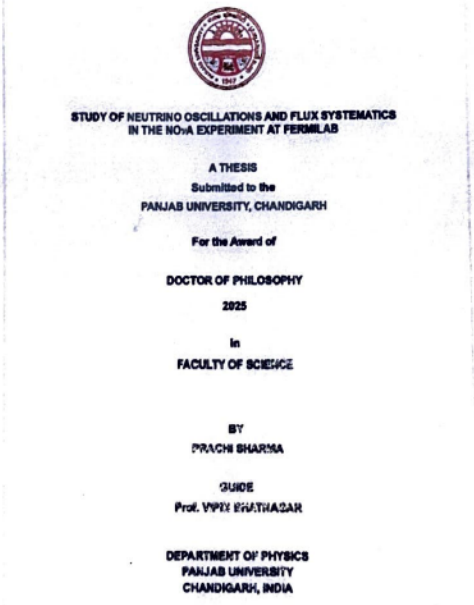

STUDY OF NEUTRINO OSCILLATIONS AND FLUX SYSTEMATICS IN THE NOvA EXPERIMENT AT FERMILAB

A THESIS

Submitted to the

PANJAB UNIVERSITY, CHANDIGARH

For the Award of

DOCTOR OF PHILOSOPHY

2025

in

FACULTY OF SCIENCE

BY

PRACHI SHARMA

GUIDE

Prof. VIPIN BHATNAGAR

DEPARTMENT OF PHYSICS

PANJAB UNIVERSITY

CHANDIGARH, INDIA

Chairperson
Department of Physics
Panjab University
Chandigarh-160014

Thesis_prachi_without_references

ORIGINALITY REPORT

9%	4%	7%	1%
SIMILARITY INDEX	INTERNET SOURCES	PUBLICATIONS	STUDENT PAPERS

PRIMARY SOURCES

1	Ferrazzi, Bruno Pereira. "A Study of Mirrors for an Aerogel Ring Imaging Cherenkov Detector", The University of Regina (Canada), 2023 Publication	<1%
2	Peter Blümler. "Magnetic Guiding with Permanent Magnets: Concept, Realization and Applications to Nanoparticles and Cells", Cells, 2021 Publication	<1%
3	indico.in2p3.fr Internet Source	<1%
4	cdcvs.fnal.gov Internet Source	<1%
5	Chvojka, J. "Anti-Neutrino Charged Current Quasi-Elastic Scattering in MINERnuA", Proquest, 2014. Publication	<1%
6	Submitted to Queen Mary and Westfield College Student Paper	<1%
7	repositories.lib.utexas.edu Internet Source	<1%
8	raiith.iith.ac.in Internet Source	<1%
9	Francesca Di Lodovico, Ryan B. Patterson, Masato Shiozawa, Elizabeth Worcester.	<1%

Chairperson
Department of Physics
Panjab University
Chandigarh-160014